

Wilfrid Laurier University

Scholars Commons @ Laurier

Theses and Dissertations (Comprehensive)

2019

Nanoscale Building Blocks: Bridging the Gap between Potential and Realized Applications

Nicole Ritter
cath9170@mylaurier.ca

Follow this and additional works at: <https://scholars.wlu.ca/etd>



Part of the [Materials Chemistry Commons](#)

Recommended Citation

Ritter, Nicole, "Nanoscale Building Blocks: Bridging the Gap between Potential and Realized Applications" (2019). *Theses and Dissertations (Comprehensive)*. 2167.
<https://scholars.wlu.ca/etd/2167>

This Dissertation is brought to you for free and open access by Scholars Commons @ Laurier. It has been accepted for inclusion in Theses and Dissertations (Comprehensive) by an authorized administrator of Scholars Commons @ Laurier. For more information, please contact scholarscommons@wlu.ca.

Nanoscale Building Blocks:

Bridging the gap between potential and realized nanoparticle applications

By

Nicole Elizabeth Ritter

Bachelor of Science, Honours Chemistry, Wilfrid Laurier University, 2009

Master of Science, Chemistry, Wilfrid Laurier University, 2011

DISSERTATION

Submitted to the Biological and Chemical Sciences Program

Faculty of Science

In partial fulfilment of the requirements for the

Doctor of Philosophy in the Biological and Chemical Sciences

Wilfrid Laurier University

2019

Abstract

The vast potential of nanoparticles and nanotechnology remains largely untapped; the crucial bottleneck being the knowledge gap between making and using nanoparticles (NPs). This PhD work bridges this gap by focusing on synthesizing nanoparticles with applications at the forefront. Four peer-reviewed publications are presented in Chapters 3-6, a safety and toxicological perspective is given in Chapter 7, and current work and future progress are summarized in Appendix 1. Bimorphic silver nanoparticles were prepared, presenting an innovative method to synthesize diverse nanostructures using polymeric surface blocking to break symmetry in seeded regrowth (Chapter 3).¹ Silver stars with D_{5h} symmetry were also synthesized using seeded regrowth and polymeric surface blocking (Chapter 4).² Both were proven to be beneficial in sensing applications, specifically surface plasmon resonance and surface enhanced Raman spectroscopy. To mediate the chemical stability of silver, gold coating and templating was used, which was also proven beneficial for sensing applications (Chapter 5).³ Using gold as a protective coating has enabled the development of metallodielectrics with a silver decahedral core, gold coating, and metal oxide shells. The method included in this work prepares shells of MnO_{2-x} , $FeOOH$, IrO_x , and SiO_2 , with varying porosities and advantages for sensing (Chapter 6).⁴ Reflecting on the contributions of this work, these four accounts present rational design pathways that are transferable to different systems, enabling properties to be tailored for the desired application. This bridges the gap between potential and realized applications.

- (1) Cathcart, N.; Kitaev, V. Symmetry Breaking by Surface Blocking: Synthesis of Bimorphic Silver Nanoparticles, Nanoscale Fishes and Apples. *Sci. Rep.* **2016**, *6*, 32561.
- (2) Cathcart, N.; Coombs, N.; Gourevich, I.; Kitaev, V. Synthesis and Sensing Properties of D_{5h} Pentagonal Silver Star Nanoparticles. *Nanoscale* **2016**, *8*, 18282–18290.
- (3) Cathcart, N.; Chen, J. I. L.; Kitaev, V. LSPR Tuning from 470 to 800 nm and Improved Stability of Au–Ag Nanoparticles Formed by Gold Deposition and Rebuilding in the Presence of Poly(Styrenesulfonate). *Langmuir* **2018**, *34*, 612–621.
- (4) Cathcart, N.; Murshid, N.; Campbell, P.; Kitaev, V. Selective Plasmonic Sensing and Highly Ordered Metallodielectrics via Encapsulation of Plasmonic Metal Nanoparticles with Metal Oxides. *ACS Appl. Nano Mater.* **2018**, *1*, 6514–6524.

Declaration of Co-Authorship

Chapter 3

This work was published in Scientific Reports by Nature Research and can be found online at:

<https://www.nature.com/articles/srep32561>.

N. Cathcart and V. Kitaev, Symmetry Breaking by Surface Blocking: Synthesis of Bimorphic Silver Nanoparticles, *Nanoscale Fishes and Apples*, *Sci. Rep.*, **2016**, *6*, 32561.

The procedure was discovered and developed by me with the assistance of V. Kitaev. My role was primarily experimental, preparation of the first draft of the manuscript, figures, and iterative refining. Images were taken by V. Kitaev.

Chapter 4

This work was published in *Nanoscale* by The Royal Society of Chemistry and is accessible online at:

<https://pubs.rsc.org/en/Content/ArticleLanding/2016/NR/C6NR07397B>

N. Cathcart, N. Coombs, I. Gourevich, and V. Kitaev, Synthesis and sensing properties of D_{5h} pentagonal silver star nanoparticles *Nanoscale* **2016**, *8*, 18282-18290.

The initial discovery and following synthetic developments were completed by me. Preparation of the manuscript was started by me, with iterative refinements as a joint effort with V. Kitaev. V. Kitaev, N. Coombs and I. Gourevich performed imaging and image processing.

Chapter 5

This work was published in *Langmuir* by The American Chemical Society and is accessible online at:

<https://pubs.acs.org/doi/abs/10.1021/acs.langmuir.7b03537>

N. Cathcart, J. I. L. Chen, and V. Kitaev, LSPR Tuning from 470 to 800 nm and Improved Stability of Au-Ag Nanoparticles Formed by Gold Deposition and Rebuilding in the Presence of Poly(Styrene sulfonate). *Langmuir* **2018**, 34, 612–621.

The discovery of the rebuilding process was made jointly by V. Kitaev and me, the computational work was completed by J.I.L. Chen. Images were taken by V. Kitaev. My primary role was experimental, preparation of the first draft of the manuscript, figures (experimental work), and iterative refining.

Chapter 6

This work was published in ACS Applied Nanomaterials by the American Chemical Society and is accessible online at: <https://pubs.acs.org/doi/abs/10.1021/acsanm.8b01964>

N. Cathcart, N. Murshid, P. Campbell, V. Kitaev, Selective Plasmonic Sensing and Highly-Ordered Metallodielectrics via Encapsulation of Plasmonic Metal Nanoparticles with Metal Oxides, *ACS Appl. Nano Mater.* **2018**, 1, 6514–6524.

My contribution to this work includes coordinating experiments and collating results. I was primarily responsible for MnO_{2-x} shells, N. Murshid for SiO₂, P. Campbell for IrO_x, and FeOOH shells were a joint effort between myself and N. Murshid. SPR measurements were completed in collaboration with N. Murshid, SERS measurements were completed by me. The first draft of the manuscript was prepared by me, figures were primarily my responsibility, with assistance by N. Murshid. Images were taken by V. Kitaev. Iterative refining of the manuscript was a joint effort between N. Murshid, V. Kitaev, and myself.

Acknowledgements

It takes a village to complete a PhD, and I'm incredibly grateful for mine. I've been privileged with supports both professionally and personally in my life that were paramount to my success, I don't take this luck for granted.

To my supervisor and mentor, Dr. Vladimir Kitaev, thank you for the opportunity for lab experience nearly 12 years ago; that has undoubtedly changed my life. Your constant support, encouragement, and guidance has enabled me to develop into a confident and capable chemist and afforded me boundless possibilities. To my committee members, Dr. Kenneth Maly, and Dr. Scott Smith, thank you for the constructive feedback and support; your advising has broadened my perspectives and encouraged me to think outside of my field. To the VK lab members, past and present, I'm proud of what we've been able to accomplish together in a fun, encouraging, and fruitful environment. Thank you for letting me develop my leadership and mentorship skills with you.

Thank you to my husband Josh, who supports my scientific endeavours, edits everything I write, and listens to every presentation practise; thank you for dreaming with me (and Rush), *the secret's told the same: life is just a candle, and a dream must give it flame*. Importantly, I want to thank my daughter Valentine, she has inspired me to be more cognizant of representation and is the source of my passion to learn, share, and advocate for women in STEM. She has also dramatically improved my scheduling skills and efficiency and puts so much into perspective. Completing this PhD as a parent would have been more challenging without the help of our families; specifically, I thank my mother in law for the free childcare every Tuesday for 3 years, and my mom and our sisters for taking on 'mom day' care for me to come to school. I'm additionally appreciative of our excellent day care provider, Coco. A special gratefulness to my wine and colouring crew, Holly and Kate, we started at the bottom (undergrad), now we're here!

I appreciatively acknowledge funding received for this work from NSERC PGS-D and QEII-OGS.

Table of Contents

List of Tables	x
List of Figures	xi
List of Abbreviations	xvii
1 General Introduction.....	1
1.1 Introduction.....	1
1.2 Objective of the Research	6
1.3 Significance.....	7
1.4 General Perspectives.....	8
1.5 References.....	13
2 Properties, Synthesis, and Applications of Nanoparticles.....	16
2.1 Localized Surface Plasmon Resonance.....	16
2.2 Electronic Properties of Silver and Gold.....	17
2.3 MNP synthesis	19
2.3.1 NP Growth: Thermodynamics vs. Kinetics.....	20
2.3.2 Surface Energy and Crystallographic Planes.....	22
2.3.3 Surface Stabilization	25
2.3.4 Symmetry Breaking.....	26
2.3.4.A Incorporation of Twin Defects.....	26
2.3.4.B Asymmetric Deposition on NP Seed (Seeded Regrowth)	28
2.4 Surface Enhanced Raman Spectroscopy	29
2.5 Surface Plasmon Resonance Spectroscopy	33

2.6 Metal Oxide Nanoparticles	35
2.7 MONP Synthesis	38
2.8 Applications of MONPs.....	41
2.9 Metallodielectric Nanoparticles (Synthesis and Applications)	44
2.10 Health and Safety Considerations	45
2.11 References.....	48
3 Symmetry Breaking by Surface Blocking: Synthesis of Bimorphic Nanoparticles, Nanoscale Fishes and Apples	61
3.1 Abstract	61
3.2 Introduction.....	62
3.3 Results and Discussions.....	63
3.4 Methods	74
3.5 Acknowledgement.....	74
3.6 Supplementary Information	74
3.7 References	97
4 Synthesis and Sensing Properties of D_{5h} Pentagonal Silver Star Nanoparticles	100
4.1 Abstract	100
4.2 Introduction.....	101
4.3 Experimental	103
4.4 Results and Discussion	106
4.4.1 Growth of Star Tips from Decahedra.....	109
4.4.2 Size and Sharpness of Stellation	111
4.4.2.A Concentration of Seed Variation	111
4.4.2.B Concentration of PANa Variation	113

4.4.3	SERS and SPR.....	117
4.4.4	Universality of the Developed Procedure of Stellated Regrowth	119
4.5	Conclusion	119
4.6	Acknowledgement.....	120
4.7	Supplementary Information	120
4.8	References.....	132
5	LSPR tuning from 470 to 800 nm and Improved Stability of Au-Ag Nanoparticles Formed by Gold Deposition and Rebuilding in the Presence of Poly(styrene sulfonate).....	136
5.1	Abstract	136
5.2	Introduction	137
5.3	Experimental Section	138
5.4	Results and Discussions.....	141
5.5	Summary and Conclusions	153
5.6	Acknowledgements	154
5.7	Supporting Information	154
5.8	References.....	181
6	Selective Plasmonic Sensing and Highly-Ordered Metallodielectrics via Encapsulation of Plasmonic Metal Nanoparticles with Metal Oxides.....	186
6.1	Abstract	186
6.2	Introduction.....	187
6.3	Results and Discussion	189
6.3.1	Formation and Properties of MO-MNPs.....	189
6.3.2	Sensing with MO _x @Au@AgDeNPs	199
6.3.3	SPR Sensing, Selective Detection of Phosphate	201

6.4	Conclusions.....	204
6.5	Methods	204
6.5.1	Reagents	204
6.5.2	Synthetic Protocols	205
6.5.3	Formation of Metal Oxide Shells onto Au@AgDeNPs	205
6.5.4	Characterization.....	206
6.6	Acknowledgements	208
6.7	Supplementary Information	208
6.8	References.....	223
7	Philosophical Takeaways.....	230
7.1	Perspectives in Biological and Chemical Sciences.....	230
7.1.1	Structure and Reactivity of Nanoscale Building Blocks	230
7.1.2	Environmental and Health Aspects of Nanoscale Building Blocks.....	234
7.1.3	Biotic Interactions of Nanoscale Building Blocks	235
7.2	General Conclusion	239
7.3	Future Perspectives.....	239
7.4	References.....	239
A1	Metal Oxide Nanoparticles as Photoelectrochemical Anodes and Their Potential for Environmental Remediation	242
A1.1	General Introduction	242
A1.2	Synthesis Methods.....	242
A1.3	Experimental Details.....	243
A1.3.1	Iron Oxide Nanoparticle Synthesis.....	243
A1.3.2	Manganese Oxide NP Synthesis	244

A1.3.3 Photoelectrochemical Set-Up	244
A1.4 Future Work – Photoelectrochemistry	246
A1.5 Future Work – Environmental Remediation	247
A1.6 References	247
A2 Methods and Glossary	250
A2.1 Decahedra NP synthesis	250
A2.2 Measuring NP size	250
A2.3 Surface plasmon resonance measurements	251
A2.4 Surface enhanced Raman spectroscopy measurements.....	253
A2.5 Glossary	254

List of Tables

3.1	Summary of experimental conditions for the formation of bimorphic AgNPs	67
3S.1	Summary of synthetic conditions for selected bi-AgNPs	75
4.1	Summary of the reaction condition for AgStDeNPs	85
5S.1	Experimental details from samples in Figure 5S.1	155
5S.2	Detailed information on simulated spectra from Figure 5.4	156
6S.1	Summary of experimental parameters for Figures 6.2 and 6S.4	208
6S.2	Values of Zet-potentials measured for MNPs and MO-MNPs	209
6S.3	N ₂ adsorption-desorption results for MnO _{2-x} @Au@AgDeNPs.....	214
A1.1	Summary of photocurrent density measured at various metal oxide photoelectrodes.....	246

List of Figures and Illustrations

1.1 Metal band gap and density of states dependence on size	2
1.2 Particle interacting with light schematic	3
1.3 Nanorainbow examples.....	5
1.4 Metal oxide valence band alignments.....	6
1.5 TEM images of apple and fish shaped NPs.....	10
1.6 TEM images and schematic of silver star NPs	10
1.7 UV-vis spectra, TEM, and calculated field intensity of Au-AgNPs	11
1.8 Schematic and EM images of metal oxide shells on MNPs	12
2.1 LSPR variations with size, shape, composition and interparticle spacing.....	17
2.2 Thermodynamic vs. kinetic control schematic	21
2.3 Equilibrium shapes of 72 elements.....	22
2.4 FCC schematics.....	24
2.5 Adsorption schematic of tricitrate and PVP on Ag	25
2.6 Twin defects schematic.....	26
2.7 Examples of twin defects in AgNPs and use for regrowth	27
2.8. Energy level transitions for IR and Raman spectroscopies	31
2.9 Examples of field enhancement and surface enhanced Raman spectroscopy enhancement	32
2.10 Schematics of metal oxide unit cells.....	36
2.11 Representative shapes of inorganic nanocrystals 0D to 3D	38
2.12 Overview of applications of iron oxide nanomaterials	43
2.13 Nanoparticle-cell interactions	46
3.1 Schematics of different growth pathways for bi-AgNP formation	64

3.2 Development of 2-D bi-AgNP morphologies with different amounts of silver	67
3.3 TEM images of diverse bi-AgNP shapes	72
3S.1 EM images demonstrating high shape yield	77
3S.2 TEM images of key bimorphic morphologies.....	78
3S.3 TEM images of high shape yield of bimorphic NPs from 3D growth	79
3S.4 TEM images and UV-vis spectra of irregular growth of bi-AgNPs.....	80
3S.5 TEM images, UV-vis spectra, and optical photographs of bi-AgNPs with increasing PAA.....	82
3S.6 TEM images of bi-AgNPs prepared with different polymers	84
3S.7 TEM images of bi-AgNPs prepared with various acids.....	86
3S.8 TEM images of bi-AgNPs with lower ratios of AgDeNPs to silver	87
3S.9 EM images, UV-vis spectra and optical photographs of bi-AgNPs with increasing ascorbic acid concentration.....	88
3S.10 TEM images of bi-AgNPs with different pH.....	90
3S.11 TEM images of bi-AgNPs prepared with bromide.....	91
3S.12 TEM images and UV-vis spectra of bi-AgNPs prepared with bromide.....	92
3S.13 TEM images of bi-AgNPs prepared with potassium chloride.....	93
3S.14 TEM images of bi-AgNPs prepared with hydrochloric acid.....	93
3S.15 TEM images of bi-AgNPs prepared with iodide	94
3S.16 TEM images of bi-AgNPs with silver platelets as seeds	94
3S.17 TEM images of bi-AgNPs galvanically replaced with tetrachloroauric acid	95
3S.18 Raman spectra from SERS experiments	96
3S.19 Coloured TEM images	96
4.1 Schematic and TEM images of silver star decahedral nanoparticles.....	107
4.2 Optical photographs and UV-vis spectra of AgStDeNPs	108

4.3 High resolution TEM images of AgStDeNPs	109
4.4 TEM images and UV-vis spectra of AgStDeNPs with different ascorbate concentrations	110
4.5 TEM images and UV-vis spectra of AgStDeNPs with different seed concentrations.....	112
4.6 TEM images and UV-vis spectra of AgStDeNPs with different sodium polyacrylate concentrations.	114
4S.1 SEM images of AgDeNPs and AgStDeNPs	120
4S.2 TEM images of AgStDeNPs prepared at different pH	121
4S.3 TEM images and UV-vis spectra of AgStDeNPs prepared with different silver concentrations	122
4S.4 TEM images and UV-vis spectra of AgStDeNPs prepared with slow and fast stirring	123
4S.5 TEM images and UV-vis spectra of AgStDeNPs prepared with varied time of ascorbate addition ..	124
4S.6 SPR response curve of AgStDeNPs over time	125
4S.7 TEM images and UV-vis spectra of AgStDeNPs with different aging treatments	126
4S.8 TEM images and UV-vis spectra of gold-coated AgStDeNPs	127
4S.9 TEM images and UV-vis spectra of AgStDeNPs aged at different pH	128
4S.10 Raman spectra from SERS measurements	129
4S.11 SPR response curves showing LSPR shifts from sequential addition of KBr	129
4S.12 SPR response curves showing LSPR shifts from different additions of KBr	130
4S.13 EM and UV-vis spectra of stellated pentagonal rods.....	131
4S.14 TEM images of stellated prisms and icosahedra.....	132
5.1 Schematics and TEM images of gold deposition on silver decahedra and post-transformations.....	142
5.2 UV-vis spectra and TEM images of AgDeNPs with varied mol. % gold	144
5.3 Optical photographs and TEM images of fresh and aged samples.....	145
5.4 FDTD simulated spectra	150
5.5 UV-vis spectra and TEM images of gold coated silver platelets	153
5S.1 Normalized UV-vis spectra demonstrating LSPR tuning of AgDeNPs, Au shells and Au-AgDeNPs...	157

5S.2 Photographs of LED and syringe pump set-ups	158
5S.3 TEM and UV-vis spectra of Au shells with different addition times	159
5S.4 LSPR peak wavelengths as a function of mol. % Au	160
5S.5 TEM images of aged Au-AgDeNPs with PVP or PSS	161
5S.6 LSPR peak tracking and UV-vis spectra of Au-AgDeNPs over time	162
5S.7 TEM images of aged Au-AgDeNPs with and without hydrogen peroxide	163
5S.8 UV-vis spectra and LSPR peak tracking for samples in Figure 5.2.....	164
5S.9 UV-vis spectra of Au-AgDeNPs before and after centrifugation.....	165
5S.10 LSPR peak tracking with time for 80 mol. % Au- AgDeNPs	166
5S.11 LSPR peak tracking with time for 80 mol. % Au- AgDeNPs	167
5S.12 FDTD simulated spectra of AgDeNPs with and without rounding	168
5S.13 FDTD calculations of electric field intensity	169
5S.14 FDTD simulated spectra of Au coating of AgDeNPs	170
5S.15 Stability test results from fresh samples.....	171
5S.16 Stability test results from aged samples	171
5S.17 Relative intensities from Figures 5S.15 and 5S.16	172
5S.18 Zeta potential measurements for Au-AgDeNPs with varied mol. % Au.....	172
5S.19 Representative zeta potential measurement	173
5S.20 Dynamic light scattering measurements for Au-AgDeNPs with varied mol. % Au	174
5S.21 Representative dynamic light scattering measurement	175
5S.22 SPR response curve for fresh Au-AgDeNPs with 10^{-8} M KI.....	176
5S.23 SPR response curve for aged Au-AgDeNPs with 10^{-8} M KI	176
5S.24 SERS enhancement factors for Au-AgDeNPs	177

5S.25 UV-vis and TEM images of Au plated Ag platelets and Au shells.....	178
5S.26 UV-vis and EM images of Au shells from silver pentagonal rods.....	179
5S.27 UV-vis and TEM images of rebuilt Au-Ag rods and Au-Ag platelets.....	180
6.1 Schematic, UV-vis spectra and EM images of MO-MNPs	191
6.2 EM images of MO-MNPs.....	195
6.3 LSPR peaks and optical photographs of MO-MNPs	197
6.4 Calculated enhancement factors for NP films as Raman substrates	201
6.5 Surface plasmon resonance response curves	203
6S.1 SPR monitoring of LSPR peaks during MO shell formation.....	210
6S.2 LSPR peak monitoring of IrO _x shell formation	210
6S.3 TEM images of samples prepared with excess Mn(II) precursors	211
6S.4 TEM images of MO-MNPs with thick and thin shells	212
6S.5 SPR response curves of stability and porosity tests.....	213
6S.6 N ₂ adsorption isotherm.....	214
6S.7 UV-vis spectra of samples from Figure 6.1 without normalization	215
6S.8 Normalized UV-vis spectra and optical photographs of dispersions and films	216
6S.9 SEM images of metallodielectric arrays.....	217
6S.10 AFM images of metallodielectric arrays.....	218
6S.11 SPR response curves of room temperature formation of SiO ₂ shells	218
6S.12 TEM and UV-vis spectra of IrO _x coated Au platelets.....	219
6S.13 UV-vis spectra, optical photos and TEM images of a scaled-up coating procedure	220
6S.14 Raman spectra from SERS measurements	221
6S.15 SPR response curves of MnO _{2-x} @Au@AgDeNPs with phosphate.....	222
7.1 Waste disposal procedure	235

7.2 Optical photographs of Ag ⁺ exposure to mold	236
7.3 Photographs of mold in silver decahedral NP solutions	237
7.4 Optical microscopy images of mold	238
7.5 EM images of mold with decahedra	238
A1.1 EM images of MONPs	243
A1.2 Photoelectrochemical cell set-up	244
A2.1 SEM images of faceted silver platelets with marked lateral dimension	251
A2.2 Photograph of OpenSPR instrument set-up	252
A2.3 Photograph of laser and sample holder set-up for SERS measurements.....	253

List of Abbreviations

2-ATP	2- aminothiophenol
AA	ascorbic acid
AFM	Atomic Force Microscopy
AgDeNPs	Silver Decahedra Nanoparticles
AgNPs	Silver Nanoparticles
AgStDeNPs	Silver Pentagonal Silver Star Nanoparticles (Silver Star Decahedra Nanoparticles)
Au@AgDeNPs	Gold coated Silver Decahedra Nanoparticles
Au-AgNPs	Gold -Silver Composite Nanoparticles
AuNPs	Gold Nanoparticles
BET	Brunauer-Emmett-Teller
bi-AgNPs	Bimorphic Silver Nanoparticles
bi-NPs	Bimorphic Nanoparticles
CTAB	cetyltrimethylammonium bromide
DOS	Density of Energy States
DTNB	5'5-dithiobis(2-nitrobenzoic acid)
EC ₅₀	Half maximal Effective Concentration
EDX	Energy Dispersive X-Ray
EM	Electron Microscopy
FCC	Face Centred Cubic
FDTD	Finite-Difference Time-Domain
FFT	Fast Fourier Transform
FTO	Fluorine-doped Tin Oxide
HER	Hydrogen Evolution Reaction
HOMO	Highest Occupied Molecular Orbital
IR	Infrared
LED	Light Emitting Diode
LSPR	Localized Surface Plasmon Resonance
LUMO	Lowest Occupied Molecular Orbital

MD	Metalodielectric
MDNPs	Metalodielectric Nanoparticles
MNP	Metal Nanoparticle
MO(x)	Metal Oxide(s)
MO-MNPs	Metal Oxide encapsulated Metal Nanoparticles
MONPs	Metal Oxide Nanoparticles
MOx@Au@AgDeNPs	Metal Oxide coated- Gold coated - Silver Decahedra Nanoparticles
NBBs	Nanoscale Building Blocks
NPs	Nanoparticles
OER	Oxygen Evolution Reaction
PAA	Poly(acrylic acid)
PANa	sodium polyacrylate
PDDA	poly(diallyldimethylammonium chloride)
PEC	Predicted Environmental Concentrations
PMMA	Poly(methyl methacrylate)
PNEC	Predicted No Effect Concentrations
PSS	Poly(styrene sulfonate)
PVP	Poly(vinylpyrrolidone)
$R_{Ag/seed}$	Ratio of new silver to silver in AgDeNP seeds
SEM	Scanning Electron Microscopy
SERS	Surface Enhanced Raman Spectroscopy
SPR	Surface Plasmon Resonance
TEM	Transmission Electron Microscopy
TEOS	tetraethyl orthosilicate
UV-vis	Ultraviolet-visible
XPS	X-Ray Photoelectron Spectroscopy

Chapter 1: General Introduction

1.1. Introduction

Achieving atomically precise control in the pursuit of perfection in the synthesis and study of nano-sized materials and nanoparticles is one of the main directions of materials chemistry.¹⁻³ Nanomaterials are within the size range bridging atomic (angstrom) and bulk (micrometer) scales, where novel and tunable properties are accessed by virtue of critical sizes.¹ These size regimes are depicted in Figure 1.1, where in bulk metals (with many atoms) there are many overlapping atomic orbitals, and a high density of states resulting in a continuum of delocalized electrons.⁴ Clusters with a small number of atoms, behave closer to atoms and molecules because their energy levels are discrete, and there is a gap (δ) between the lowest occupied molecular orbital (LUMO) and the highest occupied molecular orbital (HOMO).⁴ The density of atomic states is proportional to the number of atoms, so as the number of atoms increases, the bandwidth increases, until the critical point where the band gap ceases to exist for nanoparticles. This transition from insulator to metallic clusters and particles occurs when thermal energy (Boltzmann constant and temperature, kT) exceeds the Kubo gap, δ .⁴ Varying the size, and subsequently the number of atoms, will enable control over the density of states, and the associated properties (metallic clusters or particles vs. bulk).

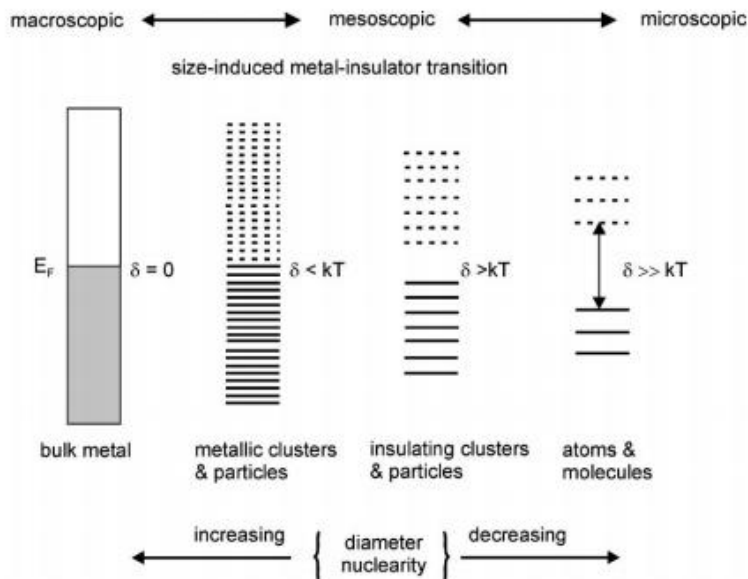


Figure 1.1. Metal band gap and density of states dependence on size. Republished from Ref.4¹

Nanoparticles feature diverse optical, electrical, magnetic, catalytic and sorption properties related to their size and surface.^{5,6} For the purpose of this research, noble metal NPs are investigated for their potential applications based on their optical⁷⁻⁹ and catalytic^{6,10} properties (closely related to electronic structure) and metal oxide NPs will be investigated for their semiconductor¹¹⁻¹³ and remediation (degradation and/or sorption) properties. This is further discussed in Chapter 2.

Desirable properties of noble metal NPs are predominantly based on their localized surface plasmon resonance (LSPR), a phenomenon only achieved when these metals are reduced in size to the nanoscale.¹⁴⁻²² The LSPR is the frequency at which free electrons on a metal NP surface oscillate in response to electromagnetic radiation. When the electric field of incoming light waves interacts with the conduction band electrons on the surface, a polarization is induced creating a dipolar oscillation of these electrons.^{7,14,17} This can be visualized by Figure 1.2.

¹ Republished with permission of *The Royal Society of Chemistry* from *Size matters: why nanomaterials are different*, Emil Roduner, 35, 2006; permission conveyed through Copyright Clearance Center, Inc.

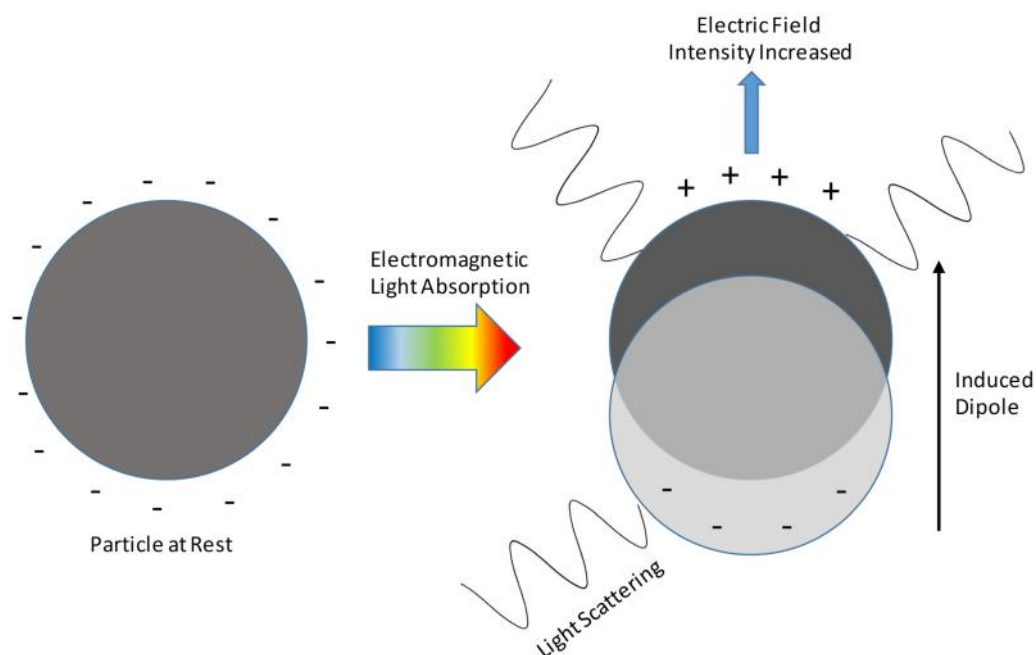


Figure 1.2. Schematic showing the transformation of a particle at rest upon interacting with light. Adapted from Ref.17.²

The size, shape, and composition of the metal nanoparticle (MNP) affects their interactions with electromagnetic radiation that directly affects the wavelength of the LSPR.²³ This resonance imparts both absorbance and scattering, therefore extinction is measured when using transmission UV-vis spectroscopy. Figure 1.3 shows several “nanorainbows” made by samples of nanoparticles with different size, shapes, and compositions. The colour associated with absorbance is complementary to the corresponding emission colour of the peak wavelength. As the size or the shape complexity increases, so does the LSPR, moving the colour of the solutions from yellow to blue (for absorbance of blue and orange light respectively). This shift also occurs with adsorption (albeit in a more moderate shift). Rainbows a and c were prepared through surface plasmon resonance sensing tests (that are described in Chapter 5) using silver decahedra (gold-coated or not) with different concentrations of target analytes including

² Adapted figure with permission from P. K. Jain, X. Huang, I. H. El-Sayed and M. A. El-Sayed, *Acc. Chem. Res.*, 2008, **41**, 1578–1586. Copyright 2008 American Chemical Society.

halides, thiols, and amines. Typical gold-coated silver decahedra have LSPR peak at 490 -500 nm, absorbing blue-cyan parts of the spectra which gives an orange colour to dispersions of these NPs. Analyte binding or pitting of the structures will shift the LSPR to higher wavelengths, which is observed by a colour change from orange to purple or blue. When silver decahedra are used, high concentrations of analytes round the vertices, lowering the LSPR to ca. 450 nm, yellow solutions. Rainbow b is prepared from silver decahedra (and platelets) of varying sizes. As these NPs get larger, their LSPR shifts to higher wavelengths, moving from pink (smaller) to purple (larger). The bicoloured appearance is due to scattering dominating absorbance in larger NPs (> ca. 50 nm). Nanorainbow in Figure 1.3d was prepared by varying the size of silver platelets (trigonal and/or hexagonal).



Figure 1.3. Different colours of NP dispersions attained in my research to display several “nanorainbows”, e.g. silver (with and without gold coating) nanoparticles of different sizes and shapes. a) and c) demonstrating colour changes from SPR testing of silver decahedra (with and without gold-coating) upon exposure to halides, thiols, and amines, b) silver decahedra and platelets of varying sizes, d) silver platelets of increasing size from right to left. Photographs from N. Ritter personal library of scientific images.

Controlling size, shape, and composition remains challenging in nanoparticle synthesis, especially with respect to balancing chemical stability and optical properties. The LSPR of metal nanoparticles is the fundamental property enabling their use in surface plasmon resonance (SPR) and surface enhanced Raman spectroscopy (SERS) sensing. These applications, as well as synthetic methods using symmetry breaking and kinetic growth, are discussed in Chapter 2.

Transition metal oxide nanoparticles have been gaining interest due to their affordable nature, and many industrial applications.^{24–26} Metal oxide nanoparticles (MONPs), as the name suggests, consist of a metal and oxygen. This combination offers a unique opportunity for electron transfer,²⁷ with improved chemical stability where the metal is in its highest oxidation state and cannot be oxidized further. The schematic presented in Figure 1.4 shows that metal oxides have a band gap that varies with composition (more so than size).

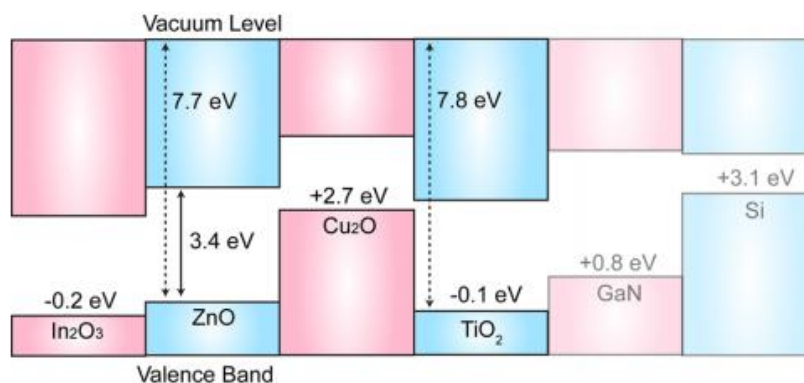


Figure 1.4. Metal oxide valence band alignments compared to GaN and Si semiconductors. Reproduced from Ref.28³

As with MNPs, the size, shape and composition dictate the properties, and as such, the grand challenge is the synthesis of MONPs with the composition, phase, size and shape control. Chapter 2 consists of a literature review of MONP synthetic methods, and potential applications.

1.2. Objective of the research:

Utilizing my experience in the preparation of nanoscale building blocks (NBBs) with well-defined and tunable functional properties, the aim of this research was to apply this knowledge to the development of nanoparticles for specific applications. In doing so, the gap between potential and real

³ (<https://pubs.acs.org/doi/abs/10.1021%2Far400115x>) with permission from the American Chemical Society (ACS). Further permissions related to the material excerpted should be directed to the ACS.

applications of nanoparticles is minimized. The objective of this research is to develop three different types of nanoparticles for the following desired applications: 1) noble metal nanoparticles (silver, gold, gold-coated silver, silver-coated-gold-coated silver) for sensing, 2) metallodielectric composites for sensing and photonics, and 3) metal oxide nanoparticles for environmental remediation and photoelectrochemistry. In addition, the toxicity of silver nanoparticles for microorganisms, particularly, mold, will be outlined in the discussion of Chapter 7. The overarching goal of this PhD work contributes to the understanding of size and shape control in the synthesis of metal, metal oxide and metal oxide coated metal NPs. Additionally, optimizing these NPs for their use in sensing (including preparation of substrates with commercialization potential), photoelectrochemistry, and environmental remediation applications will provide verification of improvement in enhancement factors, detection limits, conversion and/or contaminant removal.

1.3. Significance:

Nanoparticles have been extensively studied in recent years; however, the majority of this research concentrates on the development of synthetic methods for NP preparations.^{29,30} Currently, there are limitations with actual applications of NPs and they require significant improvement of NP quality for their realization.³¹ The main challenge is that those working on the practical use of NPs are not the same researchers preparing the NPs, and therefore application research relies on commercially available sources, which in many cases are not optimized for improved function. The control over properties via synthetic control for optimization to large-scale practical applications of NPs is a crucial bottleneck limiting current progress. To overcome these challenges, the synthesis of NPs must be such that their resulting properties can be tuned; for example, the size and shape of metal NPs are direct contributors to their optical properties, therefore control of these parameters enables tailoring of the required functional properties, e.g. plasmon/LSPR in this case. As well, surface groups and stability are key parameters for

practical applications, where surface groups are required to stabilize the NP surface, yet they may interfere with sensitivity, or NPs are unstable in conditions required for their applications.

1.4. General Perspectives

Nanoparticles have the potential to revolutionize life in diverse and interesting ways, while also bringing valid safety concerns of their use to the forefront. At the time of writing this thesis, nanoparticle news topics reflect this point. A few top headlines include the use of lipid nanoparticles for delivery of hyaluronic acid to remoisturize skin and eliminate wrinkles as a “fountain of youth” (NanoSphere Health Sciences, Inc.); a nanoparticle breakthrough to fight cancer using a targeted drug delivery system with a protective shield to inhibit protein binding (protein corona phenomenon), and therefore restricts delivery to the intended target;³² and the addition of micro- and nano- plastic in the environment to the European Commission’s Scientific Committee on Health, Environmental and Emerging Risks’ emerging issues list.³³ Other notable recent news include NPs as potential sensors for air pollution or medical diagnostics,³⁴ as illuminating agents for inflammation imaging and cancer therapy,³⁵ and the use of nanocubes as nanocargo carriers.³⁶ The grand perspective of NP sensing applications with a consideration of safety is well reflected in this PhD thesis.

The main body of this PhD thesis is based on four peer-reviewed publications. Silver decahedral nanoparticles were used as seeds, templates, and sensing substrates in Chapters 3-6; and they were chosen by virtue of their reproducible synthesis yielding highly shape- and size-uniform NPs, chemical versatility (e.g. in galvanic replacement and post-synthesis modifications), and excellent optical properties (sharp LSPR within the visible range). In Chapters 3 and 4, silver decahedra were used as seeds to form bimorphic (two shapes joined at a point) and star nanoparticles, respectively. Both of these studies utilized surface blocking with polymers to further transform the decahedral seeds to diverse nanostructures, which demonstrated potential as sensing substrates. Chapter 5 presents the use of silver decahedra as

templates for Au-Ag nanostructures with controllable LSPR over the visible range and improved chemical stability. Chapter 6 describes silver decahedra employed as cores for metallodielectrics when coated with metal oxide shells. Appendix 1 presents the use of metal oxide nanoparticles as photoelectrochemical anodes and their potential in environmental remediation. Brief descriptions of the chapters of this work are given below:

Chapter 2: Properties, Synthesis, and Applications of Nanoparticles

In this chapter, I introduce pertinent background information for the scope of this PhD work including description of the localized surface plasmon resonance (LSPR), gold and silver properties, synthetic routes to the preparation of nanoparticles, and an overview of nanoparticles applications.

Chapter 3: Symmetry Breaking by Surface Blocking: Synthesis of Bimorphic Silver Nanoparticles, Nanoscale Fishes and Apples³⁷

In this chapter I demonstrate a synthetic route to developing diverse, well-defined, asymmetric nanoparticles by using symmetry breaking and surface blocking. Protecting the surface with a polymer allows for the controllable addition of newly reduced silver at a specific point, giving a powerful method to nanoscale shape design, realizing bimorphic structures. These bimorphic NPs (two shapes, linked) exhibit strong enhancement as SERS substrates as a result of the regular cavities at the joining point and therefore regular electronic hot spots.



Figure 1.5. Coloured TEM images of apple and fish shaped nanoparticles prepared using the procedure developed in Ref. 37.

Chapter 4: Synthesis and Sensing Properties of D_{5h} Pentagonal Silver Star Nanoparticles³⁸

Silver decahedral nanoparticles were used as seeds to prepare pentagonal stars with D_{5h} symmetry, which exhibited remarkable sensitivity as SERS substrates. Femtomolar detection of a target molecule was reported in this synthetic and applied work. The LSPR of these stars are respectably sharp and were also found to be promising for SPR sensing.

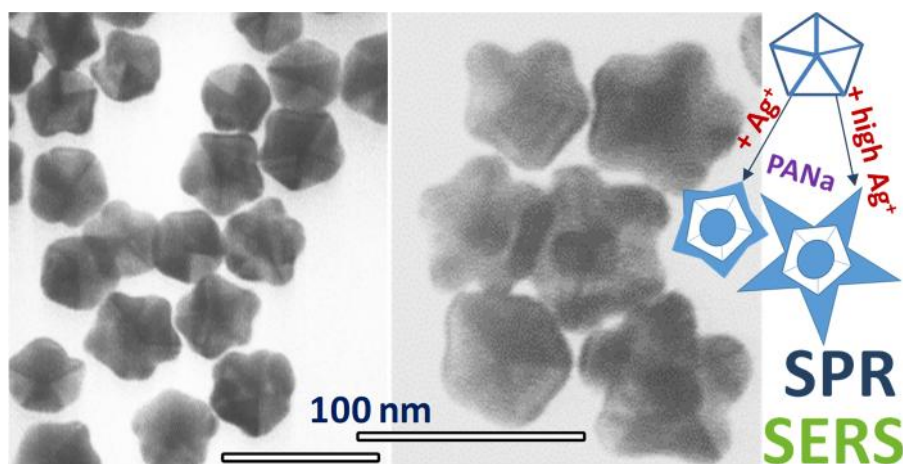


Figure 1.6. TEM images and growth schematic of silver decahedral star NPs prepared by the procedure presented in Ref.38.

Chapter 4: LSPR Tuning from 470 to 800 nm and Improved Stability of Au–Ag Nanoparticles Formed by Gold Deposition and Rebuilding in the Presence of Poly (styrene sulfonate)³⁹

In this chapter, I present a method to control the optical properties (the localized surface plasmon resonance (LSPR)) and stability of gold-silver decahedral nanoparticles in the context of sensing. Tuning the LSPR enables the enhancement of surface plasmon resonance (SPR) detection with respect to sensitivity, and selectivity of enhancement when used as substrates for surface enhanced Raman spectroscopy (SERS). This collaborative work with Dr. Jennifer I.L. Chen (York University) also includes theoretical modelling to provide further synthetic information of the interaction and replacement of silver with gold.

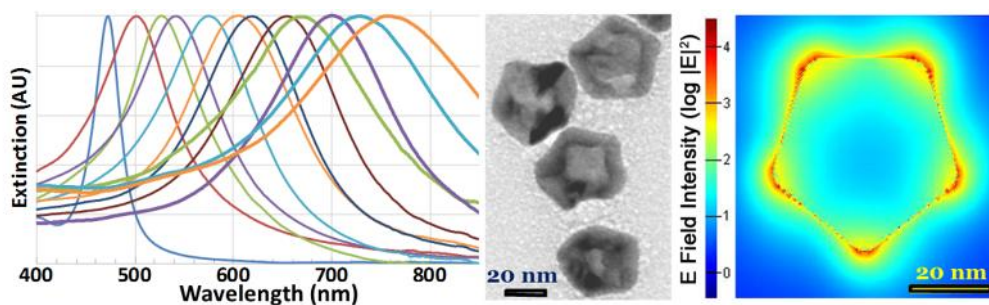


Figure 1.7. UV-vis spectra demonstrating LSPR tuning of silver and gold decahedral NPs with representative TEM image and calculated electronic field intensity from the procedure described in Ref. 39.

Chapter 6: Selective Plasmonic Sensing and Highly Ordered Metallodielectrics via Encapsulation of Plasmonic Metal Nanoparticles with Metal Oxides⁴⁰

Metallodielectrics (metallic core with metal oxide shell) have been prepared using well-defined silver decahedral nanoparticles as cores. To improve the stability and prevent etching and rounding from the addition of metal oxides, the decahedra are coated in gold that is more robust than silver. Metal oxide coating is added by hydrolysis, the resulting nanostructures exhibiting excellent optical properties (sharp LSPR of metal core is maintained), and selectivity for sensing applications. Selectivity of phosphate was

presented with MnO_{2-x} coated decahedra, and only certain peaks were enhanced when these structures were used as SERS substrates, furthering the selectivity.

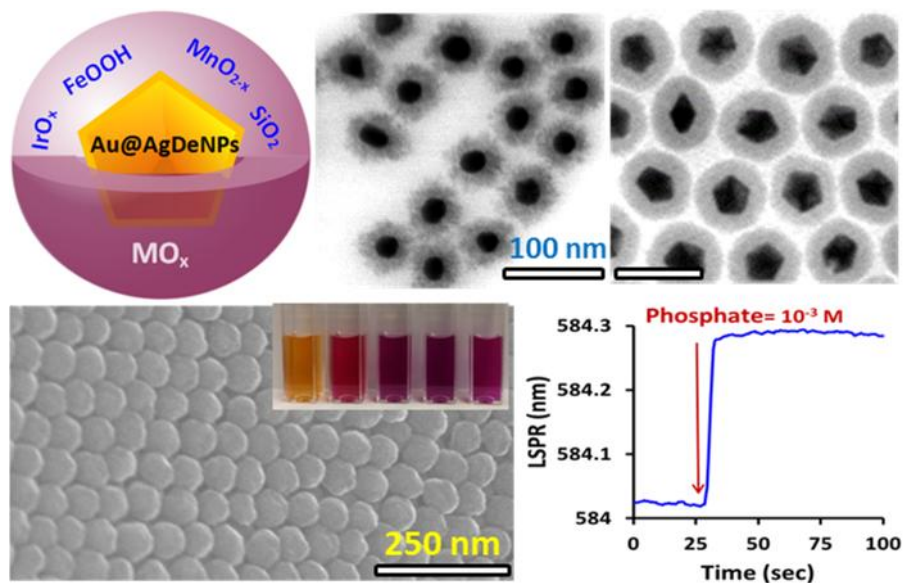


Figure 1.8. Schematic and EM images of the structure of metal oxide shells with representative SPR sensing curve detecting phosphate from Ref. 40.

Chapter 7: Philosophical Takeaways

General knowledge gained through the course of this PhD, current and future perspectives are discussed. Toxicity and safety of nanoparticles will also be considered.

Appendix 1: Metal oxide nanoparticles as photoelectrochemical anodes and their potential for environmental remediation

Metal oxide nanoparticles have been synthesized and characterized. Preliminary results of their use as photoelectrochemical anodes and considerations for environmental remediation are discussed.

Appendix 2: Methods and Glossary

In this appendix, I provide detailed methods for the preparation of silver decahedral nanoparticles, and measurements of NP size. Methods for sensing measurements with surface plasmon

resonance, and surface enhanced Raman spectroscopies are also given. A glossary of selected, relevant terms is also presented.

1.5 References

- (1) Cademartiri, L.; Kitaev, V. On the Nature and Importance of the Transition between Molecules and Nanocrystals: Towards a Chemistry of “Nanoscale Perfection”. *Nanoscale* **2011**, *3*, 3435–3446.
- (2) Yan, J.; Teo, B. K.; Zheng, N. Surface Chemistry of Atomically Precise Coinage–Metal Nanoclusters: From Structural Control to Surface Reactivity and Catalysis. *Acc. Chem. Res.* **2018**, *51*, 3084–3093.
- (3) Jin, R.; Pei, Y.; Tsukuda, T. Controlling Nanoparticles with Atomic Precision. *Acc. Chem. Res.* **2019**, *52*, 1–1.
- (4) Roduner, E. Size Matters: Why Nanomaterials Are Different. *Chem. Soc. Rev.* **2006**, *35*, 583–592.
- (5) Eustis, S.; El-Sayed, M. A. Why Gold Nanoparticles Are More Precious than Pretty Gold: Noble Metal Surface Plasmon Resonance and Its Enhancement of the Radiative and Nonradiative Properties of Nanocrystals of Different Shapes. *Chem. Soc. Rev.* **2006**, *35*, 209–217.
- (6) Sau, T. K.; Rogach, A. L.; Jäckel, F.; Klar, T. A.; Feldmann, J. Properties and Applications of Colloidal Nonspherical Noble Metal Nanoparticles. *Adv. Mater.* **2010**, *22*, 1805–1825.
- (7) Link, S.; El-Sayed, M. A. Optical Properties and Ultrafast Dynamics of Metallic Nanocrystals. *Annu. Rev. Phys. Chem.* **2003**, *54*, 331–366.
- (8) Austin, L. A.; MacKey, M. A.; Dreaden, E. C.; El-Sayed, M. A. The Optical, Photothermal, and Facile Surface Chemical Properties of Gold and Silver Nanoparticles in Biodiagnostics, Therapy, and Drug Delivery. *Arch. Toxicol.* **2014**, *88*, 1391–1417.
- (9) Kreibig, U.; Vollmer, M. *Optical Properties of Metal Clusters*; Springer Series in Materials Science; Springer Berlin Heidelberg: Berlin, Heidelberg, 1995.
- (10) Hutchings, G. J.; Haruta, M. A Golden Age of Catalysis: A Perspective. *Appl. Catal. A Gen.* **2005**, *291*, 2–5.
- (11) Bisquert, J.; Fabregat-Santiago, F.; Mora-Seró, I.; Garcia-Belmonte, G.; Barea, E. M.; Palomares, E. A Review of Recent Results on Electrochemical Determination of the Density of Electronic States of Nanostructured Metal-Oxide Semiconductors and Organic Hole Conductors. *Inorganica Chim. Acta* **2008**, *361*, 684–698.
- (12) Alexander, B. D.; Kulesza, P. J.; Rutkowska, I.; Solarska, R.; Augustynski, J. Metal Oxide Photoanodes for Solar Hydrogen Production. *J. Mater. Chem.* **2008**, *18*, 2298–2303.
- (13) Li, Y.; Zhang, W.; Niu, J.; Chen, Y. Mechanism of Photogenerated Reactive Oxygen Species and Correlation with the Antibacterial Properties of Engineered Metal-Oxide Nanoparticles. *ACS Nano* **2012**, *6*, 5164–5173.
- (14) Mulvaney, P. Surface Plasmon Spectroscopy of Nanosized Metal Particles. *Langmuir* **1996**, *12*,

- 788–800.
- (15) Liz-Marzán, L. M. Tailoring Surface Plasmons through the Morphology and Assembly of Metal Nanoparticles. *Langmuir* **2006**, *22*, 32–41.
 - (16) Jain, P. K.; El-Sayed, M. A. Plasmonic Coupling in Noble Metal Nanostructures. *Chem. Phys. Lett.* **2010**, *487*, 153–164.
 - (17) Jain, P. K.; Huang, X.; El-Sayed, I. H.; El-Sayed, M. A. Noble Metals on the Nanoscale: Optical and Photothermal Properties and Some Applications in Imaging, Sensing, Biology, and Medicine. *Acc. Chem. Res.* **2008**, *41*, 1578–1586.
 - (18) Frank, A. J.; Cathcart, N.; Maly, K. E.; Kitaev, V. Synthesis of Silver Nanoprisms with Variable Size and Investigation of Their Optical Properties: A First-Year Undergraduate Experiment Exploring Plasmonic Nanoparticles. *J. Chem. Educ.* **2010**, *87*, 1098–1101.
 - (19) Mie, G. Beiträge Zur Optik Trüber Medien, Speziell Kolloidaler Metallösungen" (Contributions to the Optics of Turbid Media, Particularly Colloidal Metal Suspensions). *Ann. Phys.* **1908**, *25*, 377–445.
 - (20) Link, S.; El-Sayed, M. A. Shape and Size Dependence of Radiative, Non-Radiative and Photothermal Properties of Gold Nanocrystals. *Int. Rev. Phys. Chem.* **2000**, *19*, 409–453.
 - (21) Kelly, K. L.; Coronado, E.; Zhao, L. L.; Schatz, G. C. The Optical Properties of Metal Nanoparticles: The Influence of Size, Shape, and Dielectric Environment. *J. Phys. Chem. B* **2003**, *107*, 668–677.
 - (22) El-Sayed, M. A. Small Is Different: Shape-, Size-, and Composition-Dependent Properties of Some Colloidal Semiconductor Nanocrystals. *Acc. Chem. Res.* **2004**, *37*, 326–333.
 - (23) Kelly, K. L.; Coronado, E.; Zhao, L. L.; Schatz, G. C. The Optical Properties of Metal Nanoparticles: The Influence of Size, Shape, and Dielectric Environment. *J. Phys. Chem. B* **2003**, *107*, 668–677.
 - (24) Chen, Z.; Jiao, Z.; Pan, D.; Li, Z.; Wu, M.; Shek, C.-H.; Wu, C. M. L.; Lai, J. K. L. Recent Advances in Manganese Oxide Nanocrystals: Fabrication, Characterization, and Microstructure. *Chem. Rev.* **2012**, *112*, 3833–3855.
 - (25) Franke, M. E.; Koplín, T. J.; Simon, U. Metal and Metal Oxide Nanoparticles in Chemiresistors: Does the Nanoscale Matter? *Small* **2006**, *2*, 36–50.
 - (26) Laurent, S.; Forge, D.; Port, M.; Roch, A.; Robic, C.; Vander Elst, L.; Muller, R. N. Magnetic Iron Oxide Nanoparticles: Synthesis, Stabilization, Vectorization, Physicochemical Characterizations, and Biological Applications. *Chem. Rev.* **2008**, *108*, 2064–2110.
 - (27) Tokura, Y.; Nagaosa, N. Orbital Physics in Transition-Metal Oxides. *Science* **2000**, *288*, 462–468.
 - (28) Walsh, A.; Butler, K. T. Prediction of Electron Energies in Metal Oxides. *Acc. Chem. Res.* **2014**, *47*, 364–372.
 - (29) You, H.; Yang, S.; Ding, B.; Yang, H. Synthesis of Colloidal Metal and Metal Alloy Nanoparticles for Electrochemical Energy Applications. *Chem. Soc. Rev.* **2013**, *42*, 2880–2904.
 - (30) Personick, M. L.; Mirkin, C. A. Making Sense of the Mayhem behind Shape Control in the

- Synthesis of Gold Nanoparticles. *J. Am. Chem. Soc.* **2013**, *135*, 18238–18247.
- (31) Saha, K.; Agasti, S. S.; Kim, C.; Li, X.; Rotello, V. M. Gold Nanoparticles in Chemical and Biological Sensing. *Chem. Rev.* **2012**, *112*, 2739–2779.
- (32) Oh, J. Y.; Kim, H. S.; Palanikumar, L.; Go, E. M.; Jana, B.; Park, S. A.; Kim, H. Y.; Kim, K.; Seo, J. K.; Kwak, S. K.; et al. Cloaking Nanoparticles with Protein Corona Shield for Targeted Drug Delivery. *Nat. Commun.* **2018**, *9*, 4548.
- (33) Scientific Committee on Emerging and Newly Identified Health Risks SCHEER. *Emerging Issues and the Role of the SCHEER; Position Paper*; European Commission; **2009**.
- (34) Hooper, D. C.; Kuppe, C.; Wang, D.; Wang, W.; Guan, J.; Odom, T. W.; Valev, V. K. Second Harmonic Spectroscopy of Surface Lattice Resonances. *Nano Lett.* **2019**, *19*, 165–172.
- (35) Xu, X.; An, H.; Zhang, D.; Tao, H.; Dou, Y.; Li, X.; Huang, J.; Zhang, J. A Self-Illuminating Nanoparticle for Inflammation Imaging and Cancer Therapy. *Sci. Adv.* **2019**, *5*, eaat2953.
- (36) Lu, F.; Xin, H.; Xia, W.; Liu, M.; Zhang, Y.; Cai, W.; Gang, O. Tailoring Surface Opening of Hollow Nanocubes and Their Application as Nanocargo Carriers. *ACS Cent. Sci.* **2018**, *4*, 1742–1750.
- (37) Cathcart, N.; Kitaev, V. Symmetry Breaking by Surface Blocking: Synthesis of Bimorphic Silver Nanoparticles, Nanoscale Fishes and Apples. *Sci. Rep.* **2016**, *6*, 32561.
- (38) Cathcart, N.; Coombs, N.; Gourevich, I.; Kitaev, V. Synthesis and Sensing Properties of D_{5h} pentagonal Silver Star Nanoparticles. *Nanoscale* **2016**, *8*, 18282–18290.
- (39) Cathcart, N.; Chen, J. I. L.; Kitaev, V. LSPR Tuning from 470 to 800 nm and Improved Stability of Au–Ag Nanoparticles Formed by Gold Deposition and Rebuilding in the Presence of Poly(styrenesulfonate). *Langmuir* **2018**, *34*, 612–621.
- (40) Cathcart, N.; Murshid, N.; Campbell, P.; Kitaev, V. Selective Plasmonic Sensing and Highly Ordered Metallo-dielectrics via Encapsulation of Plasmonic Metal Nanoparticles with Metal Oxides. *ACS Appl. Nano Mater.* **2018**, *1*, 6514–6524.

Chapter 2. Properties, Synthesis, and Applications of Nanoparticles

The great potential of nanoparticles in diverse applications has generated a plethora of research opportunities, albeit limited practical success. The following literature review aims to discuss the reported studies of nanoparticles for applied use in the context of type: metal, metal oxide, and metallodielectric. To present a comprehensive picture, the background of the localized surface plasmon resonance ((LSPR), the key optical property of metal nanoparticles being used for sensing), silver and gold properties, synthetic routes and surface chemistry will also be discussed.

2.1. Localized Surface Plasmon Resonance

In 1908, Mie explained theoretically the interaction of electromagnetic light with a small sphere with the same dielectric constant as the bulk metal by solving Maxwell's equations.¹ Maxwell's equations provide mathematical models of electromagnetism,² and gave multipole oscillations for extinction and scattering cross sections of particles as a function of radius.³ For particles greater than 20 nm, these oscillations account for absorption and scattering modes and make up the absorption spectrum.³ As size increases, a plasmon resonance is no longer observed due to the size being much larger than incidence wavelength, and the polarization of electrons is no longer supported. When the sphere is under 20 nm, and less than the wavelength of interacting light, it is only the dipole oscillation that contributes to the extinction cross section.³

More recently, Willets and Van Duyne, also using Maxwell's equations, calculated the electromagnetic field outside of a spherical particle.⁴ Main variables were found to be the metal dielectric function (composition), the geometry (shape), and the size. The general statement can then be made that depending on the size and shape of the particle, the particle's composition and media, and the interparticle separations, this oscillation will occur at different wavelengths (energies). This is experimentally confirmed by samples of Figure 2.1a,b and d. Figure 2.1a shows the LSPR increasing with

size for silver prisms, Figure 2.1b shows the different resonance modes for rod-shaped silver NPs, Figure 2.1c compares the calculated extinction spectra from Mie theory for 20 nm gold and silver particles, and Figure 2.1d shows the LSPR changes when the distance between gold nanodisks are varied.

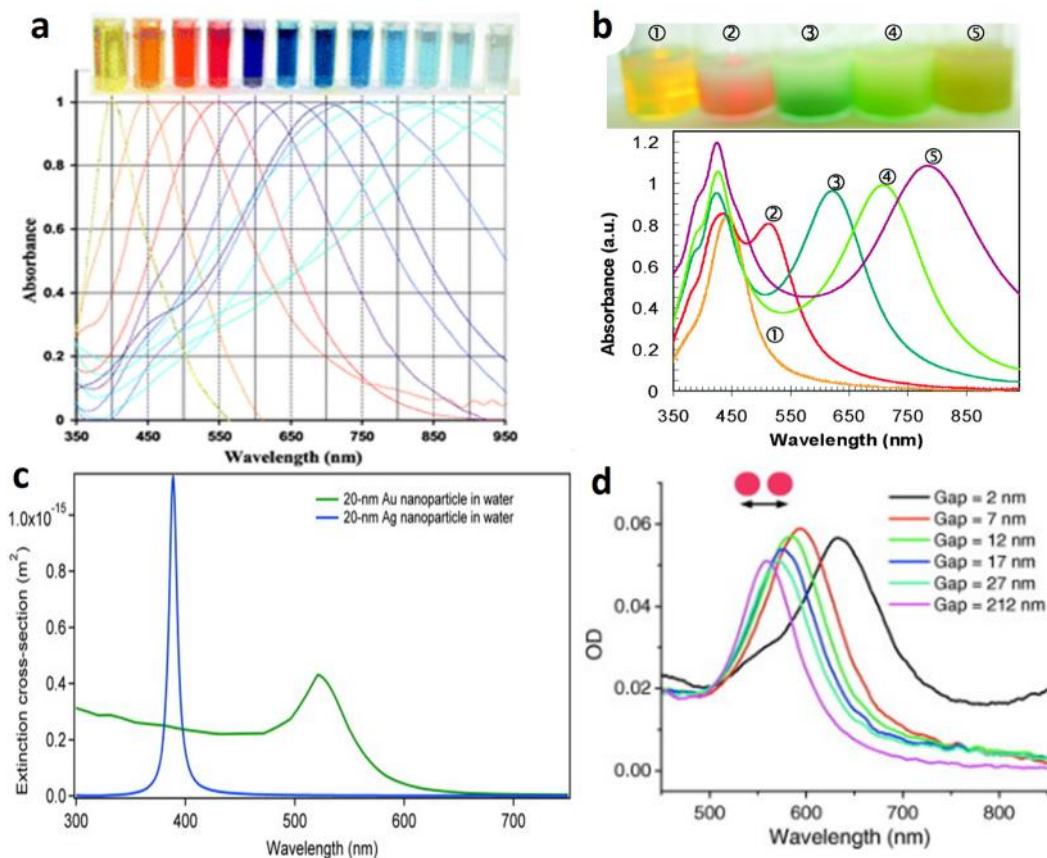


Figure 2.1. Absorbance and extinction spectra showing LSPR variations due to size, shape, composition and interparticle spacing. **a)** absorbance spectra of silver nanoprisms of various sizes and their coloured solutions,⁵ **b)** absorbance spectra of silver pentagonal rods of 4 different lengths (2-5) grown from silver decahedral nanoparticles (1),⁶ **c)** extinction spectra of 20 nm gold and silver nanospheres from Mie theory, and **d)** extinction spectra of 88 nm gold disks with varied interparticle spacing.^{7*}

2.2. Electronic Properties of Silver and Gold

Group 11 elements, often referred to as coinage metals, have unique properties with respect to reactivity and chemical resistance. Moving down the group from copper to gold, the metals are

* a) from Ref.⁵ (N. Cathcart, A. J. Frank and V. Kitaev, *Chem. Commun.*, **2009**, 6, 7170–7172.) Reproduced by permission of The Royal Society of Chemistry, b) Reprinted with permission from Ref.⁶ (B. Pietrobon, M. McEachran and V. Kitaev, *ACS Nano*, **2009**, 3, 21–26.) Copyright (2009) American Chemical Society. c) and d) reproduced from Ref.⁷ (Jain, P. K.; El-Sayed, M. A. *Chem. Phys. Lett.* **2010**, 487, 153–164.) copyright (2010) Elsevier with permission.

increasingly resistant to oxidation. Correspondingly, gold is the most easily reduced of the group. Silver and gold have full d -orbitals and a single s -electron, $4d^{10}5s^1$ and $5d^{10}6s^1$ respectively, which both contribute to their stability and reactivity. Most metals have bulk plasma frequencies higher than those of silver and gold, this is due to the constriction of d -orbitals which lower the d electron energy levels as atomic number and concomitant nuclear charge increase.⁸ Because of this constriction, noble metal plasmons occur at energies lower than electronic d - sp interband transitions.⁹⁻¹¹ During UV-vis absorbance measurements, electrons from the full d -orbital are excited to the partially empty s -, and empty p -orbitals.⁹ The gap size (energy) from d to sp in silver is larger than it is in gold, the energy of transition such that the LSPR of silver can span throughout the entire visible range, whereas gold is restricted to above 510 nm.

Additionally, it is well known that gold is resistant to oxidation by air, whereas silver tarnishes (through reaction with sulfur compounds in presence of oxygen in the air).¹² This is because gold is a more noble metal, meaning that it is more resistant to both forming and breaking bonds at the surface.¹³ To calculate “nobility”, Hammer and Nørskov studied the chemisorption of hydrogen to metal surfaces, and determined that the important factors are the degree of d -orbital filling, and the coupling matrix element.¹³ The degree of d -orbital filling increases across the transition metal series in the periodic table and the coupling matrix element increases down groups, resulting in $5d$ metals as most noble. The coupling matrix is inversely proportional to the constriction of the orbitals, which is higher across the periodic table, which results in less overlap of atomic orbitals when bonds are formed (less stable bonds).¹³ With this respect, gold is the most noble of the group 11 metals (highest d -orbital filling and coupling matrix element).¹³ An additional theory on nobility is presented by Häkkinen et al. based on the reconstruction of surface atoms.¹⁴ For face centred cubic (FCC) (110) surfaces of Ir, Pt and Au, the rearrangement of the surface to optimize electron density is well known; however, metals such as Rh, Ni, Pd, Cu and Ag do not participate in this multilayer relaxation.¹⁴ The relaxation or rearrangement of the

surface atoms produces a pseudo (111) surface with lower surface energy. Crystal lattices of FCC metals will be discussed below.

Owing to the stability of gold, the shape-selective preparation of gold nanoparticles (AuNPs) often requires harsher conditions, and few shape- and size (without requiring purification)- selective synthetic methods have been reported.¹⁵⁻¹⁹ Using a “best of both worlds” strategy, combining the superior optical properties of silver with the stability of gold has great promise for NP-based applications.²⁰⁻²²

2.3. MNP Synthesis

Michael Faraday was the first to synthesize and document metal nanoparticles in solution in 1850.²³ He prepared gold colloids for thin metallic films by reducing gold with phosphorus in water.²³ This field has greatly advanced in the past nearly 170 years, with the improvement of size uniformity and focus on property control reaching the forefront within the past decade.^{15,24-28} Main strides in this respect are the understanding that properties of NBBs are dictated by size and shape, and the advancement in synthetic size and shape control.²⁹⁻³¹

Colloidal synthetic methods follow a bottom up approach, whereby nanoparticles are formed directly, relying on the interplay of rates of atom attachment to various crystallographic facets for NP growth.^{15,27,32} These rates are controllable through reducing conditions (generation rate of those atoms),³² temperature and/or capping ligands.³³ Typical colloidal syntheses begin with a metal salt (e.g. hydrogen tetrachloroaurate (III) (HAuCl_4) as Au source, or silver nitrate (AgNO_3) as Ag source) which is reduced to metallic gold or silver in the presence of stabilizing and etching agents. Further refinement is achieved through heating, photochemical transformation or purification via separation. Three major steps take place in NP formation: 1) nucleation of small clusters from metal ions and atoms, 2) growth of nuclei to seeds with well-defined internal structures, and 3) further growth of these seeds into well-defined shapes.³⁴ The resultant NP shape is dependent on both kinetic and thermodynamic factors.

Thermodynamic factors are largely determined by the reduction potential and surface capping.³⁴ Kinetic factors are governed by concentration, temperature, involvement of other species in the reduction, and mass transport. These parameters are most influential in the first formation stage, when nuclei form, as the number of nuclei (and therefore seeds) will change the final product.³⁴ For example, a small number of nuclei for the same concentration of metal will result in larger particles being formed, whereas a large number of nuclei will result in smaller particles with the same concentration of metal. In general, the nucleation step is the most difficult to control and predict, and investigating the explicit role of a specific parameter has been a grand challenge in the NP synthetic community.^{34–38}

2.3.1. NP Growth: Thermodynamics vs. Kinetics

Recent developments in seeded regrowth as a pathway to NP synthesis has improved the size and shape control, and the understanding of the interplay of various kinetic and thermodynamic parameters. By starting with well-defined seeds and adding newly formed metal atoms, the nucleation process is separated (avoiding uncertainties), and systematic examination of the role of each reagent is possible.³⁴ An analogy to reactions forming compounds can be made where the atoms are the precursor and the NPs are the product, the free energy of these products and reactions are schematically represented in Figure 2.2:³⁴

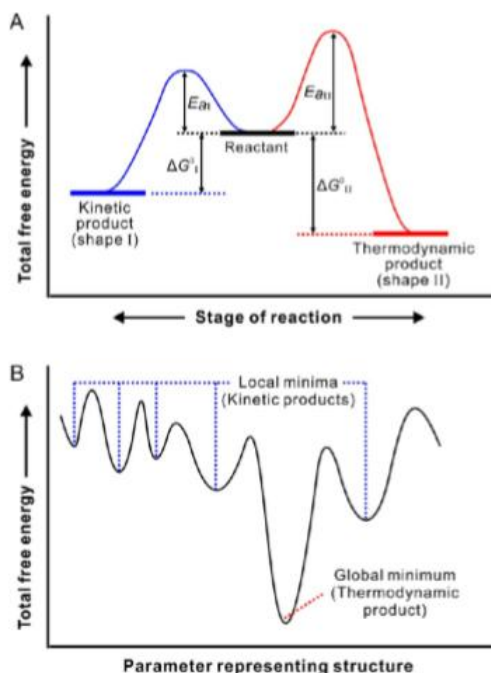


Figure 2.2. Schematic illustration of thermodynamic vs. kinetic control for **A**) two parallel reactions and **B**) a series of sequential reactions. Reprinted with permission from Ref.34.*

Figure 2.2A illustrates the formation of the kinetic product (shape I) and the thermodynamic product (shape II) from the same reactants. The pathway to shape I requires less activation energy (E_a) than that to shape II; however, the stability of shape II is thermodynamically more stable than that of shape I.³⁴ According to the Arrhenius equation (Equation 1), a simplistic method to obtain the kinetic instead of the thermodynamic product is to change the temperature: high temperature will favour the thermodynamic product and low temperature favours the kinetic product.

$$r = A e^{\frac{-E_a}{R}} \quad (1)$$

The more realistic scenario is depicted on the schematic given in Figure 2.2B, where sequential reactions occur yielding several products, one of which at a global energy minimum (thermodynamic product). Thermodynamic products can be considered to be in the equilibrium state defined by

* (Y. Xia, X. Xia and H.-C. Peng, J. Am. Chem. Soc., 2015, **137**, 7947–7966). Copyright (2015) American Chemical Society.

temperature, pressure and environment; therefore the shape and size of the resulting NPs will be altered by changing any of the parameters.³⁴ Determining the equilibrium shape requires minimization of the total surface free energy, which requires knowledge of the surface free energy of various crystallographic planes.

2.3.2. Surface Energy and Crystallographic Planes

Recently, Tran et al. calculated the equilibrium shapes with minimized surface energy for 72 elemental solids, shown in Figure 2.3.³⁹

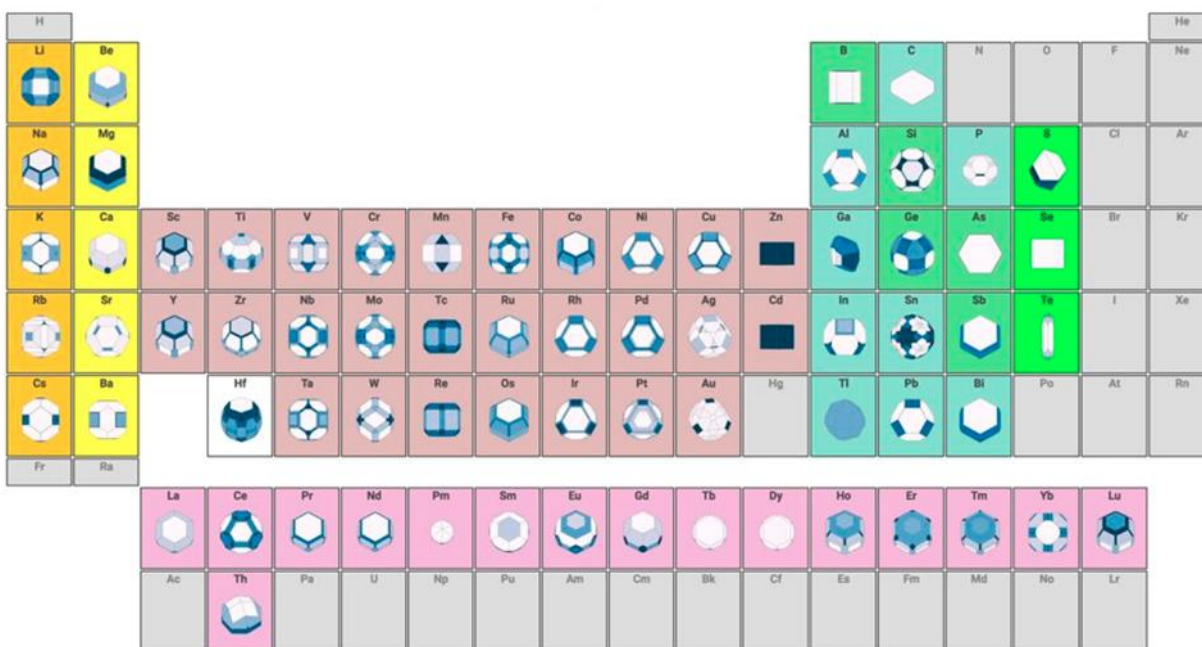


Figure 2.3. Equilibrium shapes of 72 elements from calculating minimized surface energy. Reproduced from Ref.39*

To minimize surface energy, surface area should also be lowered at a constant volume, which occurs when the NP takes a spherical shape. As evident from Figure 2.3, the calculated equilibrium shapes

* R. Tran, Z. Xu, B. Radhakrishnan, D. Winston, W. Sun, K. A. Persson and S. P. Ong, *Sci. Data*, **2016**, *3*, 160080. Licensed under CC by 4.0.

are sphere-like, but not spherical by virtue of crystallinity in atomic packing resulting in the formation of crystallographic planes. This can be calculated by equation 2, where γ_i is the specific surface free energy (per unit area) and A is the surface area.³⁴

$$\int \gamma_i dA_i = m \quad (2)$$

The specific surface free energy is the increase in free energy per unit area upon the creation of a new surface (through breaking bonds).

Gold and silver are FCC metals, where their atoms pack per Figure 2.4a and b. Figure 2.4a is representative of a FCC unit cell. Setting this unit cell to a coordinate axis (x,y,z) enables us to visualize the planes represented in Figure 2.4c-e; putting one atom (corner) at the intersection point of the axes, $x,y,z = 0$, and the distance from each corner atom = 1, will allow these planes to be constructed, e.g., one side of the unit cell is represented by the (100) plane (Figure 2.4c), a diagonal cut from the top of the unit cell is represented by the (110) plane (Figure 2.4d), and connecting the atoms at corners along the axes, $x,y,z = 1$, visualizes the (111) plane (Figure 2.4e).

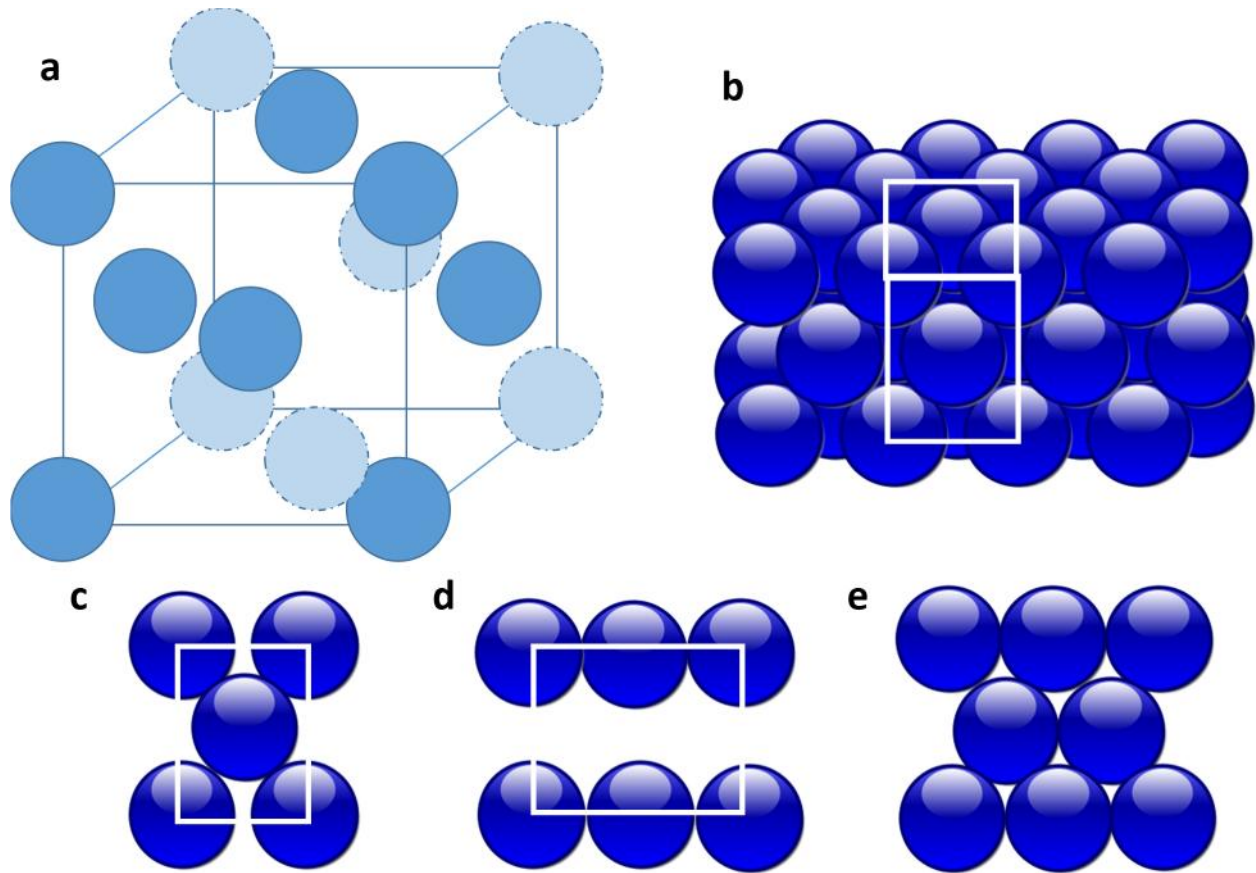


Figure 2.4. Schematics of face centred cubic crystal structure. **a)** unit cell, **b)** unit cell in aggregate of atoms, **c)** (100) plane, **d)** (110) plane, **e)** expanded (111) plane. Generated with inspiration from Ref.40.

The major three low index planes are shown schematically in Figure 2.4c-e. The surface free energy can be calculated from equation 3:³⁴

$$\gamma = \frac{1}{2} N_B \epsilon \rho_A \quad (3)$$

where N_B is the number of broken bonds per surface unit cell, ϵ is bond strength, ρ_A is number of surface atoms per area, and the factor of $\frac{1}{2}$ accounts for two atoms participating in each bond. From equation 3, it follows that surface free energies increase from (111) < (100) < (110).³⁴ This can also be easily estimated by comparing the number of bonds broken to form each surface, which are 3, 4 and 6 for (111), (100), and (110), respectively.

2.3.3. Surface Stabilization

To achieve the equilibrium shape in solutions, capping agents/ligands for the stabilization of specific facets are used. Capping agents will stabilize NPs by lowering the surface free energy, maximizing that type of facet in the shape.³⁴ For example, poly(vinylpyrrolidone) (PVP) and tricitrate are well known to stabilize Ag (100) and Ag (111) respectively, as schematically shown in Figure 2.5.³⁸ Experimentally however, PVP may not be necessary for Ag (100) stabilization.³⁵ Halides have also been shown to selectively stabilize specific planes in gold and silver.³⁷

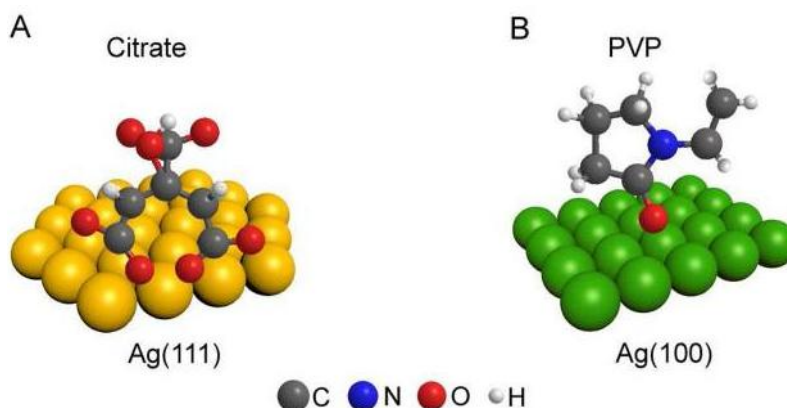


Figure 2.5. Adsorption schematic of **A)** tricitrate on Ag (111) and **B)** PVP on Ag (100). Reprinted with permission from Ref.38.*

The FCC lattice is highly symmetric, giving symmetric thermodynamic products such as cubes, cuboctahedra or octahedra depending on the relative $\langle 100 \rangle$ and $\langle 111 \rangle$ growth rates.³⁴ To achieve a variety of shapes for FCC metals, symmetry breaking or asymmetry must occur, which is governed by kinetic factors/parameters.³³

* (X. Xia, J. Zeng, Q. Zhang, C. H. Moran and Y. Xia, *J. Phys. Chem. C. Nanomater. Interfaces*, **2012**, 116, 21647–21656). Copyright (2012) American Chemical Society.

2.3.4. Symmetry Breaking

Major mechanisms for symmetry breaking include **A**) incorporating twin defects or stacking faults during growth, **B**) inducing asymmetric deposition for a symmetric seed, and **C**) aggregating seeds during growth.³⁴

2.3.4.A. Incorporation of Twin Defects

Twin defects or stacking faults are high energy regions, which minimize the overall energy of the particle. The two types of defects in a nanoprism are shown in Figure 2.6, where A-type defects are formed along a re-entrant groove (high energy region for integration of new atoms in the lattice), and B-type where atoms start new layers on the top of the surface, not integrating into the lattice.⁴¹ A-type twinning occurs 50% more readily than B-type due to higher stability and a lower energy barrier.⁴¹ The two types of twin defects are presented in Figure 2.6.

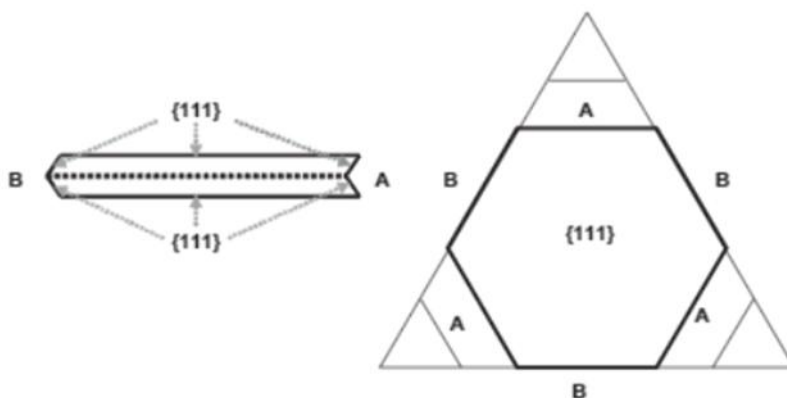


Figure 2.6. Schematic of A and B type twin defects in a nanoprism (side and top views). Reproduced with permission from Ref.42*

This schematic is experimentally confirmed for platelets by Aherne et al⁴³ and the V. Kitaev lab.⁵ Planar twinned defects are not only formed in platelets; the V. Kitaev lab has experimentally confirmed twinned defects for cubes and bipyramids,⁴⁴ and flowers.⁴⁵ Furthermore, cyclic twinned defects occur in

* © 2005 WILEY-VCH Verlag GmbH & Co. KGaA, Weinheim.

decahedra²⁶ and icosahedra.⁴⁶ Scanning electron microscopy (SEM) images and schematics of twin defects and their use as growth sites are presented in Figure 2.7.

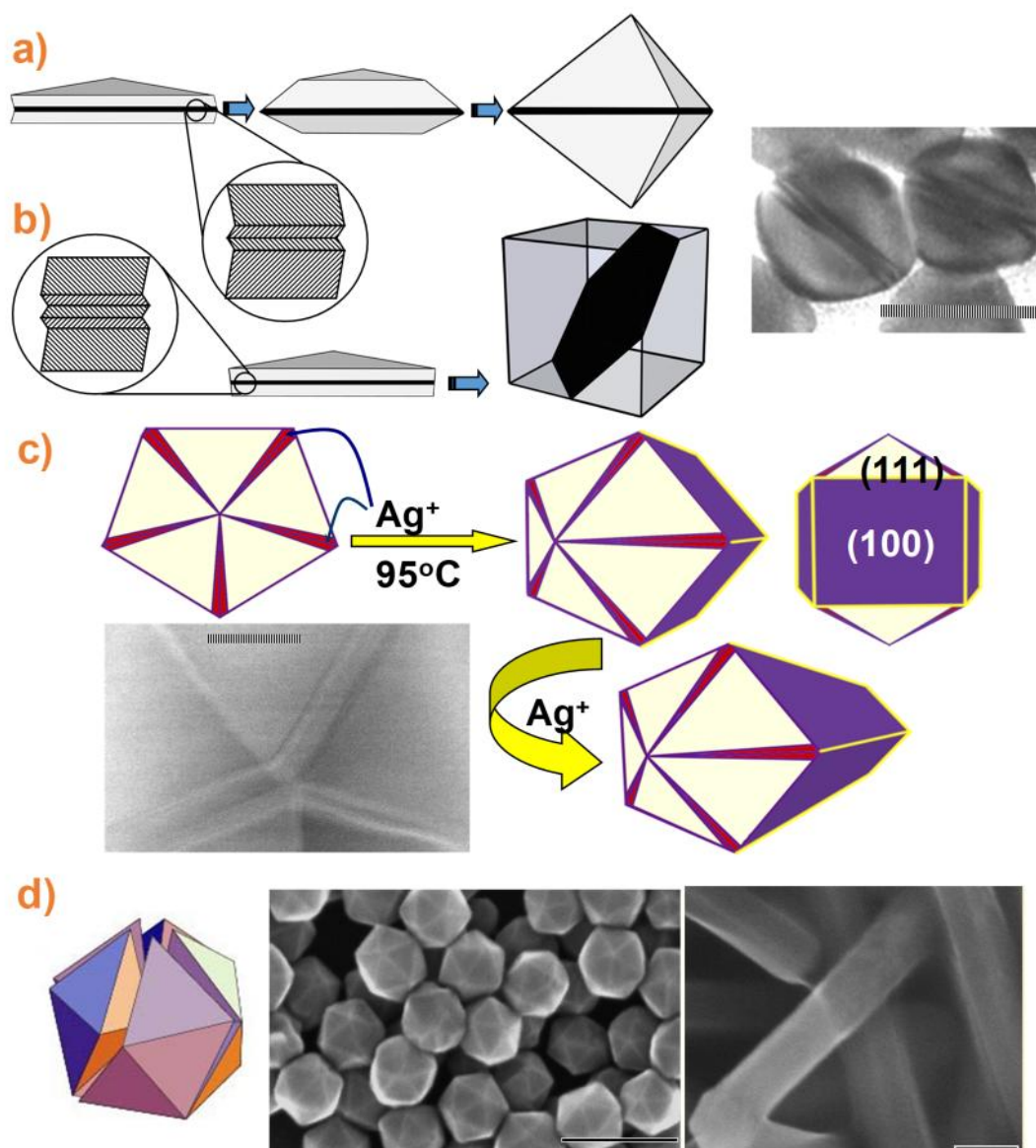


Figure 2.7. Schematics and SEM images of twin defects in AgNPs and their use for regrowth. **a)** growth schematic of bipyramids from uneven number of twin planes,⁴⁴ **b)** growth schematics of cubes from even number of twin planes and SEM image of cubes,⁴⁴ **c)** growth schematics of pentagonal rods from decahedral twin defect and SEM image of pentagonal defect,⁶ and **d)** schematics of twin defects in icosahedra and SEM images of icosahedra and pentagonal pins grown from icosahedra.⁴⁶ Scale bars are 20 nm for a/b, 5 nm for c and 100 nm for d.*

* a) and b) Reproduced from Ref.⁴⁴ *Chemical communications by CHEMICAL SOCIETY (GREAT BRITAIN) Reproduced with permission of THE SOCIETY, in the format Thesis/Dissertation via Copyright Clearance Center.* c) Reprinted with permission from Ref.⁶ (B. Pietrobon, M. McEachran and V. Kitaev, *ACS Nano*, 2009, 3, 21–26.) Copyright (2009) American Chemical Society. d) Ref.⁴⁶ - Reproduced by permission of The Royal Society of Chemistry.

The incorporation of twin defects into NPs is necessary for their formation (a deviation from the thermodynamic product). These defects are a high-energy zone for adatoms and therefore growth. Figure 2.7 shows the growth products from using platelets, decahedra and icosahedra as seeds, utilizing their twin defects. In a recent report, the twinned structure in NPs was monitored during morphological changes from decahedral nanoparticles to rhomboidal pyramids by lattice strain energy relaxation.⁴⁷

2.3.4.B. Asymmetric Deposition on NP Seeds (Seeded Regrowth)

Symmetry breaking mechanisms have received increasing attention as understanding of NP synthesis improves, and the kinetic control hypothesis enables rationalization and prediction of structures.^{24,33,48,49} When the reaction conditions deviate from normal conditions, the kinetic product is produced, expected to be different from the thermodynamic product. It should be noted that thermodynamic conditions are difficult to establish experimentally.³³ Without symmetry breaking, anisotropic structures that exhibit different properties in different directions could not be developed. A valuable technique to improve size dispersity in symmetry breaking synthesis is seeded regrowth, where additional metal ions are reduced on the surface of a particle formed previously. Seeded regrowth and the use of seeds as templates are the main synthetic focus of this PhD work. Many factors can affect the kinetics of the synthesis and they include: seed morphology and size, metal precursor, reducing agent, ratio of precursor to additives, and selectively adsorbing ligands.⁴⁹

There are three possible growth modes from seeds: 1D growth, where growth occurs in one direction, 2D growth, where growth occurs in two directions and 3D growth, where growth occurs in three directions.²⁸ A notable example of seeded 1D growth is the elongation of decahedral and icosahedral silver NPs to produce pentagonal rods⁵⁰ and pentagonal pins,⁴⁶ respectively, where additional silver preferentially reduces in site of the twinning defect in the presence of citrate as reducing agent at elevated temperature, as shown schematically in Figure 2.7c. Seeded 2D growth has been demonstrated as part of this PhD work, where platelets were grown from a vertex on silver decahedra nanoparticles (AgDeNPs)

to form bimorphic nanoparticles (bi-AgNPs) through effective surface blocking and the use of a weak reducing agent.⁵¹ With equal deposition of atoms on all faces of the seed particle, seeded 3D growth gives what is the closest to the thermodynamic product, e.g. enlargement of decahedra; however, the kinetic 3D product can still be achieved through varying conditions.⁵¹

There are several examples of MNP synthesis using thermodynamic and/or kinetic control. For example, Xia's group demonstrated control over morphology through varying the concentration of PVP and the injection speed of additional silver to Ag cubes.³² Different morphologies were achieved through a combination of thermodynamic and kinetic control, where PVP stabilized the {100} facets of the cube, and once PVP was used up, {111} facets started to form.³² Several recent reports have used microfluidics,⁵² temperature,⁵³ and halides⁵⁴ as methods to control the reaction kinetics in order to achieve their desired morphologies. Modified DNA ligands were also reported to contribute to symmetry breaking.⁵⁵ A recent report describes an example of seeded 3D growth for the formation of Au nanobottles from sacrificial templates with potential for targeted drug delivery.⁵⁶ The control over the morphology leads to great control of the properties, which is required for MNP practical use, the main focus of this PhD research.

We have experimentally used symmetry breaking to produce diverse silver nanostructures by varying the concentration of a surface blocking polymer, and pH, and by including halides, effectively controlling the resulting morphology, as shown in Figure 3.1, and further described in Chapter 3.

2.4. Surface Enhanced Raman Spectroscopy

Raman spectroscopy is a technique to analyze chemicals through their interaction with electromagnetic radiation. Upon interaction of a molecule with light, the energy is either absorbed (IR) or scattered (Raman).⁵⁷ Interactions of molecules with light may be stronger at specific frequencies, which can be related to reference spectra, and can confirm structures, almost like a molecular fingerprint. The

frequency (ν) can be calculated using a model with balls as atoms and springs for bonds, described by equation 4.⁵⁸

$$\nu = \frac{1}{\pi} \sqrt{\frac{k}{2m}} \quad (4)$$

where k is the force constant (the resistance to stretching), and m is the mass. This equation is only applicable when both masses are the same on each side of the 'spring'. For different masses, the reduced mass, μ , is used where the two masses are first multiplied and then divided by their sum. For each molecule, there are $3N-6$ vibrations ($3N-5$ for linear molecules), where N is the number of atoms in the molecule, in which internuclear distances and bond angles change, but the molecule's centre of mass remains unchanged.⁵⁸

It is important to note that not all molecular vibrations are Raman or IR active. The main criterion of Raman-active vibration is a change in polarizability of the molecule, and a change in dipole for IR active vibrations.⁵⁸ In general, a vibration is IR active, Raman active, or active in both; symmetric vibrations are only Raman active.⁵⁷

Measurements of Raman spectra are performed by irradiating the sample with a source of monochromatic radiation (typically laser), and scattered light is detected perpendicular to the beam.⁵⁷ There are two types of scattering, Rayleigh (same frequency as incident beam) and Raman (different frequency (inelastic) very weak).⁵⁷ The electronic transitions for IR and Raman are presented in Figure 2.9.

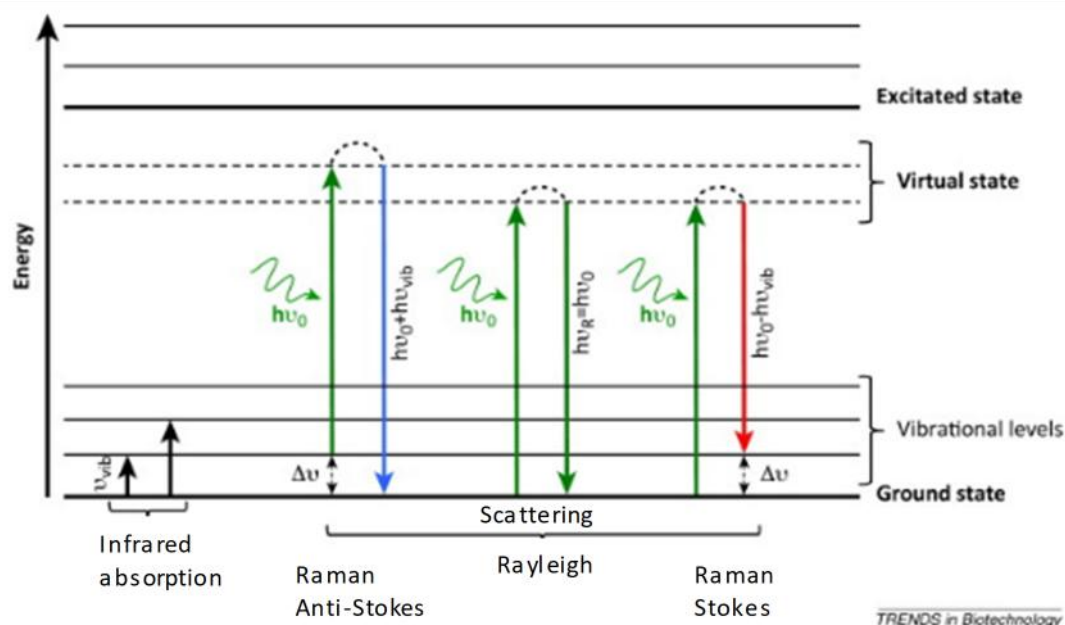


Figure 2.8. Energy level transitions for IR and Raman spectroscopies.^{59*}

In Figure 2.8, IR absorption induces a transition to a higher energy vibrational level, and Raman scattering is observed from the relaxation from a higher energy virtual state to a vibrational energy state.⁵⁷ Only one in every 10^6 photons will undergo this transition; as a result, the intensity of Raman scattering is notoriously low.⁶⁰ In order to practically detect Raman scattering, enhancement is required. The first surface enhanced Raman spectra was recorded in 1974 for pyridine on roughened silver;⁶¹ however, it was not until 1977 that Jeanmaire and Van Duyne identified the enhancement could not simply be accounted by the increased surface area of a roughened surface.⁶² This realization led to surface enhanced Raman spectroscopy (SERS). In the last 5 years, there have been over 9000 SERS publications, with citations exceeding 70000.[†] A great deal of SERS research has established that the contributing mechanism is predominantly through electromagnetic enhancement.⁶³ When interactions of molecules with light are enhanced by the LSPR excitation, Raman scattering intensity is amplified; this preferentially occurs in the sharp features and crevices of metal NPs and gaps in metal NP assemblies/films.⁶⁴ Experimentally, the

* Reprinted from *Trends in Biotechnology*, 34, J. Sulé-Suso, N.R. Forsyth, V. Untereiner, G.D. Sockalingum, *Vibrational spectroscopy in stem cell characterisation: is there a niche?*, 254-262., Copyright (2014), with permission from Elsevier.

† Per Web of Science- accessed Jan 16, 2019

electric field between two particles has been measured for a AuNP dimer,⁶⁵ and a ‘t-shaped’ dimer of AgNP,⁶⁶ where the convergence of the electric field is greatest at the cusp between particles, as shown in yellow in Figure 2.9 a and b. We have experimentally confirmed enhancement for bimorphic particles (decahedra and platelet NPs combined)⁵¹ and also silver flower NPs where those with greater faceting (crevices) gave higher enhancement factors⁴⁵ shown in panels d and c of Figure 2.9, respectively. Bimorphic nanoparticles are included in this PhD work and are further discussed in Chapter 3.

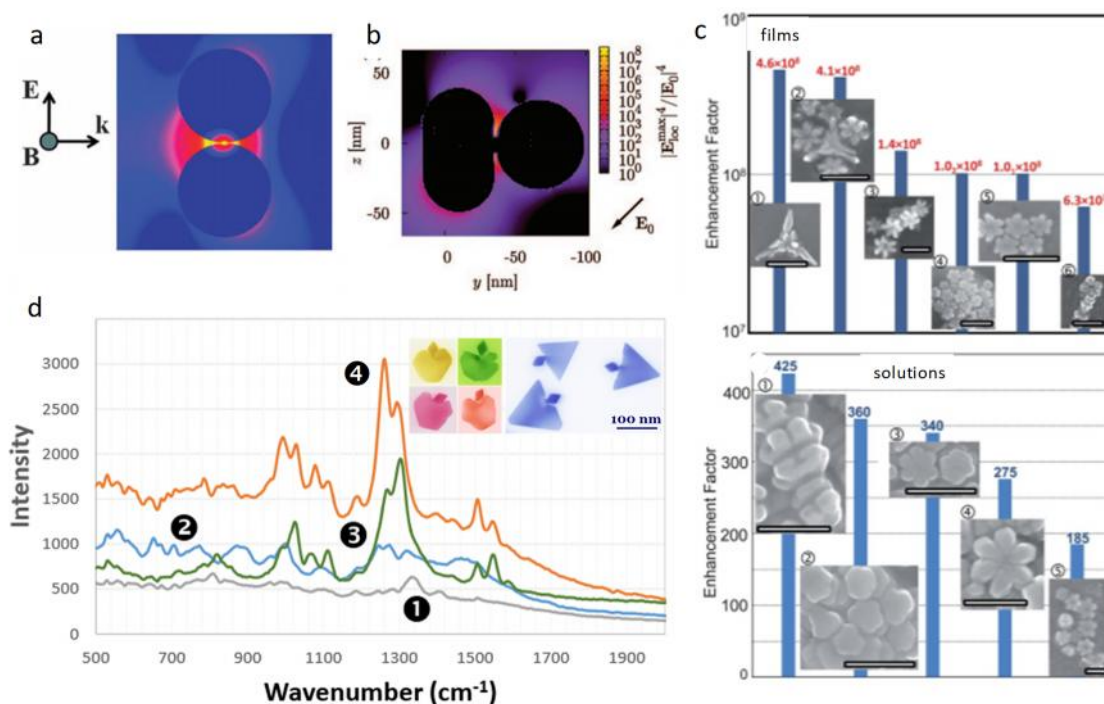


Figure 2.9. Examples of field enhancement, surface enhanced Raman spectroscopy enhancement factors and Raman spectra using various morphologies as substrates. Electric field enhancement between **a)** a gold NP dimer,⁶⁵ and **b)** a silver 'T-shaped' dimer,⁶⁶ **c)** enhancement factors for silver flowers of varying faceting,⁴⁵ **d)** Raman spectra of 1) bi-AgNP dry layer; 2) dry layer of decahedral AgNPs; 3) 1×10^{-16} mol/ cm^2 of 5'5-dithiobis(2-nitrobenzoic acid) (DTNB) over the layer of dry bi-AgNPs; and 4) 2×10^{-16} mol/ cm^2 of DTNB over the layer of dry decahedral AgNPs.^{51*}

* a) from Ref. ⁶⁵ Physical Chemistry Chemical Physics by Royal Society of Chemistry (Great Britain) Reproduced with permission of Royal Society of Chemistry in the format Thesis/Dissertation via Copyright Clearance Center., b) Reprinted with permission from Ref. ⁶⁶(J. P. Camden, J. A. Dieringer, Y. Wang, D. J. Masiello, L. D. Marks, G. C. Schatz and R. P. Van Duyne, J. Am. Chem. Soc., 2008, 130, 12616–12617). Copyright (2008) American Chemical Society. c) from Ref. ⁴⁵ reproduced by permission of The Royal Society of Chemistry and d) from Ref. ⁵¹ (N. Cathcart and V. Kitaev, Sci. Rep., 2016, 6, 32561). Licensed under CC by 4.0.

The theoretically calculated enhancement for SERS is on the order of $10^{10} - 10^{11}$.⁶⁶ Bimetallic silver and gold nanowires have been shown to feature 10^7 enhancement for 4-mercaptobenzoic acid,²¹ and a 10^5 enhancement of 2-aminothiophenol (2-ATP) has been measured from aggregated silver nanoplates.⁶⁷ Enhancement factors measured by our group using 5'-dithiobis(2-nitrobenzoic acid) (DTNB) were 10^{10} for decahedral star NPs,⁶⁸ 10^9 for decahedra NPs and bimorphic NPs,⁵¹ and 10^8 for flower shaped NPs.⁴⁵ With respect to size, SERS intensity has been measured with varying sized spherical AgNPs, resulting in the optimal size of ca. 50 nm to attain the highest enhancement.⁶⁹ Recently, the Brosseau group developed 'fab-chips' for on-body biosensing where conductive fabric is coated with AgNPs, achieving 10^8 enhancement of 4,4'-bipyridine as a proof-of-concept for the detection of biomolecules such as DNA.⁷⁰ NP-based SERS biosensors have also been produced for detection of various cancer biomarkers,⁷¹⁻⁷³ The current challenge in advancing SERS is the complex matrixes of real samples (e.g. bodily fluids), however, this can be overcome by improvements to substrates, enhancement factors, and spectral databases.⁷⁴ In this respect, the Lednev group has achieved relative success (>70% accuracy) with multi-variate analysis SERS to confirm the presence of different drugs,⁷⁵ perform diagnostics for Alzheimer's disease,⁷⁶ and predict the race origin of a sample⁷⁷ with no prior sample treatment.

2.5. Surface Plasmon Resonance Spectroscopy

Surface plasmon resonance (SPR) spectroscopy measures changes at the boundary between the metal and the external medium, where the surface plasmon resonance takes place.⁷⁸ Historically, a light source, gold film, prism and detector were used, with the light beam propagated at an angle that enables total internal reflection, with the formation of an evanescent wave and excitation of the electrons of the metal film – the conditions for surface plasmon resonance.⁷⁹ The incident angle is called the SPR angle, which will change with changes in the refractive index at the film's surface, and/or adsorption to the gold film.⁸⁰ Alternatively, changes in the wavelength, intensity, phase or polarization can be measured, and the type of sensing is classified based on the characteristic measured.⁸¹ Traditional SPR spectrometry

instrumentation is expensive, large, and sensitive to temperature and other fluid properties. It relies on illuminating an area on a film's surface at a range of angles (requires a large area for maneuvering) and detecting a shift in reflectivity when a target is immobilized. These challenging instrumental spatial requirements and the associated measurement complexities are removed by using NPs (LSPRs).⁸² As discussed above, the LSPR of MNPs is sensitive to localized changes making them ideal sensors for SPR.

The surface of NPs offers great opportunities in functionalization, as a coating of capping molecules is required to prevent aggregation and to provide a conjugating point for analytes.⁸³ The balancing act is that NPs must be sufficiently stable in hostile environments, yet sensitive to analyte interaction to change the LSPR.⁸⁴ So far a great deal of research has been focused on gold nanoparticles as sensors,⁷⁸ with limits of detections of 1 fM of Ba(II)⁸⁵ and 10 fM of miRNA⁸⁶ with colloidal AuNPs as enhancers. In the last 5 years, there have been over 17000 SPR publications, with citations exceeding 171000.* Utilizing the shift in LSPR from chemisorption, Kitaev's group has demonstrated the proof-of-concept detection limit of 3.2 pM iodide with ligand-free gold stars,⁸⁷ and 10^{-11} M KBr with pentagonal silver stars.⁶⁸ Tuning the LSPR to the maximum wavelength of the light source has also proven to be effective for maximizing sensitivity.⁸⁸ As with SERS, the main SPR challenge is minimizing the background from bodily fluids; this can be overcome by either separating the sample first, to remove larger matrix components, or by improving the signal sensitivity and detection limits, the latter is the focus of this PhD work. With respect to separating the sample first, Masson's group has developed a microanalysis channel to separate cells and platelets from whole blood samples, leaving proteins to be analyzed.⁸⁹ The microanalysis channels developed by Masson et al. have enabled the successful use of functionalized AuNPs for the sensitive detection of testosterone,⁹⁰ prostate specific antigen⁹¹ and methotrexate (cancer pharmaceutical),⁸⁹ at lower concentrations than Au films.

* Per Web of Science - accessed Jan 16, 2019

There are certainly many fruitful directions to continue with metal nanoparticles in terms of synthesis and applications, however, cost can often be a prohibitive factor with using noble metals on an industrial scale. Metal oxides and metallodielectrics (metal oxides and metal nanoparticles combined) offer a practical, relatively inexpensive route to many applications.

2.6. Metal Oxide Nanoparticles

Oxides of transition metals (groups 4-9 from the middle of the periodic table that have half-empty *d*-orbitals⁹²) have many potential and realized applications. These applications range from catalysts,⁹³⁻⁹⁶ electrodes,⁹⁷⁻⁹⁹ to conductors in films.^{97,100-102} Examples of catalytic applications are selective oxidation, ammoxidation (production of nitriles) and selective dehydrogenation.¹⁰³ Emerging in modern technology are metal oxide (MO)-based energy storage systems such as LiCoO₂ in lithium batteries,¹⁰⁴ Co₃O₄ and MnO₂ in supercapacitors,¹⁰⁵ RuO₂ and IrO₂ as photoelectrocatalyst anodes.¹⁰⁶ With respect to crystal structures of the transition metal oxides, generalizations cannot be made simply. Structures do not directly relate to stoichiometry or position in the periodic table, but they vary with formation parameters (temperature most common due to high activation energies for thermodynamically stable structures).¹⁰³ With that being said, the ionic radii of transition metals are smaller than the radius of O²⁻, so lattice packing can be conveniently represented as smaller metal ions situated in octahedral and tetrahedral holes among close packed oxygen ions.¹⁰³ Structural classes of metal oxides include corundum, rock salt, wurtzite, spinel, perovskite, rutile and layered structures, shown in Figure 2.10.

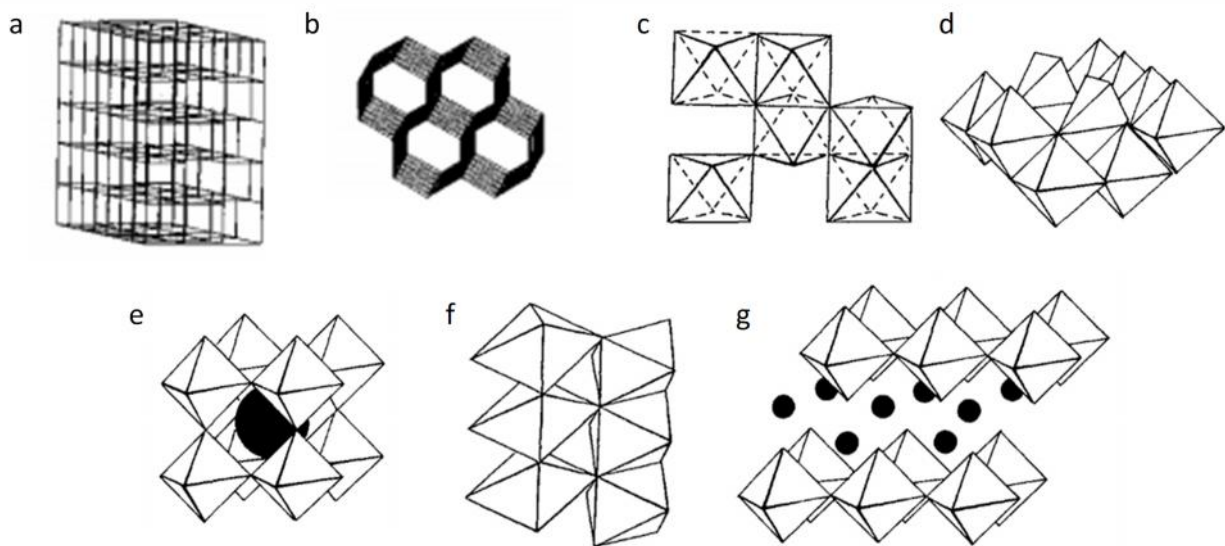


Figure 2.10. Model sketches and polyhedral structures of unit cells for **a)** rock salt, **b)** wurtzite, **c)** corundum, **d)** spinel, **e)** perovskite, **f)** rutile, and **g)** layered perovskite. a) and b) Reprinted from Ref 107, * c)-g) Reproduced from Ref.108.†

In addition to binary metal oxides of the form A_xO_2 , mixed transition-metal oxides of the form $A_xB_{3-x}O_4$ are attracting recent interest based on their electrochemical properties and the low costs of metals like cobalt, nickel, zinc, manganese, and iron.¹⁰⁴ High electrochemical activities are owing to their complex chemical compositions giving high specific capacity/capacitance; varied oxidation states of the transition metals enable the desirable electrochemical behaviour for catalysis of the oxygen reduction reaction or provide chemisorption sites for reversible adsorption of oxygen.^{109,110} High electrical conductivity is exhibited by transition metal oxides due to the electron transfer occurring between cations in different oxidation states, this property also contributes to the strength of the surface-intermediate bonds and the chemical structure of the surface. Transition metal oxides on the nanoscale are rich with electroactive sites, and also have fast electron transport through the design of the nanostructure and composition.¹⁰⁴

* (A. Wootton and P. Harrowell, *J. Chem. Phys.*, 2004, 121, 7440–7442), with the permission of AIP Publishing

† Transition Metal Oxides An Introduction to their Electronic Structure and Properties by P.A. Cox. © P.A. Cox 1992, 1995. Reproduced with permission of the Licensor through PLSclear.

The surface chemistry of the metal oxides is one of the most important parameters to investigate and control properties. Variations contributing to surface reactivity and properties include: 1) the presence of cations and anions in different stoichiometric ratios in well-defined spatial relationships, 2) the possibility of covalent and ionic bonding between cations and anions, 3) the presence of strong electric field normal to surface (Coulombic nature of ionic lattice), 4) charged adsorbed species, 5) surface acidity and basicity, 6) cationic and anionic vacancies, 7) the ability of cations to undergo oxidation and reduction, 8) the high mobility of lattice oxygen and the possibility that lattice oxygen serves as a reactant, and 9) an interaction of the solid with incident photons leading to photo-assisted surface chemical processes.¹⁰³ One of the best ways to improve catalytic activity is to tailor the morphology that is directly related to surface area and/or electroactive site density.¹⁰⁴ The density of energy states (DOS) evolves from continuous levels to discrete state with a change in dimensionality according to the relationship $\rho(E) \approx E^{D/2-1}$, where D = dimensionality (3D, 2D, 1D, or 0D).¹¹¹ This was experimentally confirmed for SnO₂ nanowires, where the electron density inside the nanowire was varied with a gate potential.¹¹² Examples of nanocrystal shapes from 0D to 3D are shown in Figure 2.11.

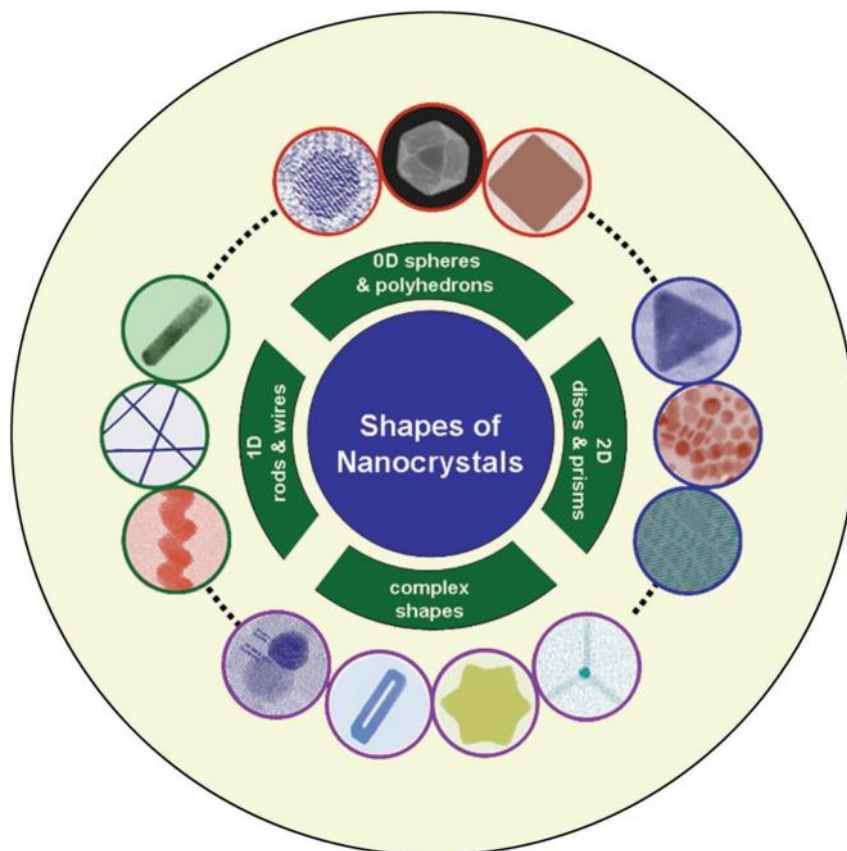


Figure 2.11. Representative shapes of inorganic nanocrystals 0D to 3D. Reproduced with permission from Ref. 113*

The methods to control properties defined by surface chemistry will be discussed in the synthesis section below, followed by the relevant applications.

2.7. MONP Synthesis

Solution-based syntheses, including hydrothermal, solvothermal and room-temperature methods, allow for the formation of metal oxide nanoparticles with diverse compositions and structures, with further control from post preparation annealing (recrystallization, volume change, gas release, etc. for high porosity/hollow structures).¹⁰⁴ Co_3O_4 , as an anode material for lithium ion batteries, has high reversible capacity and easy preparation; however, efforts have increased towards replacing the Co is ongoing as a means to reduce cost and toxicity.¹⁰⁴ Doping Co_3O_4 is well known, a CuCo_2O_4 spinel was

* Copyright © 2006, John Wiley and Sons.

prepared under high temperature-pressure conditions (solvothermal) dating back to 1975.¹¹⁴ $M_xCo_{3-x}O_4$ (M = Co, Ni, Zn) nanoarray catalysts have been prepared on channeled monolithic substrates with a urea hydrolysis process to prepare carbonate nanowires. Spinel cobaltite nanoarrays were obtained through hydrothermal treatment (90 °C for 12 hrs) followed by ambient annealing at 300 °C, mixed metals were added by including precursors containing these metals in the hydrothermal step.¹¹⁵

Room-temperature methods remain elusive in the research community, most synthesis requiring thermal decomposition (or other methods) to achieve size and shape control.¹¹⁶ Fe_3O_4 nanoparticles were prepared at room temperature by using a capping agent for size and shape control. Gallic acid modified with 1-octadecylamine (to contribute a long aliphatic chain to the surface of Fe_3O_4 nanoparticles) was combined with Fe^{2+} and Fe^{3+} iron precursors in ethanol. pH adjustment to 8 and 1 hr stirring gave a black precipitate that was washed and easily redispersed in chloroform, hexane, etc.¹¹⁶ Solid-state room-temperature synthesis procedures have also proven effective to prepare metal oxide nanostructures including ZnO, In_2O_3 , Bi_2O_3 and SnO_2 nanoparticles.¹¹⁷ Mixing and stirring the metal salt with NaOH gives highly crystalline metal oxides within 5-10 minutes, at which time the paste can be directly applied to substrates to prepare films.¹¹⁷ TiO_2 has also been prepared at room/low temperature, by hydrolyzing titanium alkoxide in acidic solution, followed by heating; different crystalline phases are achieved at different temperature and heating rates, rutile at room temperature, anatase at 100 °C heated quickly.¹¹⁸

Another novel approach to synthesize metal oxide nanocrystals of various shapes is through the direct nucleation, growth and anchoring on graphene oxide sheets.^{110,119-121} This two-stage approach uses controlled hydrolysis of the metal salt into a metal oxide on graphene oxide sheets, followed by crystallization through hydrothermal treatment in the second step.^{110,119-121} This process has proven successful for TiO_2 growth, where the coupling of the high electrical conductivity of graphene and low cost, high stability and efficient photoactivity of TiO_2 provide superior photocatalytic degradation of dye molecules.¹²⁰

Recent examples from the literature in the field are presented below in the context of growth dimensionality from spheres/cubes, that are representative of 0D shape control, to branched/star structures, representative of 3D shape control:

0D shape control (selective preparation of spheres/cubes) has been demonstrated for cube-shaped CoFe_2O_4 through thermal reactions of cobalt (II) acetylacetonate and iron (III) acetylacetonate with oleic acid and oleylamine; mild growth conditions gave cube-shaped nanocrystals and high temperature and concentrations gave spherical nanocrystals.¹²² Oleylamine was also demonstrated to be an important reactant in combination with water for the preparation of magnetite nanocubes at low (100 °C) temperatures.¹²³ A variety of γ - Fe_2O_3 nanocrystal morphologies can be prepared by the thermal decomposition of $\text{Fe}(\text{CO})_5$ in refluxing 1,2-dichlorobenzene with dodecylamine (surfactant) followed by air oxidation. The surfactant modulated the growth rate along the $\langle 111 \rangle$ direction of cubic inverse spinel iron oxide.¹²⁴

1D shape control (selective preparation of rods) was achieved for TiO_2 through the alkyl halide elimination reaction of TiCl_4 and $\text{Ti}(\text{OiPr})_4$ in a hot trioctylphosphine oxide solution with lauric acid.¹¹³ ZnO nanorods have been prepared through the thermal decomposition of zinc acetate in the presence of oleic acid.¹²⁵ Additional examples of nanorod growth including Fe_3O_4 , CoO , and ZnO can be prepared through thermal decomposition of metal oleate complexes.¹²⁶ ZnO rods and wires can also be prepared solvothermally using ethanol or water as solvents.¹²⁷ In a kinetically driven one-pot process, an acyl halide elimination reaction increases the metal oxide monomer concentration in turn promoting fast growth along the directions with the highest surface energy for the preparation of transition metal oxide nanorods (TiO_2 , $\text{W}_{18}\text{O}_{49}$, and Mn_3O_4).¹²⁸ 1D Ternary perovskite oxide BaTiO_3 and SrTiO_3 nanowires have also been prepared through a sol-gel reaction in hot organic solvent with hydrogen peroxide added by injection.¹²⁹

2D shape control (discs and prisms) is common in metallic nanoparticles,^{5,19,130,131} however reports of metal oxide platelets are limited. Examples of lanthanide oxide nanocrystals were prepared through the thermal decomposition of lanthanum benzoylacetylacetonate in a hot mixture of oleic acid and oleylamine resulting in Ln₂O₃ platelets or discs with cubic symmetry (Ln = La, Pr, Nd, Sm, Eu, Gd, Tb, Er, Y).¹³² Also, ZnO discs have been prepared solvothermally using propanol as a solvent.¹²⁷

3D shape control (star or branched shapes) can be prepared by assembling several components, for example, assemblies of rods into bi- tri- and tetra- pods.¹¹³ The morphology of TiO₂ nanocrystals has been controlled by the concentration of a long-chain carboxylic acid (lauric acid) which modulates the surface energy of different crystallographic faces when titanium tetraisopropoxide and titanium tetrachloride are combined with trioctylphosphine oxide and lauric acid. This process yields nanocrystals with shapes ranging from bullet, to diamond, rod and branched rods.¹³³ ZnO tetrapods are of interest for a variety of functional applications; as such, there are many reported methods for their synthesis, nicely summarized in a recent review.¹³⁴

2.8. Applications of MONPs

The diverse electrical, optical, magnetic, mechanical and chemical sensing properties of metal oxides enable their use in widespread applications.¹³⁵ Gas sensors based on MONPs are favoured by domestic, commercial and industrial applications for their low cost, small size and ease of production.¹³⁶ Enzymatic biosensors based on metal oxides have also been prepared.¹³⁷ Metal oxides are well known catalysts, and recent attention is especially focused on metal oxides as catalysts for water splitting.^{94,138,139} Research into the structure-catalysis relationship of manganese oxides for photochemical water oxidation catalysis has been performed, where the greatest catalytic activity was achieved for the oxide with Mn³⁺.¹³⁸ Iron oxide nanomaterials have found use in wastewater treatment as nanosorbents, photocatalysts and immobilization carriers.¹⁴⁰

Driven by the desire to depart from the use of fossil fuels, hydrogen is being explored based on its great potential as a clean energy source. The current problems in using hydrogen are two-fold – production and storage. Metal oxides have received increasing attention as anode materials for the production of hydrogen through water splitting.¹⁰⁶ A summary of photocurrent densities from a variety of metal oxide photoelectrodes and examples from this PhD work are given in Table A1.1.

Nanosized metal oxides have also been used for removal of contaminants from water and wastewater; of particular concern are heavy metals¹⁴⁸ and emerging contaminants: pharmaceutical and personal care products.¹⁴⁹ Nanoparticles present an opportunity to mediate these contaminants by virtue of their large surface area, high chemical reactivity, and material availability, along with their functional nanoscale properties.¹⁴⁹ Typically, this research focuses on the use of iron-based nanomaterials,^{140,150,151} attributed to the abundance of iron, its affordability, and well-documented use and NP synthesis;¹⁴⁹ however, there are examples using mixed metal oxides,¹⁵² manganese oxides,¹⁵³ Cu(II) oxides¹⁵⁴ or alumina.¹⁵⁵

The two main methods of contaminant removal with MONPs are through (photo)electrochemistry to convert to more benign compounds or through sorption. Figure 2.12 outlines the current applications of iron oxide nanomaterials for environmental remediation, and gaps that must be met for successful integration and improvements. One of the solutions listed to overcome the downfalls in adsorptive technology is to optimise synthesis, one of the important goals of this PhD work.

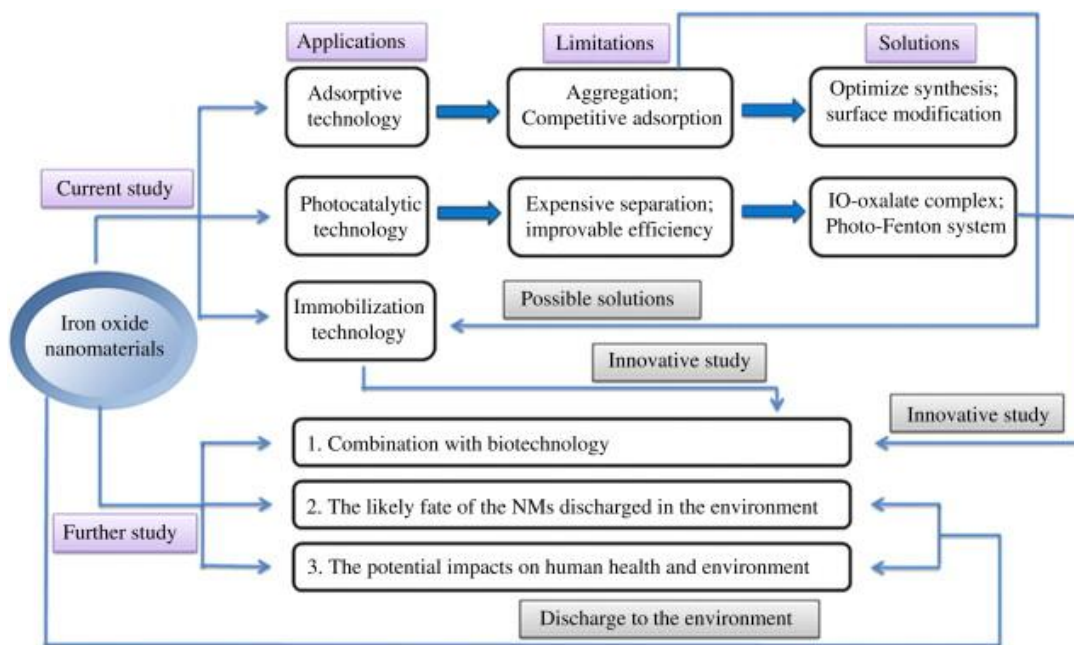


Figure 2.12. Overview of applications of iron oxide nanomaterials, limitations, solutions and further study. Reproduced with permission from Ref. 140.*

In general, removal of current contaminants from water through adsorption suffers from low selectivity, capacity, problems with generation and the formation of secondary contaminants.¹⁵⁶ H. Gray has compiled an excellent summary of adsorbent metal oxides.¹⁵⁷ Iron-based sorbents have been used widely for anion removal, as iron oxides are widespread in nature.¹⁵⁶ The akageneite structure contains chloride anions, which can participate in ion exchange with anions such as fluoride and hydroxide ions.¹⁵⁸ The adsorption and uptake of phosphate have been well studied for akageneite,^{159–161} with high selectivity and capacities exceeding 450 mg phosphate per g akageneite (nanocrystalline hybrid surfactant-modified akageneite).¹⁶¹ By optimizing the sizes and morphologies of iron oxide nanoparticles, sorption capacities can be improved further.

* Reprinted from Science of The Total Environment, Volume 424, Piao Xu, Guang Ming Zeng, Dan Lian Huang, Chong Ling Feng, Shuang Hu, Mei Hua Zhao, Cui Lai, Zhen Wei, Chao Huang, Geng Xin Xie, Zhi Feng Liu, Use of iron oxide nanomaterials in wastewater treatment: A review, pgs. 1-10, Copyright (2012), with permission from Elsevier.

2.9 Metallodielectric Nanoparticles (Synthesis and Applications)

Metallodielectric nanoparticles (MDNPs) aim to combine a MNP core with a metal oxide shell. In doing so, stability and additional properties can be achieved, while also maintaining (and improving) the LSPR functionality of MNPs. The primary benefit of combining MNPs with metal oxides is the plasmonic coupling that occurs, changing the optical properties of MNPs in solution.¹⁶² Incorporating silica as an outer shell provides an insulator and a spacer for tuning optical properties.¹⁶³ Additionally, this core-shell structure hinders aggregation, keeping colloids dispersed.¹⁶⁴ Liz-Marzán successfully coated gold nanoparticles with silica by functionalizing the gold surface with (3-aminopropyl)trimethoxysilane.¹⁶⁵ This procedure has been adapted by many scientists since 1996. More recently, Chen et al. coated gold nanoparticles with silica in a one pot method where gold, cetyltrimethylammonium bromide (CTAB), sodium hydroxide, formaldehyde, tetraethyl orthosilicate (TEOS) and ethanol were combined in sequential heating regimes.¹⁶⁶ Silica-coated metal nanoparticles are considered to be the most successful class of metallodielectric nanoparticles, as is highlighted in a detailed recent review of synthesis methods, diverse structures, and practical applications.¹⁶⁷ Concentric particles have also been prepared, where a silica core is coated with a metal and then coated with a layer of silica; they are proposed to be beneficial for use in optical components (narrow band absorbers/emitters) or for waste energy recovery by virtue of an advantageous combination of their metal conductivity and electrical insulation.¹⁶³ The development of waveguides and resonators is a goal of quantum optics to influence the interactions between light and matter.¹⁶⁸ The use of nano-sized metals has great promise with this respect, and quantum entanglement and plasmonic coupling to other materials (like metal oxides) can lead to quantum-plasmonic circuits, single photo transistors and quantum gates.^{168,169}

Recent trends in photonics include the integration of electronic and photonic devices, which are advantageous due to their reduced size, enhanced speed of operation, robustness to temperature, increased lifetime and high repetition rates.¹⁷⁰ An emerging field is “Lab-on-Fiber” where functionalized

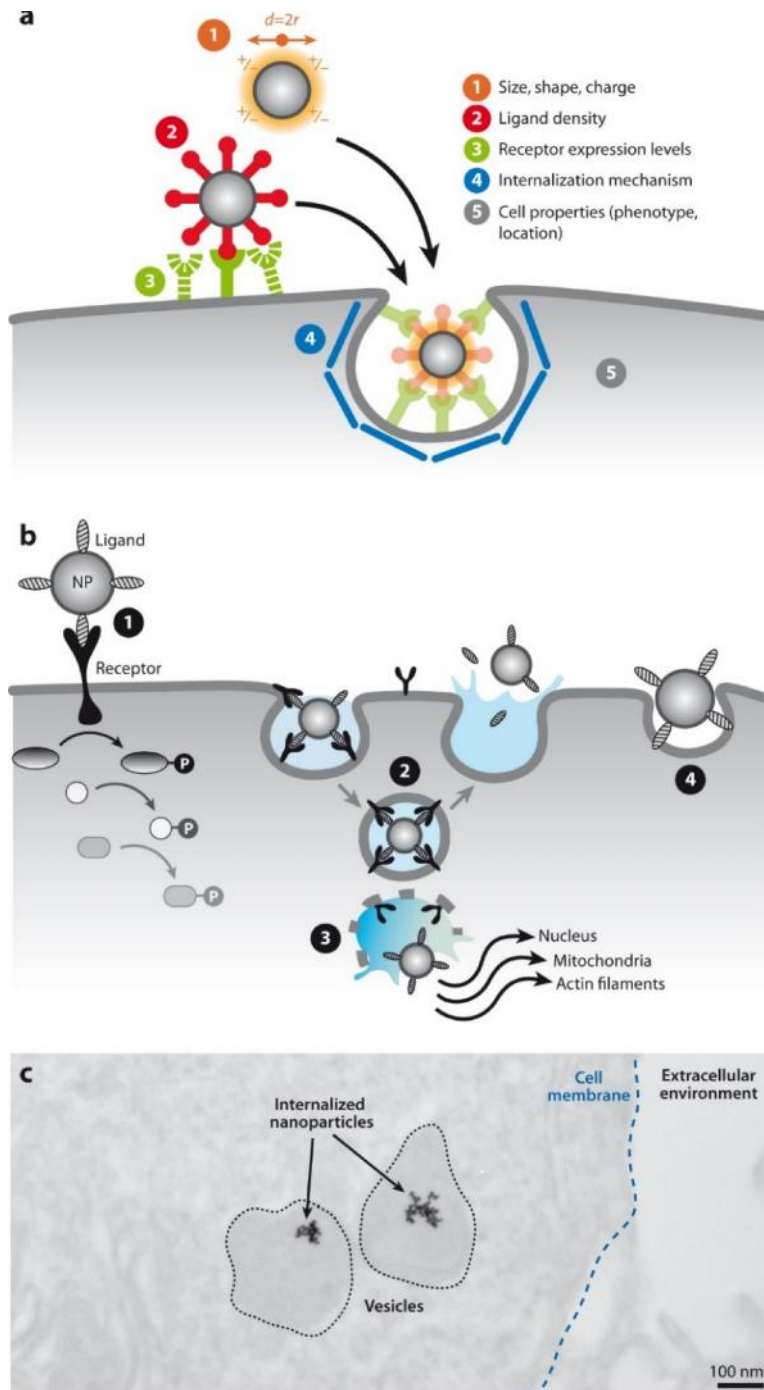
materials, devices, and components are combined as a platform for sensing.¹⁷¹ Developing light waveguides, improving functionalities and gaining understanding for light's manipulation and control remain a challenge for this field,¹⁷¹ which can be aided by improving nanostructures. "Lab-in-a-Shell" has also gained increasing attention, where core-shell nanospheres with a hollow microporous shell, prepared by encapsulating and immobilizing metal clusters, can integrate laboratory functions in an engineered microenvironment.¹⁷²

In a collaborative work of Obelleiro, Grzelczak and Liz-Marzán, gold nanorods were grown on silica spheres, which have potential as photocatalysts, biosensors, or a new class of conductive substrates (when made into films).¹⁶² Au triangles have also been modeled to form "nanoantennae" with silica, giving enhancement to the plasmon resonance intensity and could be used as a sensors.¹⁷³ Positioning of the MNP relative to the oxide has also been studied theoretically, where additional plasmonic transitions were observed with asymmetric packing.¹⁶⁴ Experimentally, metallodielectric nanoparticles with reduced symmetry have been prepared, where half of the metal core is encapsulated with metal oxide substrate making nanocups and nanocaps.¹⁷⁴ Additionally, Song et al. have shown the ability to tune metallodielectrics photonic crystals thermally.¹⁷⁵

The use of MDNPs for sensing applications by optimizing size and shape of the encapsulated MNPs, as well as the composition and thickness of the metal oxide shell for improvement of sensitivity and enhancement factors are discussed in Chapter 6.

2.10. Health and Safety Considerations

With respect to safety, size and state of NPs play important roles; especially when considering the biocompatibility with cells.¹⁷⁶ As depicted in Figure 2.13, there are 5 primary factors that govern nanoparticle-cell interactions.¹⁷⁷



Albanese A, et al. 2012.
 Annu. Rev. Biomed. Eng. 14:1–16

Figure 2.13. Nanoparticle-cell interactions. a) demonstrating the five main factors governing interactions of NPs with cells, b) ligand coating NP interacting with cells, c) internalized 50 nm NPs in a cell. Reproduced from Ref.177*

* . Republished with permission of ANNUAL REVIEWS, INC. from The Effect of Nanoparticle Size, Shape, and Surface Chemistry on Biological Systems, Albanese, A., et al., 14, 2012; permission conveyed through Copyright Clearance Center, Inc.

The optimal size for cell uptake is ca. 50 nm for spherical gold¹⁷⁸ or silica NPs,¹⁷⁹ likely due to the proper ligand-to-receptor ratio required for endocytosis to allow the NP to enter the cell; a 5 nm NP has too few ligand-receptor interactions, while a 100 nm NP has too many and is too large.¹⁷⁷ In an evaluation of the biological distribution of various sized gold nanoparticles in mice, smaller NPs (15 nm) were found in all tissues, and large 200 nm NPs were rarely found.¹⁸⁰ In a very thorough review, environment, health and safety research was compiled to assess NP use, exposure, and toxicity from 293 studies.¹⁸¹ General conclusions were that exposure from air (inhalation/aerosols) are the most concerning for human health; however, air cleaning filters are successful at removing NPs from the air. This review also characterized carbon nanotubes as potentially adverse for human health, and silver nanoparticles and titanium dioxide NPs as environmentally detrimental.¹⁸¹

In an estimation of the predicted environmental concentration of silver NPs, the largest contribution is likely due to their release during the lifecycle of consumer products.¹⁸² Of the approximately 1800 nanoparticle-containing products on the market, silver nanoparticles make up 24% (reported in 2015).¹⁸³ These products largely capitalize on antimicrobial properties of silver, which have long been used in water purification and healthcare.¹⁸⁴ Metallic silver is generally considered safe and of low toxicity to humans; however, with the increase in availability and promotion of homeopathic remedies of colloidal silver, chronic ingestion has resulted in several cases of argyria (development of blue-grey skin from excessive exposure to silver).¹⁸⁵ In an extreme case, daily ingestion of colloidal silver has caused irreversible neurologic toxicity resulting in death.¹⁸⁶ Silver nanoparticles release silver ions through oxidation, the rate at which this occurs depends on the initial size of the NP, surface coating and environmental conditions.¹⁸⁷ Solid silver is insoluble, rendering it irrelevant for bioavailability, and higher oxidation states (+2 and +3) are possible, but again not relevant for biological systems, therefore the main ion of concern is Ag⁺.¹⁸⁷ In general with AgNPs, criteria to consider are 1) the agglomeration or aggregation to larger particles (decreasing bioavailability), 2) oxidation of Ag(0) to Ag⁺ (increasing bioavailability), 3)

dissolution to dissolved Ag^+ (increased bioavailability), 4) speciation and solubility of Ag^+ (increased bioavailability), and 5) reactions modifying the reactivity of $\text{Ag}(0)$ -NPs (potentially increased bioavailability).¹⁸⁷ To experimentally prevent agglomeration and aggregation, oxidation, and dissolution, the silver nanoparticles prepared in our lab are coated with stabilizing agents (polymers, carboxylic acids, thiols, etc.).^{26,188,189} This protection also decreases bioavailability by decreasing the concentration of free Ag^+ ions on the particle surface. The toxicity of silver nanoparticles is further discussed in Chapter 7.

The case with metal oxide NPs is more complicated to determine whether the metal ion or the NP themselves are responsible for toxicity. To assess this, the antibacterial effect of CuO , Fe_2O_3 , ZnO , Co_3O_4 , Cr_2O_3 and NiO NPs on *Photobacterium phosphoreum* (a bioluminescent bacterium) was investigated. The results could be grouped into three categories, 1) ZnO toxicity solely due to Zn^{2+} release, 2) CuO effect from both Cu^{2+} and CuO , and 3) Fe_2O_3 , Co_3O_4 , Cr_2O_3 and NiO NPs themselves were responsible for toxicity.¹⁹⁰ In addition to metal oxide type, the size and morphology also contribute to interactions with cells/microorganisms, leading to a call to use size-dependent safety guidelines for NPs in contrast to only size for risk assessment.¹⁹¹

2.11. References

- (1) Mie, G. Beiträge Zur Optik Trüber Medien, Speziell Kolloidaler Metallösungen" (Contributions to the Optics of Turbid Media, Particularly Colloidal Metal Suspensions). *Ann. Phys.* **1908**, *25*, 377–445.
- (2) Monk, P. *Finite Element Methods for Maxwell's Equations*; Oxford University Press, New York, **2003**.
- (3) Link, S.; El-Sayed, M. A. Optical Properties and Ultrafast Dynamics of Metallic Nanocrystals. *Annu. Rev. Phys. Chem.* **2003**, *54*, 331–366.
- (4) Willets, K. A.; Van Duyne, R. P. Localized Surface Plasmon Resonance Spectroscopy and Sensing. *Annu. Rev. Phys. Chem.* **2007**, *58*, 267–297.
- (5) Cathcart, N.; Frank, A. J.; Kitaev, V. Silver Nanoparticles with Planar Twinned Defects: Effect of Halides for Precise Tuning of Plasmon Resonance Maxima from 400 to 900 nm. *Chem. Commun.* **2009**, *6*, 7170–7172.
- (6) Pietrobon, B.; McEachran, M.; Kitaev, V. Synthesis of Size-Controlled Faceted Pentagonal Silver Nanorods with Tunable Plasmonic Properties and Self-Assembly of These Nanorods. *ACS Nano*

- 2009**, 3, 21–26.
- (7) Jain, P. K.; El-Sayed, M. A. Plasmonic Coupling in Noble Metal Nanostructures. *Chem. Phys. Lett.* **2010**, 487, 153–164.
- (8) Wooten, F. *Optical Properties of Solids*; Academic Press: New York, **1972**.
- (9) Johnson, P. B.; Christy, R. W. Optical Constants of the Noble Metals. *Phys. Rev. B* **1972**, 6, 4370–4379.
- (10) Eustis, S.; El-Sayed, M. A. Why Gold Nanoparticles Are More Precious than Pretty Gold: Noble Metal Surface Plasmon Resonance and Its Enhancement of the Radiative and Nonradiative Properties of Nanocrystals of Different Shapes. *Chem. Soc. Rev.* **2006**, 35, 209–217.
- (11) Franzen, S. Surface Plasmon Polaritons and Screened Plasma Absorption in Indium Tin Oxide Compared to Silver and Gold. *J. Phys. Chem. C* **2008**, 112, 6027–6032.
- (12) Singh, I.; Sabita, M. P.; Altekar, V. A. Silver Tarnishing and Its Prevention — A Review. *Anti-Corrosion Methods Mater.* **1983**, 30, 4–8.
- (13) Hammer, B.; Norskov, J. K. Why Gold Is the Noblest of All the Metals. *Nature* **1995**, 376, 238–240.
- (14) Hakkinen, H.; Merikoski, J.; Manninen, M. Surface Reconstruction and Many-Atom Models. *J. Phys. Condens. Matter* **1991**, 3, 2755–2767.
- (15) Sun, Y.; Xia, Y. Shape-Controlled Synthesis of Gold and Silver Nanoparticles. *Science* **2002**, 298, 2176–2179.
- (16) Grzelczak, Marek, Pérez-Juste, Jorge, Paul, Mulvaney, Liz-Marzán, L. M. Shape Control in Gold Nanoparticle Synthesis. *Chem. Soc. Rev.* **2008**, 37, 1783–1791.
- (17) Zhao, P.; Li, N.; Astruc, D. State of the Art in Gold Nanoparticle Synthesis. *Coord. Chem. Rev.* **2013**, 257, 638–665.
- (18) Kimling, J.; Maier, M.; Okenve, B.; Kotaidis, V.; Ballot, H.; Plech, A. Turkevich Method for Gold Nanoparticle Synthesis Revisited. *J. Phys. Chem. B* **2006**, 110, 15700–15707.
- (19) Turkevich, J.; Stevenson, P. C.; James, H. A Study of the Nucleation and Growth Process in the Synthesis of Colloidal Gold. *Discuss. Faraday Soc.* **1951**, 11, 55–75.
- (20) Mayer, M.; Steiner, A. M.; Röder, F.; Formanek, P.; König, T. A. F.; Fery, A. Aqueous Gold Overgrowth of Silver Nanoparticles: Merging the Plasmonic Properties of Silver with the Functionality of Gold. *Angew. Chemie Int. Ed.* **2017**, 56, 15866–15870.
- (21) Hunyadi, S. E.; Murphy, C. J. Bimetallic Silver–gold Nanowires: Fabrication and Use in Surface-Enhanced Raman Scattering. *J. Mater. Chem.* **2006**, 16, 3929–3935.
- (22) Hobbs, K.; Cathcart, N.; Kitaev, V. Gold-Plated Silver Nanoparticles Engineered for Sensitive Plasmonic Detection Amplified by Morphological Changes. *Chem. Commun.* **2016**, 52, 9785–9788.
- (23) Faraday, M. The Bakerian Lecture: Experimental Relations of Gold (and Other Metals) to Light. *Philos. Trans. R. Soc. London* **1857**, 147, 145–181.
- (24) Petroski, J. M.; Wang, Z. L.; Green, T. C.; El-sayed, M. a. Kinetically Controlled Growth and Shape Formation Mechanism of Platinum Nanoparticles. *J. Phys. Chem. B* **1998**, 102, 3316–3320.

- (25) Liu, H.; Nosheen, F.; Wang, X. Noble Metal Alloy Complex Nanostructures: Controllable Synthesis and Their Electrochemical Property. *Chem. Soc. Rev.* **2015**, *44*, 3056–3078.
- (26) Pietrobon, B.; Kitaev, V. Photochemical Synthesis of Monodisperse Size-Controlled Silver Decahedral Nanoparticles and Their Remarkable Optical Properties. *Chem. Mater.* **2008**, *20*, 5186–5190.
- (27) Personick, M. L.; Mirkin, C. A. Making Sense of the Mayhem behind Shape Control in the Synthesis of Gold Nanoparticles. *J. Am. Chem. Soc.* **2013**, *135*, 18238–18247.
- (28) Sau, T. K.; Rogach, A. L.; Jäckel, F.; Klar, T. A.; Feldmann, J. Properties and Applications of Colloidal Nonspherical Noble Metal Nanoparticles. *Adv. Mater.* **2010**, *22*, 1805–1825.
- (29) Kelly, K. L.; Coronado, E.; Zhao, L. L.; Schatz, G. C. The Optical Properties of Metal Nanoparticles: The Influence of Size, Shape, and Dielectric Environment. *J. Phys. Chem. B* **2003**, *107*, 668–677.
- (30) El-Sayed, M. A. Small Is Different: Shape-, Size-, and Composition-Dependent Properties of Some Colloidal Semiconductor Nanocrystals. *Acc. Chem. Res.* **2004**, *37*, 326–333.
- (31) Burda, C.; Chen, X.; Narayanan, R.; El-Sayed, M. A. Chemistry and Properties of Nanocrystals of Different Shapes. *Chem. Rev.* **2005**, *105*, 1025–1102.
- (32) Xia, X.; Xia, Y. Symmetry Breaking during Seeded Growth of Nanocrystals. *Nano Lett.* **2012**, *12*, 6038–6042.
- (33) Viswanath, B.; Kundu, P.; Halder, A.; Ravishankar, N. Mechanistic Aspects of Shape Selection and Symmetry Breaking during Nanostructure Growth by Wet Chemical Methods. *J. Phys. Chem. C* **2009**, *113*, 16866–16883.
- (34) Xia, Y.; Xia, X.; Peng, H.-C. Shape-Controlled Synthesis of Colloidal Metal Nanocrystals: Thermodynamic versus Kinetic Products. *J. Am. Chem. Soc.* **2015**, *137*, 7947–7966.
- (35) Murshid, N.; Kitaev, V. Role of Poly(Vinylpyrrolidone) (PVP) and Other Sterically Protecting Polymers in Selective Stabilization of {111} and {100} Facets in Pentagonally Twinned Silver Nanoparticles. *Chem. Commun.* **2014**, *50*, 1247–1249.
- (36) Elechiguerra, J. L.; Reyes-Gasga, J.; Yacaman, M. J. The Role of Twinning in Shape Evolution of Anisotropic Noble Metal Nanostructures. *J. Mater. Chem.* **2006**, *16*, 3906–3919.
- (37) DuChene, J. S.; Niu, W.; Abendroth, J. M.; Sun, Q.; Zhao, W.; Huo, F.; Wei, W. D. Halide Anions as Shape-Directing Agents for Obtaining High-Quality Anisotropic Gold Nanostructures. *Chem. Mater.* **2013**, *25*, 1392–1399.
- (38) Xia, X.; Zeng, J.; Zhang, Q.; Moran, C. H.; Xia, Y. Recent Developments in Shape-Controlled Synthesis of Silver Nanocrystals. *J. Phys. Chem. C. Nanomater. Interfaces* **2012**, *116*, 21647–21656.
- (39) Tran, R.; Xu, Z.; Radhakrishnan, B.; Winston, D.; Sun, W.; Persson, K. A.; Ong, S. P. Surface Energies of Elemental Crystals. *Sci. Data* **2016**, *3*, 160080.
- (40) Callister Jr., W. D. *Fundamentals of Materials Science and Engineering -An Integrated Approach*, 2nd ed.; John Wiley & Sons, Inc., New York, **2005**.
- (41) Millstone, J. E.; Hurst, S. J.; Métraux, G. S.; Cutler, J. I.; Mirkin, C. A. Colloidal Gold and Silver

- Triangular Nanoprisms. *Small* **2009**, *5*, 646–664.
- (42) Lofton, C.; Sigmund, W. Mechanisms Controlling Crystal Habits of Gold and Silver Colloids. *Adv. Funct. Mater.* **2005**, *15*, 1197–1208.
- (43) Aherne, D.; Ledwith, D. M.; Gara, M.; Kelly, J. M. Optical Properties and Growth Aspects of Silver Nanoprisms Produced by a Highly Reproducible and Rapid Synthesis at Room Temperature. *Adv. Funct. Mater.* **2008**, *18*, 2005–2016.
- (44) McEachran, M.; Kitaev, V. Direct Structural Transformation of Silver Platelets into Right Bipyramids and Twinned Cube Nanoparticles: Morphology Governed by Defects. *Chem. Commun.* **2008**, *44*, 5737–5739.
- (45) Cathcart, N.; Kitaev, V. Multifaceted Prismatic Silver Nanoparticles: Synthesis by Chloride-Directed Selective Growth from Thiolate-Protected Clusters and SERS Properties. *Nanoscale* **2012**, *4*, 6981–6989.
- (46) Keunen, R.; Cathcart, N.; Kitaev, V. Plasmon Mediated Shape and Size Selective Synthesis of Icosahedral Silver Nanoparticles via Oxidative Etching and Their 1-D Transformation to Pentagonal Pins. *Nanoscale* **2014**, *6*, 8045–8051.
- (47) Song, M.; Wu, Z.; Lu, N.; Li, D. Strain Relaxation-Induced Twin Interface Migration and Morphology Evolution of Silver Nanoparticles. *Chem. Mater.* **2019**, *31*, 842–850.
- (48) Washio, I.; Xiong, Y.; Yin, Y.; Xia, Y. Reduction by the End Groups of Poly(Vinyl Pyrrolidone): A New and Versatile Route to the Kinetically Controlled Synthesis of Ag Triangular Nanoplates. *Adv. Mater.* **2006**, *18*, 1745–1749.
- (49) Sau, T. K.; Rogach, A. L. Nonspherical Noble Metal Nanoparticles: Colloid-Chemical Synthesis and Morphology Control. *Adv. Mater.* **2010**, *22*, 1781–1804.
- (50) Murshid, N.; Keogh, D.; Kitaev, V. Optimized Synthetic Protocols for Preparation of Versatile Plasmonic Platform Based on Silver Nanoparticles with Pentagonal Symmetries. *Part. Part. Syst. Charact.* **2014**, *31*, 178–189.
- (51) Cathcart, N.; Kitaev, V. Symmetry Breaking by Surface Blocking: Synthesis of Bimorphic Silver Nanoparticles, Nanoscale Fishes and Apples. *Sci. Rep.* **2016**, *6*, 32561.
- (52) Abalde-Cela, S.; Taladriz-Blanco, P.; de Oliveira, M. G.; Abell, C. Droplet Microfluidics for the Highly Controlled Synthesis of Branched Gold Nanoparticles. *Sci. Rep.* **2018**, *8*, 2440.
- (53) Krauss, E.; Kullock, R.; Wu, X.; Geisler, P.; Lundt, N.; Kamp, M.; Hecht, B. Controlled Growth of High-Aspect-Ratio Single-Crystalline Gold Platelets. *Cryst. Growth Des.* **2018**, *18*, 1297–1302.
- (54) Liu, B.; Wu, P.; Huang, Z.; Ma, L.; Liu, J. Bromide as a Robust Backfiller on Gold for Precise Control of DNA Conformation and High Stability of Spherical Nucleic Acids. *J. Am. Chem. Soc.* **2018**, *140*, 4499–4502.
- (55) Laramy, C. R.; Lopez-Rios, H.; O'Brien, M. N.; Girard, M.; Stawicki, R. J.; Lee, B.; de la Cruz, M. O.; Mirkin, C. A. Controlled Symmetry Breaking in Colloidal Crystal Engineering with DNA. *ACS Nano* **2019**, *13*, 1412–1420.
- (56) Zhang, H.; Chen, J.; Li, N.; Jiang, R.; Zhu, X.-M.; Wang, J. Au Nanobottles with Synthetically Tunable Overall and Opening Sizes for Chemo-Photothermal Combined Therapy. *ACS Appl. Mater. Interfaces* **2019**, *11*, 5353–5363.

- (57) Ferraro, J. R.; Nakamoto, K.; Brown, C. W. *Introductory Raman Spectroscopy*; Academic Press, Cambridge, MA, **2003**.
- (58) Lambert, J. B. *Organic Structural Spectroscopy*; Prentice Hall, Upper Saddle River, NJ, **1998**.
- (59) Sulé-Suso, J.; Forsyth, N. R.; Untereiner, V.; Sockalingum, G. D. Vibrational Spectroscopy in Stem Cell Characterisation: Is There a Niche? *Trends Biotechnol.* **2014**, *32*, 254–262.
- (60) Harris, D. C.; Bertolucci, M. D. *Symmetry and Spectroscopy : An Introduction to Vibrational and Electronic Spectroscopy*; Dover Publications, New York, **1989**.
- (61) Fleischmann, M.; Hendra, P. J.; Mcquillan, A. J. Raman Spectra of Pyridine Adsorbed at a Silver Electrode. *Chem. Phys. Lett.* **1974**, *26*, 163–166.
- (62) Jeanmaire, D. L.; Van Duyne, R. P. Surface Raman Spectroelectrochemistry. *J. Electroanal. Chem.* **1977**, *84*, 1–20.
- (63) Stiles, P. L.; Dieringer, J. A.; Shah, N. C.; Van Duyne, R. P. Surface-Enhanced Raman Spectroscopy. *Annu. Rev. Anal. Chem.* **2008**, *1*, 601–626.
- (64) Sharma, B.; Frontiera, R. R.; Henry, A.-I.; Ringe, E.; Van Duyne, R. P. SERS: Materials, Applications, and the Future. *Mater. Today* **2012**, *15*, 16–25.
- (65) Kleinman, S. L.; Frontiera, R. R.; Henry, A.-I.; Dieringer, J. A.; Van Duyne, R. P. Creating, Characterizing, and Controlling Chemistry with SERS Hot Spots. *Phys. Chem. Chem. Phys.* **2013**, *15*, 21–36.
- (66) Camden, J. P.; Dieringer, J. A.; Wang, Y.; Masiello, D. J.; Marks, L. D.; Schatz, G. C.; Van Duyne, R. P. Probing the Structure of Single-Molecule Surface-Enhanced Raman Scattering Hot Spots. *J. Am. Chem. Soc.* **2008**, *130*, 12616–12617.
- (67) Zou, X.; Dong, S. Surface-Enhanced Raman Scattering Studies on Aggregated Silver Nanoplates in Aqueous Solution. *J. Phys. Chem. B* **2006**, *110*, 21545–21550.
- (68) Cathcart, N.; Coombs, N.; Gourevich, I.; Kitaev, V. Synthesis and Sensing Properties of D_{5h} Pentagonal Silver Star Nanoparticles. *Nanoscale* **2016**, *8*, 18282–18290.
- (69) Stamplecoskie, K. G.; Scaiano, J. C.; Tiwari, V. S.; Anis, H. Optimal Size of Silver Nanoparticles for Surface-Enhanced Raman Spectroscopy. *J. Phys. Chem. C* **2011**, *115*, 1403–1409.
- (70) Robinson, A. M.; Zhao, L.; Shah Alam, M. Y.; Bhandari, P.; Harroun, S. G.; Dendukuri, D.; Blackburn, J.; Brosseau, C. L. The Development of “Fab-Chips” as Low-Cost, Sensitive Surface-Enhanced Raman Spectroscopy (SERS) Substrates for Analytical Applications. *Analyst* **2015**, *140*, 779–785.
- (71) Grubisha, D. S.; Lipert, R. J.; Park, H. Y.; Driskell, J.; Porter, M. D. Femtomolar Detection of Prostate-Specific Antigen: An Immunoassay Based on Surface-Enhanced Raman Scattering and Immunogold Labels. *Anal. Chem.* **2003**, *75*, 5936–5943.
- (72) Yoo, S. M.; Lee, S. Y. Optical Biosensors for the Detection of Pathogenic Microorganisms. *Trends Biotechnol.* **2016**, *34*, 7–25.
- (73) Mohs, A. M.; Mancini, M. C.; Singhal, S.; Provenzale, J. M.; Leyland-Jones, B.; Wang, M. D.; Nie, S. Hand-Held Spectroscopic Device for In Vivo and Intraoperative Tumor Detection: Contrast Enhancement, Detection Sensitivity, and Tissue Penetration. *Anal. Chem.* **2010**, *82*, 9058–9065.

- (74) Virkler, K.; Lednev, I. K. Analysis of Body Fluids for Forensic Purposes: From Laboratory Testing to Non-Destructive Rapid Confirmatory Identification at a Crime Scene. *Forensic Sci. Int.* **2009**, *188*, 1–17.
- (75) de Oliveira Penido, C. A. F.; Pacheco, M. T. T.; Lednev, I. K.; Silveira, L. Raman Spectroscopy in Forensic Analysis: Identification of Cocaine and Other Illegal Drugs of Abuse. *J. Raman Spectrosc.* **2016**, *47*, 28–38.
- (76) Ryzhikova, E.; Kazakov, O.; Halamkova, L.; Celmins, D.; Malone, P.; Molho, E.; Zimmerman, E. A.; Lednev, I. K. Raman Spectroscopy of Blood Serum for Alzheimer's Disease Diagnostics: Specificity Relative to Other Types of Dementia. *J. Biophotonics* **2015**, *8*, 584–596.
- (77) Mistek, E.; Halámková, L.; Doty, K. C.; Muro, C. K.; Lednev, I. K. Race Differentiation by Raman Spectroscopy of a Bloodstain for Forensic Purposes. *Anal. Chem.* **2016**, *88*, 7453–7456.
- (78) Zeng, S.; Baillargeat, D.; Ho, H.-P.; Yong, K.-T. Nanomaterials Enhanced Surface Plasmon Resonance for Biological and Chemical Sensing Applications. *Chem. Soc. Rev.* **2014**, *43*, 3426–3452.
- (79) Kretschmann, E. Decay of Non Radiative Surface Plasmons into Light on Rough Silver Films. Comparison of Experimental and Theoretical Results. *Opt. Commun.* **1972**, *6*, 185–187.
- (80) Tang, Y.; Zeng, X.; Liang, J. Surface Plasmon Resonance: An Introduction to a Surface Spectroscopy Technique. *J. Chem. Educ.* **2010**, *87*, 742–746.
- (81) Homola, J. Present and Future of Surface Plasmon Resonance Biosensors. *Anal. Bioanal. Chem.* **2003**, *377*, 528–539.
- (82) Haes, A. J.; Van Duyne, R. P. A Unified View of Propagating and Localized Surface Plasmon Resonance Biosensors. *Anal. Bioanal. Chem.* **2004**, *379*, 920–930.
- (83) Tonga, G. Y.; Saha, K.; Rotello, V. M. 25th Anniversary Article: Interfacing Nanoparticles and Biology: New Strategies for Biomedicine. *Adv. Mater.* **2014**, *26*, 359–370.
- (84) Howes, P. D.; Chandrawati, R.; Stevens, M. M. Colloidal Nanoparticles as Advanced Biological Sensors. *Science* **2014**, *346*, 1247390.
- (85) Ben-Amram, Y.; Tel-Vered, R.; Riskin, M.; Wang, Z.-G.; Willner, I. Ultrasensitive and Selective Detection of Alkaline-Earth Metal Ions Using Ion-Imprinted Au NPs Composites and Surface Plasmon Resonance Spectroscopy. *Chem. Sci.* **2012**, *3*, 162–167.
- (86) Shiping Fang; Hye Jin Lee; Wark, A. W.; Corn, R. M. Attomole Microarray Detection of MicroRNAs by Nanoparticle-Amplified SPR Imaging Measurements of Surface Polyadenylation Reactions. *J. Am. Chem. Soc.* **2006**, *128*, 14044–14046.
- (87) Keunen, R.; Macoretta, D.; Cathcart, N.; Kitaev, V. Stable Ligand-Free Stellated Polyhedral Gold Nanoparticles for Sensitive Plasmonic Detection. *Nanoscale* **2016**, *8*, 2575–2583.
- (88) Rodrigues, T. S.; da Silva, A. G. M.; de Moura, A. B. L.; Freitas, I. G.; Camargo, P. H. C. Rational Design of Plasmonic Catalysts: Matching the Surface Plasmon Resonance with Lamp Emission Spectra for Improved Performance in AgAu Nanorings. *RSC Adv.* **2016**, *6*, 62286–62290.
- (89) Zhao, S. S.; Bukar, N.; Toulouse, J. L.; Pelechacz, D.; Robitaille, R.; Pelletier, J. N.; Masson, J.-F. Miniature Multi-Channel SPR Instrument for Methotrexate Monitoring in Clinical Samples. *Biosens. Bioelectron.* **2015**, *64*, 664–670.

- (90) Yockell-Lelièvre, H.; Bukar, N.; McKeating, K. S.; Arnaud, M.; Cosin, P.; Guo, Y.; Dupret-Carruel, J.; Mougin, B.; Masson, J.-F. Plasmonic Sensors for the Competitive Detection of Testosterone. *Analyst* **2015**, *140*, 5105–5111.
- (91) Breault-Turcot, J.; Poirier-Richard, H.-P.; Couture, M.; Pelechacz, D.; Masson, J.-F. Single Chip SPR and Fluorescent ELISA Assay of Prostate Specific Antigen. *Lab Chip* **2015**, *15*, 4433–4440.
- (92) McNaught, A.D., Wilkinson, A. *IUPAC. Compendium of Chemical Terminology, 2nd Ed. (the “Gold Book”)*; Blackwell Scientific Publications: Oxford, **1997**.
- (93) Zhong, D. K.; Cornuz, M.; Sivula, K.; Grätzel, M.; Gamelin, D. R. Photo-Assisted Electrodeposition of Cobalt–phosphate (Co–Pi) Catalyst on Hematite Photoanodes for Solar Water Oxidation. *Energy Environ. Sci.* **2011**, *4*, 1759–1764.
- (94) Najafpour, M. M.; Moghaddam, A. N.; Dau, H.; Zaharieva, I. Fragments of Layered Manganese Oxide Are the Real Water Oxidation Catalyst after Transformation of Molecular Precursor on Clay. *J. Am. Chem. Soc.* **2014**, *136*, 7245–7248.
- (95) Mo, J.; Kang, Z.; Retterer, S. T.; Cullen, D. A.; Toops, T. J.; Green, J. B.; Mench, M. M.; Zhang, F.-Y. Discovery of True Electrochemical Reactions for Ultrahigh Catalyst Mass Activity in Water Splitting. *Sci. Adv.* **2016**, *2*, e1600690.
- (96) Rossmeisl, J.; Logadottir, A.; Nørskov, J. K. Electrolysis of Water on (Oxidized) Metal Surfaces. *Chem. Phys.* **2005**, *319*, 178–184.
- (97) Zheng, Y.-Z.; Ding, H.-Y.; Zhang, M.-L. Hydrous–ruthenium–oxide Thin Film Electrodes Prepared by Cathodic Electrodeposition for Supercapacitors. *Thin Solid Films* **2008**, *516*, 7381–7385.
- (98) Toupin, M.; Brousse, T.; Bélanger, D. Charge Storage Mechanism of MnO₂ Electrode Used in Aqueous Electrochemical Capacitor. *Chem. Mater.* **2004**, *16*, 3184–3190.
- (99) Wang, G.; Zhang, L.; Zhang, J. A Review of Electrode Materials for Electrochemical Supercapacitors. *Chem. Soc. Rev.* **2012**, *41*, 797–828.
- (100) Kim, Y.-H.; Heo, J.-S.; Kim, T.-H.; Park, S.; Yoon, M.-H.; Kim, J.; Oh, M. S.; Yi, G.-R.; Noh, Y.-Y.; Park, S. K. Flexible Metal-Oxide Devices Made by Room-Temperature Photochemical Activation of Sol-gel Films. *Nature* **2012**, *489*, 128–132.
- (101) Tench, D.; Warren, L. F. Electrodeposition of Conducting Transition Metal Oxide/Hydroxide Films from Aqueous Solution. *J. Electrochem. Soc.* **1983**, *130*, 869–872.
- (102) Tahir, A. A.; Wijayantha, K. G. U.; Saremi-Yarahmadi, S.; Mazhar, M.; McKee, V. Nanostructured α -Fe₂O₃ Thin Films for Photoelectrochemical Hydrogen Generation. *Chem. Mater.* **2009**, *21*, 3763–3772.
- (103) Kung, H. H. *Transition Metal Oxides : Surface Chemistry and Catalysis*; Elsevier, Amsterdam, **1989**.
- (104) Yuan, C.; Wu, H. Bin; Xie, Y.; Lou, X. W. D. Mixed Transition-Metal Oxides: Design, Synthesis, and Energy-Related Applications. *Angew. Chemie Int. Ed.* **2014**, *53*, 1488–1504.
- (105) Yu, Z.; Tetard, L.; Zhai, L.; Thomas, J. Supercapacitor Electrode Materials: Nanostructures from 0 to 3 Dimensions. *Energy Environ. Sci.* **2015**, *8*, 702–730.
- (106) Alexander, B. D.; Kulesza, P. J.; Rutkowska, I.; Solarzka, R.; Augustynski, J. Metal Oxide Photoanodes for Solar Hydrogen Production. *J. Mater. Chem.* **2008**, *18*, 2298–2303.

- (107) Wootton, A.; Harrowell, P. Polyhedral Ground States in Clusters of Asymmetric Hard Sphere Ions. *J. Chem. Phys.* **2004**, *121*, 7440–7442.
- (108) Cox, P. A. *Transition Metal Oxides : An Introduction to Their Electronic Structure and Properties.*; Oxford University Press, New York, **2010**.
- (109) Cheng, F.; Shen, J.; Peng, B.; Pan, Y.; Tao, Z.; Chen, J. Rapid Room-Temperature Synthesis of Nanocrystalline Spinel as Oxygen Reduction and Evolution Electrocatalysts. *Nat. Chem.* **2011**, *3*, 79–84.
- (110) Liang, Y.; Wang, H.; Zhou, J.; Li, Y.; Wang, J.; Regier, T.; Dai, H. Covalent Hybrid of Spinel Manganese–Cobalt Oxide and Graphene as Advanced Oxygen Reduction Electrocatalysts. *J. Am. Chem. Soc.* **2012**, *134*, 3517–3523.
- (111) Gaponenko, S. V. *Optical Properties of Semiconductor Nanocrystals*; Cambridge University Press, Cambridge, UK, **1998**.
- (112) Zhang, Y.; Kolmakov, A.; Chretien, S.; Metiu, H.; Moskovits, M. Control of Catalytic Reactions at the Surface of a Metal Oxide Nanowire by Manipulating Electron Density Inside It. *Nano Lett.* **2004**, *4*, 403–407.
- (113) Jun, Y.; Choi, J.; Cheon, J. Shape Control of Semiconductor and Metal Oxide Nanocrystals through Nonhydrolytic Colloidal Routes. *Angew. Chemie Int. Ed.* **2006**, *45*, 3414–3439.
- (114) Shimada, M.; Kanamaru, F.; Koizumi, M.; Yamamoto, N. Preparation of a New Cu-Substituted Cobaltite Spinel : CuCo_2O_4 . *Mater. Res. Bull.* **1975**, *10*, 733–736.
- (115) Ren, Z.; Botu, V.; Wang, S.; Meng, Y.; Song, W.; Guo, Y.; Ramprasad, R.; Suib, S. L.; Gao, P.-X. Monolithically Integrated Spinel $\text{M}_x\text{Co}_{3-x}\text{O}_4$ (M=Co, Ni, Zn) Nanoarray Catalysts: Scalable Synthesis and Cation Manipulation for Tunable Low-Temperature CH_4 and CO Oxidation. *Angew. Chemie Int. Ed.* **2014**, *53*, 7223–7227.
- (116) Guin, D.; Manorama, S. V. Room Temperature Synthesis of Monodispersed Iron Oxide Nanoparticles. *Mater. Lett.* **2008**, *62*, 3139–3142.
- (117) Patil, S. A.; Shinde, D. V.; Ahn, D. Y.; Patil, D. V.; Tehare, K. K.; Jadhav, V. V.; Lee, J. K.; Mane, R. S.; Shrestha, N. K.; Han, S.-H.; et al. A Simple, Room Temperature, Solid-State Synthesis Route for Metal Oxide Nanostructures. *J. Mater. Chem. A* **2014**, *2*, 13519–13526.
- (118) Gopal, M.; Moberly Chan, W. J.; De Jonghe, L. C. Room Temperature Synthesis of Crystalline Metal Oxides. *J. Mater. Sci.* **1997**, *32*, 6001–6008.
- (119) Wang, H.; Yang, Y.; Liang, Y.; Cui, L.-F.; Casalongue, H. S.; Li, Y.; Hong, G.; Cui, Y.; Dai, H. $\text{LiMn}_{1-x}\text{Fe}_x\text{PO}_4$ Nanorods Grown on Graphene Sheets for Ultra-High Rate Performance Lithium Ion Batteries. *Angew. Chemie* **2011**, *123*, 7502–7506.
- (120) Liang, Y.; Wang, H.; Sanchez Casalongue, H.; Chen, Z.; Dai, H. TiO_2 Nanocrystals Grown on Graphene as Advanced Photocatalytic Hybrid Materials. *Nano Res.* **2010**, *3*, 701–705.
- (121) Liang, Y.; Li, Y.; Wang, H.; Zhou, J.; Wang, J.; Regier, T.; Dai, H. Co_3O_4 Nanocrystals on Graphene as a Synergistic Catalyst for Oxygen Reduction Reaction. *Nat. Mater.* **2011**, *10*, 780–786.
- (122) Song, Q.; Zhang, Z. J. Shape Control and Associated Magnetic Properties of Spinel Cobalt Ferrite Nanocrystals. *J. Am. Chem. Soc.* **2004**, *126*, 6164–6168.

- (123) Park, B.; Kim, B. H.; Yu, T. Synthesis of Spherical and Cubic Magnetic Iron Oxide Nanocrystals at Low Temperature in Air. *J. Colloid Interface Sci.* **2018**, *518*, 27–33.
- (124) Cheon, J.; Kang, N.-J.; Lee, S.-M.; Lee, J.-H.; Yoon, J.-H.; Oh, S. J. Shape Evolution of Single-Crystalline Iron Oxide Nanocrystals. *J. Am. Chem. Soc.* **2004**, *126*, 1950–1951.
- (125) Yin, M.; Gu, Y.; Kuskovsky, I. L.; Andelman, T.; Zhu, Y.; Neumark, G. F.; O'Brien, S. Zinc Oxide Quantum Rods. *J. Am. Chem. Soc.* **2004**, *126*, 6206–6207.
- (126) Jana, N. R.; Chen, Y.; Peng, X. Size- and Shape-Controlled Magnetic (Cr, Mn, Fe, Co, Ni) Oxide Nanocrystals via a Simple and General Approach. *Chem. Mater.* **2004**, *16*, 3931–3935.
- (127) Anas, S.; Nair, P. V.; Mahesh, K. V.; Linsha, V.; Shuhailath, A.; Mohamed, A. P.; Warriar, K. G. K.; Ananthakumar, S. Engineered Hetero Structured Arrays of ZnO NanoX (X = Discs, Rods and Wires) and CdTe Quantum Dots for Advanced Electron Transport Applications. *Mater. Des.* **2018**, *141*, 267–275.
- (128) Seo, J.; Jun, Y.; Ko, S. J.; Cheon, J. In Situ One-Pot Synthesis of 1-Dimensional Transition Metal Oxide Nanocrystals. *J. Phys. Chem. B* **2005**, *109*, 5389–5391.
- (129) Urban, J. J.; Yun, W. S.; Gu, Q.; Park, H. Synthesis of Single-Crystalline Perovskite Nanorods Composed of Barium Titanate and Strontium Titanate. *J. Am. Chem. Soc.* **2002**, *124*, 1186–1187.
- (130) Cathcart, N.; Kitaev, V. Monodisperse Hexagonal Silver Nanoprisms: Synthesis via Thiolate-Protected Cluster Precursors and Chiral, Ligand-Imprinted Self-Assembly. *ACS Nano* **2011**, *5*, 7411–7425.
- (131) Austin, L. A.; MacKey, M. A.; Dreaden, E. C.; El-Sayed, M. A. The Optical, Photothermal, and Facile Surface Chemical Properties of Gold and Silver Nanoparticles in Biodiagnostics, Therapy, and Drug Delivery. *Arch. Toxicol.* **2014**, *88*, 1391–1417.
- (132) Si, R.; Zhang, Y.-W.; You, L.-P.; Yan, C.-H. Rare-Earth Oxide Nanopolyhedra, Nanoplates, and Nanodisks. *Angew. Chemie Int. Ed.* **2005**, *44*, 3256–3260.
- (133) Jun, Y.; Casula, M. F.; Sim, J.-H.; Kim, S. Y.; Cheon, J.; Alivisatos, A. P. Surfactant-Assisted Elimination of a High Energy Facet as a Means of Controlling the Shapes of TiO₂ Nanocrystals. *J. Am. Chem. Soc.* **2003**, *125*, 15981–15985.
- (134) Mishra, Y. K.; Adelung, R. ZnO Tetrapod Materials for Functional Applications. *Mater. Today* **2018**, *21*, 631–651.
- (135) Lu, J. G.; Chang, P.; Fan, Z. Quasi-One-Dimensional Metal Oxide Materials—Synthesis, Properties and Applications. *Mater. Sci. Eng. R Reports* **2006**, *52*, 49–91.
- (136) Sun, Y.-F.; Liu, S.-B.; Meng, F.-L.; Liu, J.-Y.; Jin, Z.; Kong, L.-T.; Liu, J.-H. Metal Oxide Nanostructures and Their Gas Sensing Properties: A Review. *Sensors* **2012**, *12*, 2610–2631.
- (137) Shi, X.; Gu, W.; Li, B.; Chen, N.; Zhao, K.; Xian, Y. Enzymatic Biosensors Based on the Use of Metal Oxide Nanoparticles. *Microchim. Acta* **2014**, *181*, 1–22.
- (138) Robinson, D. M.; Go, Y. B.; Mui, M.; Gardner, G.; Zhang, Z.; Mastrogiovanni, D.; Garfunkel, E.; Li, J.; Greenblatt, M.; Dismukes, G. C. Photochemical Water Oxidation by Crystalline Polymorphs of Manganese Oxides: Structural Requirements for Catalysis. *J. Am. Chem. Soc.* **2013**, *135*, 3494–3501.

- (139) Lee, Y.; Suntivich, J.; May, K. J.; Perry, E. E.; Shao-Horn, Y. Synthesis and Activities of Rutile IrO₂ and RuO₂ Nanoparticles for Oxygen Evolution in Acid and Alkaline Solutions. *J. Phys. Chem. Lett.* **2012**, *3*, 399–404.
- (140) Xu, P.; Zeng, G. M.; Huang, D. L.; Feng, C. L.; Hu, S.; Zhao, M. H.; Lai, C.; Wei, Z.; Huang, C.; Xie, G. X.; et al. Use of Iron Oxide Nanomaterials in Wastewater Treatment: A Review. *Sci. Total Environ.* **2012**, *424*, 1–10.
- (141) Sivula, K.; Zboril, R.; Le Formal, F.; Robert, R.; Weidenkaff, A.; Tucek, J.; Frydrych, J.; Grätzel, M. Photoelectrochemical Water Splitting with Mesoporous Hematite Prepared by a Solution-Based Colloidal Approach. *J. Am. Chem. Soc.* **2010**, *132*, 7436–7444.
- (142) Bora, D. K.; Braun, A.; Constable, E. C. “In Rust We Trust”. Hematite – the Prospective Inorganic Backbone for Artificial Photosynthesis. *Energy Environ. Sci.* **2013**, *6*, 407–425.
- (143) Cesar, I.; Kay, A.; Gonzalez Martinez, J. A.; Grätzel, M. Translucent Thin Film Fe₂O₃ Photoanodes for Efficient Water Splitting by Sunlight: Nanostructure-Directing Effect of Si-Doping. *J. Am. Chem. Soc.* **2006**, *128*, 4582–4583.
- (144) Sanchez, H. L.; Steinfink, H.; White, H. S. Solid Solubility of Ge, Si, and Mg in Fe₂O₃ and Photoelectric Behavior. *J. Solid State Chem.* **1982**, *41*, 90–96.
- (145) Tilley, S. D.; Cornuz, M.; Sivula, K.; Grätzel, M. Light-Induced Water Splitting with Hematite: Improved Nanostructure and Iridium Oxide Catalysis. *Angew. Chemie* **2010**, *122*, 6549–6552.
- (146) Abdi, F. F.; van de Krol, R. Nature and Light Dependence of Bulk Recombination in Co-Pi-Catalyzed BiVO₄ Photoanodes. *J. Phys. Chem. C* **2012**, *116*, 9398–9404.
- (147) Chen, Y.; Liang, S.; Wen, L.; Wu, L. A TaON Nano-Photocatalyst with Low Surface Reduction Defects for Effective Mineralization of Chlorophenols under Visible Light Irradiation. *Phys. Chem. Chem. Phys.* **2013**, *15*, 12742–12747.
- (148) Hua, M.; Zhang, S.; Pan, B.; Zhang, W.; Lv, L.; Zhang, Q. Heavy Metal Removal from Water/Wastewater by Nanosized Metal Oxides: A Review. *J. Hazard. Mater.* **2012**, *211*, 317–331.
- (149) Araújo, R.; Castro, A. C. M.; Fiúza, A. The Use of Nanoparticles in Soil and Water Remediation Processes. *Mater. Today Proc.* **2015**, *2*, 315–320.
- (150) Ren, B.; Han, C.; Al Anazi, A. H.; Nadagouda, M. N.; Dionysiou, D. D. Iron-Based Nanomaterials for the Treatment of Emerging Environmental Contaminants. *ACS Symp. Ser.* **2013**, *1150*, 135–146.
- (151) Zhang, L. F.; Wang, L.; Zhong, S. L.; Huang, Y. X.; Xu, A. W. Facile Synthesis of Concave Decahedra Enclosed by High-Index Facets and Truncated Decahedra with a Large Size. *Dalt. Trans.* **2012**, *41*, 4948–4954.
- (152) Buccolieri, A.; Serra, A.; Maruccio, G.; Monteduro, A. G.; Padmanabhan, S. K.; Licciulli, A.; Bonfrate, V.; Salvatore, L.; Manno, D.; Calcagnile, L.; et al. Synthesis and Characterization of Mixed Iron-Manganese Oxide Nanoparticles and Their Application for Efficient Nickel Ion Removal from Aqueous Samples. *J. Anal. Methods Chem.* **2017**, *2017*, 9476065.
- (153) Wan, S.; Wu, J.; Zhou, S.; Wang, R.; Gao, B.; He, F. Enhanced Lead and Cadmium Removal Using Biochar-Supported Hydrated Manganese Oxide (HMO) Nanoparticles: Behavior and Mechanism. *Sci. Total Environ.* **2018**, *616–617*, 1298–1306.
- (154) Goswami, A.; Raul, P. K.; Purkait, M. K. Arsenic Adsorption Using Copper (II) Oxide Nanoparticles.

- Chem. Eng. Res. Des.* **2012**, *90*, 1387–1396.
- (155) Saha, S.; Sarkar, P. Arsenic Remediation from Drinking Water by Synthesized Nano-Alumina Dispersed in Chitosan-Grafted Polyacrylamide. *J. Hazard. Mater.* **2012**, *227–228*, 68–78.
- (156) Kumar, E.; Bhatnagar, A.; Hogland, W.; Marques, M.; Sillanpää, M. Interaction of Inorganic Anions with Iron-Mineral Adsorbents in Aqueous Media — A Review. *Adv. Colloid Interface Sci.* **2014**, *203*, 11–21.
- (157) Gray, H. E.; Smith, D. S.; Parker, W. J. Nitrogen and Phosphorus Recycling from Wastewater Treatment Plant Effluents Using Commercially Available Sorbents. *Proc. Water Environ. Fed.* **2014**, *2014*, 3115–3128.
- (158) Stahl, K.; Nielsen, K.; Jiang, J.; Lebech, B.; Hanson, J. C.; Norby, P.; van Lanschot, J. On the Akaganeite Crystal Structure, Phase Transformations and Possible Role in Post-Excavational Corrosion of Iron Artifacts. *Corros. Sci.* **2003**, *45*, 2563–2575.
- (159) Zhao, J.; Lin, W.; Chang, Q.; Li, W.; Lai, Y. Adsorptive Characteristics of Akaganeite and Its Environmental Applications: A Review. *Environ. Technol. Rev.* **2012**, *1*, 114–126.
- (160) Kim, J.; Li, W.; Philips, B. L.; Grey, C. P. Phosphate Adsorption on the Iron Oxyhydroxides Goethite (α -FeOOH), Akaganeite (β -FeOOH), and Lepidocrocite (γ -FeOOH): A ^{31}P NMR Study. *Energy Environ. Sci.* **2011**, *4*, 4298–4305.
- (161) Deliyanni, E. A.; Peleka, E. N.; Lazaridis, N. K. Comparative Study of Phosphates Removal from Aqueous Solutions by Nanocrystalline Akaganéite and Hybrid Surfactant-Akaganéite. *Sep. Purif. Technol.* **2007**, *52*, 478–486.
- (162) Farrokhtakin, E.; Rodríguez-Fernández, D.; Mattoli, V.; Solís, D. M.; Taboada, J. M.; Obelleiro, F.; Grzelczak, M.; Liz-Marzán, L. M. Radial Growth of Plasmon Coupled Gold Nanowires on Colloidal Templates. *J. Colloid Interface Sci.* **2015**, *449*, 87–91.
- (163) Petrov, A.; Lehmann, H.; Finsel, M.; Klinke, C.; Weller, H.; Vossmeier, T. Synthesis and Characterization of Monodisperse Metallodielectric $\text{SiO}_2@Pt@SiO_2$ Core–Shell–Shell Particles. *Langmuir* **2016**, *32*, 848–857.
- (164) Nooshnab, V.; Golmohammadi, S. Revealing the Effect of Plasmon Transmutation on Charge Transfer Plasmons in Substrate-Mediated Metallodielectric Aluminum Clusters. *Opt. Commun.* **2017**, *382*, 354–360.
- (165) Liz-Marzán, L. M.; Michael Giersig, A.; Paul Mulvaney. Synthesis of Nanosized Gold–Silica Core–Shell Particles. *Langmuir* **1996**, *12*, 4329–4335.
- (166) Chen, J.; Zhang, R.; Han, L.; Tu, B.; Zhao, D. One-Pot Synthesis of Thermally Stable Gold@mesoporous Silica Core-Shell Nanospheres with Catalytic Activity. *Nano Res.* **2013**, *6*, 871–879.
- (167) Hanske, C.; Sanz-Ortiz, M. N.; Liz-Marzán, L. M. Silica-Coated Plasmonic Metal Nanoparticles in Action. *Adv. Mater.* **2018**, *30*, 1707003.
- (168) Kress, S. J. P.; Antolinez, F. V.; Richner, P.; Jayanti, S. V.; Kim, D. K.; Prins, F.; Riedinger, A.; Fischer, M. P. C.; Meyer, S.; McPeak, K. M.; et al. Wedge Waveguides and Resonators for Quantum Plasmonics. *Nano Lett.* **2015**, *15*, 6267–6275.
- (169) Atwater, H. A.; Polman, A. Plasmonics for Improved Photovoltaic Devices. *Nat. Mater.* **2010**, *9*,

205–213.

- (170) Scalora, M.; Bloemer, M. J.; Pethel, A. S.; Dowling, J. P.; Bowden, C. M.; Manka, A. S. Transparent, Metallo-Dielectric, One-Dimensional, Photonic Band-Gap Structures. *J. Appl. Phys.* **1998**, *83*, 2377–2383.
- (171) Ricciardi, A.; Consales, M.; Quero, G.; Crescitelli, A.; Esposito, E.; Cusano, A. Lab-on-Fiber Devices as an All around Platform for Sensing. *Opt. Fiber Technol.* **2013**, *19*, 772–784.
- (172) Qiao, Z.-A.; Zhang, P.; Chai, S.-H.; Chi, M.; Veith, G. M.; Gallego, N. C.; Kidder, M.; Dai, S. Lab-in-a-Shell: Encapsulating Metal Clusters for Size Sieving Catalysis. *J. Am. Chem. Soc.* **2014**, *136*, 11260–11263.
- (173) Ahmadivand, A.; Sinha, R.; Pala, N. Hybridized Plasmon Resonant Modes in Molecular Metallo-dielectric Quad-Triangles Nanoantenna. *Opt. Commun.* **2015**, *355*, 103–108.
- (174) Charnay, C.; Lee, A.; Man, S.-Q.; Moran, C. E.; Radloff, C.; Bradley, R. K.; Halas, N. J. Reduced Symmetry Metallo-dielectric Nanoparticles: Chemical Synthesis and Plasmonic Properties. *J. Phys. Chem. B* **2003**, *107*, 7327–7333.
- (175) Song, D.-P.; Li, C.; Colella, N. S.; Lu, X.; Lee, J.-H.; Watkins, J. J. Thermally Tunable Metallo-dielectric Photonic Crystals from the Self-Assembly of Brush Block Copolymers and Gold Nanoparticles. *Adv. Opt. Mater.* **2015**, *3*, 1169–1175.
- (176) Ozin, G. A.; Arsenault, A. C.; *Nanochemistry : A Chemical Approach to Nanomaterials*; Royal Society of Chemistry, Cambridge, UK, **2005**.
- (177) Albanese, A.; Tang, P. S.; Chan, W. C. W. The Effect of Nanoparticle Size, Shape, and Surface Chemistry on Biological Systems. *Annu. Rev. Biomed. Eng.* **2012**, *14*, 1–16.
- (178) Chithrani, B. D.; Chan, W. C. W. Elucidating the Mechanism of Cellular Uptake and Removal of Protein-Coated Gold Nanoparticles of Different Sizes and Shapes. *Nano Lett.* **2007**, *7*, 1542–1550.
- (179) Lu, F.; Wu, S.-H.; Hung, Y.; Mou, C.-Y. Size Effect on Cell Uptake in Well-Suspended, Uniform Mesoporous Silica Nanoparticles. *Small* **2009**, *5*, 1408–1413.
- (180) Sonavane, G.; Tomoda, K.; Makino, K. Biodistribution of Colloidal Gold Nanoparticles after Intravenous Administration: Effect of Particle Size. *Colloids Surfaces B Biointerfaces* **2008**, *66*, 274–280.
- (181) Aitken, R.; Hankin, S.; Ross, B.; Tran, C.; Stone, V.; Fernandes, T.; Donaldson, K.; Duffin, R.; Chaudhry, Q.; Wilkins, T.; et al. *EMERGNANO: A Review of Completed and near Completed Environment, Health and Safety Research on Nanomaterials and Nanotechnology (Concise Report) Defra Project CB0409*; Edinburgh, **2009**.
- (182) McGillicuddy, E.; Murray, I.; Kavanagh, S.; Morrison, L.; Fogarty, A.; Cormican, M.; Dockery, P.; Prendergast, M.; Rowan, N.; Morris, D. Silver Nanoparticles in the Environment: Sources, Detection and Ecotoxicology. *Sci. Total Environ.* **2017**, *575*, 231–246.
- (183) Vance, M. E.; Kuiken, T.; Vejerano, E. P.; McGinnis, S. P.; Hochella, M. F.; Rejeski, D.; Hull, M. S. Nanotechnology in the Real World: Redeveloping the Nanomaterial Consumer Products Inventory. *Beilstein J. Nanotechnol.* **2015**, *6*, 1769–1780.
- (184) Lansdown, A. B. G. (Alan B. G. . *Silver in Healthcare : Its Antimicrobial Efficacy and Safety in Use*; Royal Society of Chemistry, Cambridge, UK, **2010**.

- (185) Chang, A. L. S.; Khosravi, V.; Egbert, B. A Case of Argyria after Colloidal Silver Ingestion. *J. Cutan. Pathol.* **2006**, *33*, 809–811.
- (186) Mirsattari, S. M.; Hammond, R. R.; Sharpe, M. D.; Leung, F. Y.; Young, G. B. Myoclonic Status Epilepticus Following Repeated Oral Ingestion of Colloidal Silver. *Neurology* **2004**, *62*, 1408–1410.
- (187) Behra, R.; Sigg, L.; Clift, M. J. D.; Herzog, F.; Minghetti, M.; Johnston, B.; Petri-Fink, A.; Rothen-Rutishauser, B. Bioavailability of Silver Nanoparticles and Ions: From a Chemical and Biochemical Perspective. *J. R. Soc. Interface* **2013**, *10*, 20130396–20130396.
- (188) Cathcart, N.; Kitaev, V. Monodisperse Hexagonal Silver Nanoprisms: Synthesis via Thiolate-Protected Cluster Precursors and Chiral, Ligand-Imprinted Self-Assembly. *ACS Nano* **2011**, *5*, 7411–7425.
- (189) Cathcart, N.; Coombs, N.; Gourevich, I.; Kitaev, V. Synthesis and Sensing Properties of D_{5h} pentagonal Silver Star Nanoparticles. *Nanoscale* **2016**, *8*, 18282–18290.
- (190) Wang, D.; Lin, Z.; Wang, T.; Yao, Z.; Qin, M.; Zheng, S.; Lu, W. Where Does the Toxicity of Metal Oxide Nanoparticles Come from: The Nanoparticles, the Ions, or a Combination of Both? *J. Hazard. Mater.* **2016**, *308*, 328–334.
- (191) Auffan, M.; Rose, J.; Bottero, J.-Y.; Lowry, G. V.; Jolivet, J.-P.; Wiesner, M. R. Towards a Definition of Inorganic Nanoparticles from an Environmental, Health and Safety Perspective. *Nat. Nanotechnol.* **2009**, *4*, 634–641.

Chapter 3: Symmetry Breaking by Surface Blocking: Synthesis of Bimorphic Silver Nanoparticles, Nanoscale Fishes and Apples

The following publication presents a synthetic method to prepare diverse silver nanostructures using symmetry breaking by surface blocking, and an analysis of their associated properties for sensing applications. Reproduced from N. Cathcart and V. Kitaev, *Sci. Rep.*, **2016**, 6, 32561. Licensed under CC by 4.0 and accessible online at: <https://www.nature.com/articles/srep32561>, with supplementary information accessible online at:

<https://media.nature.com/original/nature-assets/srep/2016/160908/srep32561/extref/srep32561-s1.pdf>.

Symmetry Breaking by Surface Blocking: Synthesis of Bimorphic Silver Nanoparticles, Nanoscale Fishes and Apples

By Nicole Cathcart and Vladimir Kitaev

3.1 Abstract

A powerful approach to augment the diversity of well-defined metal nanoparticle (MNP) morphologies, essential for MNP advanced applications, is symmetry breaking combined with seeded growth. Utilizing this approach enabled the formation of bimorphic silver nanoparticles (bi-AgNPs) consisting of two shapes linked by one regrowth point. Bi-AgNPs were formed by using an adsorbing polymer, poly(acrylic acid), PAA, to block the surface of a decahedral AgNP seed and restricting growth of new silver to a single nucleation point. First, we have realized 2-D growth of platelets attached to decahedra producing nanoscale shapes reminiscent of apples, fishes, mushrooms and kites. 1-D bimorphic

growth of rods (with chloride) and 3-D bimorphic growth of cubes and bipyramids (with bromide) were achieved by using halides to induce preferential (100) stabilization over (111) of platelets. Furthermore, the universality of the formation of bimorphic nanoparticles was demonstrated by using different seeds. Bi-AgNPs exhibit strong SERS enhancement due to regular cavities at the necks. Overall, the reported approach to symmetry breaking and bimorphic nanoparticle growth offers a powerful methodology for nanoscale shape design.

3.2. Introduction

Metal nanoparticles (MNPs) are advantageous for diverse applications including plasmonics,^{1,2} catalysis,^{3,4} sensing^{5,6} and medicine.^{7,8} Understanding size and shape selection^{9,10} in MNPs is essential to fully capitalize on the advantageous nanoscale properties of MNPs.^{11,12} Synthetic preparation of well-defined MNP morphologies is currently a bottleneck for MNP applications.¹³ Seeded growth is an established approach to achieve nanoscale morphologies with increasing complexity.^{14,15} Seeded growth requires limiting new nucleation events, which can be achieved by the slow addition of a metal precursor¹⁶ or by utilizing ligands for complexation and selective binding.¹⁷ To control the NP shape in seeded regrowth, surface-binding species can block specific NP facets by selective adsorption.¹⁸ In particular, halides were found to play a crucial role in shape-selective synthesis of AuNPs¹⁹ and AgNPs.^{20,21}

Formation of bimorphic nanoparticles (bi-NPs) requires symmetry breaking that is postulated to be promoted by the high driving forces of reduction,²² which can be realized through maintaining the high ratio of reducing agent to metal.^{23,24} Symmetry breaking driven by the strain energy of growing NPs has been reported for Cu deposition onto Au seeds²⁵ and for binary MNPs made from cubic Pt seeds.²⁶ Preparation of diverse nanostructures in bimorphic regrowth has been described by Tsuji et al., where cubes, bipyramids, and platelets were formed from nanorods.²⁷ Bimorphic growth aims at combining two different shapes, similar to Janus particles.^{28,29} Such nanoparticles are currently prepared through anisotropic branching,³⁰ which is widely applicable but limited in shape selectivity. Overall, general

approaches for symmetry breaking and realization of bi-NPs consisting of two well-defined parts remain largely unexplored.

Herein we describe symmetry breaking resulting in bimorphic AgNPs with two well-defined constituent parts achieved through controlled blocking of the growing surface of AgNP seeds by poly(acrylic acid). In particular, controlled nucleation at the surface of decahedral AgNPs yielded single-point growth leading to size- and shape-selected bimorphic AgNPs. Different modes of bimorphic growth have been realized using halides. For 2-D growth of platelets attached to decahedra, we have elucidated conditions required for the symmetry breaking and shape selection and demonstrated that growth pathways can be judiciously controlled to engineer diverse complex nanoscale morphologies.

3.3. Results and Discussions

Key features of bi-AgNP synthesis by seeded growth of decahedral AgNPs, AgDeNPs, (pentagonal bipyramids, J_{13}) are summarized in Fig. 3.1. The symmetry breaking in regrowth of high-purity decahedra^{31,32} takes place upon the reduction of silver ions (AgNO_3) by ascorbic acid (AA) with surface blocking by poly(acrylic acid) (PAA) giving rise to shape-selective deposition of new silver.^{22,23} Several types of well-defined bi-AgNPs are attainable by controlling four main parameters, the most crucial of which is i) ***surface-blocking by an adsorbing polymer*** (PAA of different molecular weights at different concentrations); followed by ii) *the amount of new silver added*, iii) *reducing power* (AA concentration and pH of the reaction), and iv) *presence of shape-selective agents* (e.g. halides).

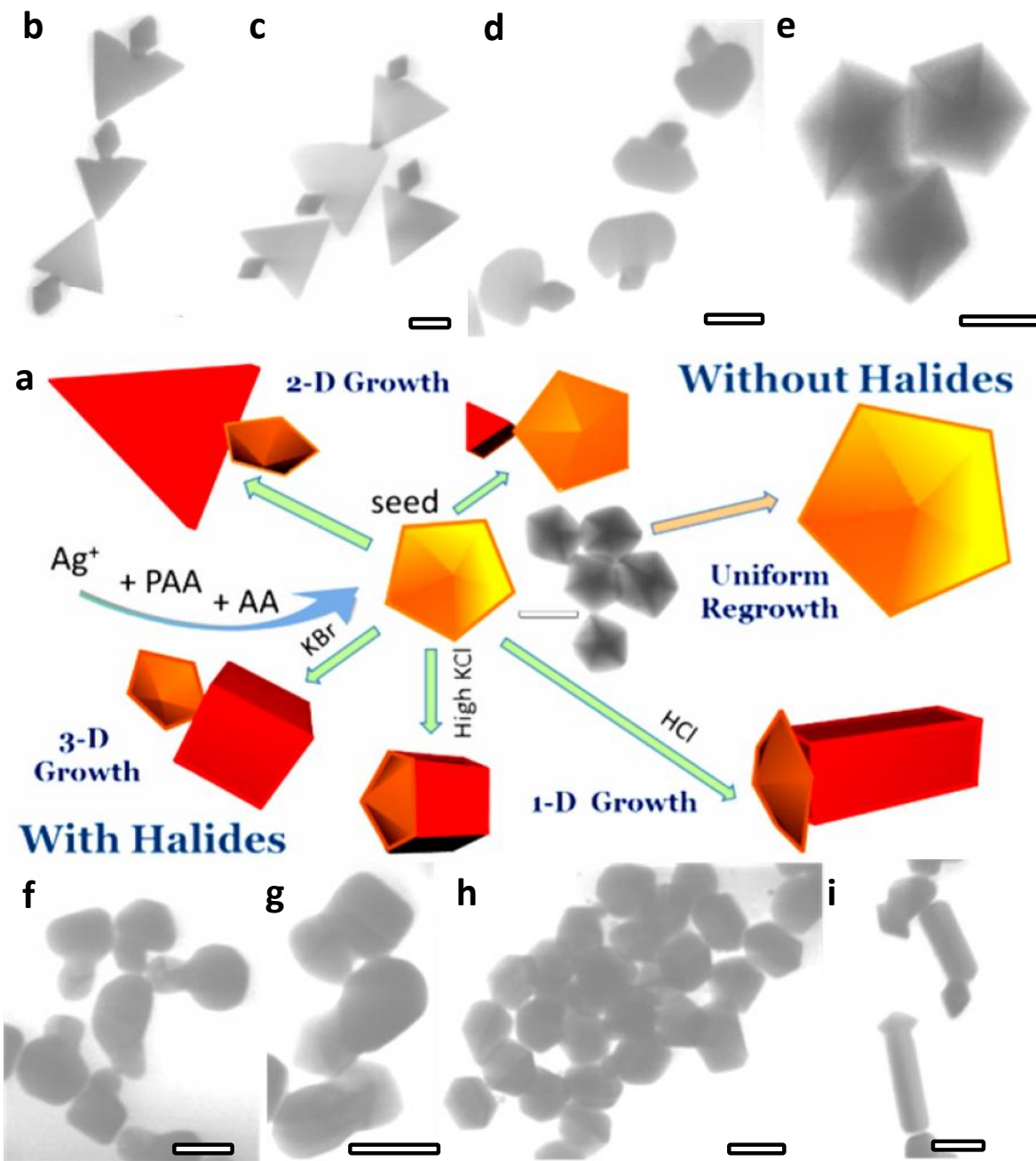


Figure 3.1. a) Schematics of different pathways of bi-AgNP formation illustrating 1-D, 2-D and 3-D growth in the system. b)-i) transmission electron microscopy (TEM) images of b)-d) representative 2-D bi-AgNP morphologies, b) and c) optimal preparation: 0.13 mM PAA 450 K, 0.04 mM AgDeNP seeds, 0.27 mM ascorbic acid, and 0.08 mM $AgNO_3$, c) low Ag, and e) uniformly 3-D enlarged decahedra (high PAA). f)-i) representative bi-AgNPs prepared in presence of halides: f)-g) 3-D bi-AgNPs, f) 75:1 Ag/KBr; g) 38:1 Ag/KBr; h) pentagonal rods with 1:12 Ag/KCl, i) 1-D bi-AgNPs with 1:5 Ag/HCl. All ratios are molar. All scale bars are 50 nm. For detailed description of samples - see Supplementary Table 3S.1.

AgNP morphologies attained in different regrowth conditions are shown in Fig. 3.1a. The main focus of this report is the uniform 2-D bimorphic growth of a platelet/prism onto a decahedral seed (Fig. 3.2 and Supplementary Fig. 3S.1). Among other growth modes of decahedra, most straightforward is uniform 3-D regrowth (uniform decahedra enlargement) where new silver deposits uniformly onto all ten (111) facets.^{31,32} In this report we have accessed 3-D regrowth of decahedra at low pH and in presence of citrate at room temperature (Fig. 3.1e and Supplementary Fig. 3S.2h). Several other regrowth modes can be accessed using halides: 1-D enlargement of decahedra resulting in pentagonal rods (Fig. 3.1i), mediated by chloride complexation and 3-D bimorphic growth of cubes and bipyramids from decahedral seeds (Fig. 3.1g and Supplementary Fig. 3S.3), directed by bromide. Different pathways of the symmetry breaking in bi-AgNP growth demonstrated by this work (Figs. 3.1 and 3.3) attest to the universality of the developed procedure. In particular, we have focused on 2-D bi-AgNPs to elucidate the role of synthetic parameters and to demonstrate control over the shape selection.

Bi-AgNP formation requires a tight set of reaction conditions, in particular the seed surface appropriately blocked/protected so that nucleation can occur only in a single point. This nucleation point is one of the equivalent high energy vertices of the pentagonal rim in decahedra. The nucleation on the polymer-blocked surface is a limiting stage in the bimorph growth. Once the nucleation is initiated growth of the bimorph proceeds rapidly through the formation of connecting 'necks' and subsequent more directional growth of the platelet part through their planar twinned defects.³³ Bi-AgNPs with two nucleated centers at different vertices (i.e. two platelets growing on the same decahedral seed) were not experimentally observed, even in minor quantities. The growth of the bimorph with the seed surface strongly blocked by an adsorbing polymer (PAA) results in high driving forces of reduction²² (per available surface) and is kinetically driven. Such growth proceeds with multiple twinning that is typical for the kinetically driven nanoparticle formation and is characteristic of the platelet growth.³³ Bi-AgNPs formed in optimized 2-D growth conditions feature platelets predominantly attached in a perpendicular

orientation relative to the pentagonal planes of the decahedral seed (Figs. 3.1b,c, 3.2, and Supplementary Figs. 3S.1, 3S.2a,b), as expected from the preferential growth at the vertices. At the same time, thin longer necks connecting platelets to decahedra (e.g. Supplementary Fig. 3S.4b,c) were formed in conditions where the decahedral seeds were allowed to equilibrate with PAA prior to silver reduction. These long necks (along with high-magnification images shown in Supplementary Fig. 3S.4a) clearly illustrate the point that there is no epitaxy and the crystalline plane orientation of the seed is not preserved in the regrowth at the heavily polymer-blocked surface.

Effects of major parameters in bi-AgNP formation are summarized in Figures 3.2 and 3S.2 (and corresponding Table 3.1 and Supplementary Table 3S.1). At higher PAA concentrations, the decahedra surface is completely blocked for the selective nucleation of the bimorphic growth and enlarged decahedra are a predominant product (Supplementary Fig. 3S.2e). At lower PAA concentrations, the bimorphic growth is less-defined, so limited shape-control can be achieved (Supplementary Fig. 3S.2f). The size of the platelet part can be controlled by the ratio of added silver to silver in AgDeNP seeds; increased added silver (300 %, Fig. 3.2a6) resulted in larger platelets, and smaller growth was achieved with lower silver (20-40%, Figs. 3.2a1,2). An effect of high AA concentration manifests in less-defined, chaotic reduction of silver resulting in rough AgNPs³⁴ (Supplementary Fig. 3S.2c); while at lower AA concentrations rounded etched decahedra form (Supplementary Fig. 3S.2d). At higher pH, the secondary nucleation dominates due to the higher reducing power of AA (Supplementary Fig. 3S.2g). At lower pH with the less reducing power and slower regrowth, enlarged decahedra are again the main regrowth product (Supplementary Fig. 3S.2h) in absence of the symmetry breaking. Table 3.1 summarizes main bi-AgNP shapes described in this work and corresponding conditions for their preparation.

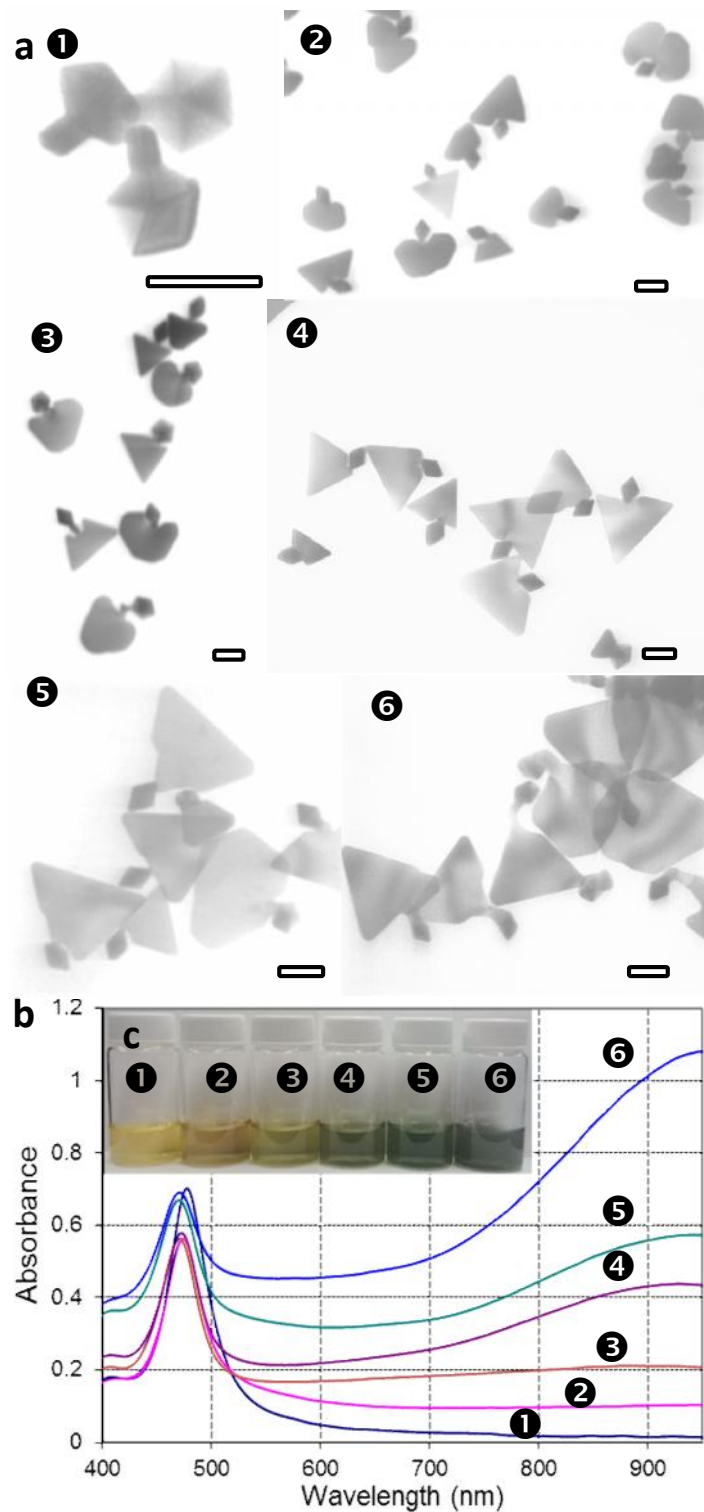
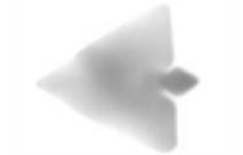

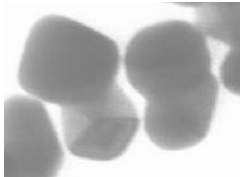





Figure 3.2. Development of 2-D bi-AgNP morphologies with different amounts of added silver (the percentage is given in brackets relative to silver present in decahedral seeds). **a)** Representative TEM images; **b)** UV-vis spectra; and **c)** optical photographs of samples: **1** 0.008 mM (20%), **2** 0.016 mM (40%), **3** 0.04 mM (100%), **4** 0.05 mM (120%), **5** 0.08 mM (200%) and **6** 0.13 mM (320%). All scale bars are 50 nm.

Table 3.1 Summary of experimental conditions for the formation of well-defined bimorphic AgNP shapes.

Morphology	Reaction Conditions*	Representative Image
Triangular platelet bi-AgNPs (fish)	Reported procedure, 0.13 mM PAA, 0.04 mM AgDeNPs, 0.27 mM ascorbic acid and 0.08 mM silver	
Rounded platelet bi-AgNPs (apples/mushrooms)	Lower Ag (0.008 mM – 0.04 mM)	
Rounded/cubic 3-D bi-AgNPs	Bromide (0.5 μM – 0.013 mM KBr)	
Rod 1-D bi-AgNPs	High pH and chloride (>0.16 mM HCl)	
1-D growth of pentagonal rod AgNPs (not bimorphs)	Chloride (>0.48 mM KCl)	
3-D uniform growth of enlarged AgDeNPs	Higher PAA (4.5 mM PAA, 1.2 mM ascorbic acid, 0.15 mM silver)	

*Concentrations are the same as reported in Methods for 2-D growth of the bimorphs with triangular platelets, unless otherwise stated

Blocking of the seed surface by PAA significantly restrains silver growth at the surface, effectively increasing the ratio of the reducing agent to reacting silver³⁵ and thus creating higher driving forces similar to what was reported in the literature for breaking symmetry during MNP regrowth.^{22,23} More details on the effect of PAA is provided in Supplementary (Supplementary Fig. 3S.5 and its description). The equilibration time of seed with PAA prior to the regrowth initiation (addition of silver nitrate and AA) was an important factor since kinetics of silver reduction plays a significant role in the formation of bi-AgNPs.¹² Formation of well-defined bi-AgNPs was attained at minimal equilibration times when AA and AgNO₃ are added right after the addition of PAA to the decahedral seeds.

PAA molecular weight and effect of other polymers have been investigated since PAA is the key reagent³⁶ in bi-AgNP synthesis. Large M_w PAA (450,000) was found to be an optimal polymer for surface blocking. Lower M_w of PAA that we have tested (such as M_w of 1,800 and 5,100) gave similar but largely inferior results with respect to the uniformity of bi-AgNP growth and resulting size-dispersity (Supplementary Figs. 3S.6b,c). More details are given in Supplementary Fig. 3S.6 and its description. Citrate (or citric acid) in replacement of or in addition to PAA has also been explored since citrate is a commonly used charge-stabilizing agent for AgNPs by virtue of its multiple carboxylic groups. We were not able to find conditions of bi-AgNP synthesis using citric acid or citrate alone. At concentrations greater than 0.03 mM, citric acid tends to promote uniform 3-D growth of the decahedral seeds to larger decahedra (Supplementary Fig. 3S.7a). Details on the effect of different acids are given in Supplementary Fig. 3S.7 and its description.

For stable, reproducible regrowth with high shape yields, the optimal concentration of AgDeNP seeds is 0.03-0.04 mM, below this concentration, more irregular platelet growth occurs (Supplementary Fig. 3S.8). With new silver added at a typical 200% molar ratio relative to silver in seeds, the total silver concentration of bi-AgNP dispersions is 0.1-0.15 mM (Fig. 3.2), typical for colloidal synthesis of metal NPs. At this range of concentrations, it is possible to largely avoid aggregation and formation of doublets in the

regrowth, as well as to minimize secondary nucleation that becomes a factor at lower seed concentrations. At ca. 300% of new silver (relative to the seeds), platelet parts can reach ca. 150-200 nm in width with typical thickness of 5-10 nm (Fig. 3.2a6), similar to platelet AgNPs prepared with citrate.^{37,38} Experiments with lower amounts of added silver (Fig. 3.2a1) confirmed that the bi-AgNP growth is initiated predominantly at the vertices of the pentagonal plane of the decahedra as the locus of the sharpest protrusions and thus the highest surface energy points. The growth initially proceeds through disordered multiple planar twinned structures and subsequently resolve in favorable conditions into well-defined platelet parts (Fig. 3.2a3-6). The role of reducing conditions is described in detail in Fig. 3S.9 in SI. Overall, optimal AA concentration range was 0.25-0.7 mM at pH of 6-6.5. pH plays a dual role in bi-AgNP synthesis: 1) due to the strongly pH-dependent reduction potential of ascorbic acid; 2) in AgNP stabilization, which is optimal in weakly basic conditions due to negative surface charge of stabilized AgNPs. Pure AgNP surface is positively charged due to silver ions present in the redox equilibrium. This positive charge is effectively reversed with common stabilizing anionic ligands, such as citrate or ionized poly(acrylic acid). The negative charge of the stabilizing ligands is neutralized at acidic pH due to protonation of carboxylic groups. Experiments with pH variation are shown in Supplementary Figure 3S.10.

Halides have rich legacy in shape control of silver nanoparticles,³⁹ e.g. bromide has been shown to be effective in transformation of Ag planar twinned morphologies into 3-D cubes and bipyramids by stabilizing (100) planes.³⁸ Bromide has been shown experimentally and computationally to strongly coordinate to silver and to drive selective facet stabilization in silver and gold nanoparticles.⁴⁰ In our work, the presence of bromide enables the transformation of 2-D bimorphic growth into 3-D by arresting platelet growth and thus first making them smaller and thicker (Fig. 3.1a) and then transforming them into rounded cubes and bipyramids, as shown in Figures 3.1f and g and Supplementary Figure 3S.11. Rounded cubes attached to decahedra can be observed at Ag/Br molar ratios as low as 138:1 (Supplementary Fig. 3S.11a), also confirmed by UV-vis spectroscopy (Supplementary Fig. 3S.12). In the

presence of bromide, the overall shape of bi-AgNPs is less defined due to etching with bromide and interference with reducing conditions by the bromide effect on silver reduction potential. Chloride exhibits a more complex and subtle effect on bi-AgNP formation. First, more than 100 times higher chloride concentrations were required to reach an effect comparable to bromide due to the appreciably larger K_{sp} of AgCl vs. AgBr. Stabilization of (100) similar to bromide was evident (Figs. 3.1h and Supplementary Fig. 3S.13). 1-D growth of decahedra to short pentagonal rods was noticeably promoted at higher Cl/Ag ratio (>12:1) (Fig. 3.1h and Supplementary Fig. 3S.13d), where the reduction is slower due to chloride both complexing silver ions and blocking the seed surface. 1-D pentagonal growth of decahedra can be distinguished from 1-D bimorphic growth, where the rods are nucleated in a single point at the surface of AgDeNPs and are not necessarily pentagonal (Fig. 3.1a). The addition of smaller chloride amounts (Ag/Cl of 20-50) had a weak positive effect on the formation of well-defined triangular platelet parts of bi-AgNPs. 1-D bimorphic growth was observed when HCl was used to adjust pH (Fig. 3.1i and Supplementary Fig. 3S.14). This growth mode takes place in mild reducing conditions where the deposition of new silver is directed by pentagonal twinning disclination with subsequent rebuilding of (100) planes,⁴¹ and protonation of PAA (Fig. 3.1i). Compared to bromide and chloride, iodide has a strong arresting effect on the development of bi-AgNPs (see Supplementary Fig. 3S.15 and description therein).

The diversity of attainable bi-AgNP morphologies is represented in Figure 3.3. Many bi-AgNP nanoshapes are reminiscent of fish (Fig. 3.3a-c), birds, mushrooms, kites and butterflies. In particular, we aimed to produce nanoscale analogues of apple-like shapes (Figs. 3.3j-m), especially apples with a bite taken out (Figs. 3.3k,l), as being culturally significant. Such bi-AgNPs with additional symmetry breaking could be prepared in slightly more etching conditions relative to optimal. A complementary nanoscale pear-like bi-AgNP is shown in Fig. 3.3m. See also supplementary Fig. 3S.19 for selected coloured images.

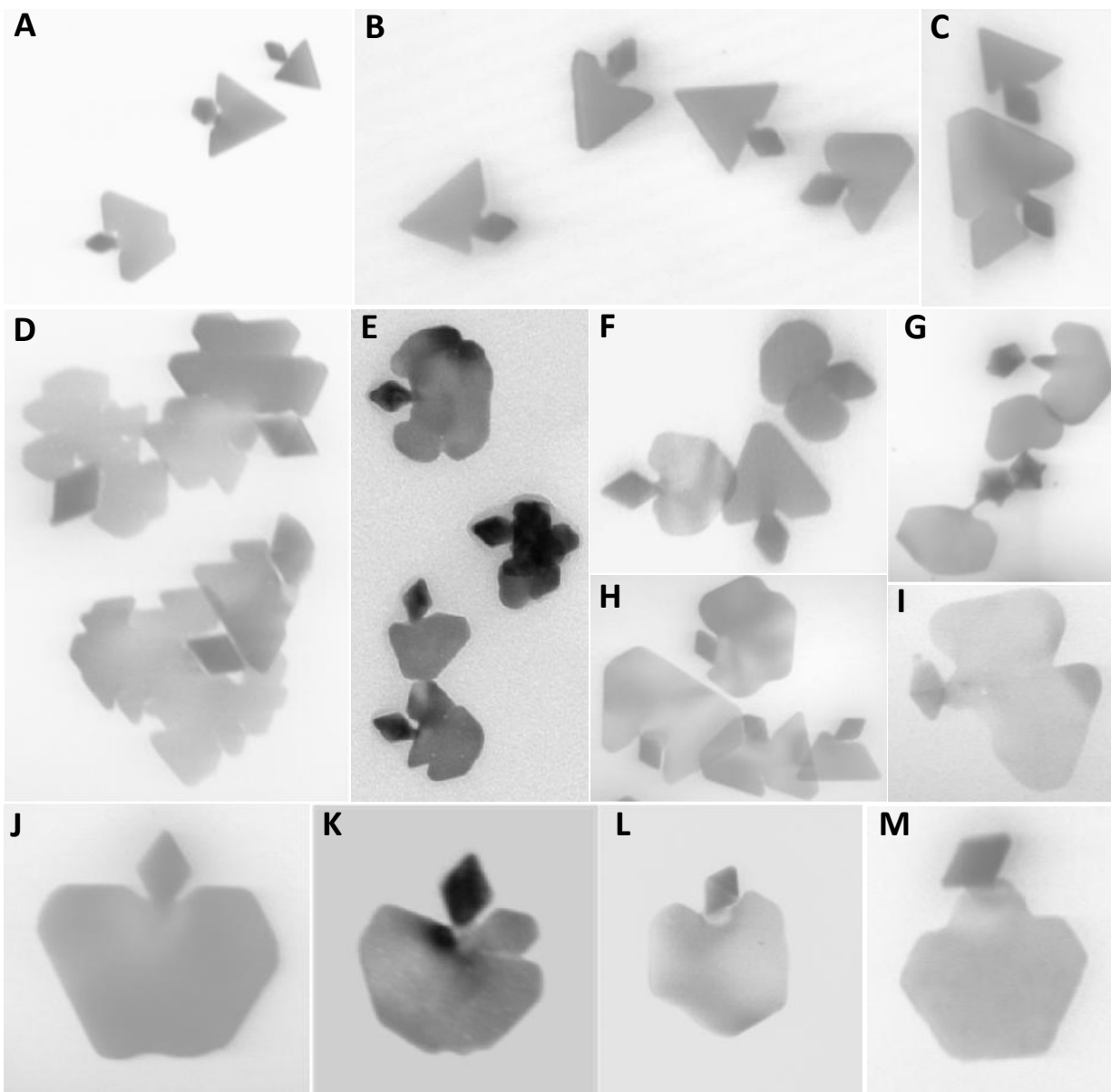


Figure 3.3. TEM images demonstrating diversity of attainable bi-AgNP shapes. The scale can be inferred from the largest dimension of the decahedral part of bi-AgNPs (a diamond shape in TEM side projection) being 41.5 ± 1.5 nm, reproducibly prepared by photochemical synthesis.³¹

Further bimorph diversity can be realized with different seed particles for the regrowth. To demonstrate such possibility, we have used silver platelets/prisms prepared using our previously reported procedure.³⁸ Using 2-D regrowth conditions, formation of the second platelet part is achieved by nucleation and growth at high-energy vertices to yield platelet-platelet bimorphic AgNPs (Supplementary

Fig. 3S.16). Therefore, any suitable seed particles are expected to be successfully used in the bimorphic regrowth with suitable polymer blocking of the seed surface.

Formation of Au coating and shells^{42,43} of bi-AgNPs was tested with H₂AuCl₄ addition. Even at lower amounts of gold relative to silver in bi-AgNPs, such as 5 mol.%, the gold deposition is highly granular, with the nucleation and growth only in selected spots on the surface (Supplementary Figs. 3S.17a,b). At ca. 20 mol.% of gold added, the resulting nanostructures become rough due to silver etching (Supplementary Fig. 3S.17c).

Bi-AgNPs show excellent SERS enhancement by virtue of their packing that creates semi-regular voids due to incompatibility with close packed lattices.³¹ Using 5,5'-dithiobis (2-nitro-benzoic acid) as a probe molecule and 785 nm laser, 10^{-16} moles/cm² could be easily detected with dry bi-AgNP films as substrates (Supplementary Fig. 3S.18), and DTNB detection limit can be estimated as ca. 5×10^{-16} moles/cm². The signal enhancement relative to pure DTNB is 7×10^9 vs. 4×10^9 of AgDeNPs. Noticeably higher SERS enhancement relative to decahedra may be attributed to the resonant SERS enhancement due to LSPR absorption at 785 nm from the platelet parts of bi-AgNPs, and to the cavity at the junction of the two bimorph parts, where the field enhancement is expected to be the highest. As highly non-centrosymmetric particles, bi-AgNPs can be also beneficial for plasmonic applications.⁴⁴

In summary, we have demonstrated that by controllably blocking the surface of the seed AgNPs with an adsorbing polymer, several modes of seeded growth from uniform (111) enlargement of decahedra to symmetry breaking with a single point nucleation result in diverse bimorphic morphologies. Universality of the formation of bimorphic nanoparticles using different seeds is also demonstrated. Bi-AgNPs exhibit strong SERS enhancement and are promising as a SERS substrate. Demonstrated approach to symmetry breaking and resulting bimorphic particles open new perspectives in nanoscale shape design.

3.4. Methods

AgDeNP seeds were prepared as described in Murshid, et al.³² AgDeNPs (prepared 2-20 days prior to bi-AgNP synthesis) were first concentrated 10 times (from 0.13 mM to 1.3 mM Ag). Representative amounts and total molarities in the final preparation (in brackets) for well-defined 2-D bi-AgNPs (shown in Fig. 3S.10 for pH=6) were as follows: 6 mL of water, 40 μ L of 0.02 M PAA ($M_w = 450,000$, 0.13 mM by monomer), 200 μ L of concentrated AgDeNPs (0.04 mM), 35 μ L of 0.05 M ascorbic acid (0.27 mM), and 100 μ L of 0.005 M AgNO₃ (0.08 mM) combined in a 20 ml vial upon magnetic stirring. Upon addition of AgNO₃, the reaction color changed from yellow-orange to greenish-bluish grey. See Supplementary Table 3S.1 for specific conditions of synthesis of other bi-AgNP morphologies. More details on reagents, procedures of bi-AgNP preparation and characterization are provided in Supplementary.

3.5. Acknowledgement

The authors would like to thank NSERC and the Government of Ontario (ERA Award) for funding. Centre for Nanostructure Imaging, University of Toronto, for access to imaging facilities, Ilya Gourevich and Neil Coombs for the support with electron microscopy.

3.6. Supplementary Information

Experimental details

Reagents. Silver nitrate (99.99%), sodium citrate tribasic dihydrate (99.5%), arginine (98%), sodium borohydride ($\geq 99\%$), hydrogen peroxide (30-32 wt%, 99.999% trace metal basis, potassium stannate inhibitor), poly(acrylic acid) (PAA, avg. $M_w = 1,800$), poly(acrylic acid) (PAA, avg. $M_w = 450,000$), poly (acrylic acid sodium salt) (PAA, avg. $M_w = 5,100$), poly (acrylamide co-acrylic acid), partial sodium salt (PA co-AA, avg. $M_w = 200,000$, 20 % acrylamide), poly (N-vinylpyrrolidone-co-2-dimethylaminoethyl methacrylate) 19+ wt. % solution in water (PVP-co-DMAEMA, avg. $M_w = 1,000,000$, Batch #14030EO), poly (sodium 4-styrenesulfonate) (PSS, avg. $M_w = 70,000$), L-ascorbic acid, (99+%), 5,5'-dithiobis (2-nitro-benzoic acid) (99%), potassium chloride (99%), potassium bromide (99%), potassium iodide (99%), potassium hydroxide (99.99%), nitric acid (65 wt.%, ACS grade), hydrochloric acid (37 wt.%, semiconductor grade), all supplied

by Aldrich; and poly (N-vinylpyrrolidone) (PVP, avg. $M_w = 40,000$) supplied by Caledon Chemicals (Caledon, Canada) were used as received. High purity deionized water ($> 18.2 \text{ M}\Omega\cdot\text{cm}$) was produced using Millipore A10 Milli-Q.

3-D growth of Decahedra with PAA. The procedure is the same as the synthesis of bimorphic NPs except for the higher PAA concentration used. In a typical preparation corresponding to the sample shown in Fig. 3S.3E, 6 mL of water, 150 μL of 0.2 M PAA 450 K (4.5 mM), 200 μL of concentrated decahedra with 1.3 mM Ag (0.04 mM), 160 μL of 0.05 M ascorbic acid (1.2 mM), and 200 μL of 0.005 M AgNO_3 (0.15 mM). Numbers in brackets are total molarities in the final preparation. After the addition of silver nitrate, the reaction mixture remains visually unchanged for 20-30 minutes, before reduction of silver on the decahedral seed surface becomes noticeable by a red-shift in the LSPR. The regrowth process was typically completed within 12-18 hours.

Preparation of SERS substrates. SERS substrates were prepared by concentrating 1.5 mL of bi-AgNP to 20-50 μL dispersions using centrifugation. The resulting total silver concentration in concentrated bi-AgNP samples was 10-20 mM. 2-10 μL of this concentrated dispersion was transferred onto a quartz slide by a pipette and spread to a size of 1 cm by 0.6 cm. The sample was dried in an oven at 55-60 $^\circ\text{C}$ for 5-10 minutes, and then used for SERS measurement without further treatment. 1-5 μL of dilute 5,5'-dithiobis(2-nitrobenzoic acid) in water (with addition of THF at higher concentrations) was dispensed directly onto the dried bi-AgNPs and then dried in an oven for 1-2 minutes.

Instrumentation. Electron microscopy (EM) imaging was done using Hitachi S-5200 with a carbon-coated formvar grid (EMS Corp.). UV-vis spectra were acquired with either an Ocean Optics QE-65000 fiber-optic UV-vis spectrometer or Cary 50Bio UV-vis spectrophotometer. Raman spectra were recorded using R-3000QE fibre-optic Raman spectrometer equipped with 290 mW laser at 785 nm (RSI). Centrifugation was performed using either VWR Clinical 100 or Thermo Scientific Legend Micro 21 centrifuges.

Table 3S.1. Summary of synthetic conditions for bi-AgNP samples presented in Figures 3.1 and 3S.2.

Ag ⁺ Added (mM)	Decahedra Seed (mM)	Polymer, MW, (mM)	Ascorbic Acid (mM)	Other Parameters	Sample #	Corresponding Figure Image/Morphology
0.069	0.039	PAA*, 1.8 K, 0.063	0.938	Tricitrate, 0.038 mM	NJ523	3.1b
0.070	0.040	PANa*, 5 K, 0.002	0.278		NN283	3.1c

0.018	0.040	PAA, 450 K, 0.096	0.438		NO487	3.1d
0.143	0.036	PAA, 1.8 K, 0.347	1.627	Citric Acid, 0.578 mM	NO77	3.1e
0.069	0.039	PAA, 450 K, 0.126	0.276	KBr, 0.002 mM	NQ396	3.1f
0.063	0.039	PAA, 450 K, 0.125	0.274	KBr, 0.006 mM	NT625	3.1g
0.062	0.039	PAA, 450 K, 0.124	0.272	KCl, 1.24 mM	NT648	3.1h
0.063	0.039	PAA, 450 K, 0.126	0.275	HCl, 0.154 mM	NT606	3.1i
0.069	0.035	PAA, 1.8 K, 0.063	0.629	Tricitrate 0.31 mM	NH909	3S.2a
0.069	0.039	PAA, 1.8 K, 0.063	0.938	Tricitrate 0.39 mM	NJ523	3S.2b
0.017	0.039	PAA, 450 K, 0.063	1.255		NO624	3S.2c
0.069	0.039	PAA, 1.8 K, 0.25	0.039	AA added last	NH999	3S.2d
0.0556	0.032	PAA, 450 K, 3.788	1.010		NO690	3S.2e
0.070	0.040	PAA, 450 K, 0.015	0.278	KBr 0.11 μ M	NP446	3S.2f
0.063	0.039	PAA, 450 K, 0.126	0.275	KOH 1.58 mM	NT517	3S.2g
0.132	0.038	PAA, 450 K, 4.506	1.201	HNO ₃ 0.15 mM	NP151	3S.2h
0.069	0.035	PAA, 450 K, 0.313	0.274		NO304	Lily pod (2D growth)
0.070	0.035	PANa, 5 K, 0.0016	0.278	NaOH 16 μ M	NQ224	Fish (2D growth)
0.009	0.035	PAA, 450 K, 0.031	1.259		NO710	Small growth (2D growth)
0.068	0.035	PAA, 1.8 K, 0.248	0.776	AA* added last	NI7	Large decahedra (3D growth)

*PAA = poly (acrylic acid); PANa = poly (acrylic acid sodium salt); AA = ascorbic acid

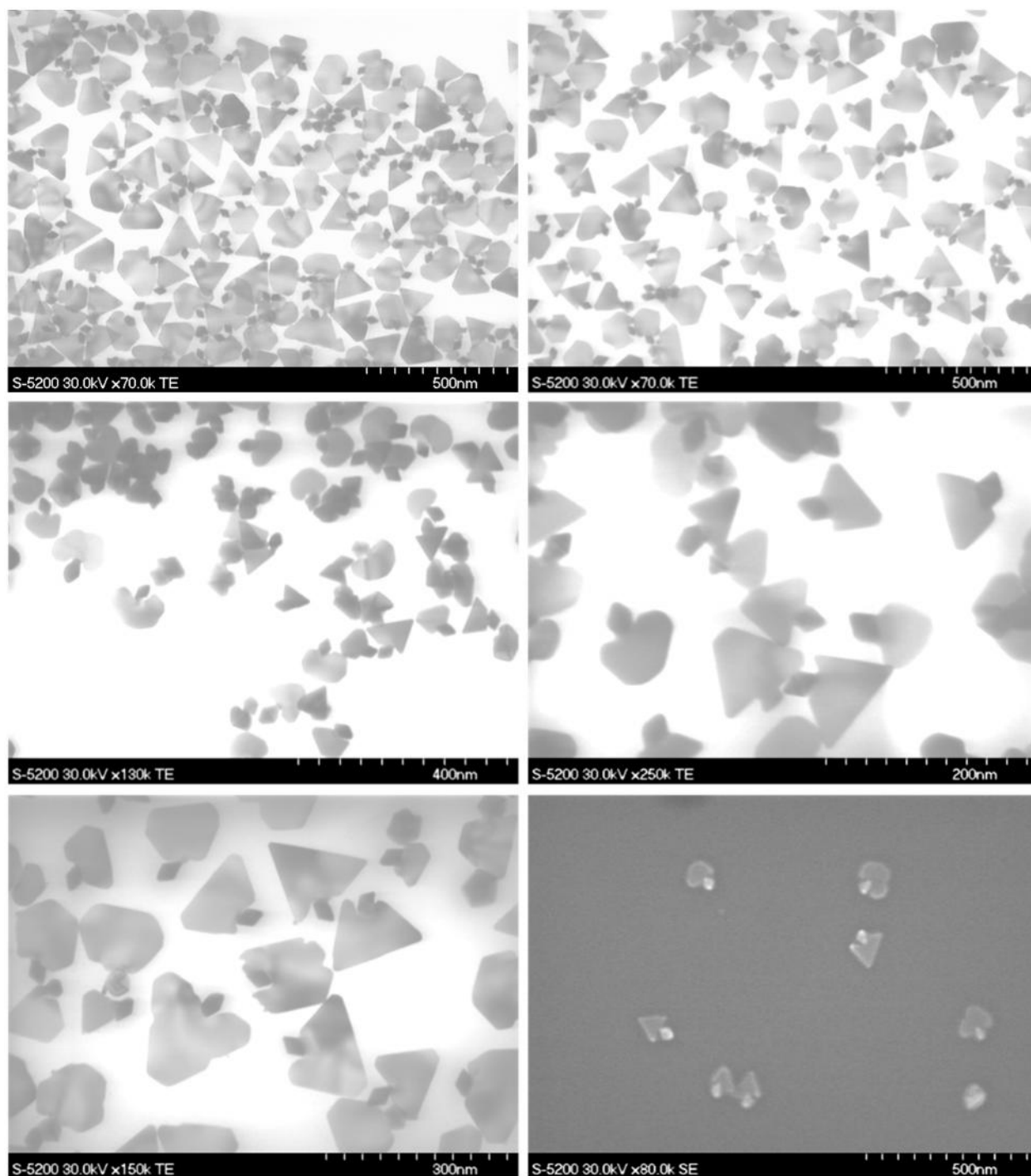


Figure 3S.1. Representative electron microscopy (EM) images demonstrating high shape yield and consistent morphologies of 2-D bi-AgNPs prepared over the course of three years.

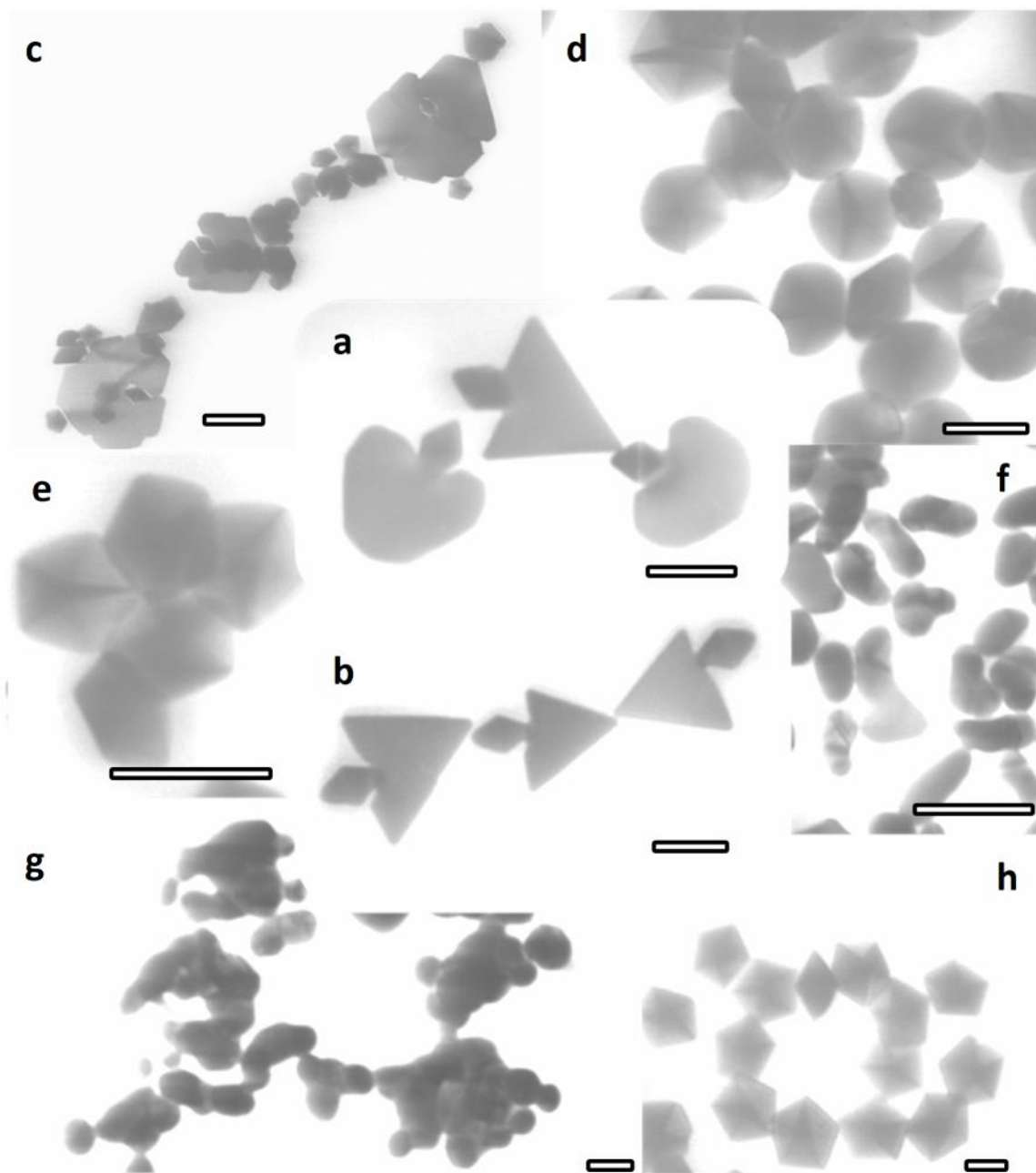


Figure 3S.2. TEM images of key bimorphic morphologies prepared in optimized synthetic conditions: **a)** and **b)**; and in synthetic conditions appreciably different from optimal: **c)** high ascorbic acid, **d)** low ascorbic acid, **e)** high PAA, **f)** low PAA, **g)** high pH and **h)** low pH. For detailed description of samples - see **Table 3S.1**. Scale bars are 50 nm for **a)**, **b)**, **d)**, **g)** and **h)**; and 100 nm for **c)**, **e)** and **f)**.

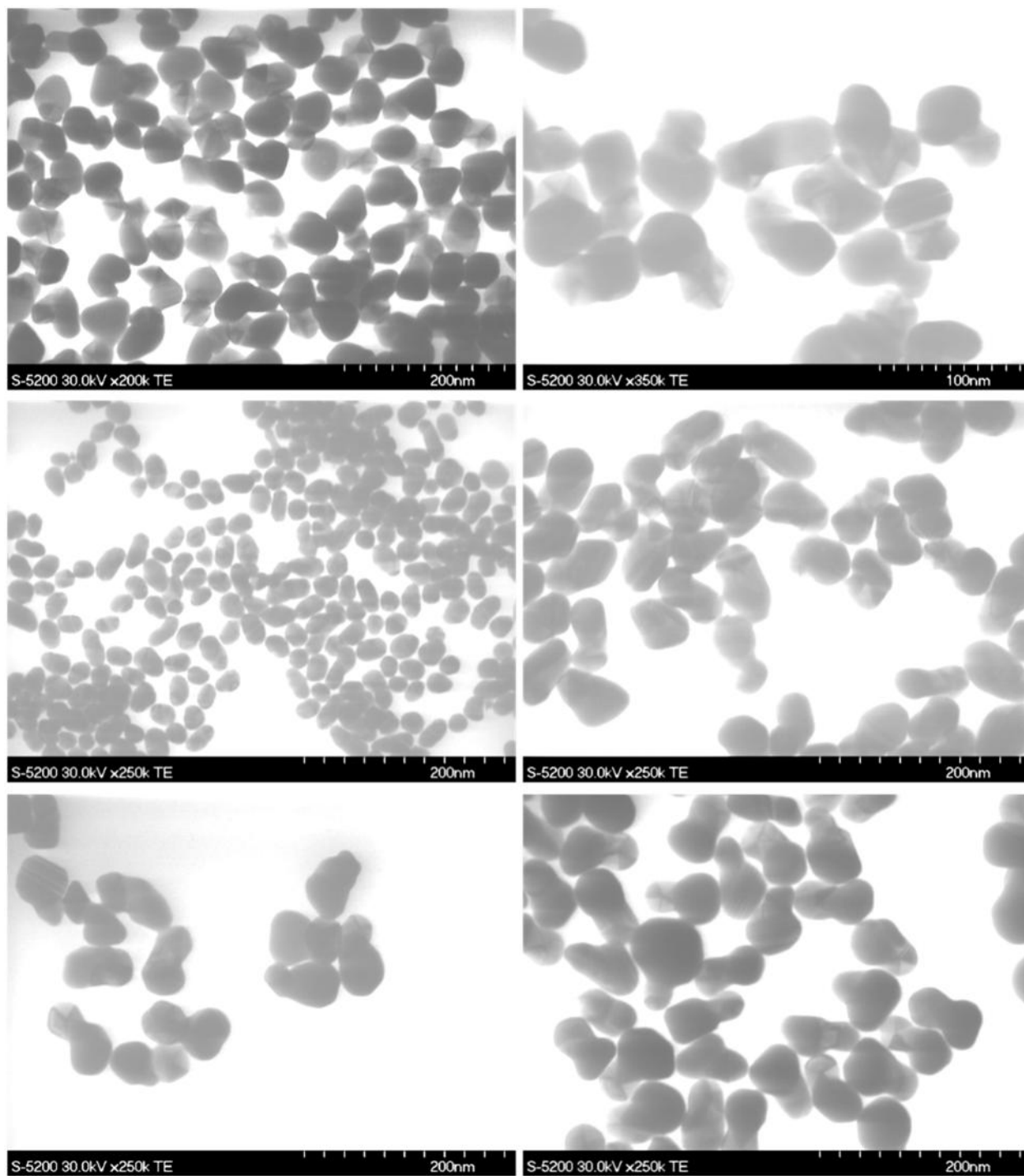


Figure 3S.3. Representative transmission electron microscopy (TEM) images showing high shape yield of 3-D bi-AgNP regrowth.

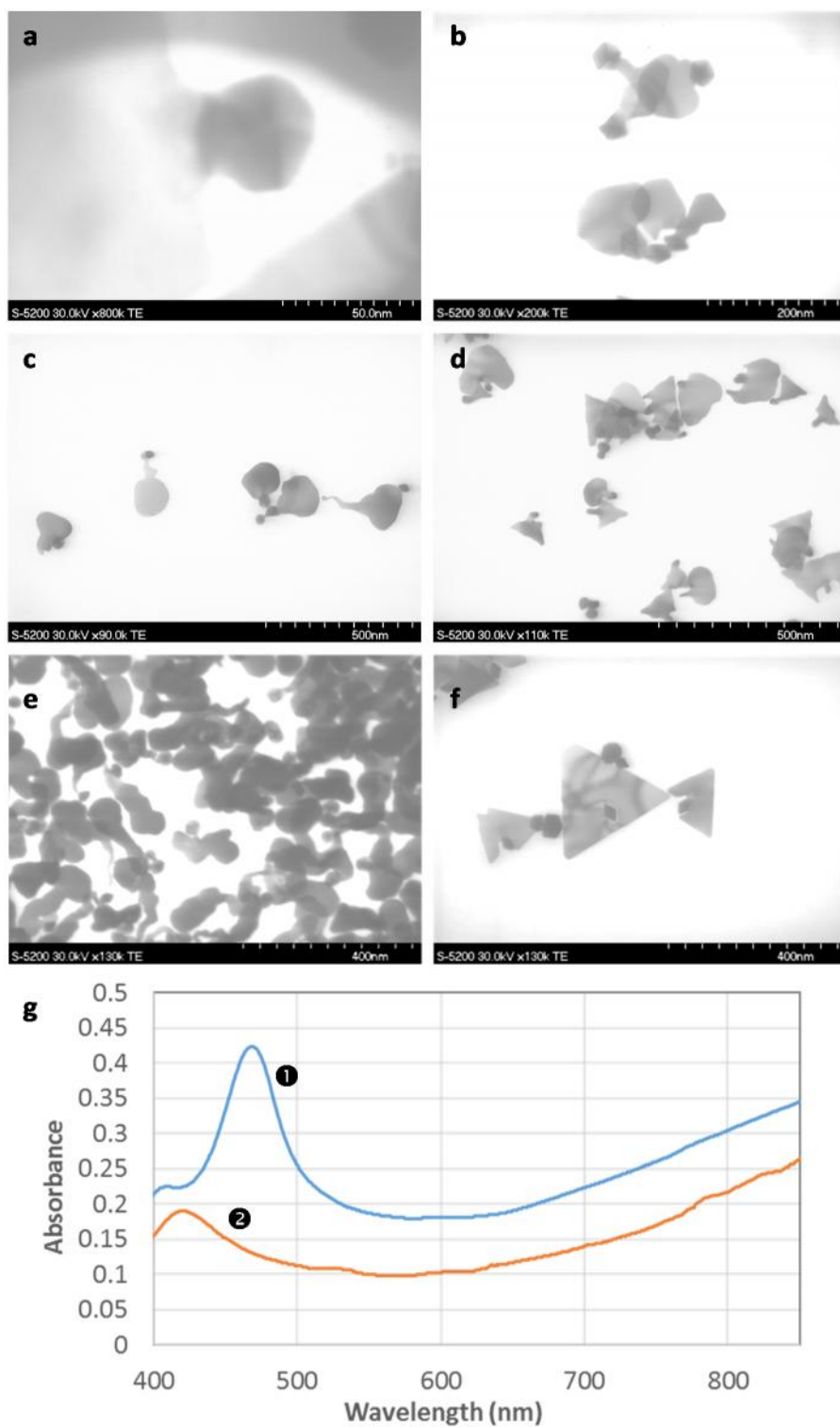


Figure 3S.4. a-f) TEM images of irregular growth due to a) higher reagent concentration (25% less water), b) high PAA, c) equilibration between PAA and decahedra (delay in development), d) aging (6 days between preparation and imaging) e) high silver, f) high silver and ascorbic acid and g) UV-vis spectra of Fig. 3S.4d aging ①- immediately after preparation, ②- 6 days after preparation (before imaging).

Thin necks of the bi-AgNPs shown in Figure 3S.4c are likely due to the slower growth initiation and corresponding higher growth rates when silver starts to deposit onto the decahedra. This faster initial growth results in more disordered growth areas at the decahedra surface that subsequently become the necks. In addition, the decahedral part of bi-AgNPs gets more etched, which is evident from EM images of Fig. 3S.4, as well as the blue shift of decahedra LSPR mode from 470-480 nm to 435-450nm (Fig. 3S.4g). The effect of the equilibration with PAA is relatively subtle, so it was difficult to point out an appreciable difference between several minutes and several hours of equilibration. When higher AA concentrations were used together with high silver concentrations, newly generated metallic silver was deposited around the decahedral seeds in a less organized fashion with the rougher platelet-like structures growing with little to no neck or tethering (Fig. 3S.4f).

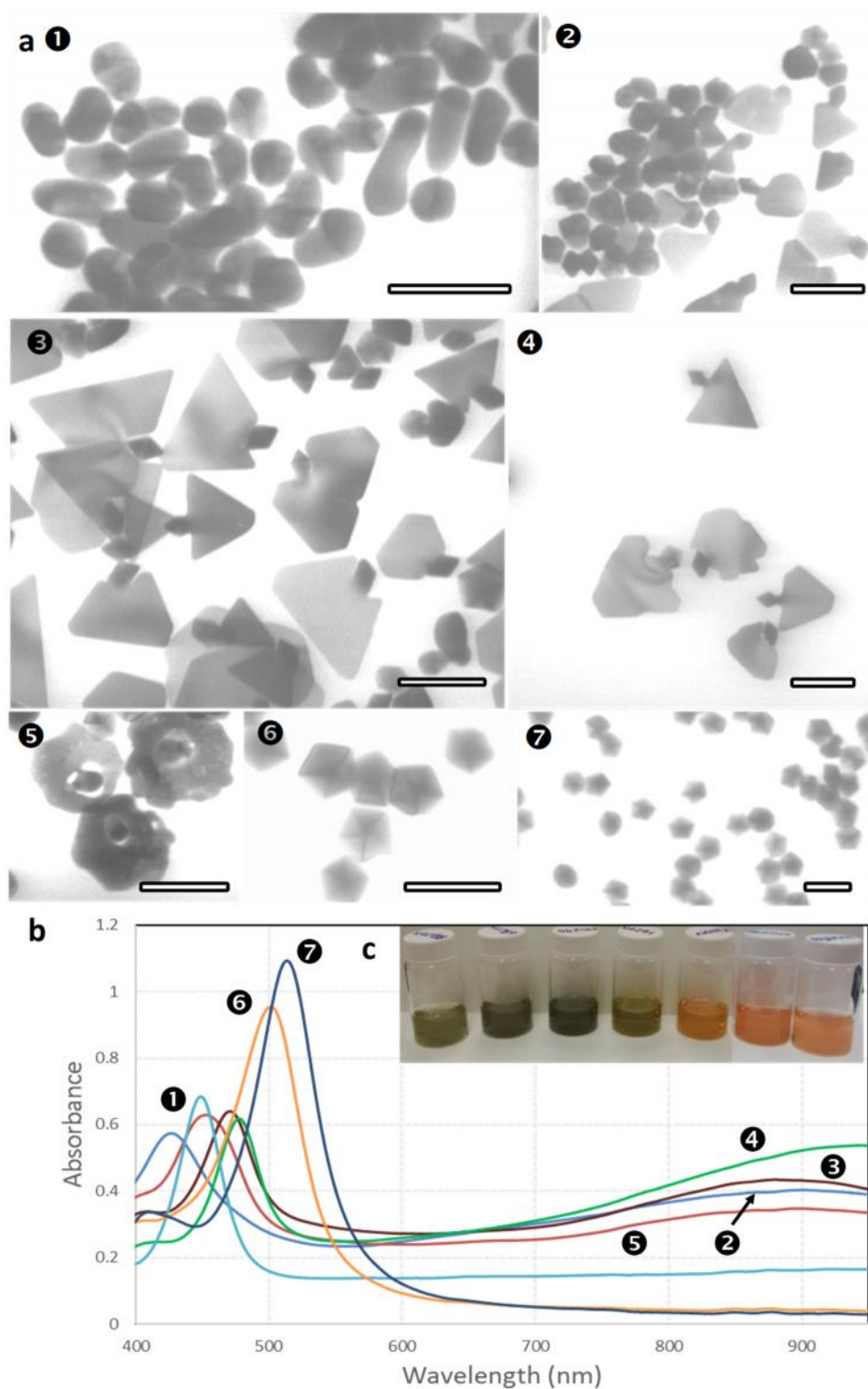


Figure 3S.5. a) TEM images, b) UV-vis spectra and c) optical photographs of representative bi-AgNP samples prepared with increasing concentrations of poly(acrylic acid) ($M_w = 450,000$): ① 0 mM, ② 0.03 mM, ③ 0.12 mM, ④ 0.25 mM, ⑤ 0.76 mM, ⑥ 1.1 mM and ⑦ 2.2 mM. All scale bars are 100 nm.

In the absence of PAA and with typical AA concentrations, the decahedra regrowth is not well defined (Fig. 3S.5a1), with Ag^+ depositing without preferential direction. At a higher but still less than optimal PAA concentration, the platelet formation starts to emerge but the bi-AgNP growth is still not well resolved (Fig. 3S.5a2). At low PAA concentrations and higher AA concentrations with corresponding higher rates of silver reduction, new silver deposits around the periphery of decahedra leading to lily-pod morphologies (Fig. 3S.8a) and decahedra encapsulation (Figs. 3S.9a3 and 3S.4f). At optimal PAA concentrations at 0.12-0.14 mM (ca. 1:1 molar ratio to total silver), well defined triangular platelets with the preservation of the decahedral part form (Fig. 3S.5a3). At higher than optimal PAA concentrations, the decahedra surface becomes partially blocked to the extent that a significant portion of the decahedra seeds do not grow (Fig. 3S.5a5). Consequently, the fast growth is initiated only on a fraction of decahedra seeds and proceeds in effectively less than optimal conditions – higher AA and silver concentration relative to the growing seeds. As a result, the silver deposition gets noticeably perturbed with the new silver depositing disorderly around the periphery of the decahedral seeds (Figs. 3S.5a5 and 3S.9a3) due to a larger effective ratio of new silver to the available growth surface in the seeds.

At even higher PAA concentrations (ca. 10-20 times higher than optimal, see Experimental), the surface of decahedral seeds becomes uniformly blocked to such an extent that the fast growth (5-10 seconds to minutes) is no longer possible and the deposition is switched to the slow (15-30 minutes to several hours) uniform 3-D growth of decahedra where (111) surfaces are homogeneously rebuilt (Figs. 3S.5a6, 3S.5a7). The transition between the 2-D bimorphic growth and 3-D decahedra enlargement is observed at PAA concentrations in a range of 0.8 to 1 mM (ca. 7-8 PAA/Ag molar ratio) and higher.

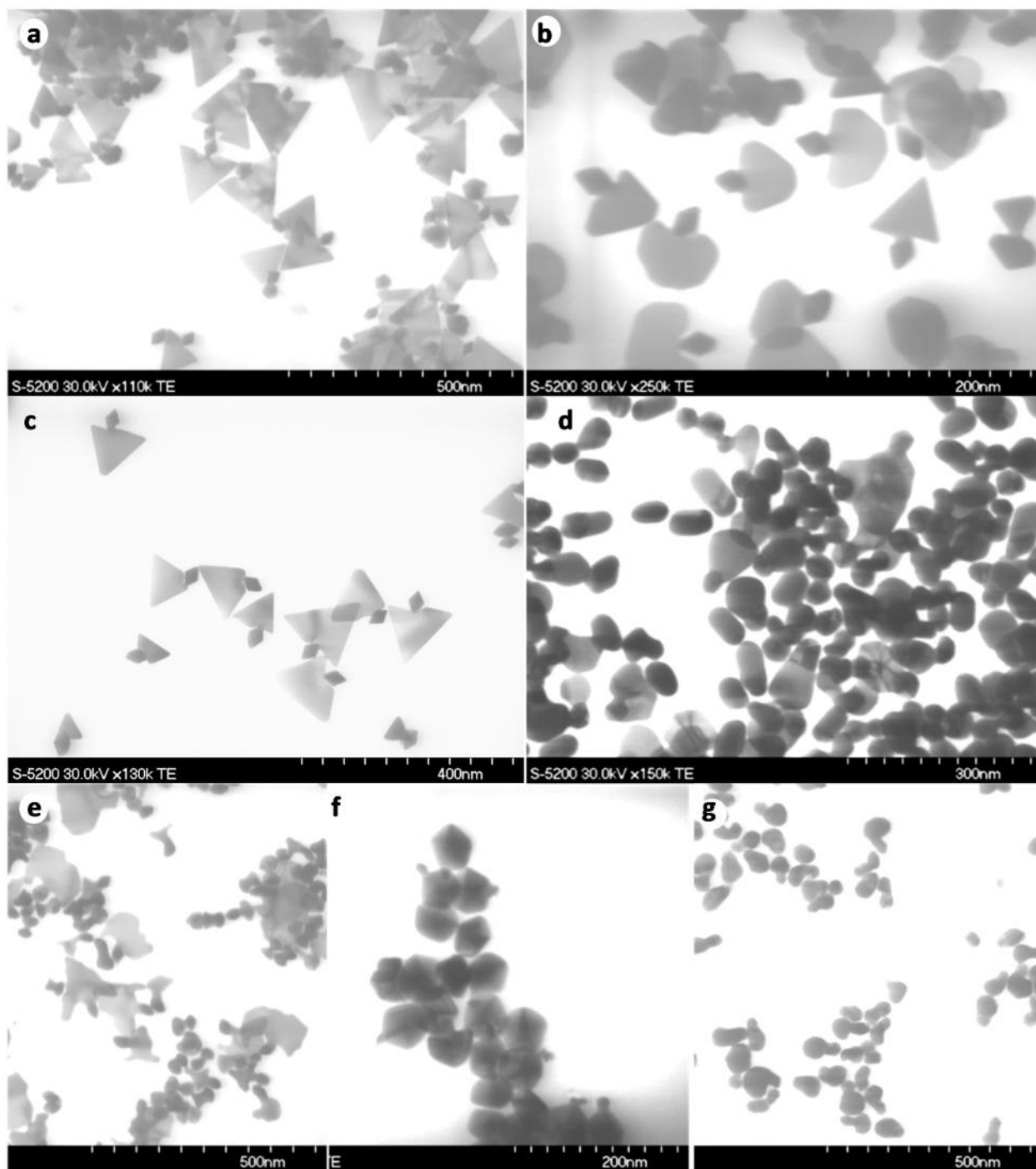


Figure 3S.6. TEM images of bi-AgNP samples prepared using different polymers: **a)** poly(acrylic acid) 450 K, **b)** poly(acrylic acid) 1.8 K, **c)** poly(acrylic acid sodium salt) 5.1 K, **d)** poly(N-vinylpyrrolidone) 40 K, **e)** poly(acrylamide co-acrylic acid), partial sodium salt 200 K, **f)** poly(N-vinylpyrrolidone-co-2-dimethylaminoethyl methacrylate) 1,000 K, **g)** poly(sodium 4-styrenesulfonate) 70 K.

Poly(acrylic acid sodium salt) (PANA) with a MW of 5,100 produced noticeably well-defined triangular platelets in several samples, with more random attachment points to the decahedral part (Fig. 3S.6c). A

copolymer of acrylic acid with acrylamide was also explored (see Experimental). This copolymer supported growth of bi-AgNPs but with less-defined and more random platelet growth and less preserved decahedral parts of bi-AgNPs (Fig. 3S.6e). Stabilization with poly(N-vinylpyrrolidone), PVP, and a copolymer of N-vinylpyrrolidone with dimethylaminoethyl methacrylate did not produce well-defined morphologies likely due to weak binding to the surface of AgNPs in absence of carboxylic groups (Figs. 3S.6d,f). Poly(styrenesulfonate), PSS, provided weaker surface blocking of the decahedral seeds and the resulting bi-AgNPs becoming more rounded, with close attachment of the decahedra and platelet components (Fig. 3S.6g).

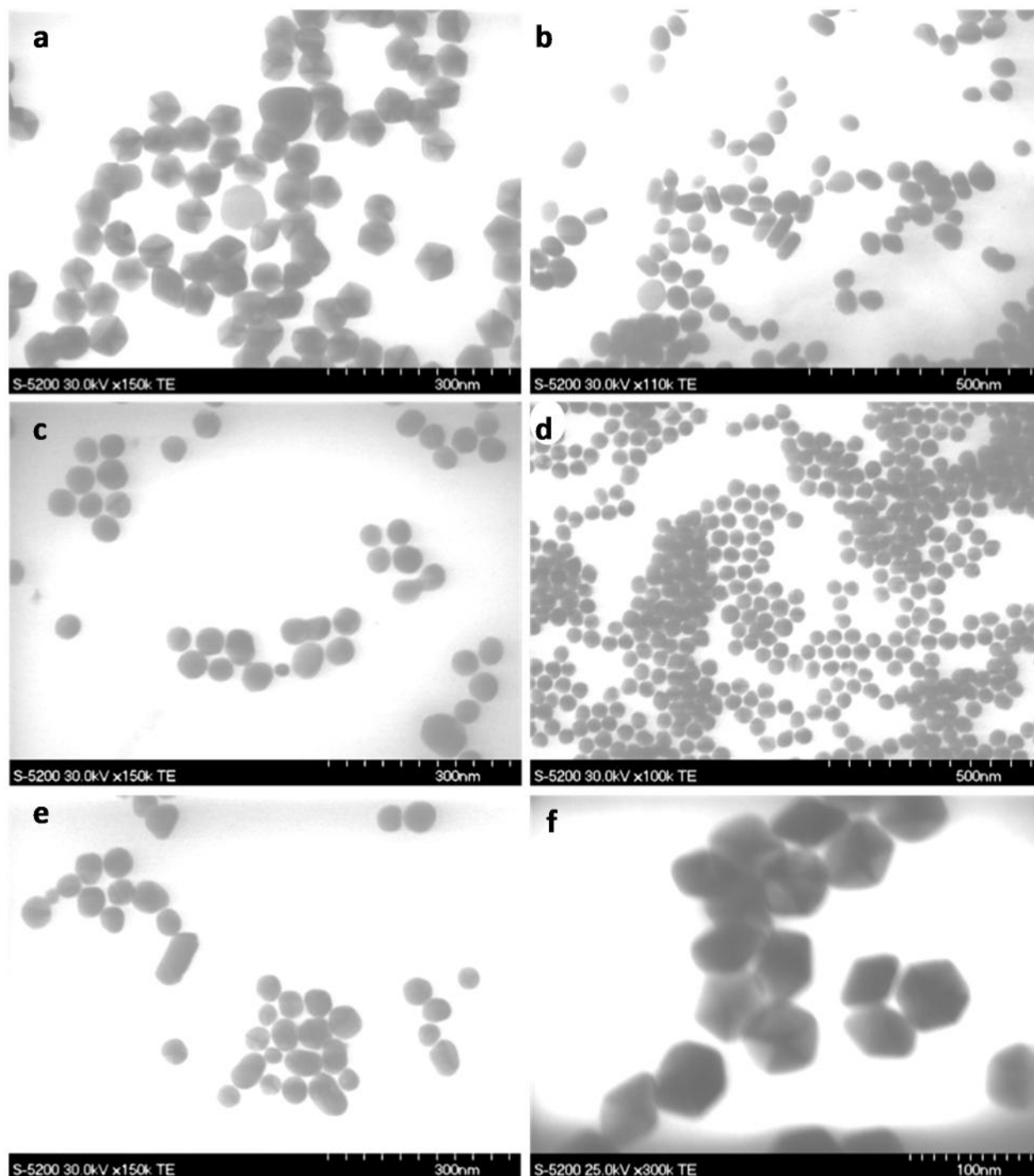


Figure 3S.7. TEM images of samples prepared with various acids in replacement of PAA: **a)** citric acid, **b)** boric acid, **c)** nitric acid, **d)** trimesic acid, **e)** phosphoric acid, and **f)** tartaric acid.

At lower concentrations of citric acid and in the absence of PAA, the insufficient surface blocking and platelet stabilization result in uncontrolled growth. At the same time, citric acid or citrate could be used together with PAA, since they did not significantly affect bimorphic growth at concentrations up to 0.05 mM. These findings confirm the importance of long polymer chains of PAA in modulating the growth of AgNPs and the carboxylic groups playing a primary role in binding to the AgNP surface.

We have also conducted a series of experiments using several different acids in place of PAA to access their effect on bi-AgNP formation. As can be seen in Figure 3S.7, all acids with exception of trimesic acid (Fig. 3S.7d) etch the decahedra surface and yield either larger rounded decahedra or shapeless aggregated AgNPs. The preservation of decahedral shape with trimesic acid is due to the fact that it is a tricarboxylic acid similar to citric acid and it similarly stabilizes (111) planes in AgNPs.

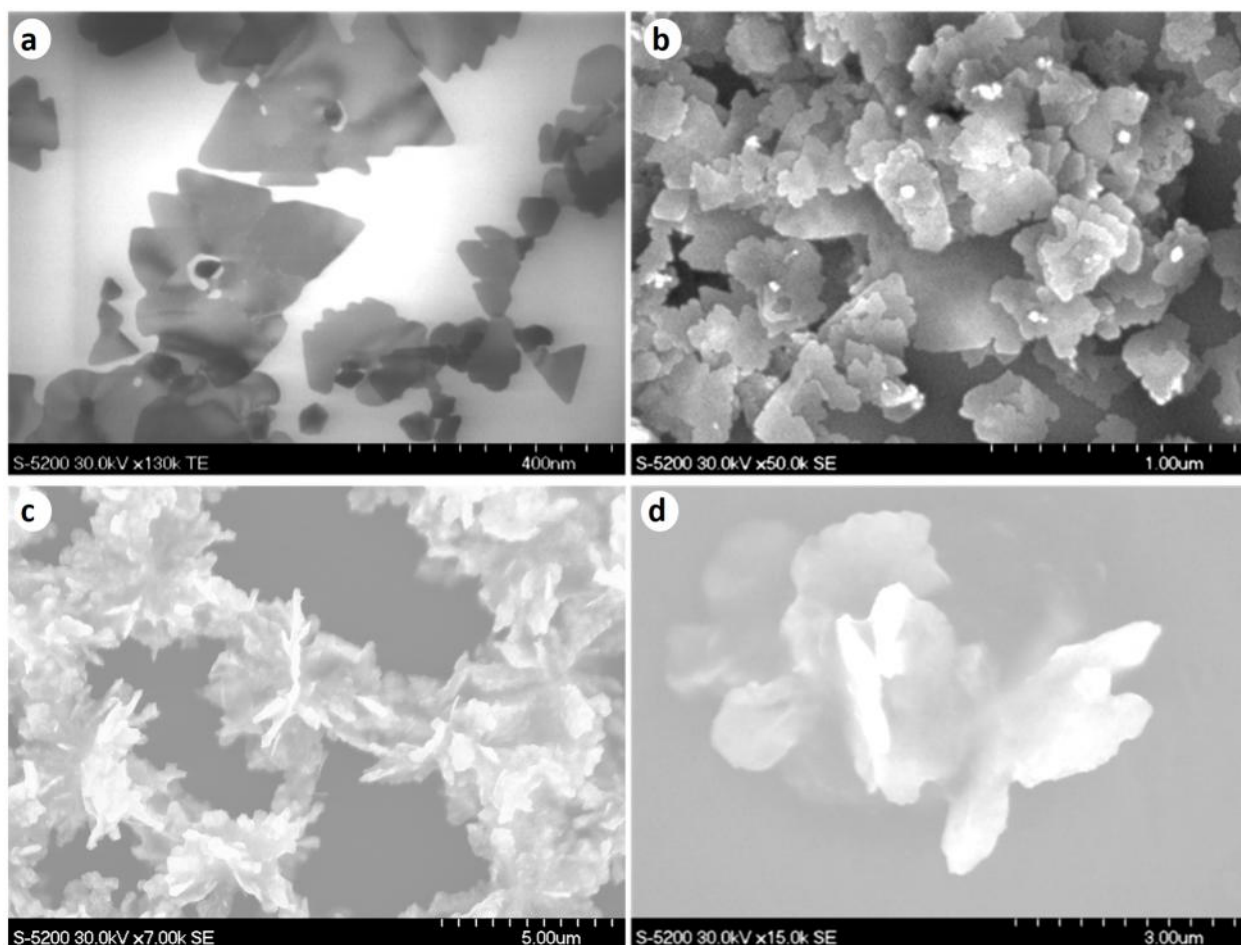


Figure 3S.8. EM images (all SEM with the exception **a**), which is TEM) of bi-AgNP samples prepared with lower than optimal ratio of decahedral seeds to silver added in the regrowth: **a**) 1/2 compared to the optimal (See Experimental), **b**) 1/20, **c**) and **d**) no decahedral seeds.

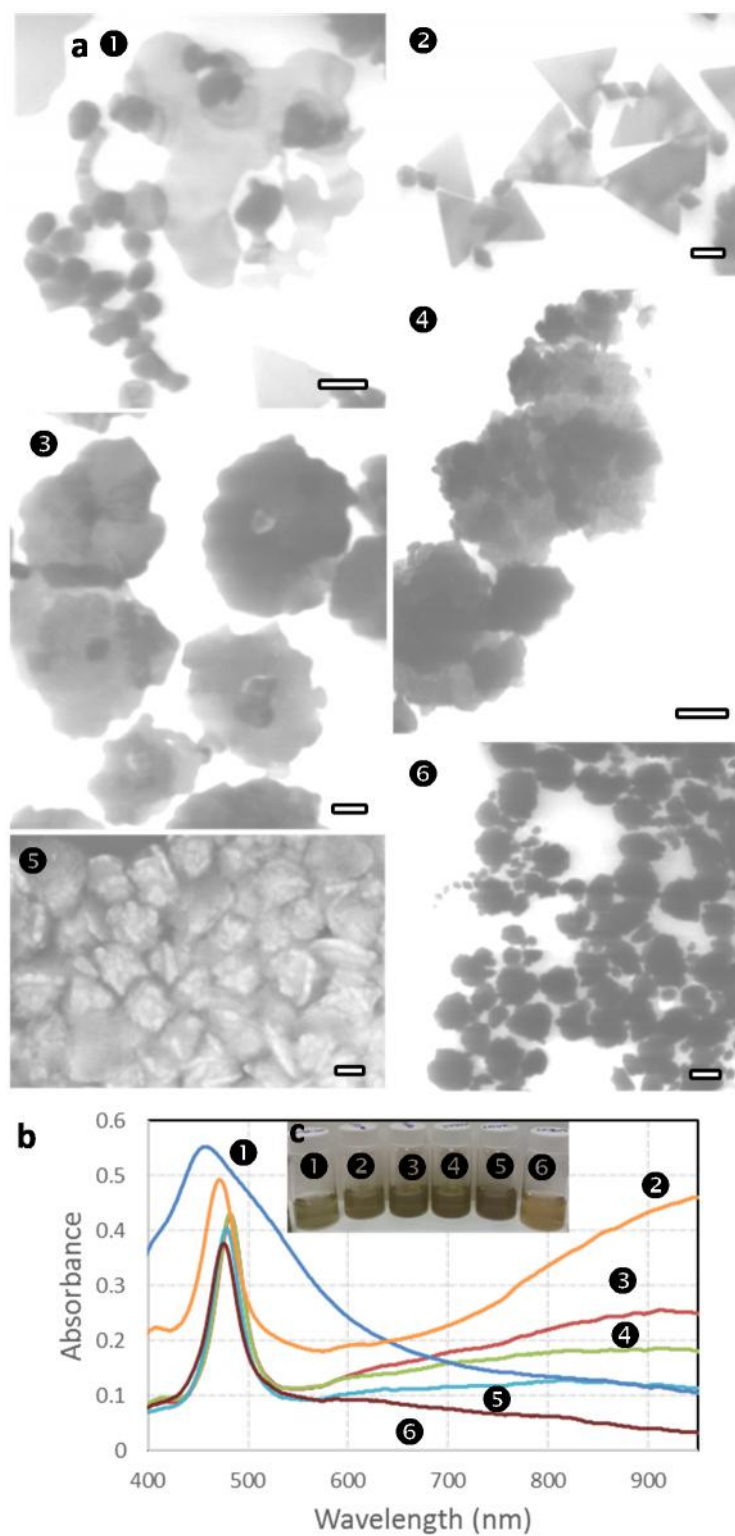


Figure 35.9. a) Representative EM (all TEM, except **5** is SEM) images; b) UV-vis spectra; and c) optical photographs of samples prepared with increasing concentration of ascorbic acid: **1** 0.08 mM, **2** 0.3 mM, **3** 0.7 mM, **4** 1.4 mM, **5** 2.8 mM, and **6** 6.2 mM. Scale bars are 50 nm for **1**, **2** and **3**, and 100 nm for **4**, **5** and **6**.

The process of bi-AgNP formation involves the reduction of silver precursors, so the role of a reducing agent in the synthesis is important. In conditions of slow growth, e.g. photochemical transformations with citrate,⁵¹ the decahedra enlargement in a 3-D growth mode is favoured. A commonly used reducing agent, sodium borohydride, is too powerful for bi-AgNP formation since it readily promotes secondary nucleation. Ascorbic acid proved to be optimal; first, by its moderate reducing strength and, second, because its reducing potential can be controlled (and thus fine-tuned) not only by concentration but also by pH, so that the reduction can be adjusted to proceed relatively fast but avoiding secondary nucleation. A common problem with the ascorbic acid is that it tends to induce faster growth with limited shape selection⁵² (similar to what is shown in Figs. 3S.9a3&4), so the reduction conditions need to be tightly controlled to produce well-defined uniform AgNP morphologies.

In a series of samples with varying AA concentration, shown in Figure 3S.9, the prevailing trends can be readily seen. At lower AA concentrations, the excess of unreduced silver ions etches silver decahedra and the growth of planar twinned morphologies becomes less defined (Fig. 3S.9a1). At higher than optimal AA concentration, the bimorphic growth becomes too rapid to lead to shape selection. The predominant observed morphologies are multiple platelets fused together, first around the rim of decahedra (Fig. 3S.9a3) and then entirely around the seed particle resulting in 3-D aggregates (Figs. 3S.9a4-6). A similar scenario is observed when less seed particles are used and fused platelets grow into large quasi-spherical structures (Fig. 3S.8).

⁵¹ Murshid, N., Keogh, D. & Kitaev, V. Optimized synthetic protocols for preparation of versatile plasmonic platform based on silver nanoparticles with pentagonal symmetries. *Part. Part. Syst. Charact.*, **31**, 178–189 (2014).

⁵² Lu, L., Kobayashi, A., Tawa, K. & Ozaki, Y. Silver nanoplates with special shapes: controlled synthesis and their surface plasmon resonance and surface-enhanced Raman scattering properties. *Chem. Mater.*, **18**, 4894–4901 (2006).

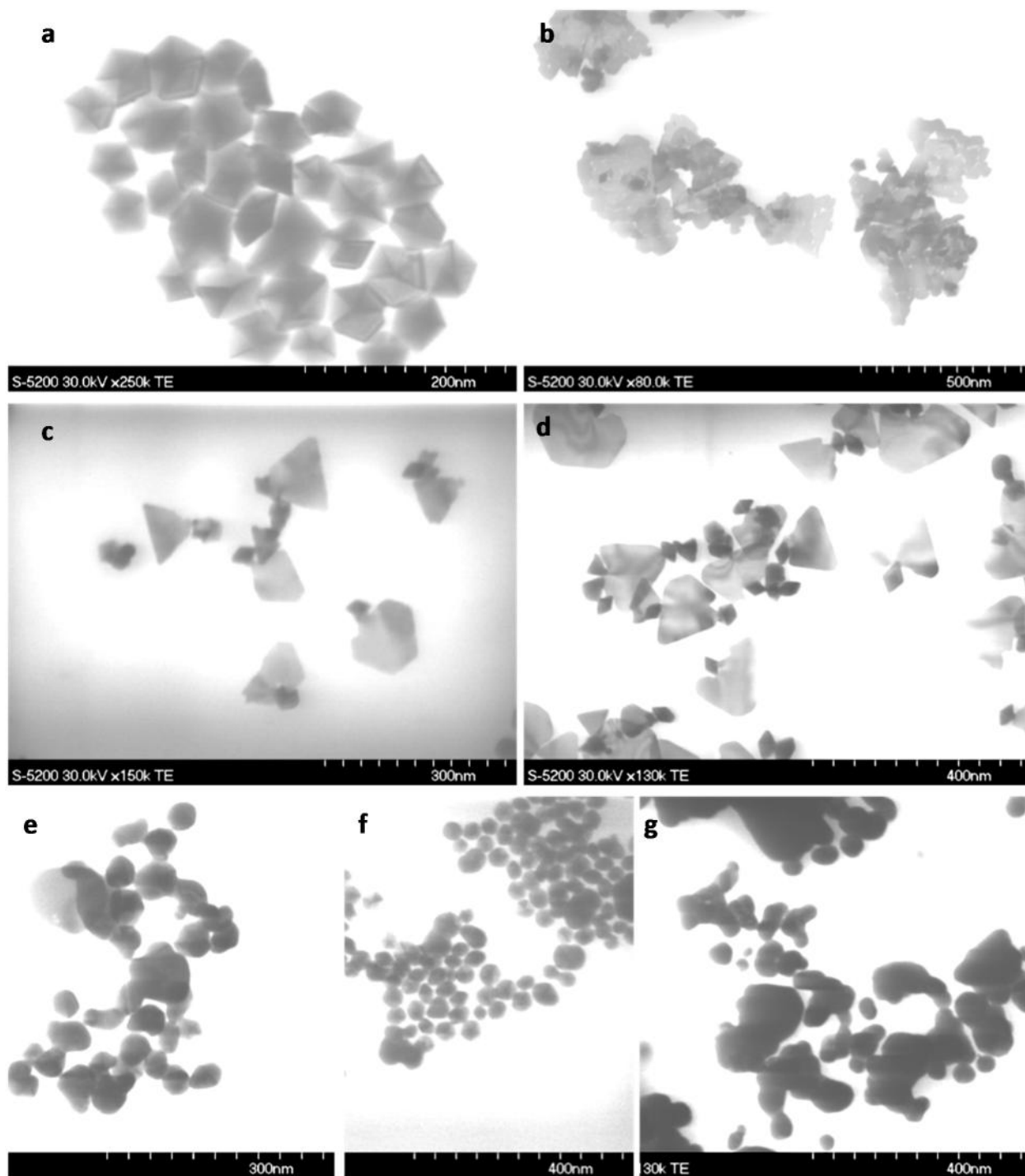


Figure 3S.10. TEM images of bi-AgNP samples prepared at different pH: a) 5, b) 5.5, c) 6, d) 6.5, e) 7, f) 7.5 and g) 8.

In experiments with pH variation, the best bi-AgNPs are produced in a fairly narrow pH range of 6.0 to 6.5 (Fig. 3S.10). At more acidic pH, AgNPs are expectedly etched, destabilized and aggregated. At higher pH, it is likely that PAA becomes fully deionized and blocks the surface more effectively that results

in more disturbed growth of bimorphic structures (Fig. 3S.10). In addition, the higher reduction potential of ascorbate at higher pH may play a significant interfering role. At the same time, the effect of pH on the AA reduction potential can be potentially counteracted or fine-tuned by adjusting the concentration of ascorbic acid.

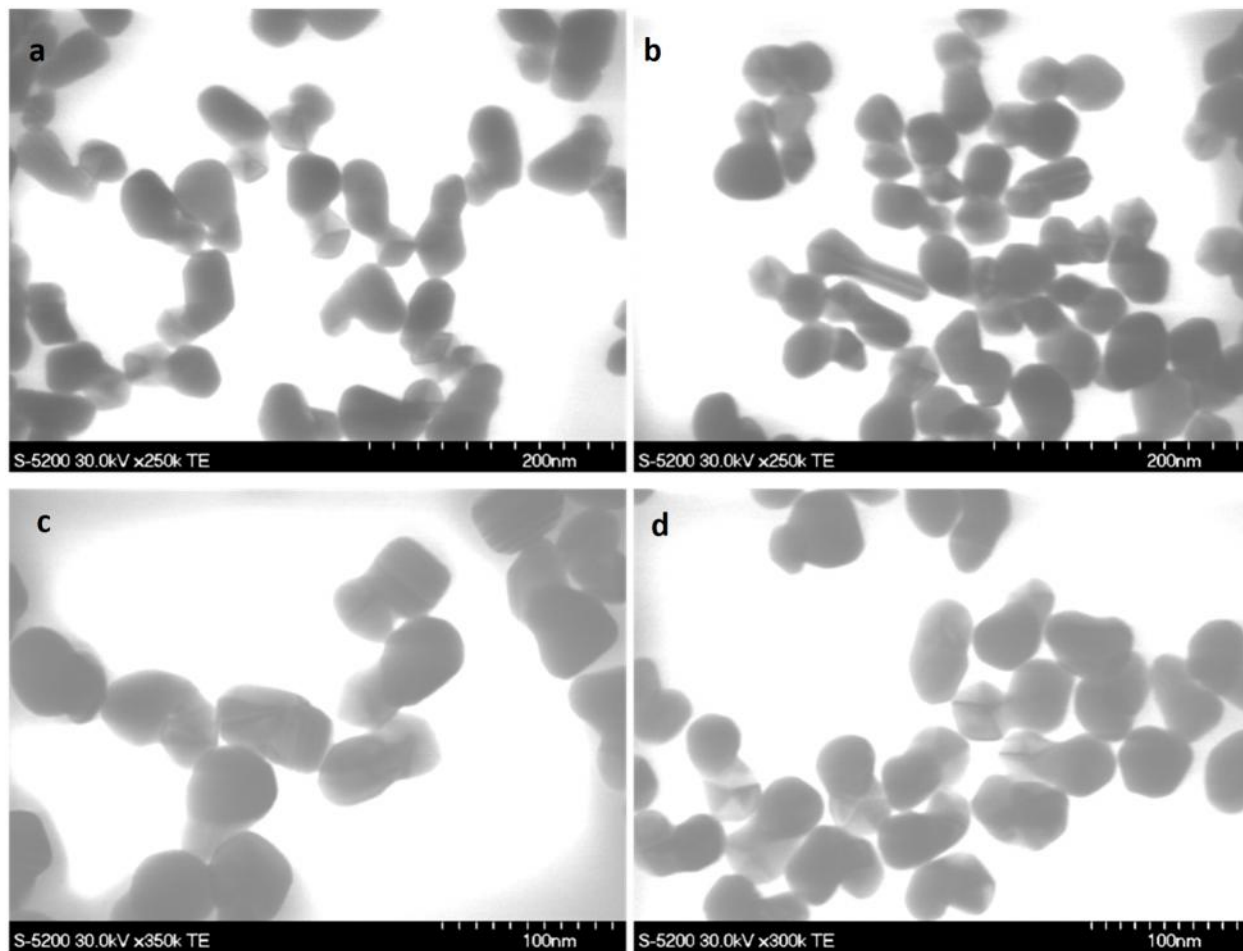


Figure 3S.11. TEM images of bi-AgNP samples prepared using potassium bromide with Ag/Br molar ratio of a) 138:1, b) 25:1, c) 12:1 and d) 6:1.

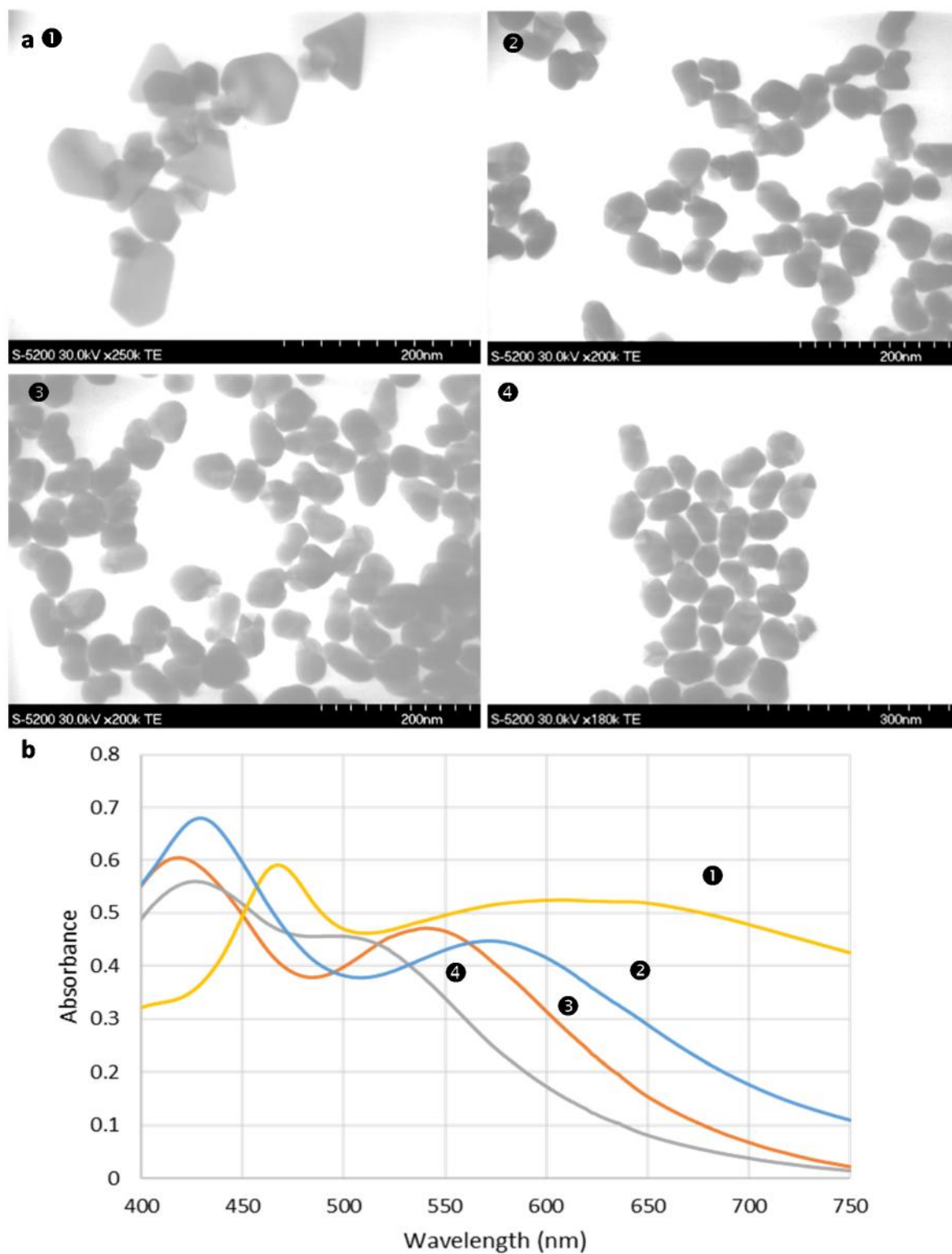


Figure 3S.12. Development of 3-D bi-AgNPs morphologies with different amounts of bromide. **a)** Representative TEM images; and **b)** UV-vis spectra of samples with Ag/Br molar ratio of: **①** 750, **②** 75, **③** 23, **④** 7.5.

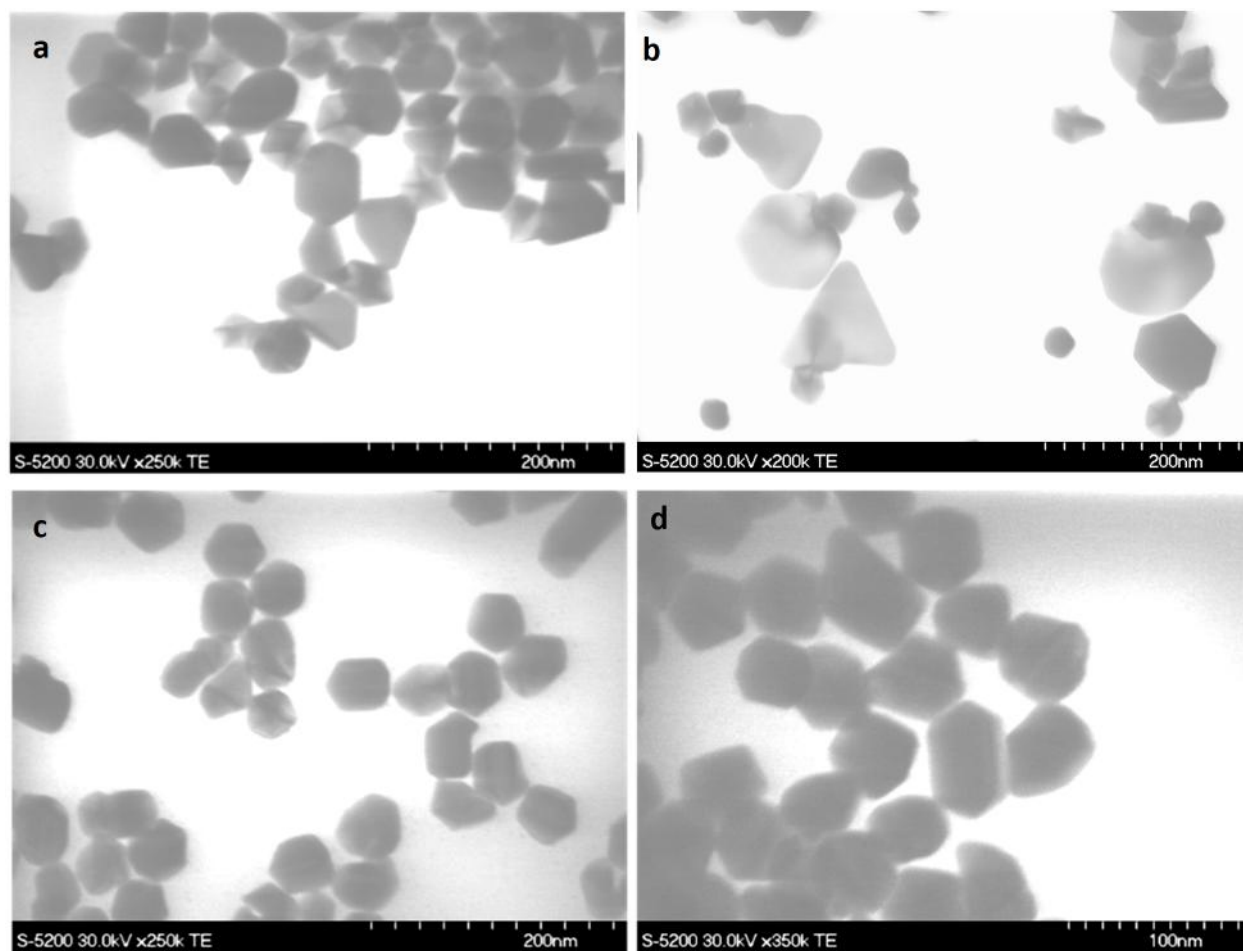


Figure 3S.13. TEM images of bi-AgNP samples prepared using potassium chloride with Ag/Cl molar ratio of a) 16:1, b) 8:1, c) 1:6 and d) 1:12.

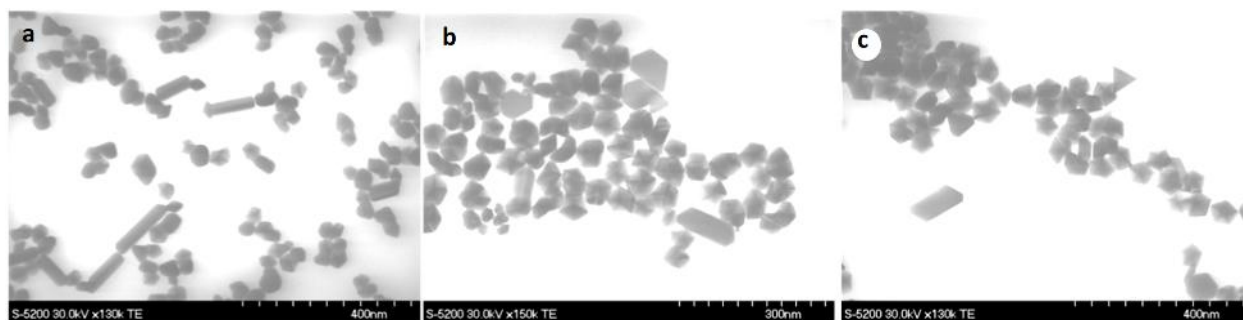


Figure 3S.14. TEM images of bi-AgNP samples prepared using HCl with Ag/Cl molar ratio of a) 1:2, b) 1:4 and c) 1:8.

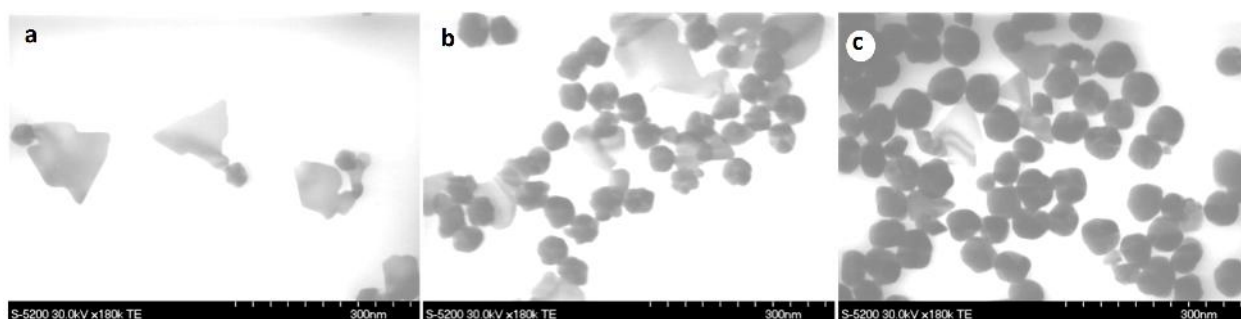


Figure 3S.15. TEM images of bi-AgNP samples prepared using KI with Ag/I molar ratio of **a)** 312:1, **b)** 138:1 and **c)** 6:1.

Iodide interferes with the development of bi-AgNPs even at very low iodide concentrations (sub- μM) corresponding to Ag/I ratio of 312 to 1 (Fig 3S.15a), where rounding of the decahedral seed is observed in addition to the more disturbed growth of the platelet part (Figs. 3S.15b,c). Such effect of iodide is likely due to the fact that AgI does not have the same rock salt structure as AgCl and AgBr, which stabilizes (100) planes. At the same time, K_{sp} of AgI is the lowest of the halides, so the strongest iodide binding is very disruptive for the bi-AgNP regrowth.

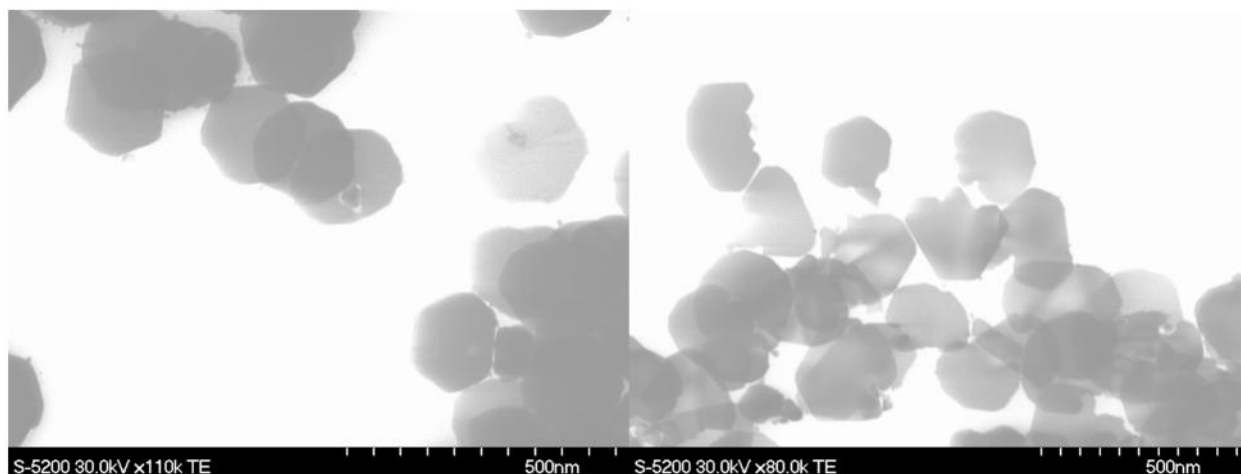


Figure 3S.16. TEM images of bi-AgNPs prepared using silver platelets/prisms as seeds instead of AgDeNPs.

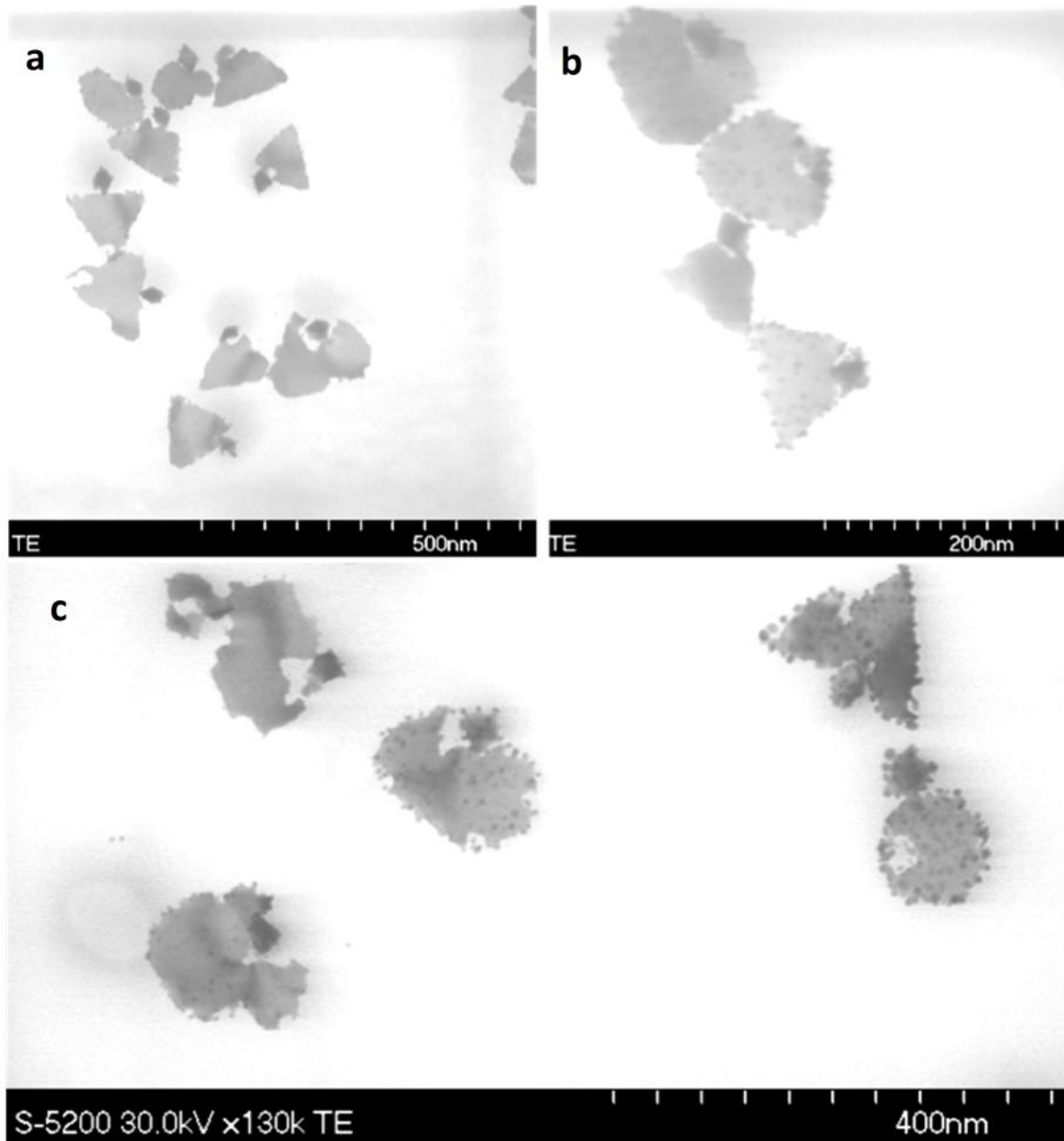


Figure 3S.17. TEM images of bi-AgNP samples that underwent galvanic replacement with tetrachloroauric acid: a), b) 5 mol.%; and c) 20 mol.% of gold relative to silver in bi-AgNPs.

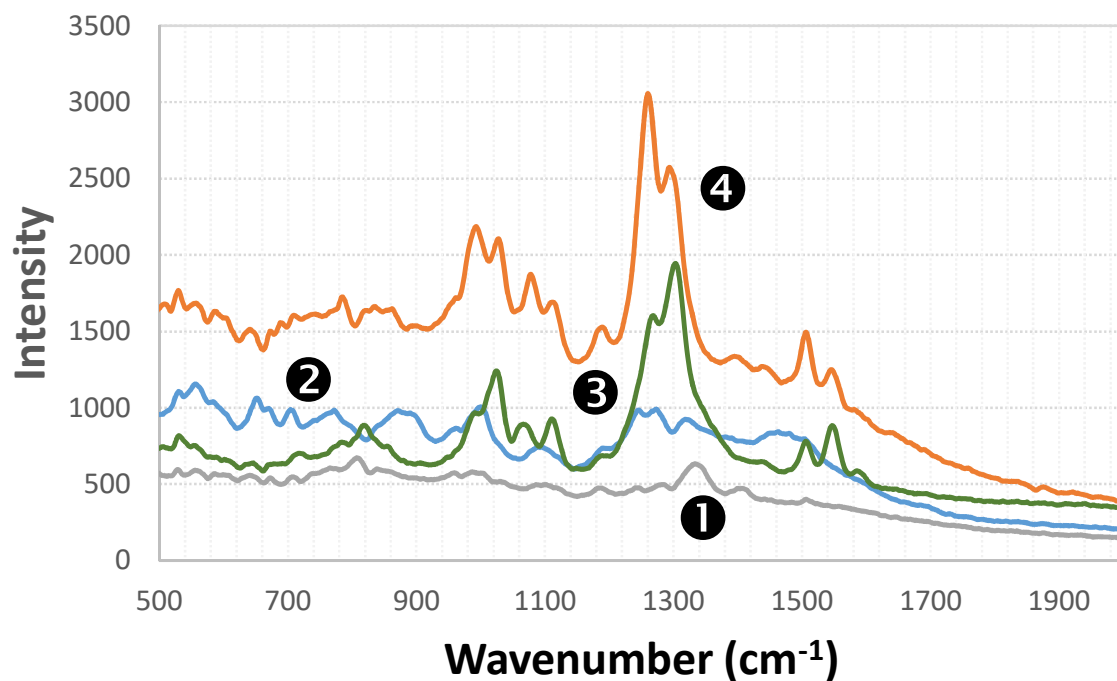


Figure 3S.18. Raman spectra of **1** bi-AgNP dry layer; **2** dry layer of decahedral AgNPs; **3** 1×10^{-16} mol/cm² of 5'5-dithiobis(2-nitrobenzoic acid) (DTNB) over the layer of dry bi-AgNPs; and **4** 2×10^{-16} mol/cm² of DTNB over the layer of dry decahedral AgNPs.

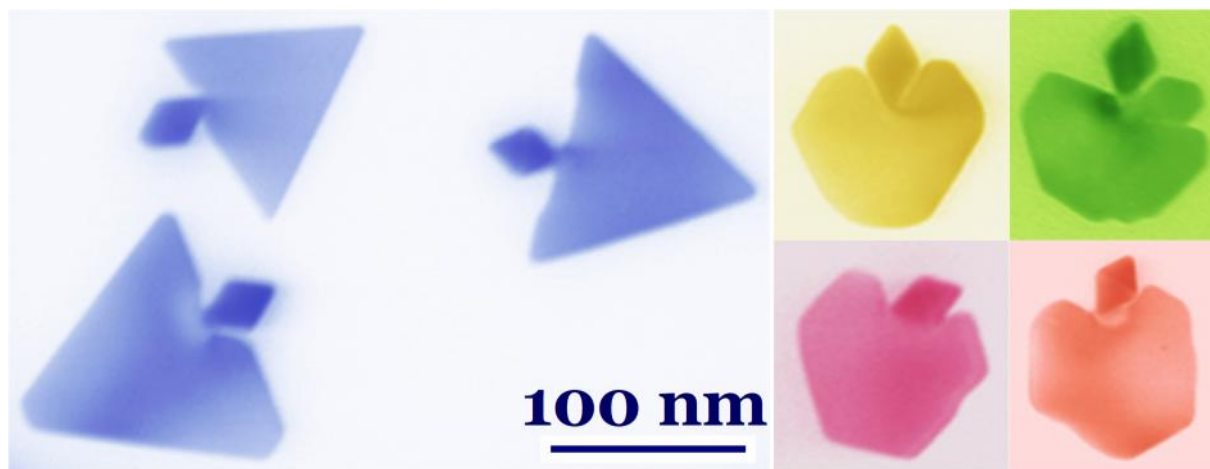


Figure 3S.19. Coloured TEM images of bi-AgNPs resembling fish and apples.

The procedure was discovered and developed by me with the assistance of V. Kitaev. My role was primarily experimental, preparation of the first draft of the manuscript, figures, and iterative refining. Images were taken by V. Kitaev.

3.7. References

- (1) Baffou, G.; Quidant, R. Nanoplasmonics for Chemistry. *Chem. Soc. Rev.* **2014**, *43*, 3898–3907.
- (2) Tame, M. S.; McEnery, K. R.; Özdemir, Ş. K.; Lee, J.; Maier, S. A.; Kim, M. S. Quantum Plasmonics. *Nat. Phys.* **2013**, *9*, 329–340.
- (3) Linic, S.; Aslam, U.; Boerigter, C.; Morabito, M. Photochemical Transformations on Plasmonic Metal Nanoparticles. *Nat. Mater.* **2015**, *14*, 567–576.
- (4) Cheng, H.; Fuku, K.; Kuwahara, Y.; Mori, K.; Yamashita, H. Harnessing Single-Active Plasmonic Nanostructures for Enhanced Photocatalysis under Visible Light. *J. Mater. Chem. A* **2015**, *3*, 5244–5258.
- (5) Giljohann, D. A.; Seferos, D. S.; Daniel, W. L.; Massich, M. D.; Patel, P. C.; Mirkin, C. A. Gold Nanoparticles for Biology and Medicine. *Angew. Chemie Int. Ed.* **2010**, *49*, 3280–3294.
- (6) Langer, J.; Novikov, S. M.; Liz-Marzán, L. M. Sensing Using Plasmonic Nanostructures and Nanoparticles. *Nanotechnology* **2015**, *26*, 322001.
- (7) Yang, X.; Yang, M.; Pang, B.; Vara, M.; Xia, Y. Gold Nanomaterials at Work in Biomedicine. *Chem. Rev.* **2015**, *115*, 10410–10488.
- (8) Chinen, A. B.; Guan, C. M.; Ferrer, J. R.; Barnaby, S. N.; Merkel, T. J.; Mirkin, C. A. Nanoparticle Probes for the Detection of Cancer Biomarkers, Cells, and Tissues by Fluorescence. *Chem. Rev.* **2015**, *115*, 10530–10574.
- (9) Burda, C.; Chen, X.; Narayanan, R.; El-Sayed, M. A. Chemistry and Properties of Nanocrystals of Different Shapes. *Chem. Rev.* **2005**, *105*, 1025–1102.
- (10) Kusada, K.; Kitagawa, H. A Route for Phase Control in Metal Nanoparticles: A Potential Strategy to Create Advanced Materials. *Adv. Mater.* **2016**, *28*, 1129–1142.
- (11) Motl, N. E.; Smith, A. F.; DeSantis, C. J.; Skrabalak, S. E. Engineering Plasmonic Metal Colloids through Composition and Structural Design. *Chem. Soc. Rev.* **2014**, *43*, 3823–3834.
- (12) Xia, Y.; Xia, X.; Peng, H.-C. Shape-Controlled Synthesis of Colloidal Metal Nanocrystals: Thermodynamic versus Kinetic Products. *J. Am. Chem. Soc.* **2015**, *137*, 7947–7966.
- (13) Niu, W.; Lu, X. *Metallic Nanostructures: From Controlled Synthesis to Applications*; Springer International Publishing: New York, **2015**.
- (14) Weiner, R. G.; Kunz, M. R.; Skrabalak, S. E. Seeding a New Kind of Garden: Synthesis of Architecturally Defined Multimetallic Nanostructures by Seed-Mediated Co-Reduction. *Acc. Chem. Res.* **2015**, *48*, 2688–2695.
- (15) Liz-Marzán, L. M. Increasing Complexity While Maintaining a High Degree of Symmetry in Nanocrystal Growth. *Angew. Chemie Int. Ed.* **2015**, *54*, 3860–3861.

- (16) Gao, C.; Goebel, J.; Yin, Y. Seeded Growth Route to Noble Metal Nanostructures. *J. Mater. Chem. C* **2013**, *1*, 3898–3909.
- (17) Ling, D.; Hackett, M. J.; Hyeon, T. Surface Ligands in Synthesis, Modification, Assembly and Biomedical Applications of Nanoparticles. *Nano Today* **2014**, *9*, 457–477.
- (18) Huang, M. H.; Rej, S.; Hsu, S. C. Facet-Dependent Properties of Polyhedral Nanocrystals. *Chem. Commun.* **2014**, *50*, 1634–1644.
- (19) Millstone, J. E.; Wei, W.; Jones, M. R.; Yoo, H.; Mirkin, C. A. Iodide Ions Control Seed-Mediated Growth of Anisotropic Gold Nanoparticles. *Nano Lett.* **2008**, *8*, 2526–2529.
- (20) Lohse, S. E.; Burrows, N. D.; Scarabelli, L.; Liz-Marzán, L. M.; Murphy, C. J. Anisotropic Noble Metal Nanocrystal Growth: The Role of Halides. *Chem. Mater.* **2014**, *26*, 34–43.
- (21) Cathcart, N.; Kitaev, V. Multifaceted Prismatic Silver Nanoparticles: Synthesis by Chloride-Directed Selective Growth from Thiolate-Protected Clusters and SERS Properties. *Nanoscale* **2012**, *4*, 6981–6989.
- (22) Viswanath, B.; Kundu, P.; Halder, A.; Ravishankar, N. Mechanistic Aspects of Shape Selection and Symmetry Breaking during Nanostructure Growth by Wet Chemical Methods. *J. Phys. Chem. C* **2009**, *113*, 16866–16883.
- (23) Xia, X.; Xia, Y. Symmetry Breaking during Seeded Growth of Nanocrystals. *Nano Lett.* **2012**, *12*, 6038–6042.
- (24) Gilroy, K. D.; Hughes, R. A.; Neretina, S. Kinetically Controlled Nucleation of Silver on Surfactant-Free Gold Seeds. *J. Am. Chem. Soc.* **2014**, *136*, 15337–15345.
- (25) Wang, Z.; Chen, Z.; Zhang, H.; Zhang, Z.; Wu, H.; Jin, M.; Wu, C.; Yang, D.; Yin, Y. Lattice-Mismatch-Induced Twinning for Seeded Growth of Anisotropic Nanostructures. *ACS Nano* **2015**, *9*, 3307–3313.
- (26) Habas, S. E.; Lee, H.; Radmilovic, V.; Somorjai, G. A.; Yang, P. Shaping Binary Metal Nanocrystals through Epitaxial Seeded Growth. *Nat. Mater.* **2007**, *6*, 692–697.
- (27) Tsuji, M.; Tang, X.; Matsunaga, M.; Maeda, Y.; Watanabe, M. Shape Evolution of Flag Types of Silver Nanostructures from Nanorod Seeds in PVP-Assisted DMF Solution. *Cryst. Growth Des.* **2010**, *10*, 5238–5243.
- (28) Nie, Z.; Zhang, P.; Gong, J.; Hood, T. C.; He, J.; Liu, Y. Asymmetric Organic/Metal(Oxide) Hybrid Nanoparticles: Synthesis and Applications. *Nanoscale* **2013**, *5*, 5151–5166.
- (29) Pang, X.; Wan, C.; Wang, M.; Lin, Z. Strictly Biphasic Soft and Hard Janus Structures: Synthesis, Properties, and Applications. *Angew. Chemie Int. Ed.* **2014**, *53*, 5524–5538.
- (30) Ye, E.; Regulacio, M. D.; Zhang, S.-Y.; Loh, X. J.; Han, M.-Y. Anisotropically Branched Metal Nanostructures. *Chem. Soc. Rev.* **2015**, *44*, 6001–6017.
- (31) Pietrobon, B.; Kitaev, V. Photochemical Synthesis of Monodisperse Size-Controlled Silver Decahedral Nanoparticles and Their Remarkable Optical Properties. *Chem. Mater.* **2008**, *20*, 5186–5190.
- (32) Murshid, N.; Keogh, D.; Kitaev, V. Optimized Synthetic Protocols for Preparation of Versatile Plasmonic Platform Based on Silver Nanoparticles with Pentagonal Symmetries. *Part. Part. Syst. Charact.* **2014**, *31*, 178–189.

- (33) Chen, S.; Carroll, D. L. Silver Nanoplates: Size Control in Two Dimensions and Formation Mechanisms. *J. Phys. Chem. B* **2004**, *108*, 5500–5506.
- (34) Lu, L.; Kobayashi, A.; Tawa, K.; Ozaki, Y. Silver Nanoplates with Special Shapes: Controlled Synthesis and Their Surface Plasmon Resonance and Surface-Enhanced Raman Scattering Properties. *Chem. Mater.* **2006**, *18*, 4894–4901.
- (35) Wang, Y.; Peng, H.-C.; Liu, J.; Huang, C. Z.; Xia, Y. Use of Reduction Rate as a Quantitative Knob for Controlling the Twin Structure and Shape of Palladium Nanocrystals. *Nano Lett.* **2015**, *15*, 1445–1450.
- (36) Nishimura, S.; Mott, D.; Takagaki, A.; Maenosono, S.; Ebitani, K. Role of Base in the Formation of Silver Nanoparticles Synthesized Using Sodium Acrylate as a Dual Reducing and Encapsulating Agent. *Phys. Chem. Chem. Phys.* **2011**, *13*, 9335–9343.
- (37) Métraux, G. S.; Mirkin, C. A. Rapid Thermal Synthesis of Silver Nanoprisms with Chemically Tailorable Thickness. *Adv. Mater.* **2005**, *17*, 412–415.
- (38) Cathcart, N.; Frank, A. J.; Kitaev, V. Silver Nanoparticles with Planar Twinned Defects: Effect of Halides for Precise Tuning of Plasmon Resonance Maxima from 400 to 900 nm. *Chem. Commun.* **2009**, *6*, 7170–7172.
- (39) Tani, T. *Silver Nanoparticles: From Silver Halide Photography to Plasmonics Tadaaki Tani*; Oxford University Press, Oxford, **2015**.
- (40) Almora-Barrios, N.; Novell-Leruth, G.; Whiting, P.; Liz-Marzán, L. M.; López, N. Theoretical Description of the Role of Halides, Silver, and Surfactants on the Structure of Gold Nanorods. *Nano Lett.* **2014**, *14*, 871–875.
- (41) Pietrobon, B.; McEachran, M.; Kitaev, V. Synthesis of Size-Controlled Faceted Pentagonal Silver Nanorods with Tunable Plasmonic Properties and Self-Assembly of These Nanorods. *ACS Nano* **2009**, *3*, 21–26.
- (42) Au, L.; Lu, X.; Xia, Y. A Comparative Study of Galvanic Replacement Reactions Involving Ag Nanocubes and AuCl_2^- or AuCl_4^- . *Adv. Mater.* **2008**, *20*, 2517–2522.
- (43) Lu, X.; Tuan, H.-Y.; Chen, J.; Li, Z.-Y.; Korgel, B. A.; Xia, Y. Mechanistic Studies on the Galvanic Replacement Reaction between Multiply Twinned Particles of Ag and HAuCl_4 in an Organic Medium. *J. Am. Chem. Soc.* **2007**, *129*, 1733–1742.
- (44) Weng, L.; Zhang, H.; Govorov, A. O.; Ouyang, M. Hierarchical Synthesis of Non-Centrosymmetric Hybrid Nanostructures and Enabled Plasmon-Driven Photocatalysis. *Nat. Commun.* **2014**, *5*, 4792.

Chapter 4: Synthesis and Sensing Properties of D_{5h} Pentagonal Silver Star Nanoparticles

The following publication details the synthesis of D_{5h} pentagonal silver star nanoparticles by blocking the surface of a seed nanoparticle with a protective polymer. The resulting nanoparticles were then tested in sensing applications surface plasmon resonance, and surface enhanced Raman spectroscopy. The following is reproduced from N. Cathcart, N. Coombs, I. Gourevich, and V. Kitaev, *Nanoscale* 2016, 8 (43), 18282-18290 with permission from The Royal Society of Chemistry and is accessible online at: <https://pubs.rsc.org/en/Content/ArticleLanding/2016/NR/C6NR07397B>.

Supplementary figures are accessible online at:

<http://www.rsc.org/suppdata/c6/nr/c6nr07397b/c6nr07397b1.pdf>

Synthesis and Sensing Properties of D_{5h} Pentagonal Silver Star Nanoparticles

By Nicole Cathcart, Neil Coombs,²¹ Ilya Gourevich,²¹ and Vladimir Kitaev.

4.1 Abstract

In this work, we use silver decahedral nanoparticle (AgDeNP) seeds to synthesize pentagonal silver stars (AgStDeNPs) and study sensing properties of these nanoparticles. The regrowth process of AgStDeNPs is kinetically-controlled, so the purity of the seed NPs is critical to avoid secondary deposition in highly non-equilibrium reduction. To control the regrowth process, surface blocking with sodium polyacrylate (PANA) was implemented. PANA moderates rough silver nanostructures typically obtained by reduction with ascorbic acid. To modulate polymer binding to the surface and thus to tune surface blocking, pH served as a key synthetic parameter. In optimal regrowth conditions, new silver was deposited on the highest energy sites of the decahedra – the vertices of the rims – to yield pentagonal

²¹ Centre for Nanostructure Imaging, Department of Chemistry, University of Toronto, 80 St. George St. Rm. 50, Toronto M5S 3H6

stars. The universality of this regrowth process was established with several different seed particles. The sharpness and size of the stellated tips is tuneable by the amount of added silver. Gold deposition onto AgStDeNPs enables the preparation of diverse structures with enhanced stability. Ease of transformation, e.g. rounding, of star branches opens a promising venue for enhanced SPR sensing. As well, AgStDeNPs enables femtomolar detection of 5,5-dithiobis(2-nitro-benzoic acid) in SERS.

4.2 Introduction

Nanoparticle design is shaping advances in nanoscale synthesis, in particular of metal nanoparticles (MNPs).^{1,2} MNPs have established importance in applications including plasmonics,^{3,4} catalysis,⁵⁻⁷ sensing^{8,9} and medicine.¹⁰ Silver is the most conductive and reflective of noble metals, therefore silver nanoparticles (AgNPs) offer superior properties in optical and plasmonic applications.¹¹ Silver is also versatile with respect to chemical reactivity and offers great morphological variability.^{12,13} Size- and shape- control are essential to realize functional properties of nanoscale structures,^{14,15} and the understanding of synthesis conditions to achieve such control has improved in recent years.^{16,17} Limitations in reproducible procedures are short-cutting the development and applications of diverse, well-defined MNP morphologies. Seeded regrowth is one of the reliable strategies for the preparation of MNPs with increasing complexity and therefore novel properties and new potential applications.^{18,19} In general, seeded regrowth approaches focus on reduction control of the new (added) metal; through either the ratio of seed to metal salt,^{18,20} complexation with ligands or the strength of the reducing agent.²¹ Seed nanoparticles (NPs) act as nucleation centres and catalysts; higher ratios of seed to new metal promote quicker reduction,²⁰ and enables the utilization of weak reducing agents.²² To retain the low size dispersity of the seeds, and minimize size dispersity in the resulting NPs, preventing nucleation events is required, which can be accomplished by slow addition of the metal precursor or by using ligands for complexation and selective binding.^{21,23} Lui et al., demonstrated the use of acetonitrile as an efficient ligand for silver ions to decrease the silver reduction potential and to slow down reaction kinetics,

minimizing secondary nucleation.²⁰ Surface binding species have also been shown to be effective to control NP growth in preferential directions²⁴ through selective adsorption (surface blocking).^{21,25} Our group previously reported on the use of chloride for the selective growth of flower-shaped multifaceted prismatic silver nanoparticles.²⁶ Polymers have also been shown to be effective in the shape control of NPs.^{27,28} Specifically, poly vinylpyrrolidone (PVP) has been shown to stabilize higher index planes in Au concave decahedra,²⁹ establishing polymer blocking for the preparation of complex multifaceted and stellated NP structures.

Control over NP growth can be achieved by varying reduction conditions, either through reducing agent strength or concentration of reductants.³⁰ Common reducing agents for silver include citrate,³¹ borohydride,³² and ascorbic acid.³³ Ascorbic acid readily reduces silver ions to metallic silver and oxidizes to dehydroascorbic acid.³⁴ The kinetics of silver reduction with ascorbic acid was reported in 1974 by Mushran et al,³³ with the increased rate of reduction observed for higher pH, which is consistent with the pH-dependence of the reduction potential of ascorbic acid. In several studies, the rapid reduction with ascorbic acid was demonstrated to lead to the development of highly branched silver structures.^{35–37} For example, Fukuyo and Imai, were able to vary the stellation of silver crystals by varying the concentration of ascorbic acid and the solution pH (and therefore ascorbic acid reducing power).³⁵

Branched and multifaceted MNP morphologies are advantageous for surface plasmon resonance (SPR) sensing, where stellation enhances sensitivity.⁹ Furthermore, sharper features and cavities offer better sensing in surface enhanced Raman spectroscopy (SERS).²⁶ The strongest electromagnetic field, and therefore enhancement, has been experimentally observed, and theoretically confirmed in the gap between several NPs,^{38,39} and in the vicinity of sharp tips.^{40,41} Recently, high enhancement factors of 3.78×10^8 from silver nanoparticle rings with controllable openings⁴² and 1.0×10^9 from bimorphic Ag-Au 'mushroom' nanoparticles⁴³ were reported owing to the inherent gaps of the structures. As well, our group has reported 4.6×10^8 enhancement from flower-shaped platelet AgNPs with variable faceting.²⁶

Herein we describe the synthesis of pentagonal silver star nanoparticles (AgStDeNPs) using a seeded regrowth approach with ascorbate reduction and polymer surface blocking. Ascorbate allows for the rapid generation of star branches from silver decahedral seed particles (AgDeNPs) and sodium polyacrylate enables effective blocking of the surface of AgDeNP seeds for directed growth at high energy vertices. Well-defined stellation and the universality of the regrowth procedure were demonstrated. Sensing properties of AgStDeNPs in SERS and SPR experiments are presented and discussed.

4.3 Experimental

Reagents. Silver nitrate (99.9%), sodium citrate tribasic dihydrate (99.5%), arginine (98%), sodium borohydride ($\geq 99\%$), hydrogen peroxide (30-32 wt.%, 99.999% trace metal basis, potassium stannate inhibitor), poly (acrylic acid sodium salt) (PANA, avg. $M_w = 5,100$), poly (sodium 4-styrenesulfonate) (PSS, avg. $M_w = 70,000$), L-ascorbic acid, (99+%), 5,5'-dithiobis (2-nitro-benzoic acid) (99%), potassium chloride (99%), potassium bromide (99%), potassium iodide (99%), potassium hydroxide (99.99%), nitric acid (65 wt.%, ACS grade), hydrochloric acid (37 wt.%, semiconductor grade), all supplied by Aldrich; and poly (N-vinylpyrrolidone) (PVP, avg. $M_w = 40,000$) supplied by Caledon Chemicals (Caledon, Canada) were used as received. High purity deionized water ($> 18.2 \text{ M}\Omega\text{-cm}$) was produced using Millipore A10 Milli-Q.

Synthesis of pentagonal silver star nanoparticles. Decahedral particles used as seeds were prepared according to the procedure developed previously by our group.⁴⁴ Briefly, citrate, arginine, PVP, silver nitrate and sodium borohydride were mixed to form a precursor solution. Subsequently, hydrogen peroxide was added, and the resulting mixture was exposed to 450 nm LEDs for 14 hours.

Decahedral AgNP seeds prepared 2-20 days prior to the regrowth were first concentrated 10 times (from 0.13 mM to 1.3 mM Ag) by centrifuging 16 ml of as prepared AgDeNP sample at 3800 g for 30 minutes, removing the supernatant, and diluting the sedimented particles to 1.6 mL. The concentrated seed AgDeNPs were used within the same day due to their limited colloidal stability at higher

concentrations. Ascorbate was prepared by combining ascorbic acid and potassium hydroxide in a 1:1 ratio; ascorbate solutions were used within a day in order to limit their oxidation.

In a 20 mL vial, 6 mL of water was combined with potassium hydroxide, sodium polyacrylate (PANa), 200 μ L of the concentrated decahedral seeds (1/8th of the sample described above), and silver nitrate. Ascorbate was added to the intensely stirred solution (500 rpm with a 3 mm by 12.7 mm magnetic stir bar) by quick injection with a pipette (under 1 s). Amounts and total molarities (in brackets) in the final preparation of well-defined AgStDeNPs (e.g. shown in Figs. 4.4[Ⓢ] and 5[Ⓢ]) were as follows: 6 mL of water, 40 μ L of 0.1 M KOH (0.61 mM), 120 μ L 0.02 M PANa 5.1 K (0.37 mM), 200 μ L of concentrated centrifuged decahedra with 1.3 mM of silver (0.04 mM), 100 μ L of 0.005 M AgNO₃ (0.08 mM), and 120 μ L of 0.05 M ascorbate (0.91 mM). Upon addition of ascorbate, the solution changed in colour from yellow through bicoloured pink and green to purple representative of the stellated growth. See Table 4.1 for specific conditions that were used to produce AgStDeNPs with varying degrees of stellation. Particle size and size distribution were calculated from electron microscopy images by measuring >1000 particles.

Universality of the procedure experiments were further established by replacing decahedra with silver pentagonal rod, platelets and icosahedra AgNPs as seeds. Pentagonal rods were prepared according to the procedure developed previously by our group.⁴⁵ Briefly, decahedra were heated in the presence of citrate and silver which elongated the pentagonal bipyramids along their five-fold axis. Platelets were prepared as previously reported by our group,³² where silver nitrate is reduced by sodium borohydride in the presence of citrate and hydrogen peroxide. Icosahedra were prepared by reducing silver nitrate by sodium borohydride in the presence of citrate, PVP, copper sulfate, and hydrogen peroxide and then exposing to 409 nm LEDs for 14 hours.⁴⁶

The prepared alternative seeds were centrifuged similar to decahedra, as described above, and used as direct replacement for decahedra in the procedure (all reagents and concentrations remained the same). In the case with stellated rods, upon the addition of ascorbate, the solution (originally either blue

or green for rods of 60-100 nm in length) became murky from light scattering due to growing stellated structures. The development of stellation on platelets and icosahedra as seeds was accompanied by a colour change from blue to grey and yellow to orange, respectively.

Preparation of SERS substrates. SERS substrates were prepared by concentrating 1.5 mL of AgStDeNPs to 20-50 μL dispersions using centrifugation. The resulting total silver concentration in concentrated AgStDeNP samples was 10-20 mM. 20 μL of this concentrated dispersion was transferred onto a quartz slide by a pipette and spread to an area of 0.5 cm by 0.3 cm. The quartz slide with AgStDeNPs was dried in an oven at 55-60 $^{\circ}\text{C}$ for 5-10 minutes, and then used for SERS measurement without further treatment. 10 μL of dilute 5,5'-dithiobis(2-nitrobenzoic acid) in water (with addition of THF at higher concentrations) was dispensed directly onto the dried AgStDeNPs uniformly and then dried in an oven for 1-2 minutes. Measurements for pure 5,5'-dithiobis(2-nitrobenzoic acid) were performed by making a concentrated paste of 74 mg powder in 10 μL THF on a quartz slide, spreading to 1.8 cm^2 and drying in an oven for 10 minutes. Additional reference samples of 5,5'-dithiobis(2-nitrobenzoic acid) were prepared by making a solution of 4.5 mg in 20 μL THF (0.57 M), 10 μL of which was transferred onto a quartz slide by pipette and spread onto the quartz surface with an area of 1.2 cm by 0.9 cm. For SERS measurements in dispersions (liquid phase), as prepared AgStDeNPs were combined in a quartz half-cell with 5,5'-dithiobis(2-nitrobenzoic acid) dissolved in THF (usually 0.05 M). The measurement times were 300 s to detect weaker signals. The highest measurements for pure 5,5'-dithiobis(2-nitrobenzoic acid) (DTNB) were used to calculate enhancement factors.

Preparation of AgDeStNPs for imaging. 1.5 mL of the as prepared AgDeStNP solutions were centrifuged at 3500 g for 20 minutes, after which the supernatant was removed and discarded, and the pellet was dispersed in Milli-Q water to the initial volume. The dispersed AgDeStNPs were centrifuged for another 20 minutes at 3500 g, followed by supernatant removal. Approximately 0.1 μL of the remaining pellet of particles was dispensed onto a carbon-coated formvar grid and air-dried the day before imaging.

Instrumentation. Electron microscopy (EM) imaging in both SEM and TEM modes was performed using Hitachi S-5200 with a STEM detector and 30 kV accelerating voltage. Droplet of concentrated centrifuged dispersions were deposited on a carbon-coated formvar grid (EMS Corp.) and dried at ambient conditions. High-resolution electron microscopy images were made with JEOL JEM-2010 at 200 kV. UV-vis spectra were acquired with either an Ocean Optics QE-65000 fiber-optic UV-vis spectrometer or Cary 50Bio UV-vis spectrophotometer. Raman spectra were recorded using R-3000QE fibre-optic Raman spectrometer equipped with 290 mW laser at 785 nm (RSI) with integration times of 5-10 seconds for solid films and 100-300 seconds for solutions. Centrifugation was done using either VWR Clinical 200 or Thermo Scientific Legend Micro 21 centrifuges. SPR measurements were performed using an OpenSPR instrument by Nicoya Lifesciences (Waterloo, Ontario).

4.4. Results and Discussion

General aspects of AgStDeNP synthesis. The schematic of the formation of AgStDeNPs is shown in Figure 4.1. Here, high-purity silver decahedra (pentagonal bipyramids, J_{13}) are used as seeds for the growth of stellated silver morphologies with controllable localized surface plasmon resonance (LSPR) wavelength. The optimized procedure yielded AgStDeNPs with relatively low size dispersity (68 ± 9 nm). The rapid stellated growth takes place when the decahedral seed surface is blocked by sodium polyacrylate (PANA) and added silver is reduced by ascorbate. Representative scanning electron microscopy (SEM) images of decahedral seeds and developed stars are given in Figure 4S.1. Overall, two parameters can be used to control the reaction: 1) the growth of star tips from decahedra can be controlled synthetically by reducing conditions (ascorbate concentration and pH), and 2) the size and sharpness of the stellation can be mediated through a) the ratio of seed to new silver and b) the concentration of the surface blocking polymer (PANA).

The optimal growth pathway to symmetric stellated AgStDeNPs is summarized schematically in Figure 4.1A. As it has been described in our earlier reports,^{44,47} the expected, thermodynamically

favourable growth pathway is decahedra enlargement through uniform deposition of new silver on all ten (111) decahedra surface planes. AgStDeNP formation requires the rapid reduction of silver ions and their preferential deposition at the higher energy vertices of the decahedra. Importantly, the AgDeNP seeds must have high purity in order to prevent secondary nucleation. Attesting to the quality of the seeds, the formation of secondary seeds was not observed, even in minor quantities. In extreme growth conditions, the formation of pentapods takes place at low PANA concentrations and deviations from optimal reduction (Figure 4.1).

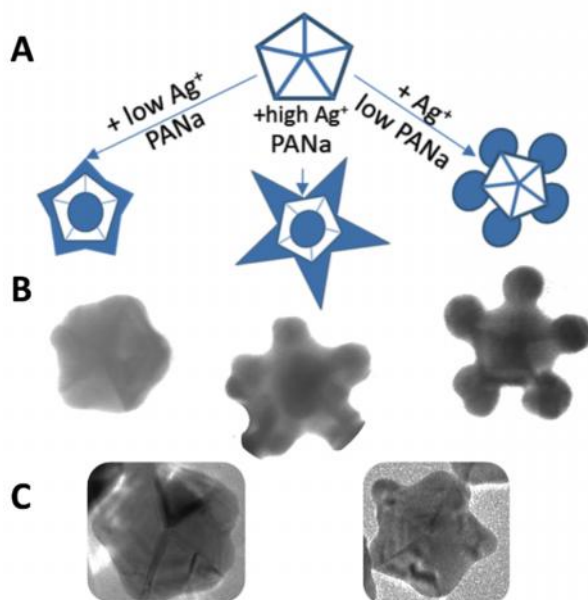


Figure 4.1. **A)** Schematic of the synthetic pathways, **B)** Transmission Electron Microscopy (TEM) images and **C)** HR-TEM images of representative AgStDeNPs with varying degrees of stellation controlled by reaction conditions. Lateral size of images is 60, 72 and 62.5 nm from left to right for **B** and 60 and 72 from left to right for **C**.

The localized surface plasmon resonance (LSPR) of AgStDeNPs can be controllably tuned from 490 to 690 nm by varying the degree of stellation and the size of AgStDeNPs, as shown in Figure 4.2. Larger stars, prepared by increasing the ratio of silver ions to silver in AgDeNP seeds have higher stellation, and larger LSPR wavelengths. The LSPR of AgStDeNPs can also be controlled by the concentration of PANA. With increasing PANA concentration the surface of AgDeNPs becomes appropriately blocked resulting in the predominant deposition onto higher energy vertices and higher stellation, as well as greater lateral

size of the stars (and therefore greater LSPR wavelength). Stellation at higher PANA concentrations is also less symmetric due to the higher driving force of the deposition onto the limited areas of the partially blocked surface. Further details of these conditions are summarized in Table 4.1 and described below.

Figure 4.3 presents high-resolution transmission electron microscopy images of AgStDeNPs.

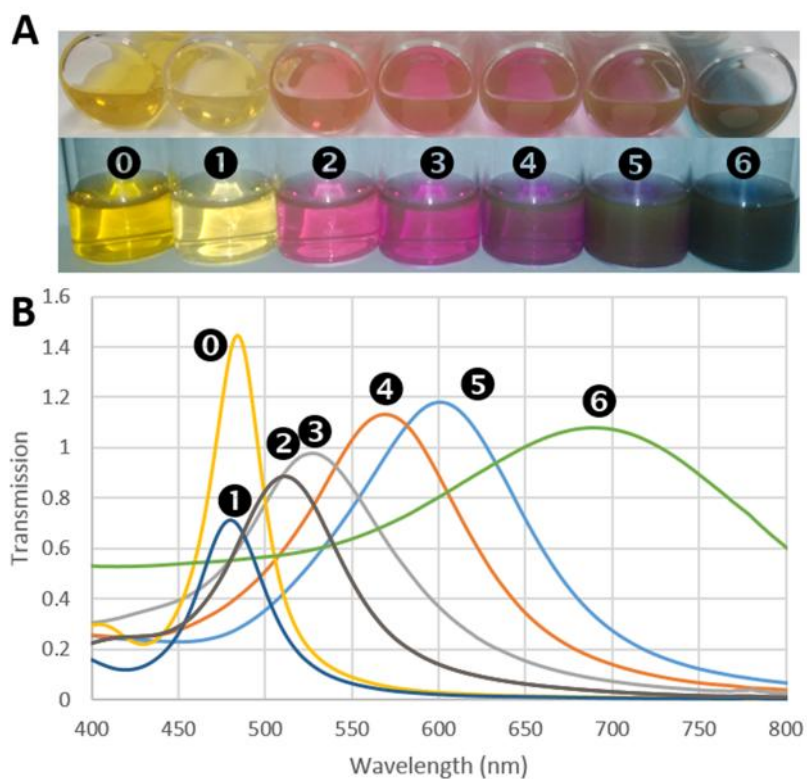


Figure 4.2. A) Optical photographs of the sample vials and B) UV-vis spectra of AgStDeNPs with LSPR maxima wavelengths varying from 490 nm to 690 nm. The spectrum of precursor AgDeNP seeds is labeled as ❶. Synthetic details for preparation of AgStDeNP samples are presented in Table 4.1.

Table 4.1. Summary of the reaction conditions for preparation of AgStDeNP samples described in Figure 4.2.

[PANA] (mM)	[KOH] (mM)	[AgDeNP seed] (mM Ag)	[AgNO ₃] (mM)	[Ascorbate] (mM)	λ_{\max} (nm)	Spectrum #
0.37	0.61	0.038	0.008	0.92	490	❶
0.37	0.61	0.038	0.038	0.92	515	❷
0.31	0.61	0.038	0.08	0.76	530	❸
0.18	0.61	0.038	0.08	0.92	570	❹
0.54	0.60	0.038	0.08	0.90	600	❺
0.37	0.61	0.038	0.15	0.90	690	❻

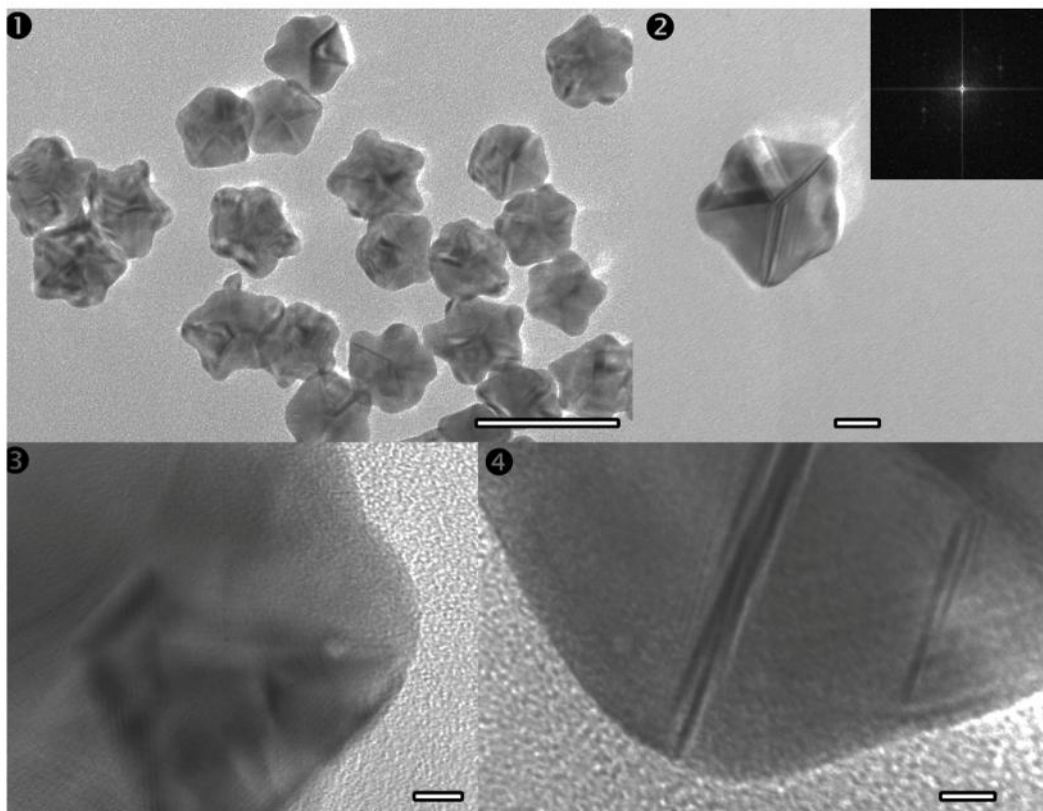


Figure 4.3. High resolution TEM images of AgStDeNPs with fast Fourier transform (FFT) image in the inset. Scale bars are 1) 100 nm, 2) 20 nm, 3 and 4) 5 nm.

4.4.1 Growth of Star Tips from Decahedra

Ascorbate reduction of silver was found to be the most important factor in the developed procedure of the formation of AgStDeNPs. As shown in Figure 4.4, samples prepared with low ascorbate concentrations (under ca. 0.35 mM) did not form stars due to the slower speed of silver reduction. Instead of formation of stellated structures, blob-like ill-defined structures or etched AgDeNP seeds became the main product (Figures 4.4A❶ and 4.4A❷). At ascorbate concentrations between 0.76 and 0.99 mM, the reduction of silver ions was rapid enough to generate AgStDeNPs with retained symmetry of the AgDeNP seeds (Figures 4.4A❸ and 4.4A❹). Higher concentrations of ascorbate resulted in greater variability of stellation and stability challenges due to the thermodynamically favourable rearrangement of silver to compact structures resulting in smaller, more rounded pentagonal stars upon aging (Figure 4.4A❺).

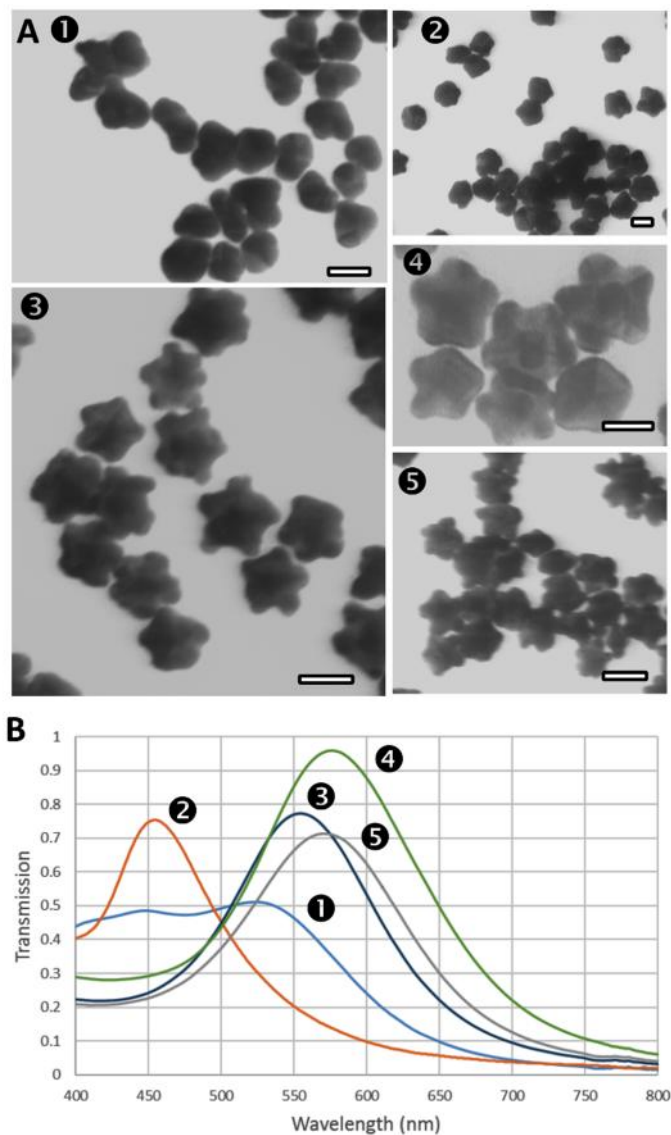


Figure 4.4 A) TEM images and B) UV-vis spectra of AgStDeNP samples prepared with varying ascorbate concentrations, ❶ – 0.08 mM, ❷ – 0.31 mM, ❸ – 0.76 mM, ❹ – 0.99 mM, and ❺ – 1.36 mM. The optimal concentration range of ascorbate is 0.76-0.99 mM (pH = 6 of the prepared samples). Concentrations of reagents not varied were as follows: KOH – 0.61 mM, PANa – 0.37 mM, silver in AgDeNP seeds – 0.038 mM, and AgNO₃ – 0.076 mM. All scale bars are 50 nm.

The reduction potential of ascorbate (and hence pH) is crucial for the growth of AgStDeNPs. Figure 4S.2 shows transmission electron microscopy (TEM) images of samples prepared at different pH. pH was varied by either adding HNO₃ or KOH to the sample solution prior to ascorbate addition (see Experimental for details on concentrations of reagents). The optimal pH for stellated growth is in the range of 5.6 to

6.3. For samples prepared at lower pH (Figure 4S.2②, pH = 5.3), platelet growth initiated from one of the vertices is the predominant growth pathway, which has been recently explored and reported by our group.⁴⁸ At even lower pH, the more thermodynamically favourable growth pathway of silver deposition onto all (111) decahedra facets to yield larger decahedra (Figure 4S.2①, pH = 4.3) dominates. For samples prepared at higher pH, the reduction rate is increased,³³ resulting in more irregular, higher stellation and less regular growth (Figures 4S.2③ and 4S.2④). Also important in the growth of AgStDeNPs is the stirring, and rate of ascorbate addition (described in the section on additional synthesis aspects below). Additionally, the ratio of silver ions to silver in AgDeNP seed (section 4.4.2.A.) and extent of the surface blocking by PANa (section 4.4.2.B.) were found to have a direct effect on the size and sharpness of stellation.

4.4.2 Size and Sharpness of Stellation

4.4.2.A By varying the concentration of AgDeNP seeds in the synthesis, the size and sharpness of stellation could be regulated directly, as shown in Figure 4.5. The optimal ratio of new silver to silver in AgDeNP seeds ($R_{\text{Ag}/\text{seed}}$) for the formation of regular well-defined AgStDeNPs was found to be between 130 % and 200 % (Figures 4.5A⑥ and 4.5A⑤, respectively). In the absence of seeds (Figure 4.5A①), dendritic growth of highly-branched AgNPs takes place, supporting the role of ascorbate in formation of stellated structures. By increasing $R_{\text{Ag}/\text{seed}}$, the degree of stellation decreases as there is less silver available relative to the seeds. Amounts of silver ions higher than the optimal ratio of 200% ($R_{\text{Ag}/\text{seed}}$) promote a symmetry-breaking pathway, resulting in highly branched, irregular and large particles (Figures 4.5A② - 4.5A④). Optically, these large dendritic particles feature noticeably higher LSPR wavelengths compared to AgStDeNPs that can be attributed to both their high degree of stellation and their increased size (Figure 4.5B② - 4.5B④). For lower added silver amounts, pentagonal symmetry is preserved, resulting in less stellated, rounded AgStDeNPs (Figures 4.5A⑦ and 4.5A⑧). The LSPR maxima of the regrown particles blue shift with increasing seed concentration, and decreasing stellation (Figure 4.5B). A similar trend is

observed upon varying $R_{Ag/seed}$ through the concentration of silver ions (Figure 4S.3). Larger amounts of added silver yield larger, more stellated AgStDeNPs, and vice versa. In addition to the $R_{Ag/seed}$ ratio, the stellation can be further mediated through the seed surface blocking.

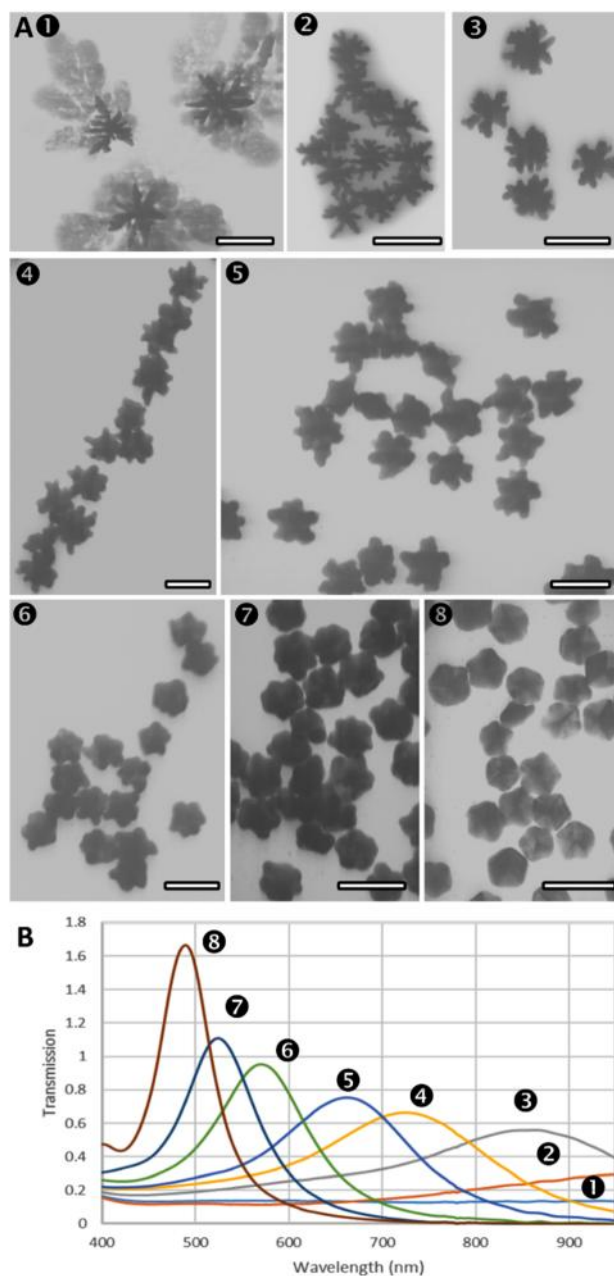


Figure 4.5. A) TEM images and B) UV-vis spectra of AgStDeNPs prepared with varying seed concentration, presented as concentration (in mM) of silver in AgDeNP seeds and $R_{Ag/seed}$ (percentage in brackets): **1** – 0 mM (no seed), **2** – 0.008 mM (950 %), **3** – 0.019 mM (400 %), **4** – 0.03 mM (250 %), **5** – 0.038 (200 %), **6** – 0.057 mM (130 %), **7** – 0.076 mM (100%), and **8** – 0.152 mM (50 %). Concentrations of reagents not varied were as follows: KOH – 0.61 mM, PANa – 0.37 mM, $AgNO_3$ – 0.076 mM and ascorbate – 0.76 mM. Scale bars are 250 nm for **1** and **2**, 150 nm for **3** and 100 nm for **4-8**.

4.4.2.B. PANA acts as an effective surface blocking agent to direct the deposition of added silver onto the high energy vertices of the AgDeNP seeds. As can be seen in Figure 4.6, AgStDeNPs prepared without PANA exhibit growth from the AgDeNP seeds, which is however, more random and irregular (Figure 4.6A❶). With increasing PANA concentrations, the growth is moderated through the effective surface blocking and thus improving the regularity of the stellation. Optimal PANA to silver ratio was found to be in a range between 1.6:1 and 3.4:1 (Figure 4.6A❷ and 4.6A❸). Lower PANA concentrations were ineffective at blocking the seed surface and thus ineffective for the formation of symmetric stars, so it induced symmetry breaking, as evidenced by broader LSPR peaks (Figure 4.6). Whereas higher PANA concentrations resulted in greater variability in both the average size and the degree of stellation of the resulting AgStDeNPs (Figure 4.6A❹). It should also be mentioned that the stirring, and the speed of addition of ascorbate also affect the degree of stellation.

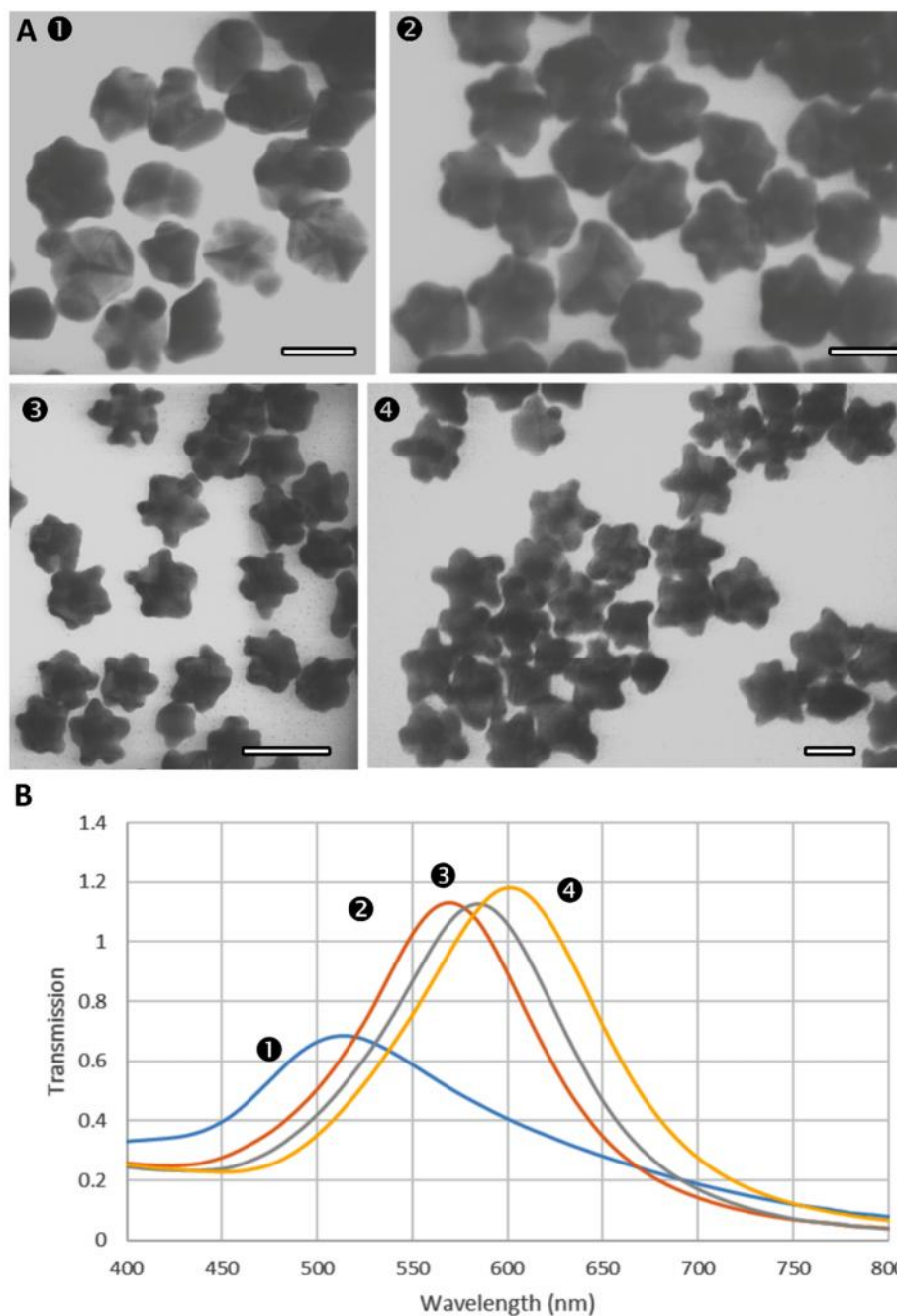


Figure 4.6. A) TEM images and B) UV-vis spectra of AgStDeNP samples prepared with varying concentrations of sodium polyacrylate (PANA): ❶ – 0 mM, ❷ – 0.18 mM, ❸ – 0.30 mM, ❹ – 0.54 mM. Optimal concentration of PANA is between 0.18 and 0.37 mM. Concentrations of reagents not varied were as follows: KOH – 0.61 mM, silver in AgDeNP seeds – 0.038 mM, AgNO₃ – 0.076 mM, and ascorbate – 0.76 mM. All scale bars are 50 nm.

Additional factors affecting AgStDeNP formation. The primary driving force for the growth of AgStDeNPs is the fast reduction,³³ hence the reducing agent, ascorbate, must be delivered fast and

uniformly mixed into the reaction in order to avoid gradients. To assure proper fast mixing of ascorbate, a high stirring rate was employed. Figure 4S.4 compares AgStDeNP samples prepared with low (200 rpm) and high (500 rpm) stirring. In the sample prepared with low stirring (Figure 4S.4❶), some decahedra remained unreacted, even etched, and some featured irregular growth (Figure 4S.4❷). A similar effect is also observed at low and high ascorbate concentrations, respectively (Figs. 4.4A❶ and 4.4A❷). The rate of ascorbate addition is also crucial for the silver reduction rate and thus stellation. Figures 4S.5A❶ and 4S.5A❷ compare the AgStDeNP samples prepared with ascorbate added in 1 second and 1 minute, respectively. When ascorbate is added too slowly, the rapid reduction rate required for the growth of AgStDeNPs is not achieved, and irregular growth is observed. Figure 4S.5A❸ illustrates this case, where slower reduction results in rod-like, quasi-spherical and ill-defined growth with characteristic broad LSPR peaks and poor LSPR reproducibility (Figure 4S.5B❸). Narrow LSPR peaks with high intensity, indicative of narrow AgStDeNP size distribution, can be achieved by adding ascorbate in two portions, each over 1 second, with 1 minute between additions, as seen in Figure 4S.5B❹. However, there is greater variability in the stellation of these AgStDeNPs, as observed by transmission electron microscopy (TEM) (Figure 4S.5B❹). While the above sections detail the important synthetic parameters for the formation of AgStDeNPs, it is important to note that the highly stellated AgStDeNPs may round more readily, and become more compacted stars over time in accordance with the minimization of their surface energy.

Stability and surface energy minimization. Over time, LSPR maxima of the AgStDeNPs were observed to blue-shift, indicative of diminished stellation (or degree of branching) and decrease in high-energy protrusions. The rate of the stellation changes can be monitored with surface plasmon resonance (SPR) spectroscopy by following the LSPR peak shift with time (Figure 4S.6❶). In all tested AgStDeNP samples, the blue shift is rapid at first and then stabilizes after ca. 16-17 hours. In general, the magnitude of the LSPR peak shift observed was 30 to 100 nm, with greater rounding occurring for larger, more stellated AgStDeNPs.

Stability of both LSPR and stellation is a main criterion for AgStDeNP performance in sensing applications such as surface plasmon resonance (SPR) spectroscopy and surface enhanced Raman spectroscopy (SERS). Therefore, we have explored several pathways to minimize or arrest the decrease in stellation including i) the addition of sulfur-containing molecules (e.g. ampicillin and cysteine) as surface-stabilizing ligands; ii) gold coating, and iii) increasing pH. Figure 4S.7 shows the comparison of LSPR preservation of a sample split into two portions, one treated with ampicillin after ascorbate, and one left untreated. The sample that was not treated (Figure 4S.7A^① and 4S.7B^①), became noticeably rounded, as can be seen by electron microscopy, and its LSPR blue shifted ca. 60 nm, whereas the sample treated with 10^{-4} M ampicillin (Figure 4S.7A^② and 4S.7B^②) blue shifted noticeably less, ca. 25 nm, with retained stellation. Comparative SPR responses of AgStDeNPs prepared with ampicillin and cysteine are shown in Figures 4S.6^② and 4S.6^③, respectively.

Gold coating of AgStDeNPs within 10 minutes of preparation limited the decay (as shown in Figure 4S.8B) in contrast to the quick blue shift typically observed for not modified AgStDeNPs (Figure 4S.6^①). For each sample, the UV-vis spectra were measured after one week for samples ^① and ^③, and 5 months for sample ^②, and compared with original spectra. SPR response curve of samples immediately after gold coating is shown in Figure 4S.6^④. TEM images of gold coated AgStDeNPs demonstrate preserved stellation with 4 molar % gold coating, relative to total silver (Figure 4S.8A^①). With higher gold amounts (Figures 4S.8A^② and 4S.8A^③), non-uniform coating is formed. Relatively rough surfaces with gold deposition can be attributed to silver etching. It is also likely that gold is reduced quickly upon addition to AgStDeNP dispersion due to the presence of ascorbate, leading to more granular coating.

Another successful approach to preserve stellation and LSPR stability was to increase the solution pH after AgStDeNP formation (Figure 4S.2^③ and 4S.9^②). After one week, the AgStDeNP sample with added KOH to increase the pH (6.8 from 5.6), exhibited a LSPR blue shift from 618 nm to 575 nm (33 nm). When the control sample (at pH of 5.6) was re-measured after 1 week, the LSPR blue shifted from 561 nm

to 498 nm (63 nm). In this case, owing to the higher reduction potential of ascorbate at higher pH, the redox equilibrium for silver is likely shifted to more metallic silver, reducing the driving force for silver rearrangement.

4.4.3. SERS and SPR

AgStDeNPs exhibit excellent Raman enhancement on the basis of the incompatibility of their D_{5h} symmetry with self-assembled close-packed lattices, as well as their stellation providing protrusions and cavities for electromagnetic 'hot spots'. The non-close packing of the AgStDeNP films allows for semi-regular voids on the order of 10-30 nm, beneficial for SERS. Figure 4S.10 shows an estimated Raman enhancement of 1.8×10^{10} achieved when comparing the intensity of the 1130 cm^{-1} peak of 5',5'-dithiobis(2-nitrobenzoic acid) with and without an AgStDeNP film. Enhancement is estimated by taking the peak intensity of SERS signal and dividing it by moles per area (mol/cm^2) and then dividing the resulting value by the peak divided per moles per area for the reference. The calculated enhancement is higher than that measured for AgDeNPs (4×10^9), as expected for the increased stellation in AgStDeNPs.

In solution SERS measurements, AgStDeNPs gave a low enhancement factor of 10 ± 1.5 , compared to 5 ± 1 for decahedra. These enhancements clearly show that there is some noticeable increase with stellation, but at the same time the produced cavities are not sufficient in size for a strong single-particle enhancement. Single-particle enhancement is typically realized for appreciably larger cavities of ca. 50-100 nm that were achieved, for example, with highly faceted prisms (silver nanoflowers), where enhancement factors exceeded 400.²⁶

Motivated by AgStDeNPs sharp LSPR peaks, SPR experiments were performed to measure both detection of adsorption of analytes and stability of the AgStDeNPs. SPR experiments measure shifts in the LSPR maxima of plasmonic MNPs due to changes in NP dimensions or effective refractive index at the nanoparticle-medium interface. As discussed previously, the AgStDeNPs exhibit surface energy minimization through rounding, which although is becoming relatively stable after 6 hours, continues for

2-3 days (Fig. 4S.6). For quantitative experiments, this decay can be subtracted from the SPR response, or the AgStDeNPs should be aged prior to use. The following proof of concept experiments demonstrate the ability of AgStDeNPs to respond sensitively to the physisorption of KBr. Figure 4S.11 shows the typical response of AgStDeNPs to the sequential increase in KBr concentration in ten-time increments from 10^{-10} M to 10^{-4} M KBr. Each arrow indicates an additional portion of KBr, starting from 10^{-10} M for the first arrow to 10^{-4} M for the last arrow before the drastic LSPR blue shifts (decrease in peak wavelength) due to etching of AgStDeNPs at high bromide concentrations. Small detectable increases in the LSPR with addition of KBr can be associated with bromide physisorption. The inset of Figure 4S.11 shows the SPR response curve of AgStDeNPs at low concentrations of KBr (10^{-10} and 10^{-9} M). Addition of 10^{-10} M KBr to AgStDeNPs causes a LSPR shift of 0.2 nm (Fig. 4S.10 inset) relative to background noise. The detection limit can be estimated by extrapolating the response of 0.2 nm for 10^{-10} M KBr to 0.035 nm (1.5 times signal to noise ratio) as 1.5×10^{-11} M at $S/N = 1.5$ which gives 1.75×10^{-11} M KBr with LSPR signal noise of under 0.02 nm or 20 pm peak-to-peak. The intrinsic high sensitivity of LSPR maxima resolution is prone to external disturbances, such as movements of the cell and removal of cell cap. The signal disturbance by the removal of the cell cap is thus included on the inset curve. Taking into account signal fluctuation associated with cell disturbances from cap removal and mixing (at worst ca. 0.1 nm), the detection limit can be approximated to be 3.5×10^{-11} M.

SPR experiments were also performed using individual samples of AgStDeNPs for each concentration of KBr from 10^{-9} M to 10^{-5} M (Fig. 4S.12). As the LSPR peak needs to be stabilized after preparation (see above section), AgStDeNP samples were used approximately 3 hours after development. Larger red shifts (shifts to higher wavelengths) were obtained with higher concentrations (10^{-6} M KBr, Fig. 4S.12, curve 4), which is expected. A more rapid decrease in LSPR wavelength was observed with the addition of 10^{-5} M KBr (Fig. 4S.12, curve 5), which is lower compared to the sequential response, described Figure 4S.11. The difference can be attributed to bromide gradually blocking the surface in sequential

addition experiments as AgStDeNPs age providing for better stability. We are currently exploring SPR sensing where the sensitivity of AgStDeNP to etching reagents, such as thiols, can enhance SPR response.

4.4.4. Universality of the developed procedure of stellated regrowth

The developed regrowth procedure has been shown to develop stellation on pentagonal rods, silver platelets/prisms, and icosahedral nanoparticles (Figures 4S.13 and 4S.14). Utilizing the same reaction conditions, as reported in Experimental, with the three different silver morphologies as seeds, stellated structures were successfully produced. Pentagonal rods,⁴⁴ platelets³² and icosahedra,⁴⁶ were prepared as reported previously, and used as direct replacement for AgDeNPs in the reported procedure. A LSPR shift to higher wavelengths accompanied this regrowth, indicative of the formation of stellation (Figure 4S.13B for stellated pentagonal rods). The star tips formed preferentially on the higher energy vertices of the seeds with the majority of growth on the junction of a pentagonal cap and sides of the rods (Fig. 4S.13A), and vertices of platelets and icosahedra (Fig. 4S.14). Side edges of the rods were stellated by the deposition as well. The formation of the stellated rods, platelets and icosahedra attest to the universality of the reported procedure for the formation of stellated structures.

4.5. Conclusion

In conclusion, an efficient and reproducible seeded regrowth procedure leading to the formation of stars from silver nanoparticle seeds has been demonstrated. Roles of reducing agent, surface blocking and stabilization have been elucidated. Stability of AgStDeNPs and its effect on localized surface plasmon resonance (LSPR) were studied. The stability was shown to be enhanced by gold coating, as well as the presence of sulphur-containing ligands. The functionality of AgStDeNPs has been demonstrated in SERS and SPR experiments, and the universality of the reported regrowth procedure has been validated using different seed particles.

4.6. Acknowledgement

The authors would like to thank NSERC (Discovery and PGS-D for NC) for funding and the Centre for Nanostructure Imaging, University of Toronto, for access to imaging facilities.

4.7. Supplementary Information

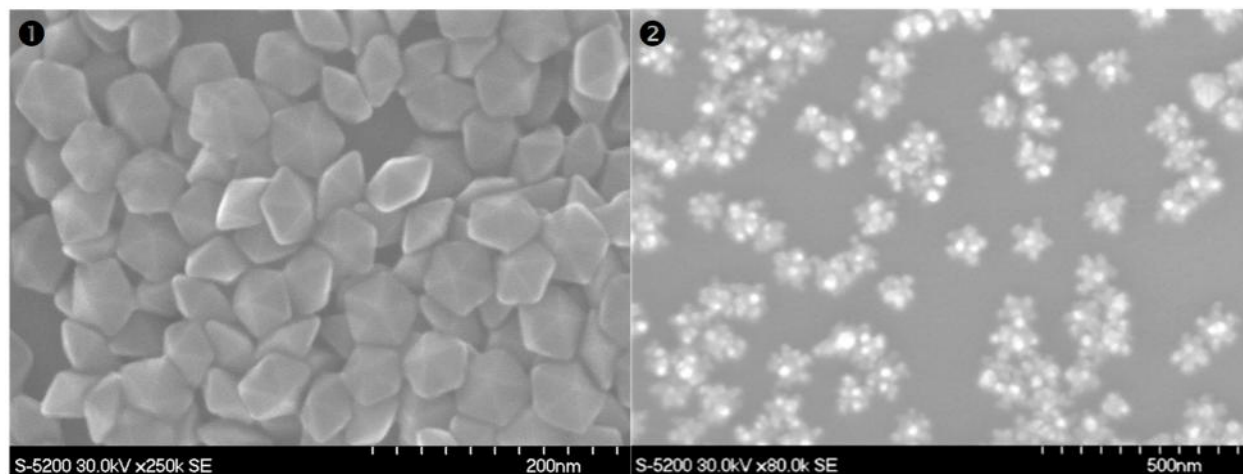


Figure 4S.1. Scanning electron microscopy (SEM) images of **1**) silver decahedral nanoparticles (AgDeNPs) and **2**) silver decahedral star nanoparticles (AgStDeNPs) prepared from AgDeNP seeds.

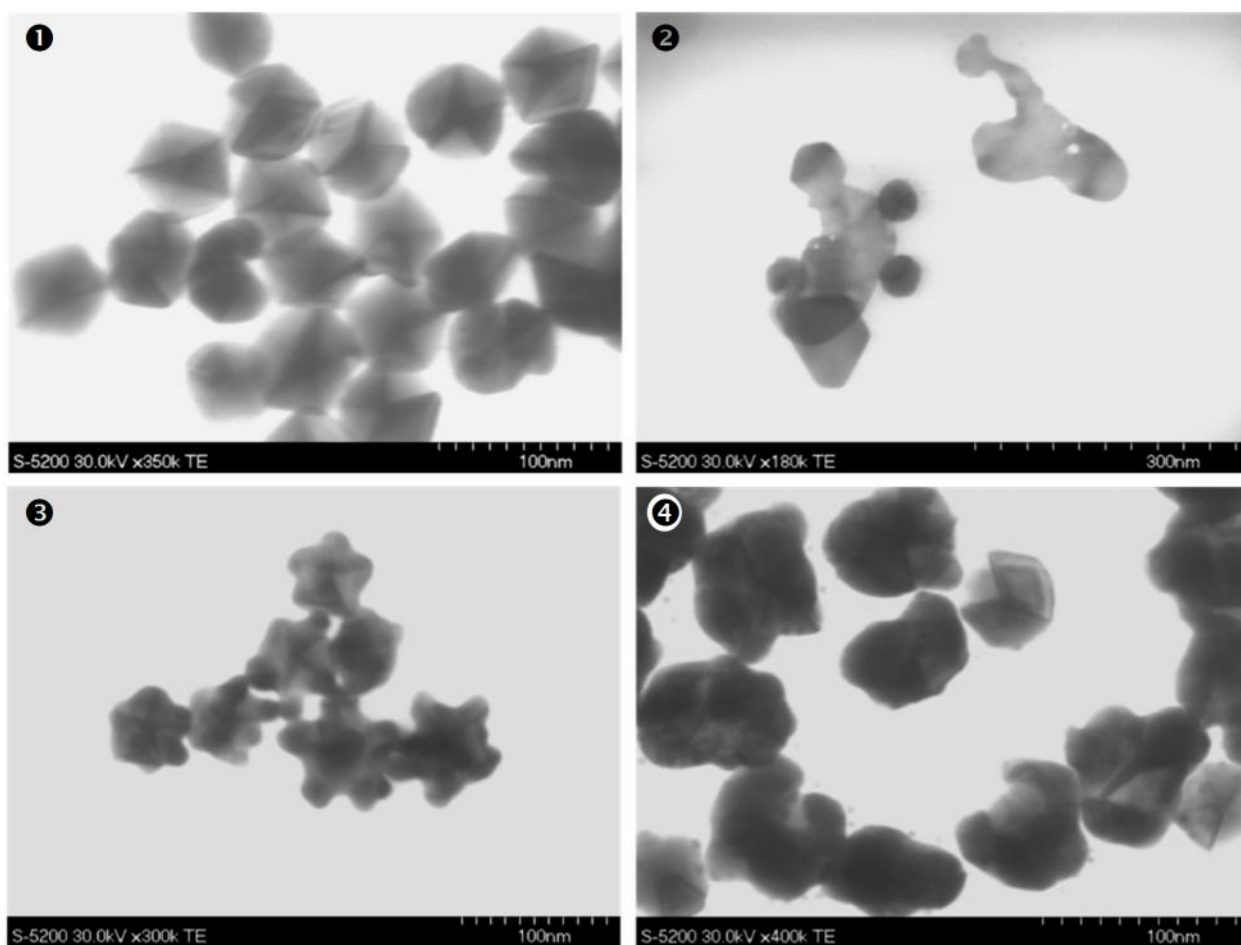


Figure 4S.2. Transmission electron microscopy (TEM) images of AgStDeNP samples prepared at different pH (± 0.2), **1)** 4.7, **2)** 5.3, **3)** 6.8, and **4)** 10.5; pH of the optimized procedure is 5.9. pH was varied by addition of either HNO₃ or KOH to the synthetic preparation described in Experimental.

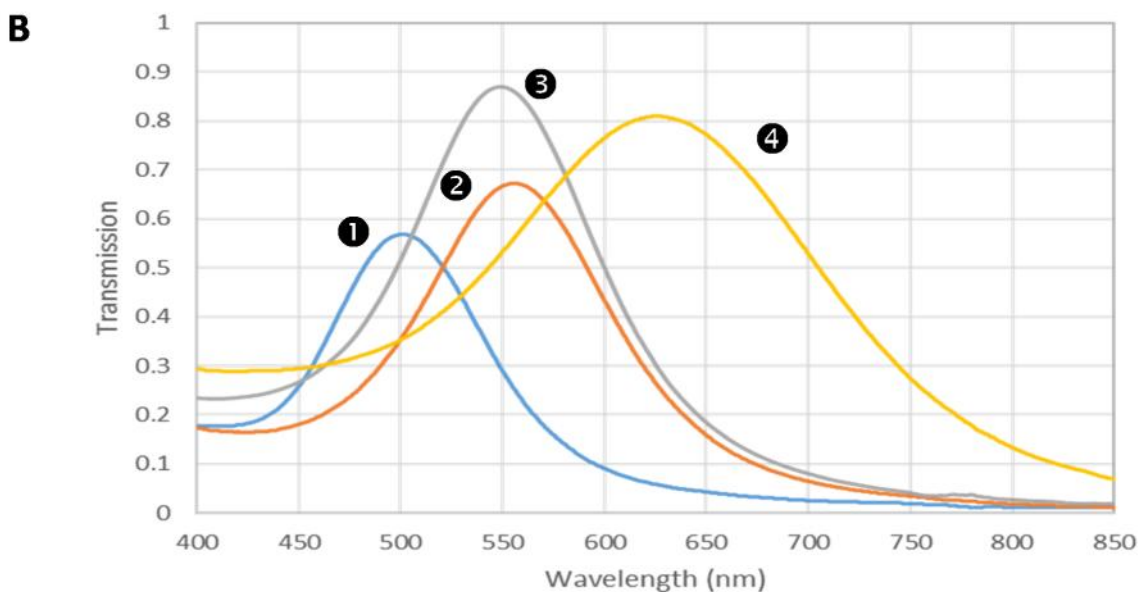
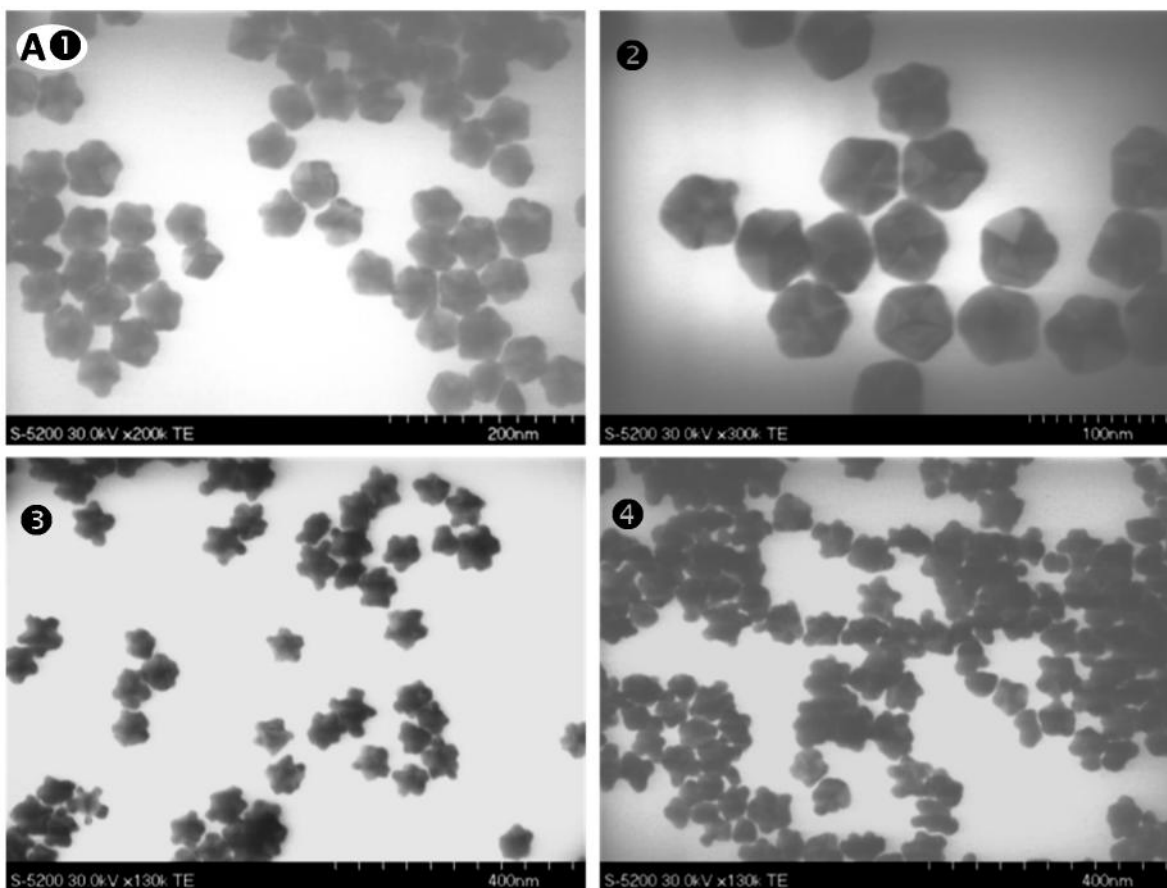


Figure 4S.3. A) TEM images and B) UV-vis spectra of AgStDeNPs prepared with different amounts of added silver (presented as concentration of added silver in mM and ratio of new silver to silver in AgDeNP seeds, given in brackets), 1) 0.034 mM (1:1), 2) 0.051 mM (1.5:1), 3) 0.067 mM (2:1), and 4) 0.10 mM (3:1). Concentrations of reagents not varied were as follows: KOH – 0.61 mM, PANA – 0.37 mM, silver in AgDeNP seeds – 0.038 mM, and ascorbate – 0.76 mM.

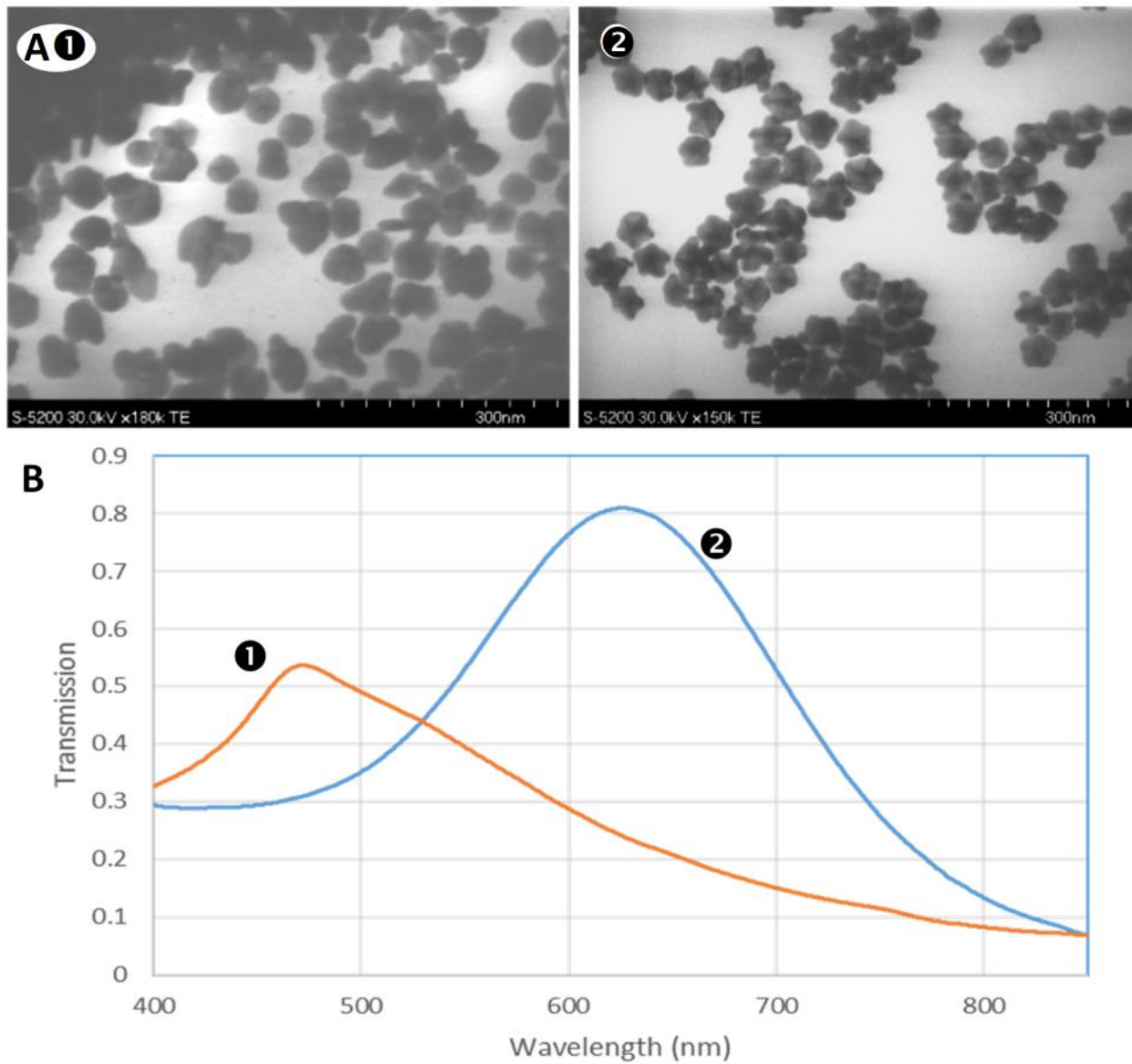


Figure 4S.4. A) TEM images and B) UV-vis spectra of AgStDeNP samples prepared with 1) slow stirring (200 rpm) and 2) fast stirring (500 rpm) using a 3-mm stir bar.

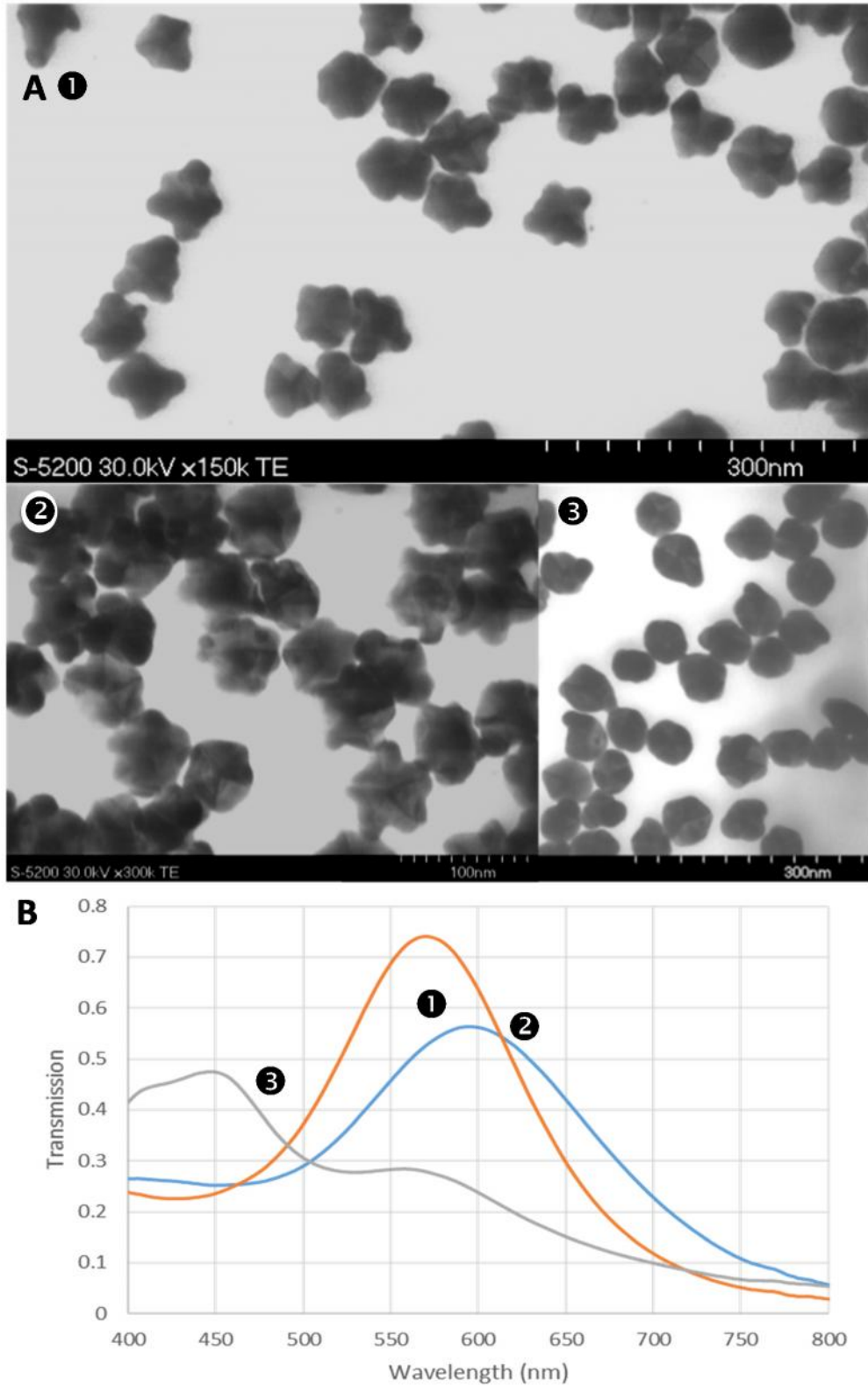


Figure 4S.5. A) TEM images and B) UV-vis spectra of AgStDeNP samples prepared with ascorbate added over different periods of time: 1) 1 second; 2) two portions, 1 second each; 1 minute in between; and 3) 1 minute.

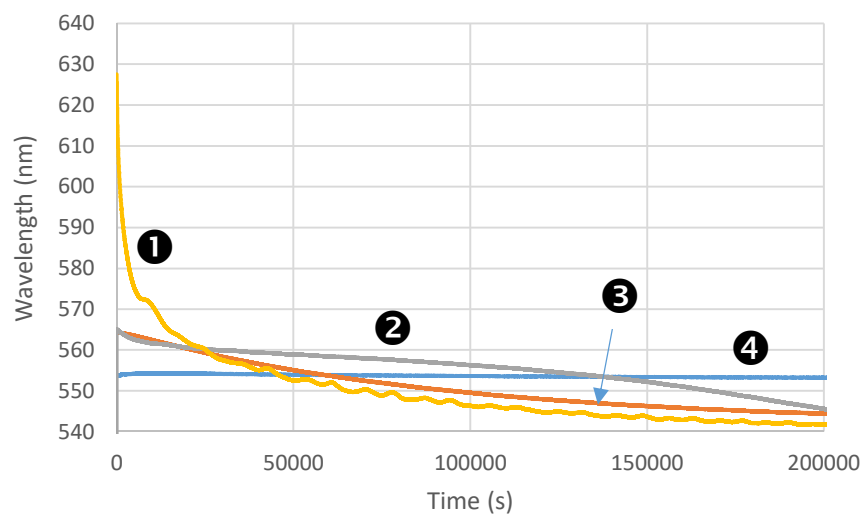


Figure 4S.6. SPR response curve showing LSPR shift of AgStDeNPs over time: **1**) representative non-modified AgStDeNPs (280% $R_{Ag/seed}$), **2**) AgStDeNPs (200 % $R_{Ag/seed}$) with 0.27 mM ampicillin, **3**) AgStDeNPs (200 % $R_{Ag/seed}$) with 0.18 mM cysteine, **4**) AgStDeNPs (200 % $R_{Ag/seed}$) with gold coating (3% molar relative to silver).

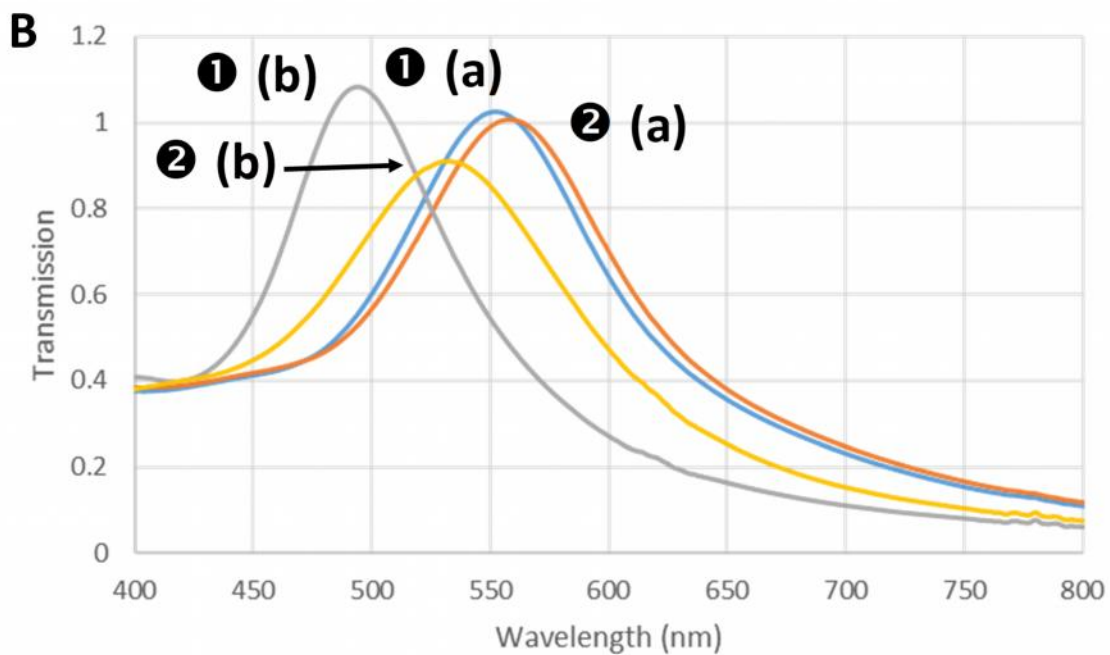
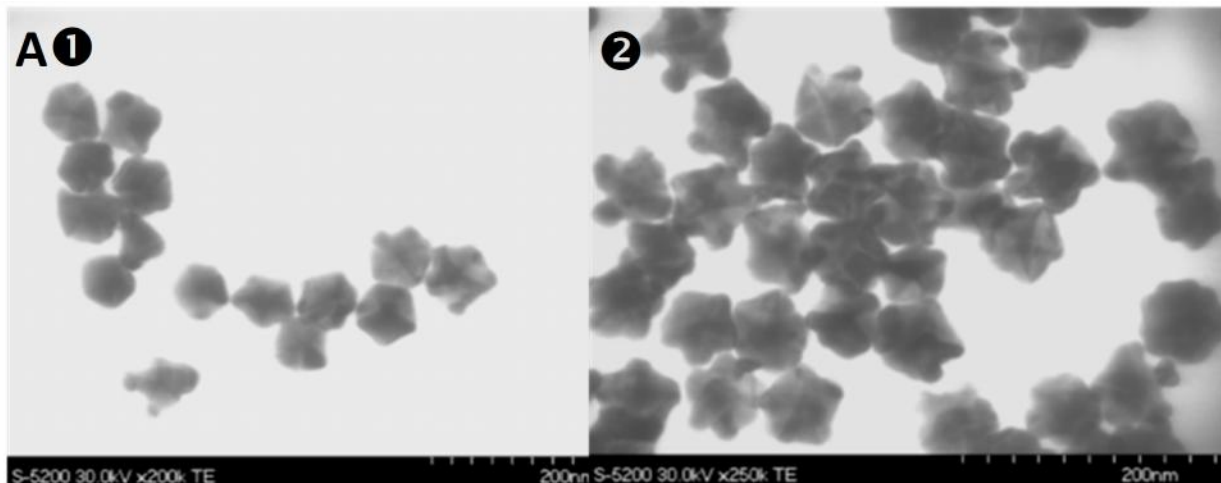


Figure 4S.7. A) TEM images and B) UV-vis spectra of the same AgStDeNP sample, divided into two portions and aged 4 days. **1)** control sample, **2)** portion treated with 10^{-4} M ampicillin. UV-vis spectra labeled (a) are measured for original, as prepared AgStDeNPs, (b) after 4 days.

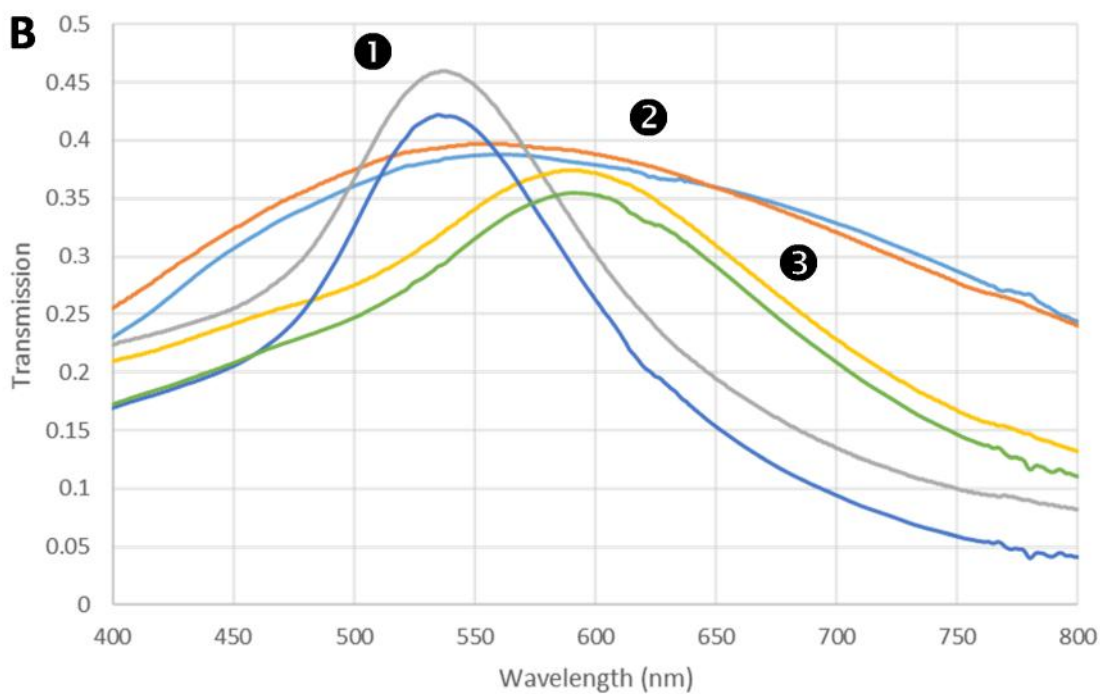
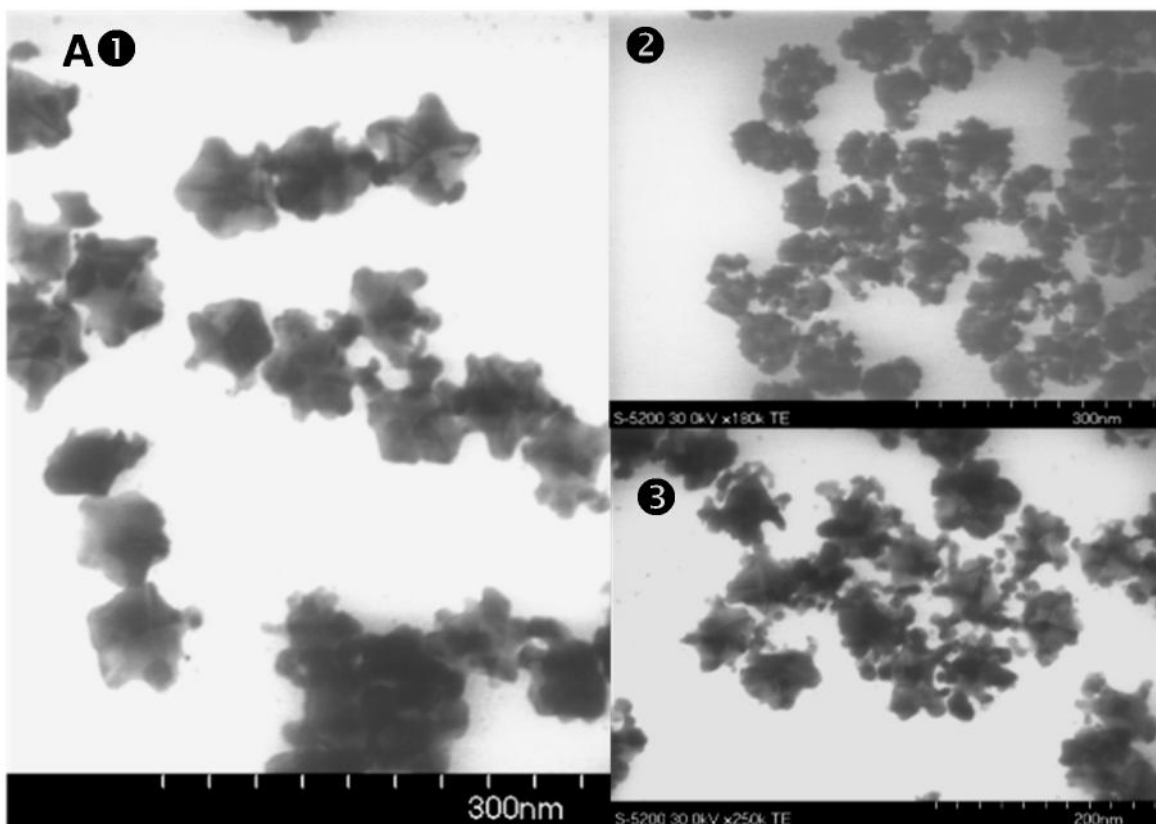


Figure 4S.8. A) TEM images and B) UV-vis spectra of gold-coated AgStDeNP samples prepared with 1) 4 %, 2) 7 %, and 3) 8 % of added gold, relative to total silver (molar ratio). Lower intensity spectra of each pair are measurements performed on original, as prepared, samples; higher intensity spectra are measured after one week for 1 & 3, and after 5 months for 2.

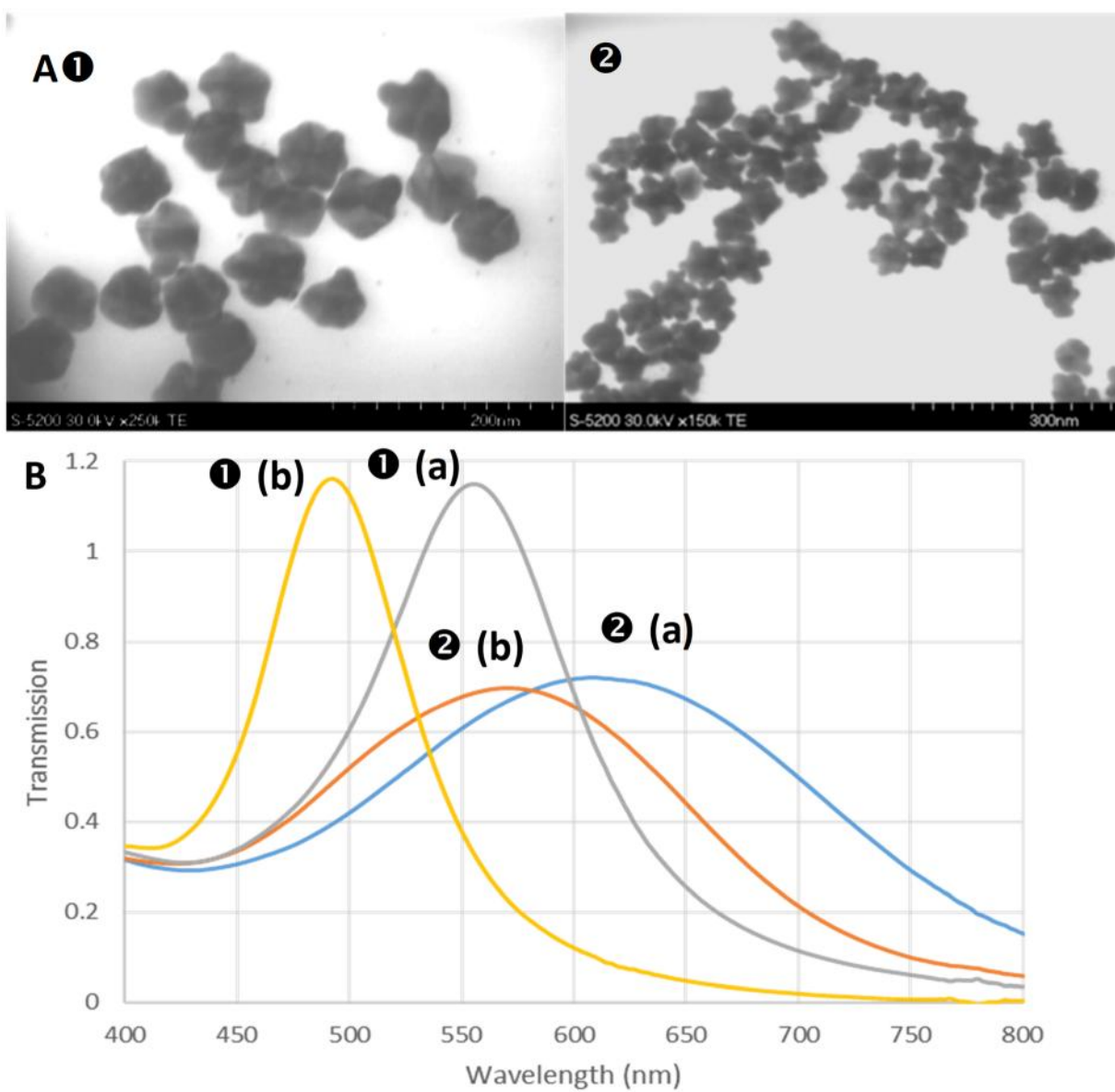


Figure 4S.9. **A)** TEM images of aged AgStDeNP samples and **B)** UV-vis spectra of original and aged AgStDeNP samples prepared **1)** in absence of additional KOH, pH = 5.6 and **2)** with additional KOH (3 mM total), pH = 6.8. UV-vis spectra are labeled (a) for original AgStDeNP samples and (b) for these samples aged for 1 week.

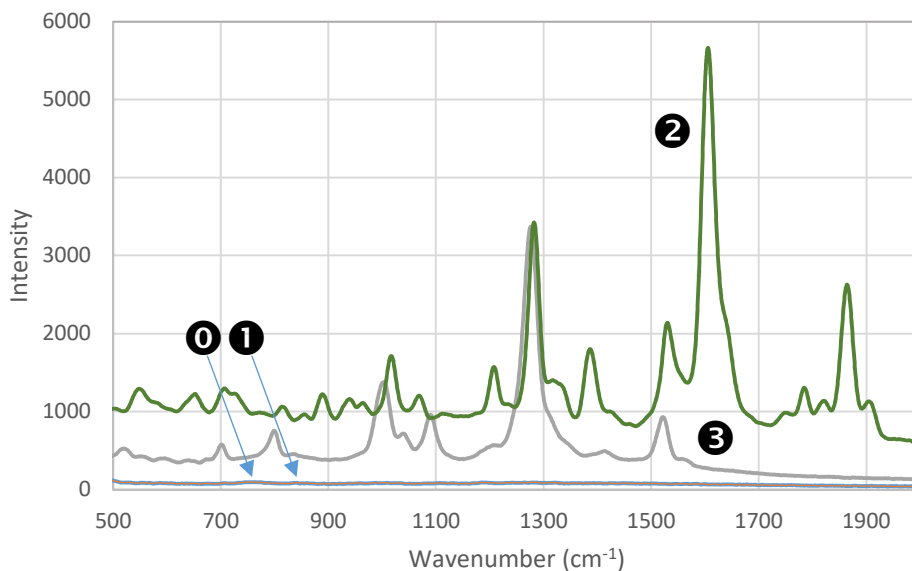


Figure 4S.10. Raman spectra showing the effect of surface enhancement with AgStDeNPs. **0)** blank quartz, **1)** AgStDeNP film, **2)** AgStDeNPs with 10^{-16} moles of 5',5'-dithiobis(2-nitrobenzoic acid) spread over 0.15 cm^2 , **3)** 1.87×10^{-5} moles of 5',5'-dithiobis(2-nitrobenzoic acid) spread over 1.8 cm^2

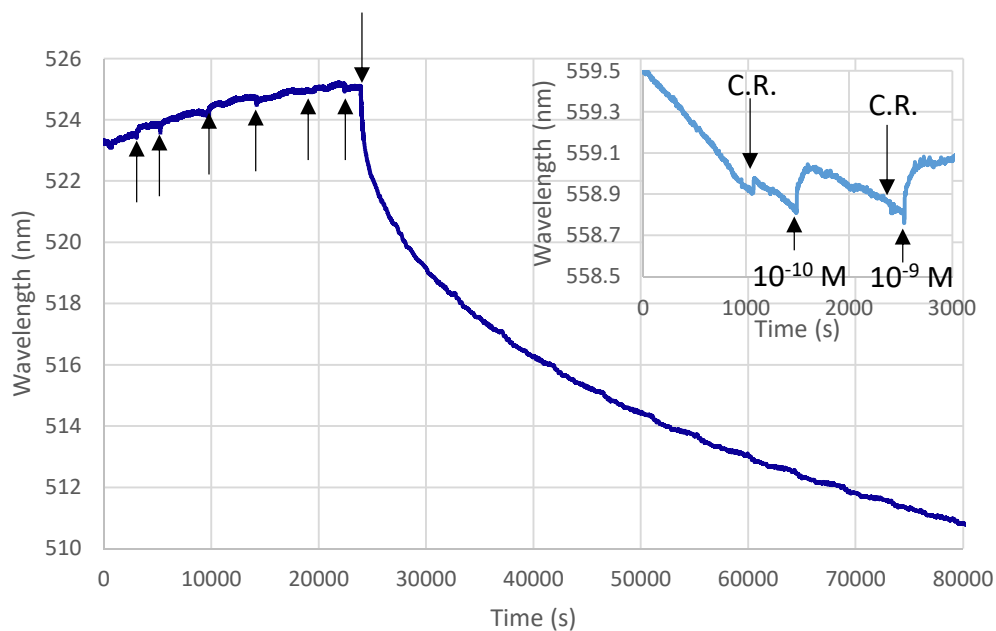


Figure 4S.11. SPR response curve showing LSPR shifts of AgStDeNPs upon sequential exposure to KBr. Arrows represent additions of increasing concentrations of KBr in 10-times increments from 10^{-10} M to 10^{-4} M . Inset is SPR curve showing the effect of low concentrations upon addition of 10^{-10} and 10^{-9} M KBr. C.R. is where the cell cap was removed to represent the cell disturbance.

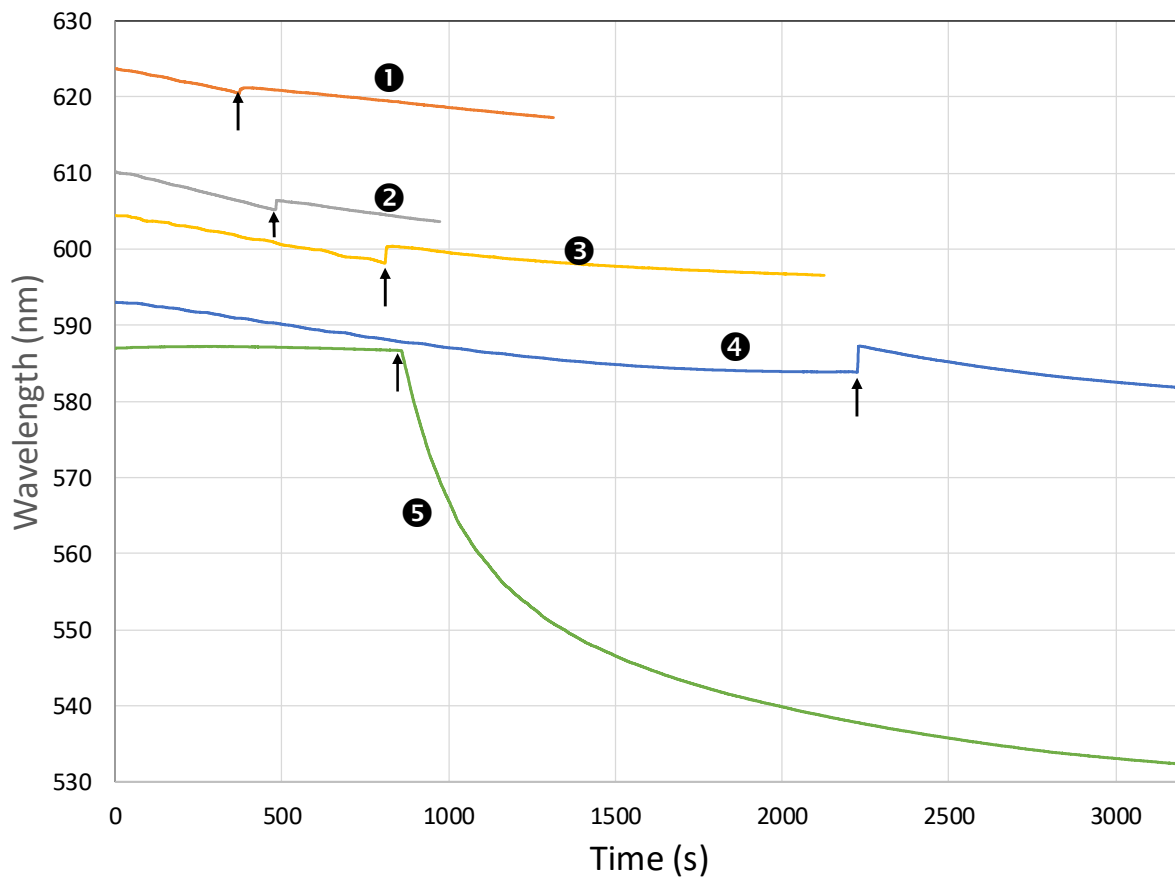


Figure 4S.12. SPR response curve showing LSPR shifts of AgStDeNPs upon exposure to different concentrations of KBr performed for independent samples. Arrows represent additions of KBr of varying concentrations: 1) 10^{-9} M, 2) 10^{-8} M, 3) 10^{-7} M, 4) 10^{-6} M, and 5) 10^{-5} M.

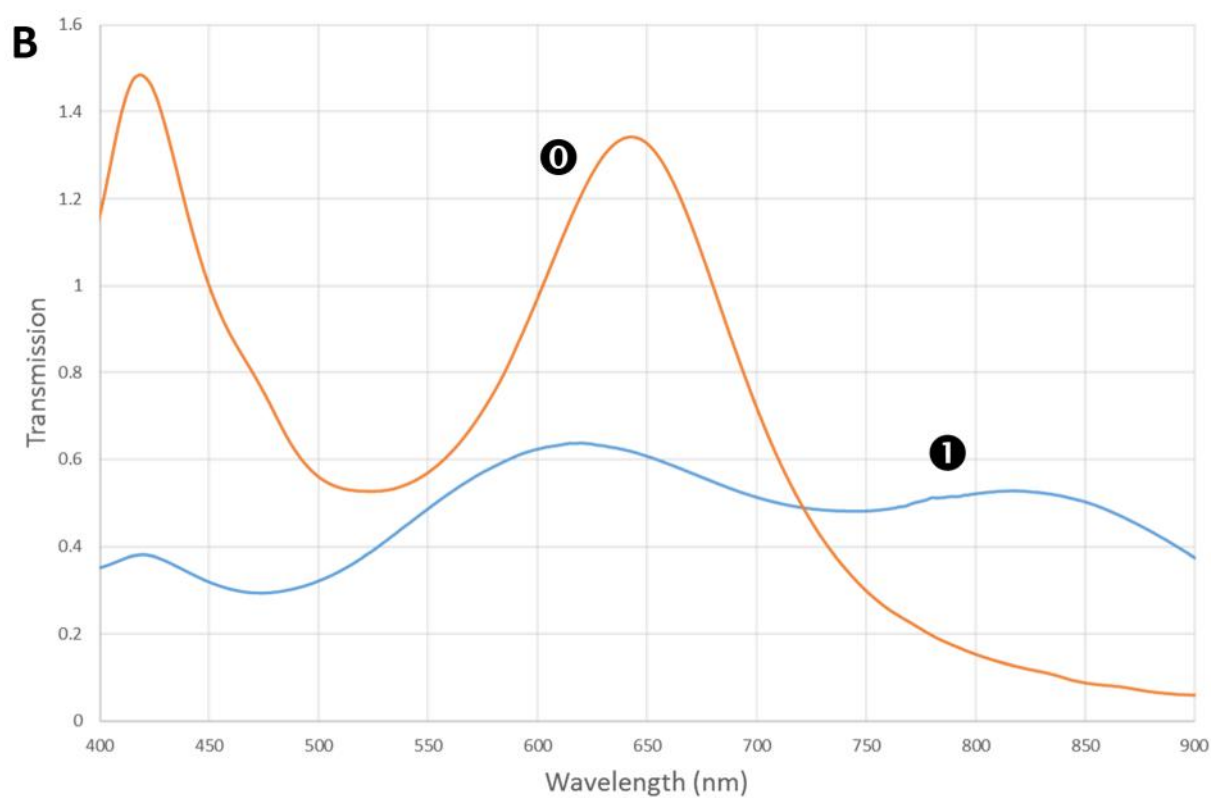
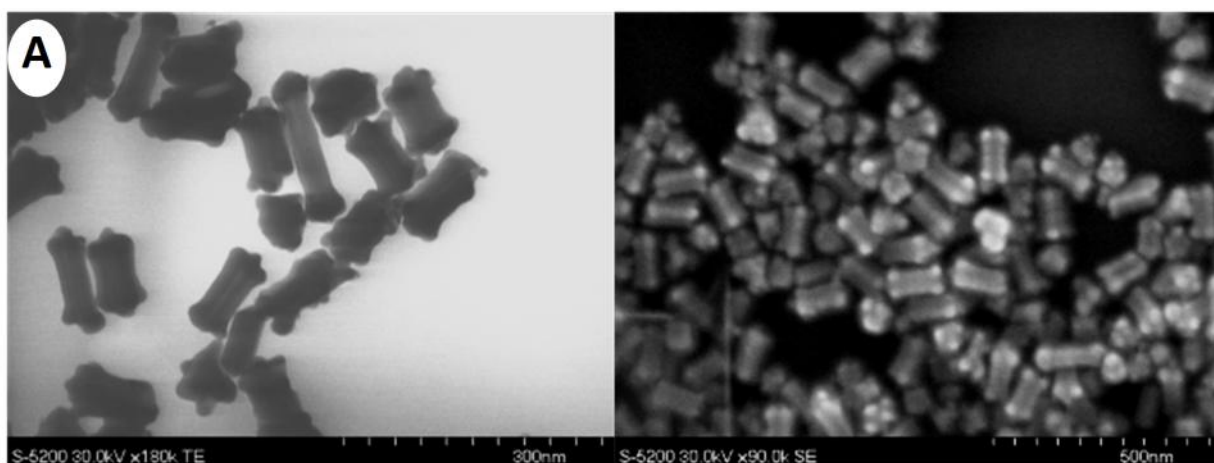


Figure 4S.13. Stellated pentagonal rods prepared with the developed procedure using silver pentagonal rods as seeds instead of AgDeNPs. **A)** TEM (left) and scanning electron microscopy (SEM) (right) images and **B)** UV-vis spectra of **0)** pentagonal rod seeds and **1)** stellated pentagonal rods.

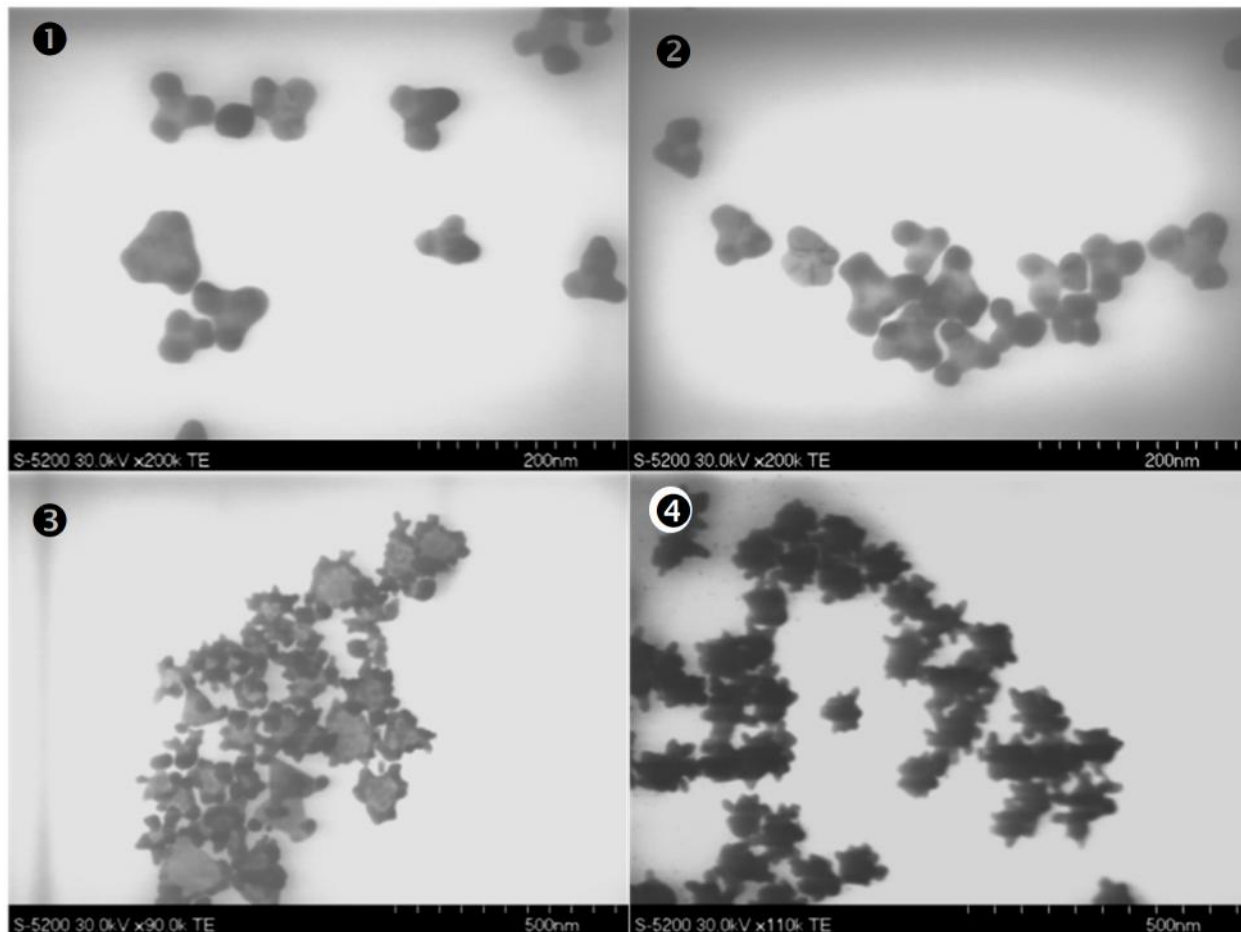


Figure 4S.14. TEM images of stellated prisms (1-3) and icosahedra (4) prepared with the developed procedure using silver prisms or icosahedra, respectively, as seeds instead of AgDeNPs.

The initial discovery and following synthetic developments were completed by me. Preparation of the manuscript was started by me, with iterative refinements as a joint effort with V. Kitaev. V. Kitaev, N. Coombs and I. Gourevich performed imaging and image processing.

4.8. References

- (1) Motl, N. E.; Smith, A. F.; DeSantis, C. J.; Skrabalak, S. E. Engineering Plasmonic Metal Colloids through Composition and Structural Design. *Chem. Soc. Rev.* **2014**, *43*, 3823–3834.
- (2) O’Brien, M. N.; Jones, M. R.; Brown, K. A.; Mirkin, C. A. Universal Noble Metal Nanoparticle Seeds Realized Through Iterative Reductive Growth and Oxidative Dissolution Reactions. *J. Am. Chem. Soc.* **2014**, *136*, 7603–7606.
- (3) Tame, M. S.; McEnery, K. R.; Özdemir, Ş. K.; Lee, J.; Maier, S. A.; Kim, M. S. Quantum Plasmonics. *Nat. Phys.* **2013**, *9*, 329–340.

- (4) Baffou, G.; Quidant, R. Nanoplasmonics for Chemistry. *Chem. Soc. Rev.* **2014**, *43*, 3898–3907.
- (5) Burda, C.; Chen, X.; Narayanan, R.; El-Sayed, M. A. Chemistry and Properties of Nanocrystals of Different Shapes. *Chem. Rev.* **2005**, *105*, 1025–1102.
- (6) Cheng, H.; Fuku, K.; Kuwahara, Y.; Mori, K.; Yamashita, H. Harnessing Single-Active Plasmonic Nanostructures for Enhanced Photocatalysis under Visible Light. *J. Mater. Chem. A* **2015**, *3*, 5244–5258.
- (7) Linic, S.; Aslam, U.; Boerigter, C.; Morabito, M. Photochemical Transformations on Plasmonic Metal Nanoparticles. *Nat. Mater.* **2015**, *14*, 567–576.
- (8) Giljohann, D. A.; Seferos, D. S.; Daniel, W. L.; Massich, M. D.; Patel, P. C.; Mirkin, C. A. Gold Nanoparticles for Biology and Medicine. *Angew. Chemie Int. Ed.* **2010**, *49*, 3280–3294.
- (9) Langer, J.; Novikov, S. M.; Liz-Marzán, L. M. Sensing Using Plasmonic Nanostructures and Nanoparticles. *Nanotechnology* **2015**, *26*, 322001.
- (10) Yang, X.; Yang, M.; Pang, B.; Vara, M.; Xia, Y. Gold Nanomaterials at Work in Biomedicine. *Chem. Rev.* **2015**, *115*, 10410–10488.
- (11) Rycenga, M.; Cogley, C. M.; Zeng, J.; Li, W.; Moran, C. H.; Zhang, Q.; Qin, D.; Xia, Y. Controlling the Synthesis and Assembly of Silver Nanostructures for Plasmonic Applications. *Chem. Rev.* **2011**, *111*, 3669–3712.
- (12) Langille, M. R.; Personick, M. L.; Mirkin, C. A. Plasmon-Mediated Syntheses of Metallic Nanostructures. *Angew. Chemie Int. Ed.* **2013**, *52*, 13910–13940.
- (13) Wang, Y.; Wan, D.; Xie, S.; Xia, X.; Huang, C. Z.; Xia, Y. Synthesis of Silver Octahedra with Controlled Sizes and Optical Properties *via* Seed-Mediated Growth. *ACS Nano* **2013**, *7*, 4586–4594.
- (14) Wiley, B.; Sun, Y.; Chen, J.; Cang, H.; Li, Z.-Y.; Li, X.; Xia, Y. Shape-Controlled Synthesis of Silver and Gold Nanostructures. *MRS Bull.* **2005**, *30*, 356–361.
- (15) Grzelczak, Marek, Pérez-Juste, Jorge, Paul, Mulvaney, Liz-Marzán, L. M. Shape Control in Gold Nanoparticle Synthesis. *Chem. Soc. Rev.* **2008**, *37*, 1783–1791.
- (16) Niu, W.; Lu, X. *Metallic Nanostructures: From Controlled Synthesis to Applications*; Springer International Publishing: New York, **2015**.
- (17) Xia, Y.; Xia, X.; Peng, H.-C. Shape-Controlled Synthesis of Colloidal Metal Nanocrystals: Thermodynamic versus Kinetic Products. *J. Am. Chem. Soc.* **2015**, *137*, 7947–7966.
- (18) Weiner, R. G.; Kunz, M. R.; Skrabalak, S. E. Seeding a New Kind of Garden: Synthesis of Architecturally Defined Multimetallic Nanostructures by Seed-Mediated Co-Reduction. *Acc. Chem. Res.* **2015**, *48*, 2688–2695.
- (19) Sun, Y. Interfaced Heterogeneous Nanodimers. *Natl. Sci. Rev.* **2015**, *2*, 329–348.
- (20) Liu, X.; Yin, Y.; Gao, C. Size-Tailored Synthesis of Silver Quasi-Nanospheres by Kinetically Controlled Seeded Growth. *Langmuir* **2013**, *29*, 10559–10565.
- (21) Gao, C.; Goebel, J.; Yin, Y. Seeded Growth Route to Noble Metal Nanostructures. *J. Mater. Chem. C* **2013**, *1*, 3898–3909.

- (22) Liz-Marzán, L. M. Increasing Complexity While Maintaining a High Degree of Symmetry in Nanocrystal Growth. *Angew. Chemie Int. Ed.* **2015**, *54*, 3860–3861.
- (23) Ling, D.; Hackett, M. J.; Hyeon, T. Surface Ligands in Synthesis, Modification, Assembly and Biomedical Applications of Nanoparticles. *Nano Today* **2014**, *9*, 457–477.
- (24) Kuo, C.-H.; Huang, M. H. Synthesis of Branched Gold Nanocrystals by a Seeding Growth Approach. *Langmuir* **2005**, *21*, 2012–2016.
- (25) Huang, M. H.; Rej, S.; Hsu, S. C. Facet-Dependent Properties of Polyhedral Nanocrystals. *Chem. Commun.* **2014**, *50*, 1634–1644.
- (26) Cathcart, N.; Kitaev, V. Multifaceted Prismatic Silver Nanoparticles: Synthesis by Chloride-Directed Selective Growth from Thiolate-Protected Clusters and SERS Properties. *Nanoscale* **2012**, *4*, 6981–6989.
- (27) Ohta, S.; Glancy, D.; Chan, W. C. W. DNA-Controlled Dynamic Colloidal Nanoparticle Systems for Mediating Cellular Interaction. *Sci.* **2016**, *351*, 841–845.
- (28) Lohse, S. E.; Murphy, C. J. The Quest for Shape Control: A History of Gold Nanorod Synthesis. *Chem. Mater.* **2013**, *25*, 1250–1261.
- (29) Zhang, L. F.; Wang, L.; Zhong, S. L.; Huang, Y. X.; Xu, A. W. Facile Synthesis of Concave Decahedra Enclosed by High-Index Facets and Truncated Decahedra with a Large Size. *Dalt. Trans.* **2012**, *41*, 4948–4954.
- (30) Agnihotri, S.; Mukherji, S.; Mukherji, S. Size-Controlled Silver Nanoparticles Synthesized over the Range 5–100 nm Using the Same Protocol and Their Antibacterial Efficacy. *RSC Adv.* **2014**, *4*, 3974–3983.
- (31) Bastús, N. G.; Merkoçi, F.; Piella, J.; Puntès, V. Synthesis of Highly Monodisperse Citrate-Stabilized Silver Nanoparticles of up to 200 nm: Kinetic Control and Catalytic Properties. *Chem. Mater.* **2014**, *26*, 2836–2846.
- (32) Cathcart, N.; Frank, A. J.; Kitaev, V. Silver Nanoparticles with Planar Twinned Defects: Effect of Halides for Precise Tuning of Plasmon Resonance Maxima from 400 to 900 nm. *Chem. Commun.* **2009**, *6*, 7170–7172.
- (33) Mushran, S. P.; Agrawal, M. C.; Mehrotra, R. M.; Sanehi, R. Kinetics and Mechanism of Reduction of Silver(I) by Ascorbic Acid. *J. Chem. Soc. Dalt. Trans.* **1974**, *0*, 1460–1462.
- (34) AL-Thabaiti, S. A.; Al-Nowaiser, F. M.; Obaid, A. Y.; Al-Youbi, A. O.; Khan, Z. Formation and Characterization of Surfactant Stabilized Silver Nanoparticles: A Kinetic Study. *Colloids Surfaces B Biointerfaces* **2008**, *67*, 230–237.
- (35) Fukuyo, T.; Imai, H. Morphological Evolution of Silver Crystals Produced by Reduction with Ascorbic Acid. *J. Cryst. Growth* **2002**, *241*, 193–199.
- (36) Cheng, L.-C.; Huang, J.-H.; Chen, H. M.; Lai, T.-C.; Yang, K.-Y.; Liu, R.-S.; Hsiao, M.; Chen, C.-H.; Her, L.-J.; Tsai, D. P. Seedless, Silver-Induced Synthesis of Star-Shaped Gold/Silver Bimetallic Nanoparticles as High Efficiency Photothermal Therapy Reagent. *J. Mater. Chem.* **2012**, *22*, 2244–2253.
- (37) Liang, H.; Li, Z.; Wang, W.; Wu, Y.; Xu, H. Highly Surface-Roughened "Flower-Like"

- Silver Nanoparticles for Extremely Sensitive Substrates of Surface-Enhanced Raman Scattering. *Adv. Mater.* **2009**, *21*, 4614–4618.
- (38) Camden, J. P.; Dieringer, J. A.; Wang, Y.; Masiello, D. J.; Marks, L. D.; Schatz, G. C.; Van Duyne, R. P. Probing the Structure of Single-Molecule Surface-Enhanced Raman Scattering Hot Spots. *J. Am. Chem. Soc.* **2008**, *130*, 12616–12617.
- (39) Laurence, T. A.; Braun, G.; Talley, C.; Schwartzberg, A.; Moskovits, M.; Reich, N.; Huser, T. Rapid, Solution-Based Characterization of Optimized SERS Nanoparticle Substrates. *J. Am. Chem. Soc.* **2009**, *131*, 162–169.
- (40) Brus, L. Noble Metal Nanocrystals: Plasmon Electron Transfer Photochemistry and Single-Molecule Raman Spectroscopy. *Acc. Chem. Res.* **2008**, *41*, 1742–1749.
- (41) Rodríguez-Lorenzo, L.; Álvarez-Puebla, R. A.; Pastoriza-Santos, I.; Mazzucco, S.; Stéphan, O.; Kociak, M.; Liz-Marzán, L. M.; García de Abajo, F. J. Zeptomol Detection Through Controlled Ultrasensitive Surface-Enhanced Raman Scattering. *J. Am. Chem. Soc.* **2009**, *131*, 4616–4618.
- (42) Khanafer, M.; Izquierdo-Lorenzo, I.; Akil, S.; Louarn, G.; Toufaily, J.; Hamieh, T.; Adam, P.-M.; Jradi, S. Silver Nanoparticle Rings of Controllable Size: Multi-Wavelength SERS Response and High Enhancement of Three Pyridine Derivatives. *ChemistrySelect* **2016**, *1*, 1201–1206.
- (43) Shen, J.; Su, J.; Yan, J.; Zhao, B.; Wang, D.; Wang, S.; Li, K.; Liu, M.; He, Y.; Mathur, S.; et al. Bimetallic Nano-Mushrooms with DNA-Mediated Interior Nanogaps for High-Efficiency SERS Signal Amplification. *Nano Res.* **2015**, *8*, 731–742.
- (44) Murshid, N.; Keogh, D.; Kitaev, V. Optimized Synthetic Protocols for Preparation of Versatile Plasmonic Platform Based on Silver Nanoparticles with Pentagonal Symmetries. *Part. Part. Syst. Charact.* **2014**, *31*, 178–189.
- (45) Pietrobon, B.; McEachran, M.; Kitaev, V. Synthesis of Size-Controlled Faceted Pentagonal Silver Nanorods with Tunable Plasmonic Properties and Self-Assembly of These Nanorods. *ACS Nano* **2009**, *3*, 21–26.
- (46) Keunen, R.; Cathcart, N.; Kitaev, V. Plasmon Mediated Shape and Size Selective Synthesis of Icosahedral Silver Nanoparticles via Oxidative Etching and Their 1-D Transformation to Pentagonal Pins. *Nanoscale* **2014**, *6*, 8045–8051.
- (47) Pietrobon, B.; Kitaev, V. Photochemical Synthesis of Monodisperse Size-Controlled Silver Decahedral Nanoparticles and Their Remarkable Optical Properties. *Chem. Mater.* **2008**, *20*, 5186–5190.
- (48) Cathcart, N.; Kitaev, V. Symmetry Breaking by Surface Blocking: Synthesis of Bimorphic Silver Nanoparticles, Nanoscale Fishes and Apples. *Sci. Rep.* **2016**, *6*, 32561.

Chapter 5: LSPR Tuning from 470 to 800 nm and Improved Stability of Au-Ag Nanoparticles Formed by Gold Deposition and Rebuilding in the Presence of Poly(styrene sulfonate)

The following publication presents a synthetic route to tune the localized surface plasmon resonance of Au-Ag nanoparticles through gold deposition on Ag seeds, galvanic replacement, and rebuilding to alloyed nanostructures. Reprinted with permission from N. Cathcart, J. I. L. Chen, and V. Kitaev, LSPR Tuning from 470 to 800 nm and Improved Stability of Au-Ag Nanoparticles Formed by Gold Deposition and Rebuilding in the Presence of Poly(Styrene sulfonate). *Langmuir* **2018**, 34, 612–621. Copyright (2018) American Chemical Society, and is accessible online at:

<https://pubs.acs.org/doi/abs/10.1021/acs.langmuir.7b03537>.

It is complete in combination with supporting information, available online at:

https://pubs.acs.org/doi/suppl/10.1021/acs.langmuir.7b03537/suppl_file/la7b03537_si_001.pdf.

LSPR tuning from 470 to 800 nm and Improved Stability of Au-Ag Nanoparticles Formed by Gold Deposition and Rebuilding in the Presence of Poly(styrene sulfonate)

By Nicole Cathcart, Jennifer I.L. Chen (York University), and Vladimir Kitaev

5.1. Abstract

Stability and precise control over functional properties of metal nanoparticles remains a challenge for the realization of prospective applications. Our described process of shell formation and rebuilding can address both these challenges. Template silver nanoparticles (AgNPs) stabilized by poly(styrene sulfonate) are first transformed with gold deposition, after which the resulting shell rebuilds with the replaced silver. The shell formation and rebuilding are accompanied by large shifts in localized surface

plasmon resonance (LSPR) peak position, which enables LSPR tuning in a range from 470 nm to 800 nm. Furthermore, chemical stability of Au-AgNPs is significantly improved compared to AgNPs due to gold stability. Silver templates of different shapes and sizes were demonstrated to transform to AuAg composite NPs to further extend the accessible LSPR range tuning. Stabilization of template AgNPs with poly(styrene sulfonate), in contrast to commonly used poly(vinylpyrrolidone), was found to be a key factor for shell rebuilding. The developed Au-AgNPs were demonstrated to be advantageous for surface plasmon resonance (SPR) detection and surface enhanced Raman spectroscopy (SERS) owing to their tunable LSPR and enhanced stability.

5.2. Introduction

Metal nanoparticles (MNPs) in general, and plasmonic nanoparticles in particular, have been proven essential for a wide range of advanced applications^{1,2} including plasmonics^{3,4} and surface enhanced Raman spectroscopy (SERS).^{5,6} To realize the full potential of MNPs in all these applications, several factors need to be addressed: chemical and colloidal stability of MNPs, realization of shape selection^{7,8} and narrow distribution of sizes^{9,10} due to nanoscale size/shape-property dependence,¹¹ the surface chemistry^{12,13} and ease of preparation with these tuneable properties.^{14,15} Bimetallic nanoparticles have received increasing attention due to ample opportunities in tuning structure and composition, especially for plasmonic applications of gold and silver NPs.^{16–18} Gold and silver NPs are best for plasmonic applications, while copper NPs may offer advantageous cost-effective catalytic and electrical properties.^{19,20} Gold nanoparticles offer superior chemical stability, however their optical properties are limited by the LSPR range (>510 nm) and the plasmon resonance is dampened due to *d-sp* transitions. Silver features superior optical properties in the visible that are translated to well-defined LSPR and correspondingly the strongest Raman enhancement by AgNPs as a substrate. Silver chemical reactivity is beneficial for shape selection and AgNPs are available in diverse well-defined morphologies.^{18,21} At the same time, AgNP chemical stability is limited, which is especially restrictive for their use in physiological

conditions where chloride, sulphides and thiols readily degrade AgNPs. Templating well-defined morphologies of AgNPs with gold was pioneered by Younan Xia group²² with the formation of gold shells,²³ boxes,²⁴ and cages²⁵ of cubes. A large number of works followed in this field,²⁶ including examples of silver nanoplates coated with Au, Pt, or Pd,²⁷ Pd shells on Au seeds¹⁴ and many others.^{28–30} Templating AgNPs with gold was studied by our group, demonstrating some limitations in what can be achieved including uniform plating vs. frame-like coating and advantages for surface plasmon resonance (SPR) sensors.^{31–33} Gold plating was advantageously explored by other groups, demonstrating uniform gold coating and realization of applications.^{34,35} Overall, formation of gold-silver composite NPs is a fertile and actively researched direction to achieve nanoscale control of the stability and, importantly, of the localized surface plasmon resonance (LSPR) for advanced applications.^{36,37,38}

In this work we systematically explored the process of silver rebuilding subsequent to gold shell formation and described key practical findings to take advantage of the resulting Au-AgNPs with tuneable LSPR from 470 to 800 nm (Figures 1 and 5S.1 and Table 5S.1) and improved stability for several important applications of plasmonic nanoparticles, such as SPR and SERS.

5.3. Experimental Section

Reagents

Silver nitrate (99%), sodium citrate tribasic dihydrate (99.5%), L-arginine (98%), sodium borohydride (>99%), hydrogen peroxide with the potassium stannate inhibitor 30–32 wt.%, 99.999% trace metal basis, tetrachloroauric acid (99%), poly(sodium 4-styrenesulfonate) (PSS, $M_w = 70,000$), potassium iodide (99%), potassium bromide (99%), thiosalicylic acid (97%), all supplied by Aldrich, and poly(vinylpyrrolidone) (PVP, $M_w = 40,000$) supplied by Caledon Chemicals (Caledon, Canada) were used as received. High-purity deionized water (>18.2 M Ω cm) was produced using a Millipore A10 Milli-Q.

Synthetic procedures

Preparation of template AgNPs. Silver decahedral NPs were adapted from previously reported synthesis^{39,40} by using poly(styrene sulfonate) instead of PVP. The reagents were combined in the following order to produce the listed total concentrations in aqueous solution: 1.68 mM sodium tricitrate, 0.07 mM poly(styrene sulfonate), 8 μ M L-arginine, 0.13 mM silver nitrate, 1.29 mM sodium borohydride while stirring at 400 rpm using a 12.7 by 3.2 mm stir bar in a 20 mL borosilicate vial. (Detailed information on specific volumes and concentrations is provided in SI). Upon the addition of the sodium borohydride the solution became pale yellow and darkened over one hour of constant stirring. After one hour, 0.2 M hydrogen peroxide was added. The stir bar was then removed, and the sample was capped and exposed to a 450 nm LED for 14 hours.⁴⁰ LED setup is shown in Figure 5S.2A. Pentagonal rod AgNPs and prismatic NPs were prepared using previously reported procedures.^{40,41}

Gold addition, formation of plated nanoparticles and shells. In the first step of preparation of Au-Ag composite nanostructures, tetrachloroauric acid (HAuCl_4) of varying concentrations was added to the as-prepared AgDeNP solution (15.7 mL) under stirring (400 rpm with 12.7 by 3.2 mm stir bar) via syringe pump (KDSscientific) at a rate of 0.25 mL/hr. Concentration of HAuCl_4 was varied for plating or shellation regimes. For example Au shell NPs with 80 mol.% Au (% relative to that of silver in AgDeNPs) were prepared by loading 3 mL of 0.53 mM HAuCl_4 into a 5 mL syringe attached to Teflon tubing (PTFE #18 AWG, Cole Parmer) sealed with ethylene-vinyl acetate hot glue. Alternatively, smaller volumes of 80 mol.% Au shell NPs were prepared by measuring 3 mL of silver decahedra solution into a new 20 mL vial with a stir bar, and delivering 3 mL of 0.1 mM HAuCl_4 using a 5-mL syringe. The syringe pump setup is shown in Figure 5S.2B in SI.

Post-transformation. Au shell NPs can transform/rebuild into different Au-AgNPs by thermal reduction of galvanically replaced silver ions either by slow reduction at room temperature for several weeks (protected from ambient light) or accelerated reduction by heating near boiling (95 °C) using a hot

plate (Heidolph MR3004). An additional post-transformation route was accomplished by addition of 70 mM to 0.1 M hydrogen peroxide to the gold shell NPs.

Characterization

Electron microscopy (both TEM and SEM) was performed using Hitachi S-5200 with the operating voltage of 30.0 kV. LEO 912B 120 kV energy filtered TEM with LaB₆ filament was used for HRTEM. NP dispersions were deposited on a carbon-coated formvar grid (EMS Corp.). UV-vis spectra were acquired with either Ocean Optics QE65000 fiber-optic UV-vis spectrometer or Cary 50Bio UV-vis spectrophotometer. Zeta potential and size measurements were done using Malvern Zetasizer Nano ZS. SPR studies were performed using OpenSPR by Nicoya Lifesciences. SERS measurements were acquired using R-3000QE fibre-optic Raman spectrometer equipped with 290 mW laser at 785 nm (RSI). Centrifugation was done using either Thermo Scientific Legend Micro 21, or Medifuge centrifuges. Plasma cleaning was performed using Harrick PDC-32G.

Finite-Difference Time-Domain simulations. Finite-difference time-domain (FDTD) calculations were performed using Lumerical FDTD Solutions (version 8.16.903, Lumerical Solutions Inc.). Dielectric constant data for bulk silver and gold were taken from CRC handbook³ and Palik,⁴ respectively. Dielectric constant data for the AuAg alloy were taken from Rioux *et al.*⁵ Other dielectric constant data for silver^{4,6} were examined, but CRC data was found to give convergence more readily. All calculations were performed using a mesh size of 0.3 nm near the particle. The decahedra structure was modelled by extruding pentagons at an angle of 30.45 degrees (total 200 slices). Additional rounding at the interface of the bipyramid and the vertices were employed. The particle was placed in a uniform background medium with a dielectric constant of 1.33 (for water). Excitation of the azimuthal plasmon mode was achieved using circularly polarized light with electric field in the plane of the pentagonal base.

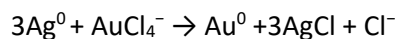
SPR measurements. 1 mL Au-AgNP sample is measured into a PMMA cell and inserted into an OpenSPR outfitted with cell holder. After approximately 500 seconds of equilibration, 10 μ L 10⁻⁶ M KI is

injected, a cell cap is put onto the cell, the cell is removed and shaken roughly 10 times, and is then reinserted. The LSPR shift is measured as the difference between the maximum LSPR after injection and the equilibrated LSPR before injection.

SERS measurements. 1 mL of AgDeNPs and Au-AgNPs were centrifuged at 3000 g for 30 minutes to prepare a concentrated 10 μ L dispersion. The concentrated dispersion was dispensed onto a plasma cleaned quartz slide, spread to ca. 1 cm^2 and then dried in an oven at 60 $^\circ\text{C}$. 10^{-5} M thiosalicylic acid was spread to the same 1 cm^2 area over the film in 10 μ L increments. Peak heights at ca. 1020 cm^{-1} for the known concentration of thiosalicylic acid relative to peak heights for pure thiosalicylic acid were used to calculate enhancement factors. Measurements were performed at 290 mW laser power with 30 s integration and frame sizes.

5.4. Results and Discussions

General features. Figure 5.1 provides an overview of the different formation pathways of Au-AgNPs. Gold is introduced to template AgNPs in a form of a gold salt. We have used tetrachloroauric acid, HAuCl_4 , as a commonly available stable gold precursor. Upon instantaneous addition of HAuCl_4 rough, stellated, shell structures are formed (Figure 5S.3A1). Consequently, addition of the gold precursor to AgNPs over a period of several hours was found to be optimal for the formation of smoother Au shells with more defined LSPR peaks (Figure 5S.3A3-5).⁴⁰ In the first stage of gold addition, with relatively low gold amounts (up to ca. 15-20 mol. % relative to silver of AgDeNPs), gold plating (pathway i) in Figure 5.1A) can be achieved with the minimal disturbance of the Ag template core, as it was previously described.⁴² Upon further increase in the amount of added gold to 30-40 mol. %, the AgNP core no longer remains intact, and formation of pits and shellated structures is observed (pathway ii) in Figure 5.1A). The formation of Au shells takes place through the galvanic replacement reaction:



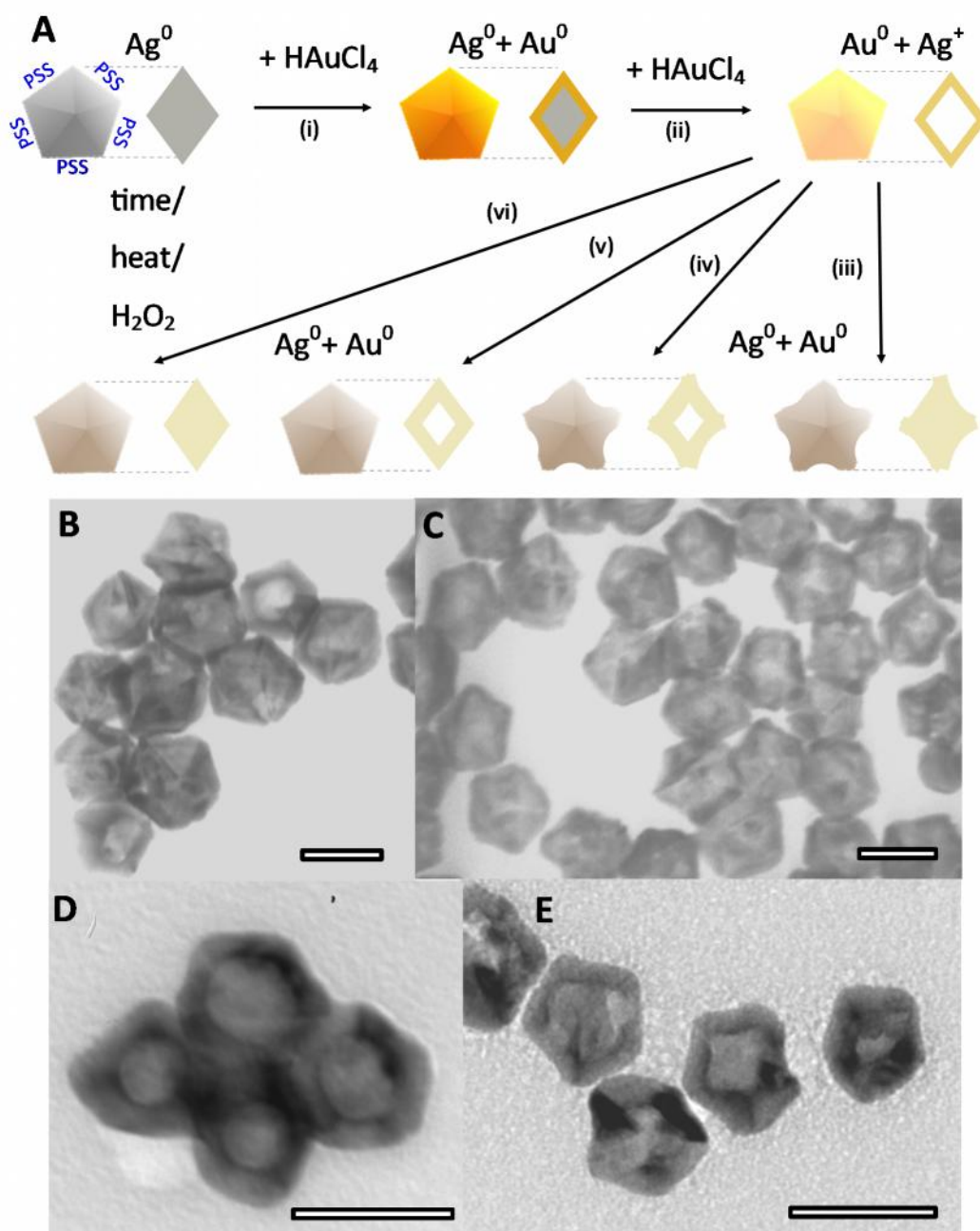


Figure 5.1. A) Schematics of the main pathways starting with i) PSS-protected AgDeNPs coated with gold (10-30 mol. % relative to Ag in AgDeNPs), followed by ii) additional gold deposition to yield gold shells (hollow gold NPs) and subsequent post-transformations iii)-iv) by silver rebuilding; B)-E) Corresponding transmission electron microscopy (TEM) images of B) 40 mol. % gold plated AgDeNPs, C) 80 mol. % gold shell NPs, D) 50 mol. % rebuilt Au-AgNPs and E) 100 mol. % rebuilt Au-AgNPs. All scale bars are 50 nm.

Following the stoichiometry, shell formation becomes a dominant process starting at ca. 40 mol. % Au (Figure 5.2B), at which regime the LSPR peak splitting is observed in the UV-vis spectra (Figure 5.2A). LSPR peak wavelength dependence on mol. % Au added is given in Figure 5S.4.

Shell formation has been documented extensively in the previous works in the field.^{14,27,38} What we have found instructive and consequential for the rebuilding process is that if PVP is used as a stabilizing polymer for AgNPs, Au shells become the final product of the gold templating with limited post-transformation. At the same time, if PSS is used as a sterically stabilizing polymer (or in absence of protective polymers for AgNPs, where it is synthetically possible) the resulting Au shells are originally rougher (Figure 5S.5) but can significantly rebuild with Ag ions reducing back to form diverse Au-AgNPs. The progression of the rebuilding process is shown in Figure 5S.6, where the LSPR wavelength was monitored for the period of 20 days for 80 mol. % Au shells formed using AgDeNPs stabilized with PSS and PVP, respectively (Figure 5S.6A). It is likely that PVP serves as a protective ligand⁴³ for the formation of the Au shells that are smoother, more compact and sealed, so they have much more limited rebuilding with silver.

The rebuilding process can be tuned to form Au-AgNPs that are both hollow ((pathways **iv**) and **v**) in Figure 5.1A, EM images in Figures 5.1C and 5S.7B1) and solid (pathways **iii**) and **vi**) in Figure 5.1A, EM images in Figures 5.1B,E, 5S.7A, and 5S.2b). The rebuilding process can also take place with a noticeable deformation of the gold shells leading to partial stellation (pathways **iii**) and **iv**) in Figure 5.1A, EM images in Figures 5.1D, 5S.7B1). The diversity of the post-transformation pathways enables convenient LSPR and stability tuning of the resulting Au-AgNPs.

Au addition to AgDeNPs. The details on Au shell formation with AgDeNP templates are illustrated in Figure 5.2. The time of the gold addition is an important parameter. Considering an example of Au shell NPs with 80 mol. % Au, rough Au coating with correspondingly broad LSPR peaks were produced when the gold precursor was delivered at once and during shorter time periods up to ca. 1 hour (Figures 5S.3A1

and A2). The smoothest coating with the respectively narrowest LSPR peak was achieved upon 48-hr addition (Figure 5S.3A5). At the same time, very close results were obtained with 12-hr gold addition, so this time was typically used for the overall efficiency of the preparation protocol (Figure 5S.3A4). The Au shell NPs feature broad LSPR peaks in the range of 650 to 750 nm and can be conveniently used in applications where gold stability and LSPR in the biologically transparent window are advantageous.

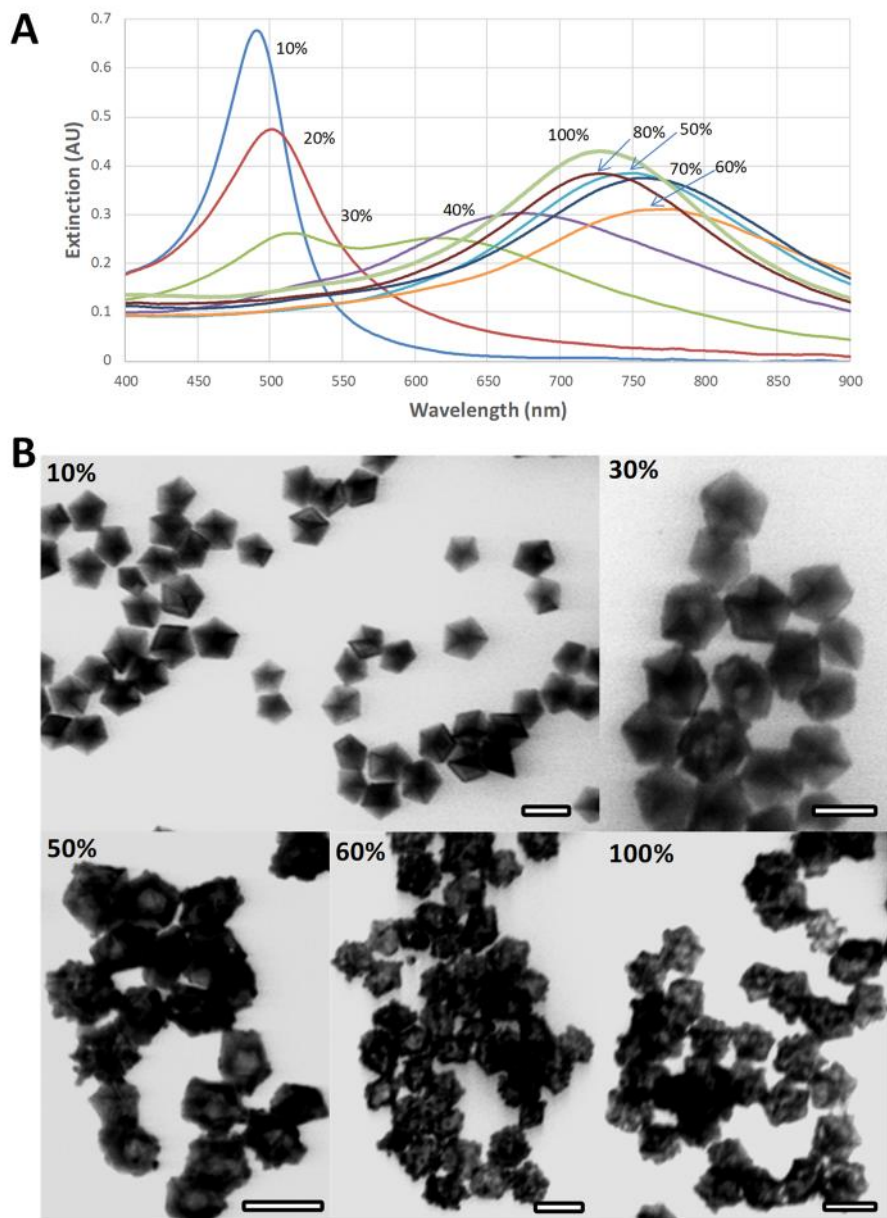


Figure 5.2. A) UV-vis spectra and B) TEM images of AgDeNPs with varying mol. % gold added labelled on individual images and spectra.

The rebuilding process. With the Au shell structures templated using PSS-protected AgNPs, the galvanically replaced silver, remaining in the solution, as Ag^+ , can rebuild the Au shells forming different Au-AgNPs. Figure 5.3A shows the optical photograph of the as-prepared dispersions of Au shells together with the representative TEM image of 100 mol. % Au gold shell. Such gold shell samples can rebuild with Ag thermally slowly (at room temperature over the period of approximately one week), given the presence of citrate in solution that serves as a reducing agent. The resulting rebuilt Au-AgNPs feature significantly blue shifted LSPR peaks, with the bluish colour of gold shells transformed to red and pink with the accompanying deepening of the colours for the aged Au-AgNP samples (Figure 5.3B). The LSPR blue shift takes place due to both forming more solid structures and surface silver dominating the plasmonic response, as it will be discussed in more details below in the section on LSPR modelling. The TEM images of samples with 100 mol. % Au in Figure 5.3 confirm the rebuilding of the shells, where the original sample (Figure 5.3C) has thinner walls, while the rebuilt sample (Figure 5.3D) shows solid thick-wall morphologies of Ag-AuNPs. The deposition of silver occurs predominantly in the interior of the particles, since they are higher in energy for the deposition and their surface is not blocked by the polymer.

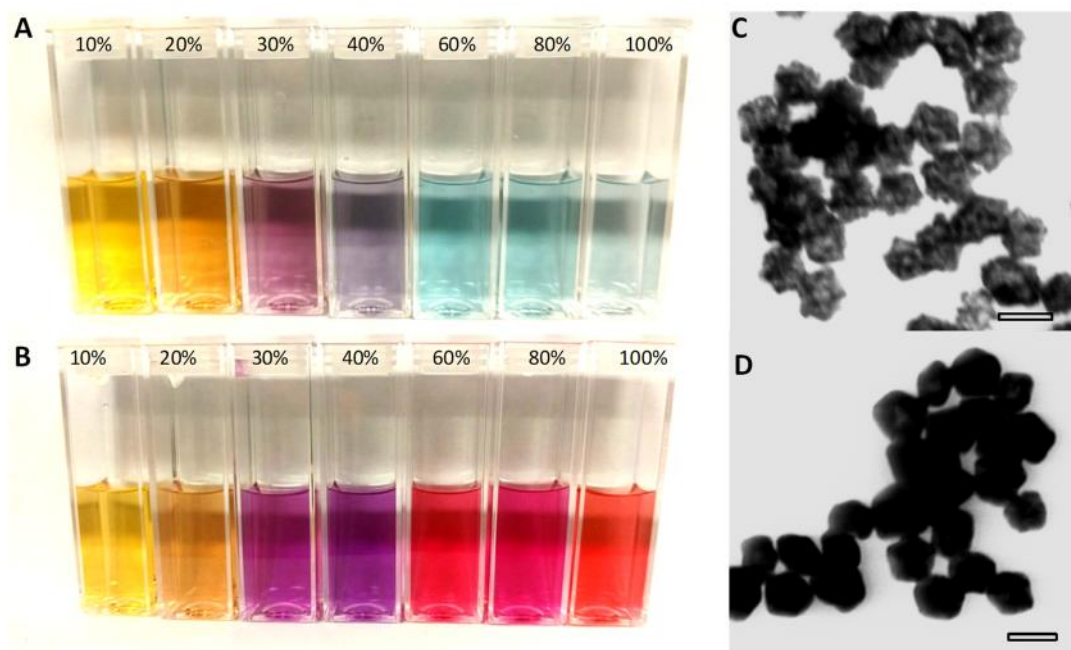


Figure 5.3. Optical photographs of Au-AgNPs **A)** immediately after coating, and **B)** 6 months after coating. TEM images are of **C)** fresh and **D)** aged 100 mol. % Au samples. All scale bars are 50 nm.

The rebuilding process was monitored by UV-vis spectroscopy and tracked in real time using an SPR setup. For the samples described in Figure 5.2, Figure 5S.8A shows the UV-vis spectra after one week, where the shells with greater than 30 mol. % Au have blue shifted significantly. Tracking the LSPR peaks of these samples over 7 days enabled monitoring and quantification of the blue shifts observed (Figure 5S.8B). Specifically, all samples with greater than 30 mol. % Au exhibited quite similar rates (slopes) of the LSPR blue shift, indicating the similar kinetics of the rebuilding for different Au shells. Given the stoichiometry of galvanic replacement, the complete dissolution of Ag^0 takes place starting at higher than 33 mol. % Au, so it is logical that these samples with the galvanically replaced silver are most active in the rebuilding process.

When the same samples were subjected to accelerated aging by thermal treatment at 95 °C (Figures 5S.8C and D), the rebuilding process was significantly expedited, completing the transformations (judged by reaching the minimum LSPR wavelength) in 2 hours. After the rebuilding process, accelerated by heating, the resulting Au-AgNP structures remained stable with minimal further LSPR changes of < 5 nm.

An alternative procedure of accelerating the rebuilding process is treatment with hydrogen peroxide (Figures 5S.8E and F), which works well for samples with greater than 50 mol. % Au, though with less pronounced LSPR shifts compared to the thermal treatment (Figures 5S.8C and D). Using hydrogen peroxide to rebuild silver may seem counterintuitive, since hydrogen peroxide can be used to dissolve silver at the neutral pH used in this work (pH range from 6.8 to 7.4).^{42,44} Two factors make hydrogen peroxide work for the rebuilding in this system: presence of citrate as a reducing agent, and the formation of a silver-gold alloy stable to hydrogen peroxide. Hydrogen peroxide may likely activate reduction by citrate through radical generation, as is well-known for the system of hydrogen peroxide and ascorbic acid.⁴⁵ Consistent with alloy formation, the rebuilding with H_2O_2 stops working for the lower mol. % Au. Instead, a red shift of the LSPR peaks for 40 mol. % Au (Figure 5S.8F curve 4) was observed, that is

indicative of the dissolution of residual silver in the Au-AgNPs with the lower Au content. Rebuilding with hydrogen peroxide for the samples with the higher Au content attests to the greatly improved stability of Au-AgNPs due to the formation of a Au-Ag alloy.

To arrest the rebuilding process, Ag^+ could be removed by centrifuging samples at 5500 g for 30 minutes, and then redispersing the centrifuged particles in water or a solution of citrate and PSS (Figure 5S.9). UV-vis spectra of samples aged after centrifugation are shown in Figures 5S.8G and H, where the LSPR undergoes only minor changes over the 7 days of aging. The other processes that slow the rebuilding process are treatment with potassium iodide to bind Ag^+ ions and block the rebuilding process. In a broader picture, the factors that enhance the rebuilding of Au-AgNPs include thermal treatment, exposure to light and hydrogen peroxide. The corresponding LSPR graphs are presented in SI for the rebuilding of Au-AgNPs of 80 mol. % Au with light exposure (Figure 5S.10 curve 3), peroxide (Figure 5S.11 curves 2 and 4) and iodide treatments (Figure 5S.10 curve 8).

Importantly, silver does not form any other small NPs during the rebuilding process, as confirmed by UV-vis spectroscopy and EM microscopy, since the reduction process is appreciably slow and most energetically favourable deposition on already existing surface occurs. Furthermore, concentration of silver ions is low (<0.1 mM) for the nucleation of new AgNPs in the system.

Finally, we could observe a second cycle of rebuilding after the dissolution of silver from Au-AgNPs using hydrogen peroxide and iodide and then subjecting the samples to the heat treatment with citrate. Such transformations should be useful for the fine-tuning of the LSPR peaks, which can be accomplished with the precision of ca. 5 nm.

Understanding transformations in Au-AgNPs by FDTD modelling. While the overall process of shell formation and rebuilding is fairly clear and understandable, the details on remaining silver in Au shells and distribution of the metals in the Au-AgNPs, especially the plasmonically important surface layer,⁴⁶ are far from straightforward. In our previous work⁴² we realized that there are limitations of EDX

and XPS for nanoparticles characterization, further exacerbated by inhomogeneities in metal distribution. As a result, we have employed FDTD modelling to quantify Ag and Au in the surface layer and to provide further insight on shell formation and rebuilding in Au-AgNPs.

The simulated spectra of AgDeNPs are highly sensitive to the optical constant of metal used in the modelling and rounding of the vertices of the structures.⁴⁷ Using different data on optical constants of silver (e.g. Palik⁴⁸ and Johnson and Christy⁴⁹) yields differences as large as 10 nm in the LSPR peak wavelength of AgDeNPs. Such variations are pointed out recently in the literature in the field.⁵⁰ The effect of rounding on pure AgDeNPs can be seen in Figure 5S.12, where the LSPR undergoes blue shift with the increasing rounding. Because of the sensitivity of the optical properties to the fine structure of the decahedra and the materials dispersion of Ag, a qualitative instead of absolute comparison between modelled and experimental results are discussed. Moreover, surface ligands were not incorporated in the modelling as their effects, which are not only governed by their dielectric properties, but also by the chemical interaction with the nanoparticle,⁵¹ would be secondary compared to the high sensitivity of LSPR to the decahedra geometry and composition. The details on the modelling are provided in SI, as well as representative FDTD calculations of electric field intensity (Figure 5S.13).

At the initial Au plating stage, the LSPR red shifts and weakens in intensity due to the red-shifted relative to silver and *d-sp* dampened plasmonic response of gold. This spectral shape of the LSPR peaks of plated NPs could be best matched by the formation of alloy shells of $\text{Au}_x\text{Ag}_{100-x}$, where x and the shell thickness both increase with the increasing mol. % Au. Specifically, we modelled 10 mol. % Au, extensively explored in our previous work,⁴² by formation of 2-nm shell of $\text{Au}_{50}\text{Ag}_{50}$ on the Ag decahedra – such an alloy shell results in a LSPR red shift of 19 nm relative to that of AgDeNPs that has been observed experimentally (Figure 5S.14, Table 5S.2). At the same time, based on the gold-to-silver ratio and the size of the decahedra, 10 mol. % of Au would correspond to 0.9 nm of pure Au shell. However when thin layers of pure Au are used to model the surface layer, the spectra broaden drastically with much larger red shifts

and dampening in the intensity, as compared to the experimental data (Figure 5S.14). Likewise, the sample with 20 mol. % Au is successfully modelled by incorporating 2.5-nm shell of $\text{Au}_{80}\text{Ag}_{20}$ on AgDeNPs, which results in a LSPR shift of 43 nm relative to the LSPR of AgDeNPs. At the same time, if the shell is modelled to be composed of pure Au, the LSPR spectra undergo much larger red shifts with drastic broadening and dampening in the intensity, compared to experimental data (Figure 5S.14, Table 5S.2). Consequently, it is plausible that Au-Ag alloy shells are formed in the plating process, which offers an important insight in the plating process and formation of Au shells.

Experimentally, 30 mol. % Au yields a mixture of hollow shell structures and plated decahedra. At > 40 mol. % Au, hollow shell structures dominate. The modelled spectra 3-7 in Figure 5.4 illustrate the underlying changes to the shell composition, thickness and NP size with increasing mol. % Au. (see Table 5S.2 for details). We modelled 40 and 50 mol. % Au samples with 44 nm $\text{Au}_{80}\text{Ag}_{20}$ DeNPs in which the former has an inner layer of Ag. Spectra 3 and 4 (Figure 5.4) show that dissolution of silver in the inner layer leads to a red shift in the LSPR. Upon increasing Au content in Au shells, the shell thickens and more Au-rich or pure Au structures are formed. We modelled these structures with 46 and 48 nm of DeNPs with shell compositions of $\text{Au}_{90}\text{Ag}_{10}$ and finally Au. The morphological changes beyond 50 mol. % (spectra 5-6) lead to a slight blue shift in the LSPR peak accompanied by an increase in LSPR intensity with increasing Au content – in line with the experimental observations. The presence of Ag in the shells of 80 mol. % Au sample was experimentally confirmed by silver removal. On the other hand, similar tests for 100 mol. % Au sample suggests the particles are pure Au. In summary, the effect of increasing Au content can be separated in two regimes: in the initial plating stage Au dampens LSPR; in the subsequent stages where shell structures are formed, higher Au content results in stronger LSPR. Note that rounding and roughening of the decahedral structures during the shell formation, which were observed experimentally, are not accounted for in the simulation. When combined with increasing size distribution, these factors

may account for the lower LSPR intensity observed for Au shells experimentally compared to the modelling.

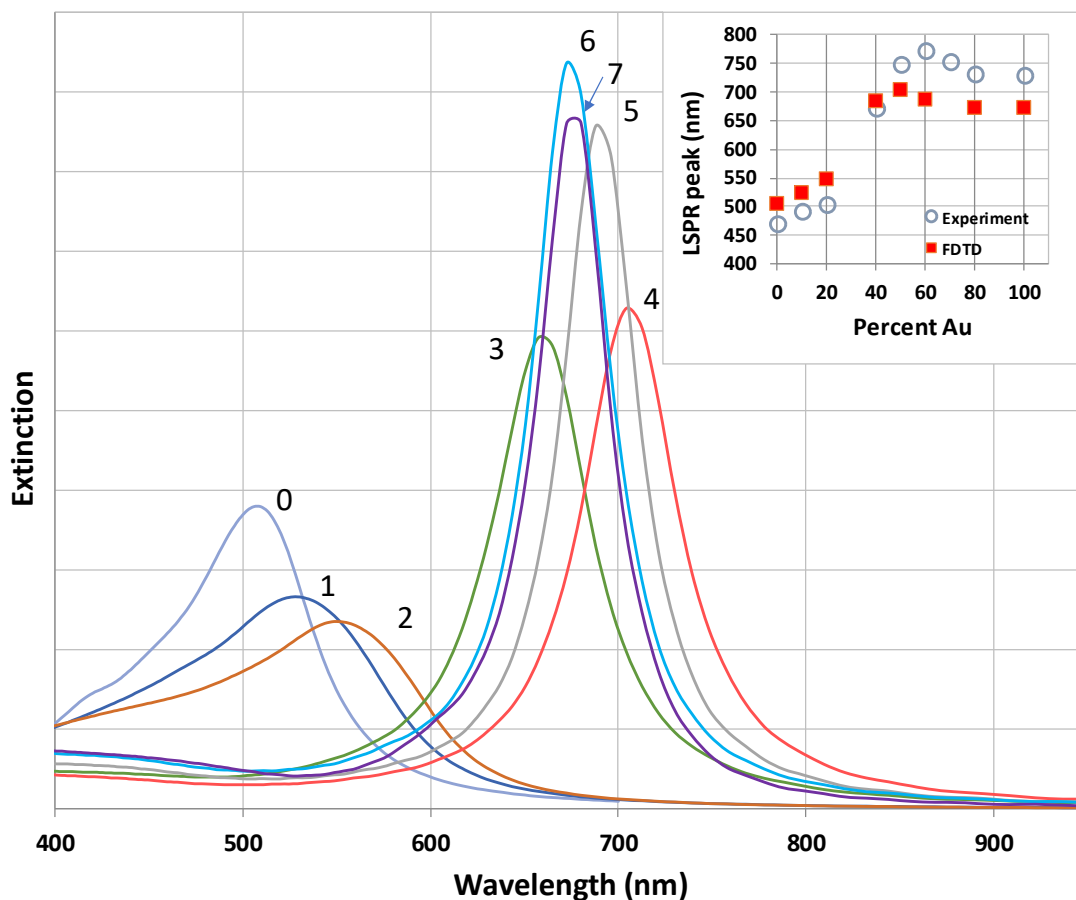


Figure 5.4. FDTD simulated extinction spectra of different compositions and sizes of solid and hollow decahedra mimicking the samples with various mol. % Au in the experiment: 0 – 0%; 1 – 10%; 2 – 20%; 3 – 40%; 4 – 50%; 5 – 60%; 6 – 80%; 7 – 90-100%. The details of the parameters (composition, size) used in the simulations are listed in Table 5S.2. Inset shows the LSPR peak wavelengths of experiments compared to FDTD simulations.

Chemical and colloidal stability. The gold content of the shells and Au-AgNPs is expected to lead to their significantly improved chemical stability compared to original AgDeNPs. To confirm and quantify this, stability tests of Au shells and rebuilt Au-AgNPs were performed using sodium hydrosulfide (up to 1 mM) and hydrogen peroxide (0.5 M) (Figures 5S.15-5S.17). Figures 5S.15 and 5S.16 present changes in the wavelength of LSPR peaks, while Figure 5S.17 documents the changes in the intensities of the LSPR peaks. The time of exposure (15 minutes) was chosen to be close to a typical time frame of SPR and SERS

experiments. The data for the stability in 2 hours (not shown) are very similar. Freshly prepared Au shells with mol. % Au greater than 90 were slightly susceptible to hydrosulfide, where a red shift of LSPR was observed (Figure 5S.15). Aged Au-AgNP samples exhibited significantly improved stability, especially at higher concentrations of hydrosulfide (Figure 5S.16). Au shells with 40 mol. % Au were most susceptible to H₂O₂ and exhibited most transformation, likely due to their mixed population of plated structures and shells. Overall, the chemical stability of rebuilt Au-AgNPs, especially at higher mol. % Au, is significantly improved relative to original AgDeNPs, as well as freshly prepared samples.

The colloidal stability of Au shells and Au-AgNPs was also tested and confirmed by measurement of zeta potentials for the series of the samples prior and after the rebuilding process (Figures 5S.18 and 5S.19). With zeta potentials of ca. – 40 mV, Au shells and Au-AgNPs clearly remain colloidally stable, since citrate and PSS provide charge and steric stabilization. The comparison of aged Au-AgNPs and freshly prepared samples (Figure 5S.18) demonstrates that the stability is not compromised both during the rebuilding process and upon extended storage. Size measurements for the same samples, as in zeta potential measurements, were also performed (Figure 5S.20). The measured sizes, determined based on the diffusion coefficients, are in a reasonably good correlation with the results of electron microscopy. At the same time, it should be noticed that the values of polydispersity index (PDI) and corresponding standard deviation in the estimated size are much larger than expected for the observed particle size distribution, which likely occurs due to strong multiple scattering.⁵² The standard deviation and the absolute errors of the measurements are the highest for the samples with the LSPR peaks close to the laser wavelength (633 nm) used for the measurements (Figure 5S.21).

Applications of Au-AgNPs: SPR and SERS. Practically, in terms of the combination of the LSPR tuning and stability, 80 mol. % Au is the optimal system, which is chemically stable (Figures 5S.15-5S.17) and features the largest LSPR range: Au shells with the LSPR peak at ca. 700 nm (Figures 5.2 and 5S.8) that can be rebuilt into Au-AgNPs with the LSPR at 500nm (Figures 5.2 and 5S.16).

Formation of Au shells and Au-AgNPs with tuneable LSPR and enhanced stability are advantageous for plasmonic applications. We have explored SPR and SERS to demonstrate the applicability and merits of the developed Au-AgNPs. Figures 5S.22 and 5S.23 show the SPR sensing of low iodide concentrations, as a model system to compare the response of different NPs.⁵³ The largest sensitivity is observed for the Au shells with 80 mol. % Au. The Au shells produce larger SPR shifts despite their broader LSPR peaks, which can be likely attributed to morphological changes.³³ The rebuilt Au-AgNPs are more rounded and compact with a smoother surface, so their SPR response is not as strong as for Au shells (Figure 5S.23).

Figure 5S.24 presents a comparison of several prepared samples as SERS substrates. Interestingly, 10 mol. % Au plating showed the best relative enhancement, even compared to AgDeNPs. We have tested both as prepared and plasma cleaned AgDeNPs to assure that PSS or other ligands are not a factor in the comparison. The formation of Au-Ag alloy on the surface, supported by FDTD modelling, is likely responsible for such results. Expectedly, Au shells display lower enhancement due to lower efficiency of gold in SERS. With the increasing Ag content, the rebuilt Au-AgNPs feature appreciably higher enhancement. Specifically, the samples with 80 and 100 mol. % Au proved to be optimal for SERS measurements due to their combination of enhancement and chemical stability.

Au-AgNPs with other templating AgNPs. To attest the universality of the procedure of formation of Au-AgNPs, template AgNPs other than decahedra were explored. Figure 5.5 presents the results of shell formation and rebuilding with silver platelet NPs. Similar to AgDeNPs, well-defined LSPR shifts can be observed from the original AgNPs to the Au shells and then back to the rebuilt Au-AgNPs (Figure 5.5A). Corresponding EM images Au shells and rebuilt structures are shown in Figures 5.5C and 5S.25. Using silver pentagonal rods as template NPs, similar LSPR shifts were observed, although less defined (Figures 5S.26 and 5S.27), likely due to more fragile (100) surfaces of the pentagonal rods. With the Ag platelets we have also tested the effect of the absence of stabilizing polymer, which worked reasonably well in

terms of structural transformation. These results demonstrate that PVP exerts strong influence on formation of Au shells and likely renders the shells more sealed for the rebuilding with silver. Formation of Au-AgNPs at different PVP and PSS concentrations and in presence of different polymers, such as poly(acrylic acid) will be further explored in future work.

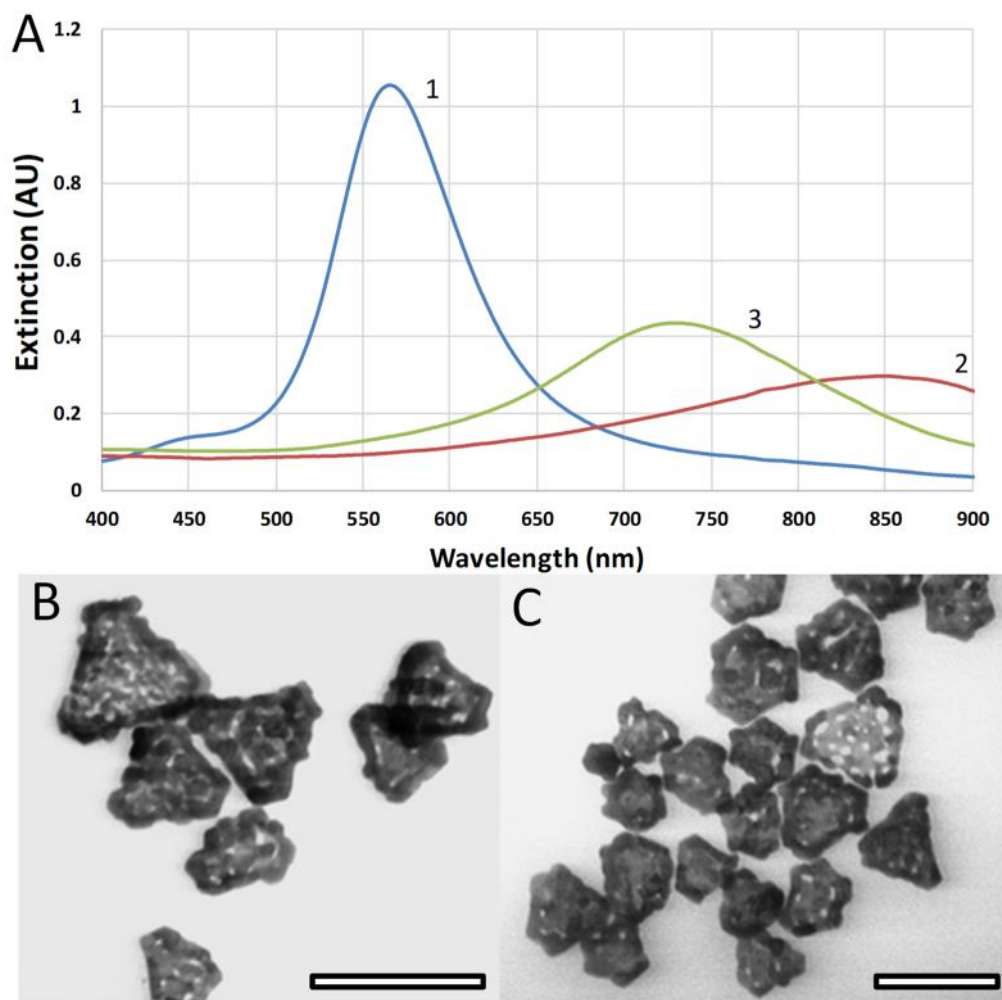


Figure 5.5. A) UV-vis spectra of **1**) original Ag platelets, **2**) 80 mol. % Au shells and **3**) Au-AgNPs after the rebuilding process by thermal treatment at 95 °C for 2 hours. B)-C) TEM images of B) 80 mol. % Au shells and C) rebuilt Au-AgNPs, corresponding to spectra **2**) and **3**) in A), respectively. All scale bars are 100 nm.

5.5. Summary and Conclusions

The formation of Au shells and rebuilding of silver to form Au-AgNPs were studied for different parameters, including amount of gold, conditions of post-transformation and template AgNPs. The

absence of PVP was identified as the main criteria for the optimal rebuilding process. The protocols were developed and described to achieve nanoparticles with superior stability and a wide range of LSPR peak tuning (470 nm to 800 nm) that are advantageous for SPR and SERS applications.

5.6. Acknowledgements

The authors are grateful to NSERC (Discovery and PGS) for the funding support. Ashley Nguyen and Stefen Stangherlin are thanked for providing samples of silver pentagonal rods and platelets, respectively. Ilya Gourevich and Neil Coombs are acknowledged for their invaluable support with the electron microscopy and Centre for Nanostructure Imaging, University of Toronto, for access to imaging facilities.

5.7. Supporting Information.

Additional synthetic details

AgDeNP synthesis. In a 20 mL borosilicate glass vial with 12.7 x 3.2 mm stir bar, 14 mL high purity deionized water is combined with 520 μ L sodium tricitrate (0.05 M), 23 μ L poly(styrene sulfonate) (0.05 M), 25 μ L arginine (0.005 M), 400 μ L silver nitrate (0.005 M), and 200 μ L sodium borohydride (0.1 M). After the solution colour darkens, 300 μ L hydrogen peroxide (10.4 M) is added, and the vial is exposed to LED (455 nm, 1 W) light for 14 hours.^{22,23}

²² Pietrobon, B.; Kitaev, V. Photochemical Synthesis of Monodisperse Size-Controlled Silver Decahedral Nanoparticles and Their Remarkable Optical Properties. *Chem. Mater.* **2008**, *20*, 5186-5190.

²³ Murshid, N.; Keogh, D.; Kitaev, V. Optimized Synthetic Protocols for Preparation of Versatile Plasmonic Platform Based on Silver Nanoparticles with Pentagonal Symmetries. *Part. Part. Syst. Charact.* **2014**, *31*, 178-189.

Table 5S.1. Experimental details of samples presented in **Figure 5S.1.**

LSPR wavelength (nm)	Mol. % Au	Treatment	NP structure	Sample #
472	0	N/A	AgDeNPs	NY69
501	20		Au-plated AgDeNPs	NY183
526	40	Aged 4 months	Rebuilt Au-AgNPs	NU631
541	80	Treated with H ₂ O ₂ , aged 3 months	Rebuilt Au-AgNPs	NU437P
574	80	Treated with H ₂ O ₂	Rebuilt stellated Au-AgNPs	NU496P
605	100	Heated at 95 °C, aged 6 days	Partially rebuilt Au-AgNPs	NY190A
618	100	Aged 7 days	Partially Rebuilt Au-AgNPs	NY190
653	70	Aged 7 days	Au shells	NY188
669	80	Centrifuged and redispersed, then aged 3 months	Au shells	NY438
700	60	Centrifuged and redispersed	Au shells	NY187B
728	100		Au shells	NY190
756	70		Au shells	NY188
772	80	Aged 2 months	Au shells	NV60
792	80	Aged 2 months	Au shells	NV59

Table 5S.2. Detailed information on the simulated spectra presented in **Figure 5.4.**

%Au	Experimental		FDTD			
	Size (nm)	LSPR (nm)	Size (nm)	Shell material, thickness	Core material	LSPR (nm)
0	39.4-41	470	41	N/A	Ag	506
10	43.2	493	41	Au ₅₀ Ag ₅₀ , 2nm	Ag	525
20		504	41	Au ₈₀ Ag ₂₀ , 2.5 nm	Ag	549
40	44.0	673	44	Au ₈₀ Ag ₂₀ , 3 nm	1 nm Ag under shell, hollow interior	685
50	44.8	749	44	Au ₈₀ Ag ₂₀ , 3 nm	Hollow	704
60	47.6	772	46	Au ₉₀ Ag ₁₀ , 3.5 nm	Hollow	688
80	48.3	732	48	Au ₉₀ Ag ₁₀ , 4 nm	Hollow	673
90 - 100	48- 49.1	729	48	Au, 4.5 nm	Hollow	673

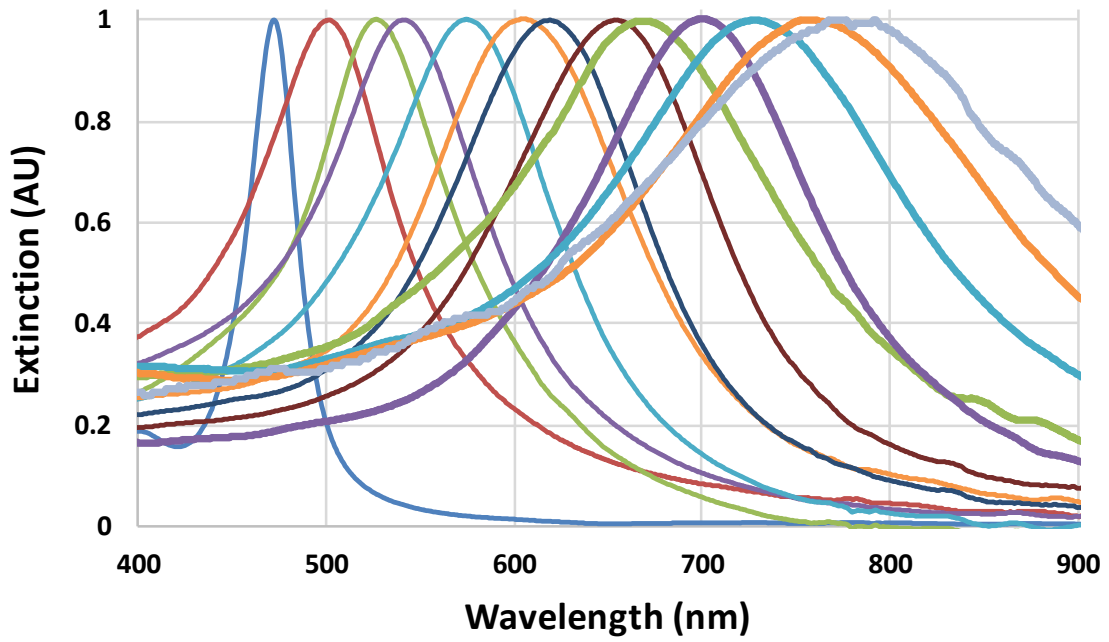


Figure 5S.1. Normalized extinction UV-vis spectra with a representative range of LSPR tuning for AgDeNPs, Au shells and Au-AgNPs covering the visible-near IR range of the electromagnetic spectrum. Experimental details on specific samples are summarized in Table 5S.1.

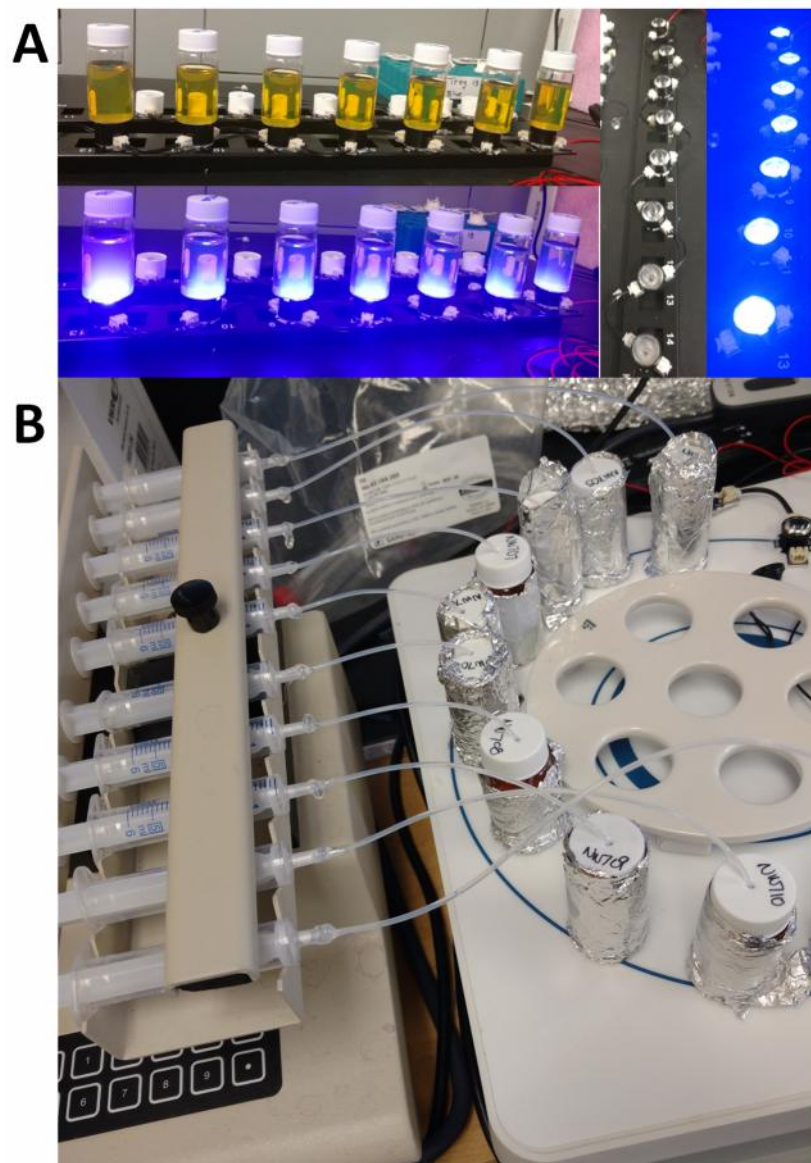


Figure 5S.2. Photographs of **A)** LED setup for synthesis of AgDeNPs and **B)** syringe pump assembly for tetrachloroauric acid addition.

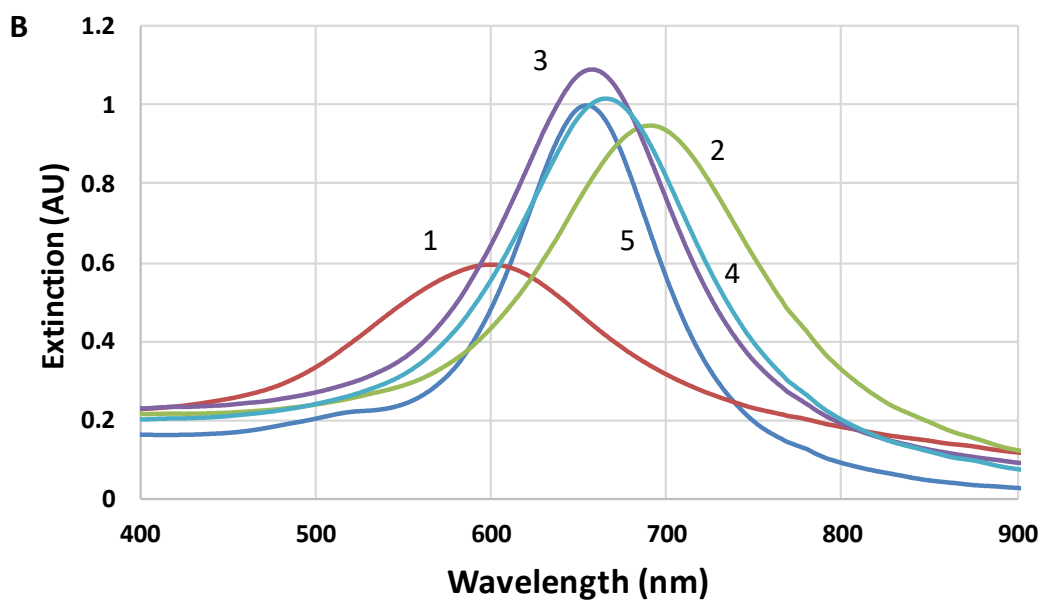
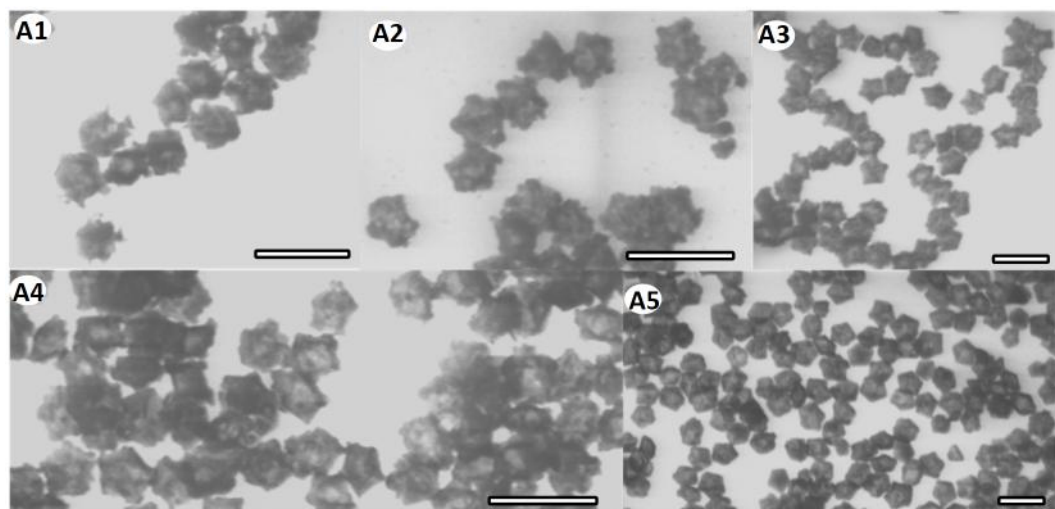


Figure 5S.3. A) Transmission electron microscopy (TEM) images and **B)** UV-vis spectra of Au shells with 80 mol. % Au prepared by varying the time of the gold precursor addition: **1** – at once, **2** – 1 hour, **3** – 4 hours, **4** – 12 hours, and **5** – 48 hours. All scale bars are 100 nm.

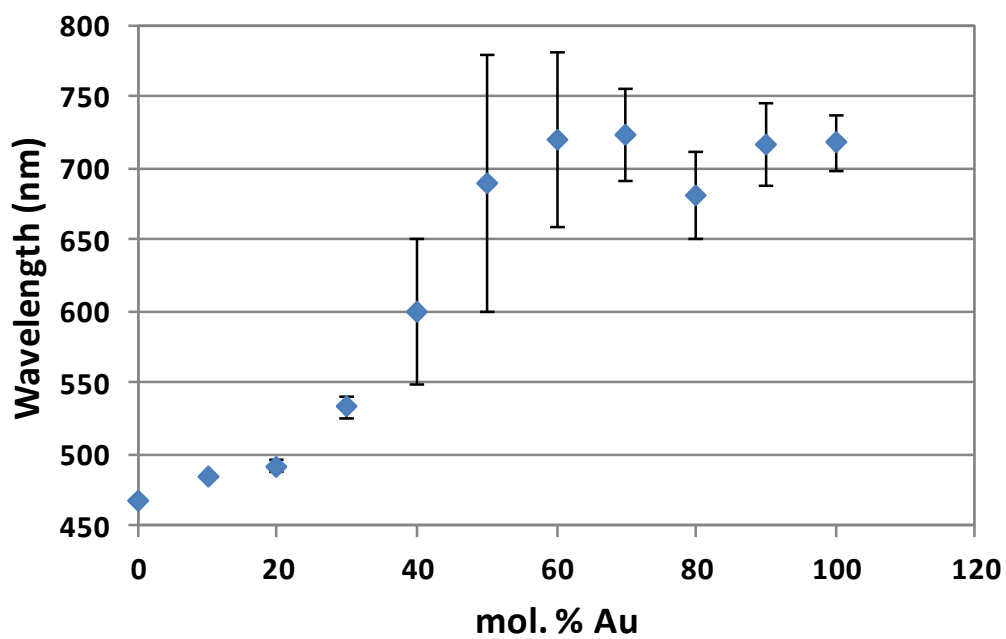


Figure 5S.4. LSPR peak wavelength as a function of the mol. % Au added demonstrating the reproducibility of the procedure. Each individual point is averaged for 4-25 samples, with the standard deviation represented as error bars.

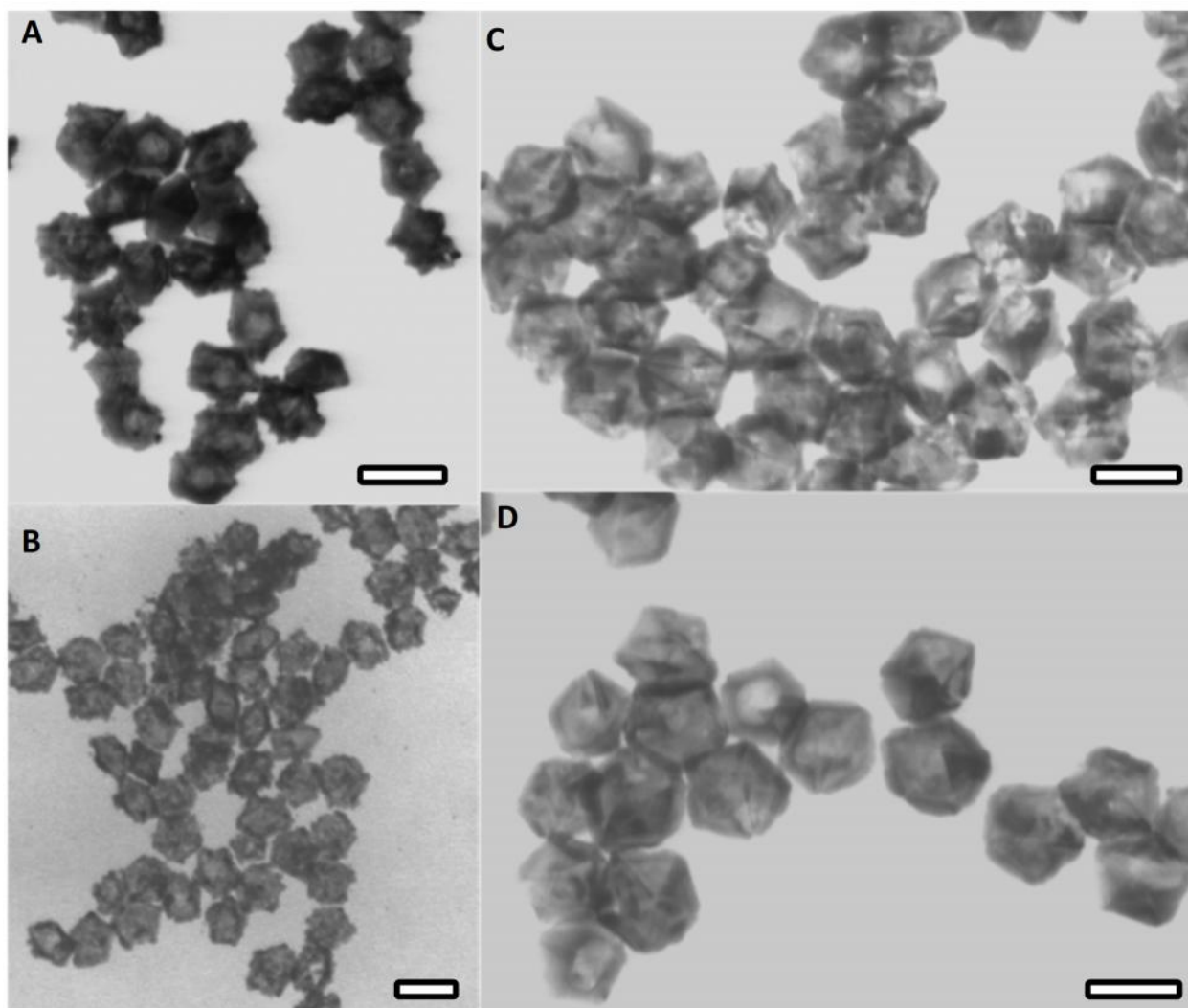


Figure 5S.5. TEM images of A) 50, B) 70, C) 60, and D) 40 mol. % Au-AgDeNPs prepared with PSS (A and B) or PVP (C and D). All scale bars are 50 nm.

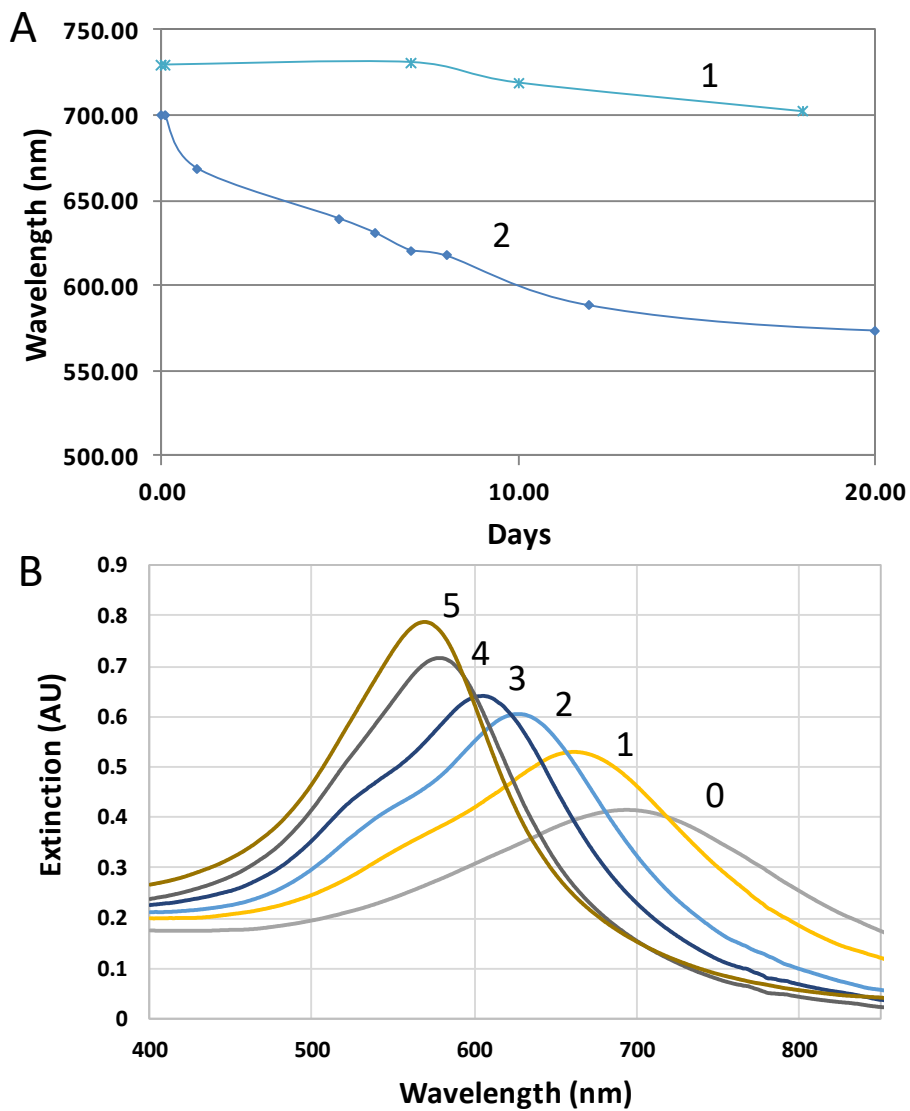


Figure 5S.6. A) LSPR peak tracking with time for 80 mol. % Au added to AgDeNPs prepared (and stabilized) with either PVP (1) or PSS (2) and **B)** UV-vis spectra of 80 mol. % Au added to AgDeNPs prepared with PSS monitoring the room-temperature rebuilding process at different times: **0)** as prepared, **1)** after 1 day, **2)** after 5 days, **3)** after 8 days, **4)** after 12 days, and **5)** after 20 days.

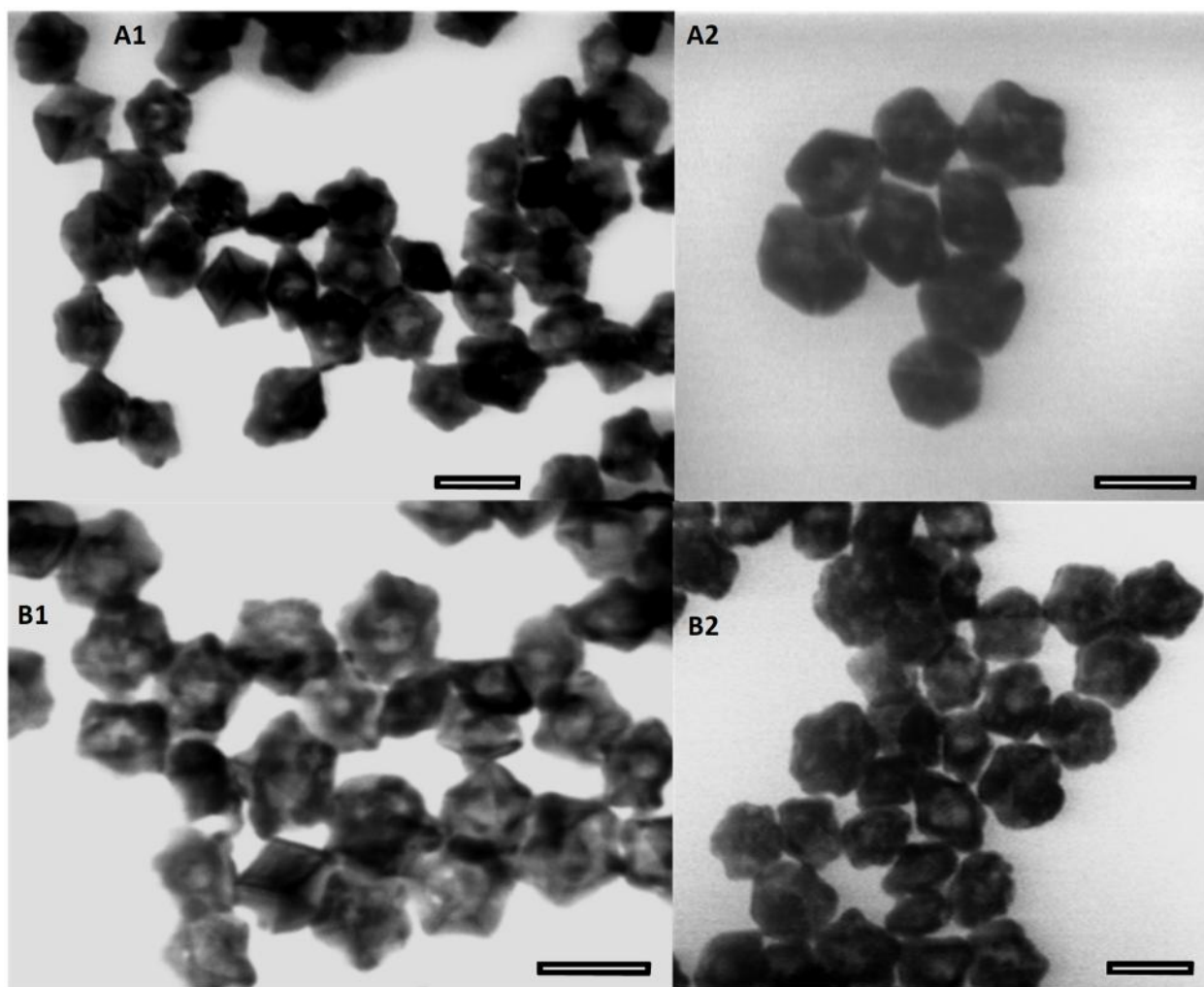


Figure 5S.7. TEM images of aged samples treated with 0.5 M hydrogen peroxide. 1) 50 mol. % Au, 2) 80 mol. % Au. A) aged sample, B) after treatment with hydrogen peroxide. All scale bars are 50 nm.

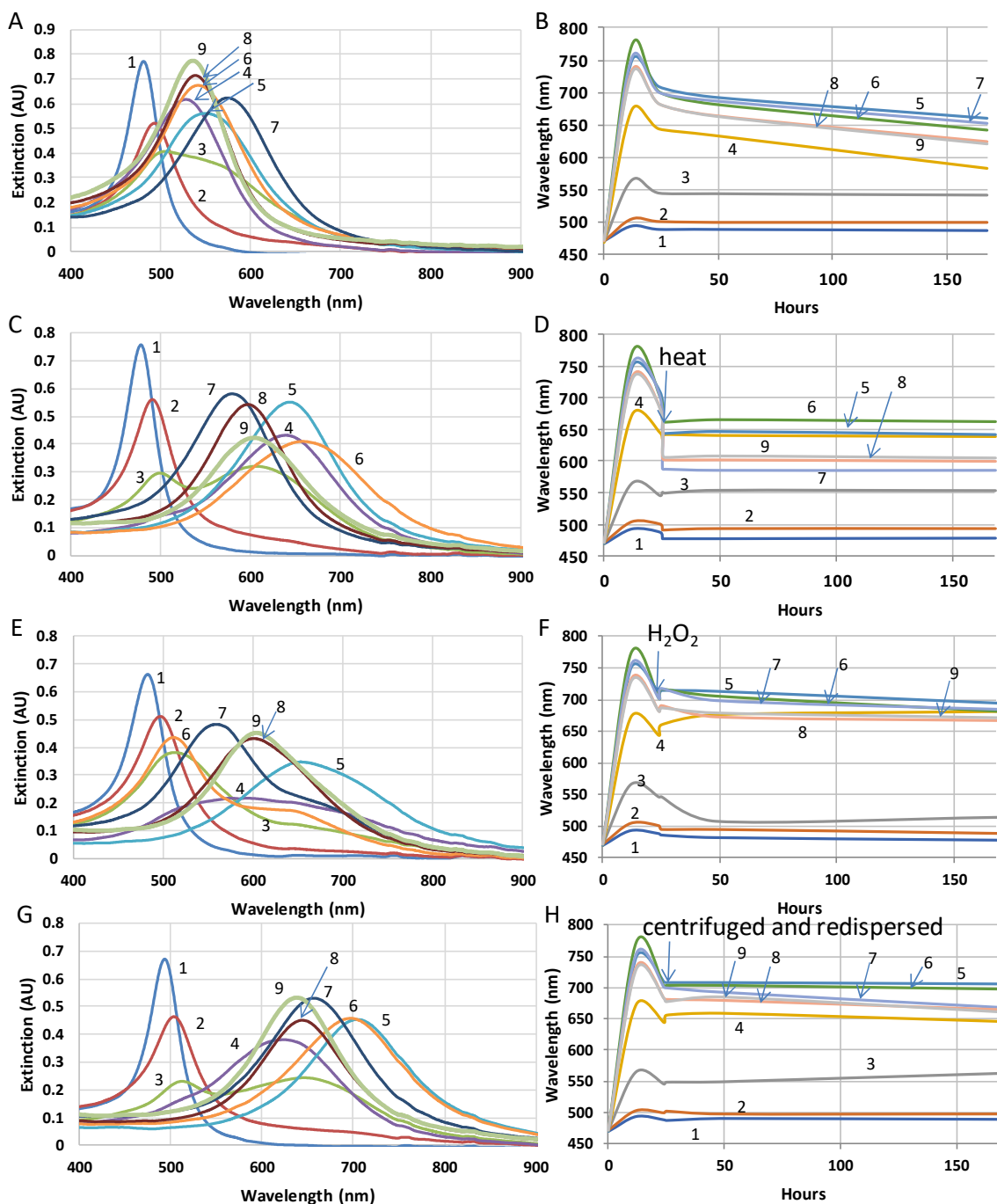


Figure 5S.8. UV-vis spectra (A,C,E,G) and LSPR peak tracking (B,D,F,H) for samples presented in Figure 5.2. Each sample from Figure 2 was portioned into 4 aliquots and monitored either with no treatments (A&B) or after heating at 95 °C for 2 hours (C&D), after 1.3 mM hydrogen peroxide treatment (E&F) or after centrifugation and redispersal in water (G&H). UV-vis spectra are of the samples after 7 days. LSPR peak tracking start with silver decahedra LSPR at hour 0, gold addition at hour 2, and different treatments at 24 hours (point is labeled on day vs LSPR column). Percentages of added gold are as follows (mol. % Au): **1-** 10 mol. %, **2-** 20 mol. %, **3-** 30 mol. %, **4-** 40 mol. %, **5-** 50 mol. %, **6-** 60 mol. %, **7-** 70 mol. %, **8-** 80 mol. %, and **9-** 100 mol. %. For ease of LSPR representation, two peaks of sample 3 (30 mol. %) were averaged, if bimodal.

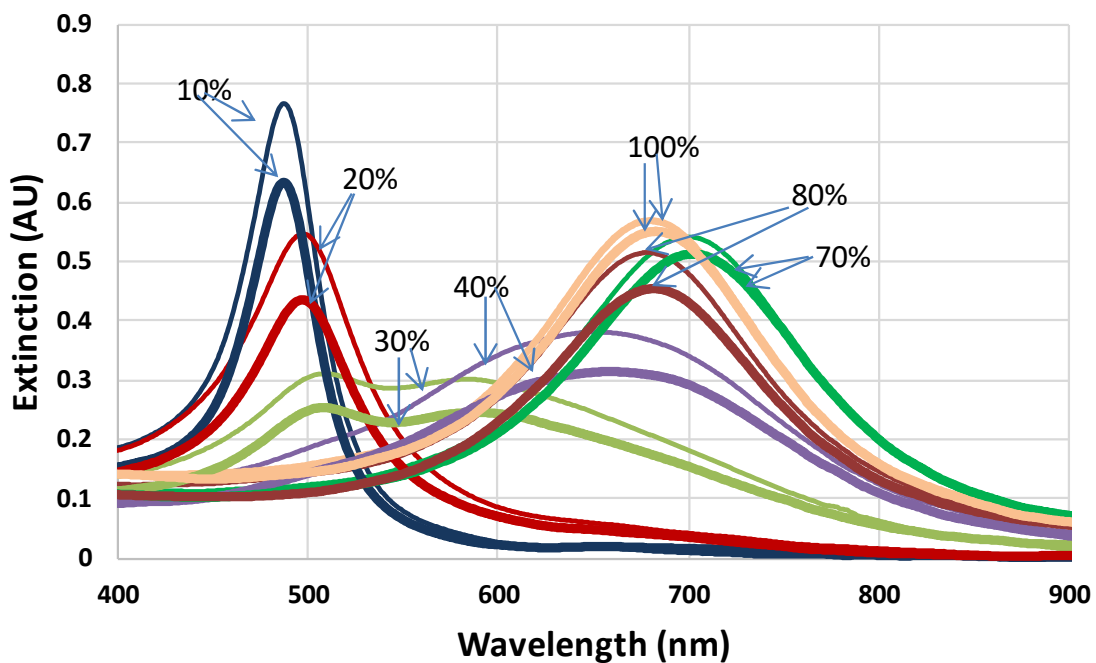


Figure 5S.9. UV-vis spectra of gold coated AgDeNPs (mol. % Au labeled on individual spectra) before and after centrifugation and redispersal in water. Thin curves are original samples and thicker curves are after centrifugation and redispersal.

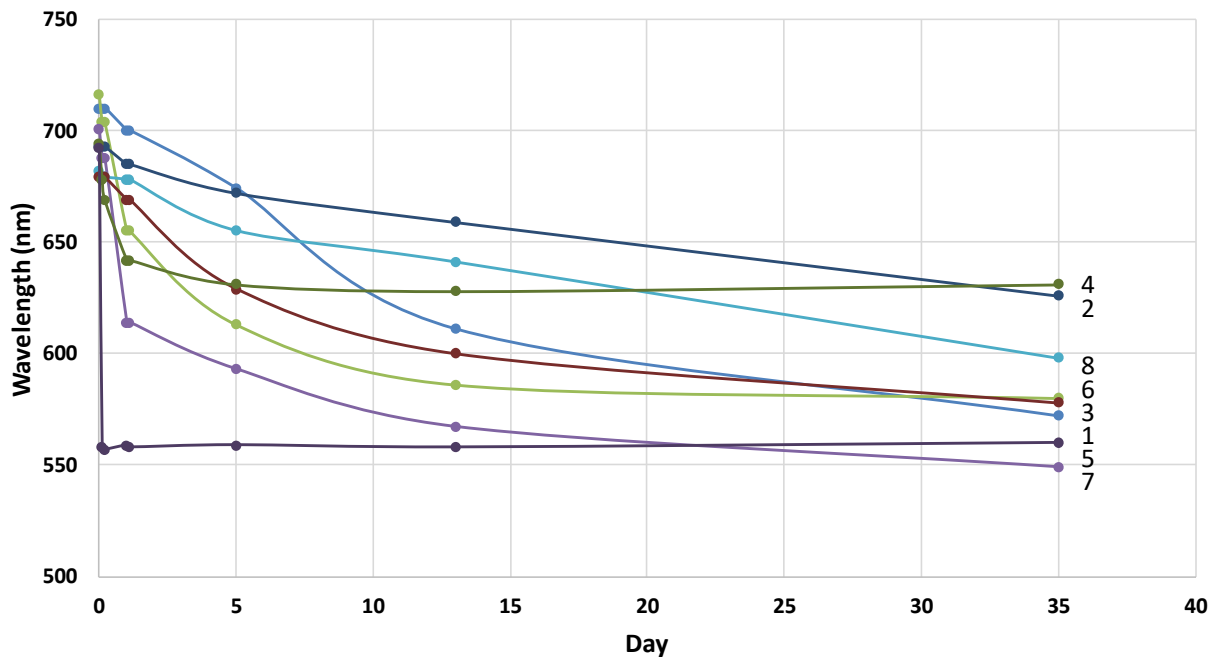


Figure 5S.10. LSPR tracking with time (in days) for 80 mol. % Au coated decahedra (gold shells) with varying treatments. 1) as prepared, 2) dark, 3) exposed to ambient sun light near the window, 4) heating at 60 °C overnight, 5) heating at 95 °C for 2 hours, 6)-8) treatment with 6) 0.2 M hydrogen peroxide, 7) 0.4 M hydrogen peroxide, and 8) 10^{-4} M KI.

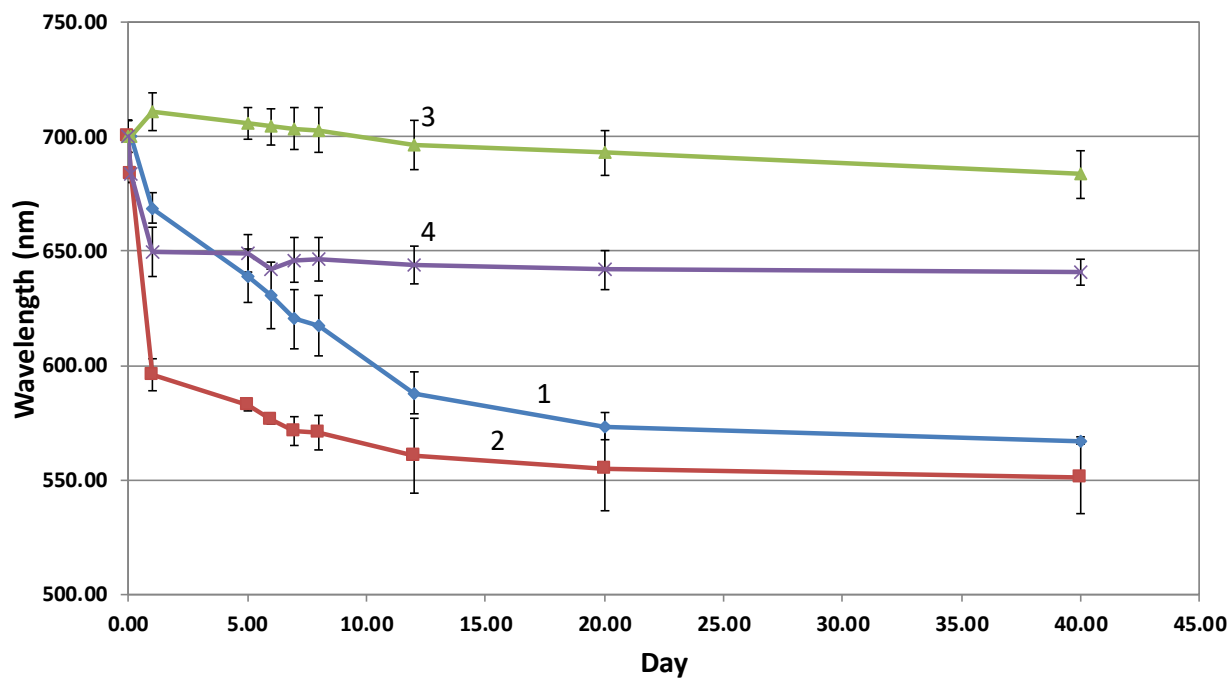


Figure 5S.11. LSPR tracking with time (in days) of 80 mol. % Au coated decahedra (gold shells) subjected to different treatments: **1)** as is, **2)** treated with 0.1 M peroxide, **3)** centrifuged and redispersed, and **4)** treated with 0.1 M peroxide followed by centrifugation and redispersal in water.

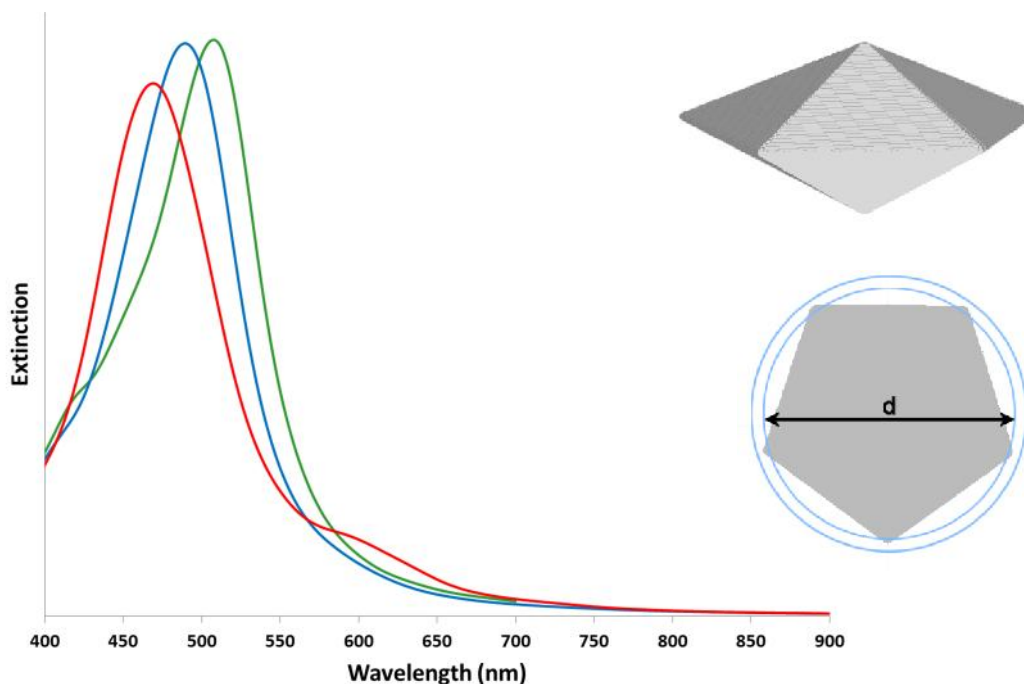


Figure 5S.12. FDTD simulated spectra of Ag decahedra with different rounding of the edges of AgDeNPs. The as-extruded decahedron (shown in top inset) has 1 nm rounding of the pentagonal vertices. Dielectric rings ($n=1.33$) of different inner diameters were employed as etch material to simulate additional rounding: $d = 42$ nm (green), 40 nm (blue) and 38 nm (red). The top inset shows the perspective view of the decahedron; the bottom inset shows the top-view of the structure.²⁴⁻²⁷

²⁴ Hagemann, H. J.; Gudat, W.; Kunz, C. Optical constants from the far infrared to the x-ray region: Mg, Al, Cu, Ag, Au, Bi, C, and Al_2O_3 . *J. Opt. Soc. Am.*, **1975**, *65*, 742-744.

²⁵ Palik, E. D. *Handbook of optical constants of solids*. Academic Press: Orlando, **1985**; Vol. 1.

²⁶ Rioux, D.; Vallières, S.; Besner, S.; Muñoz, P.; Mazur, E.; Meunier, M. An analytic model for the dielectric function of Au, Ag, and their alloys. *Adv. Opt. Mater.* **2014**, *2*, 176-182.

²⁷ Johnson, P. B.; Christy, R. W. Optical Constants of the Noble Metals. *Phys. Rev. B*, **1972**, *6*, 4370-4379.

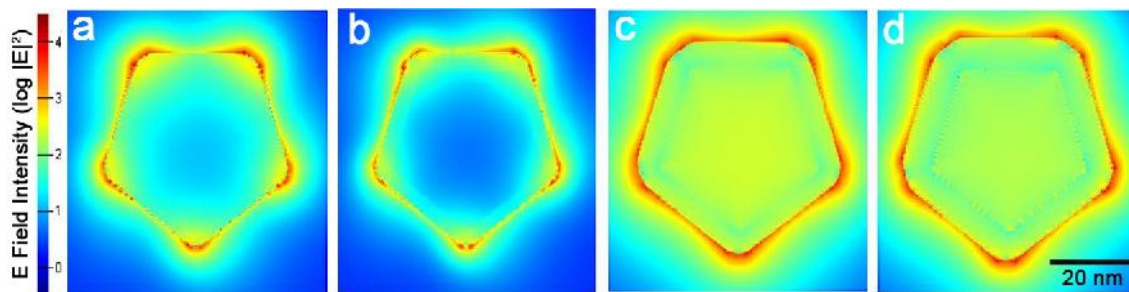


Figure 5S.13. FDTD calculations of electric field intensity ($|E|^2$) at peak LSPR of the decahedra used for modelling structures with different mol. % of Au: **a)** 0%, **b)** 20%, **c)** 60% and **d)** 100%.

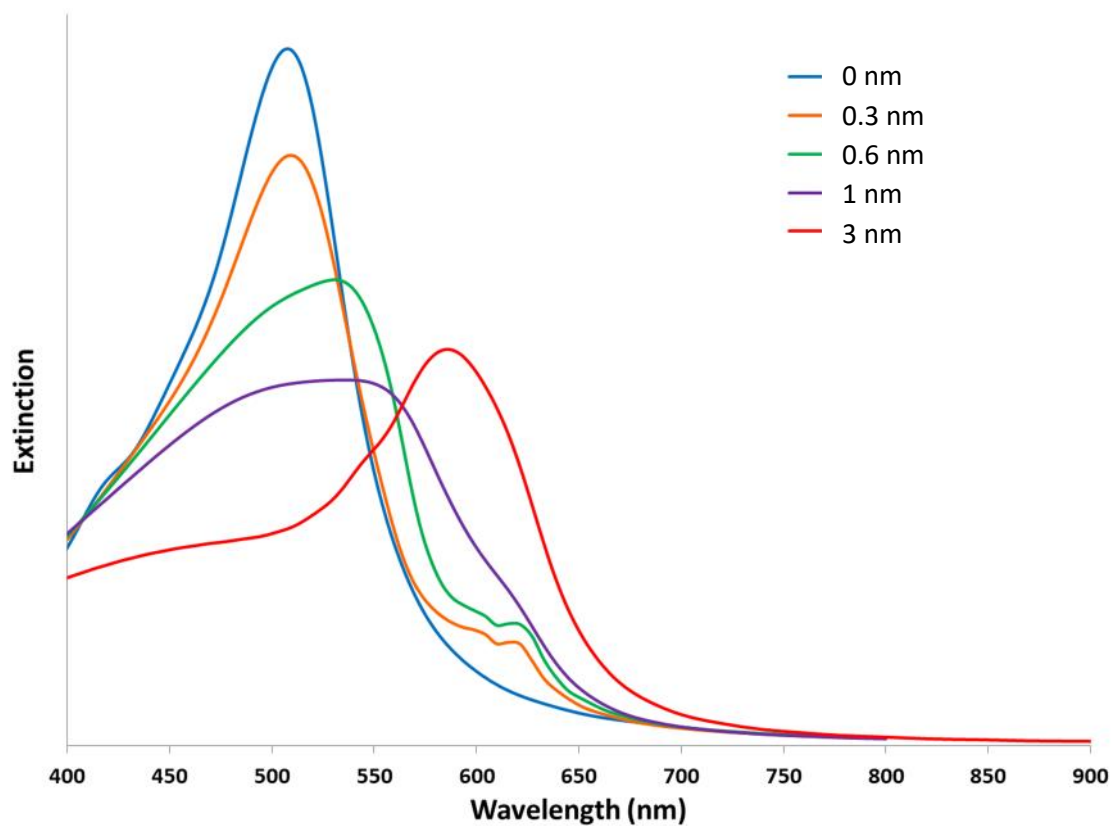


Figure 5S.14. FDTD simulated extinction spectra of pure Au plating on AgDeNPs with Au thicknesses of: 0 nm (blue), 0.3 nm (orange), 0.6 nm (green), 1 nm (purple) and 3 nm (red).

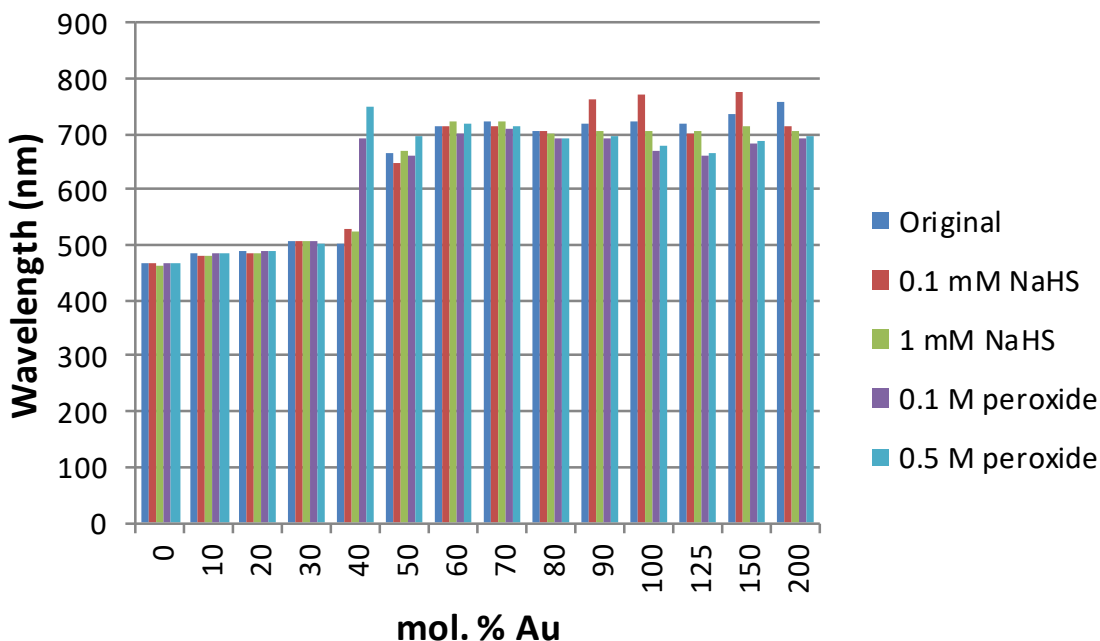


Figure 55.15. Stability tests of **freshly prepared samples** with varying mol. % Au. Columns from left to right are the wavelength of original LSPR peak, followed by the wavelength of LSPR peaks 15 minutes after treatment with 0.1 mM NaHS, 1 mM NaHS, 0.1 M hydrogen peroxide and 0.5 M hydrogen peroxide.

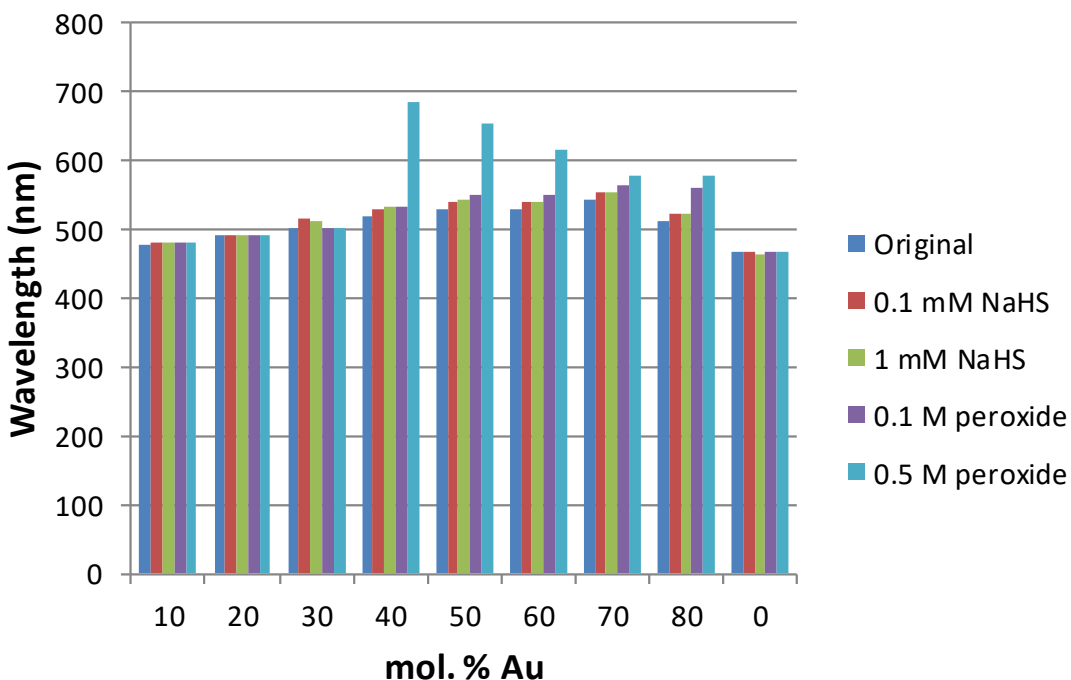


Figure 55.16. Stability tests of **aged samples** with varying mol. % Au. Columns from left to right are the wavelength of original LSPR peak, followed by the wavelength of LSPR peaks 15 minutes after treatment with 0.1 mM NaHS, 1 mM NaHS, 0.1 M hydrogen peroxide and 0.5 M hydrogen peroxide.

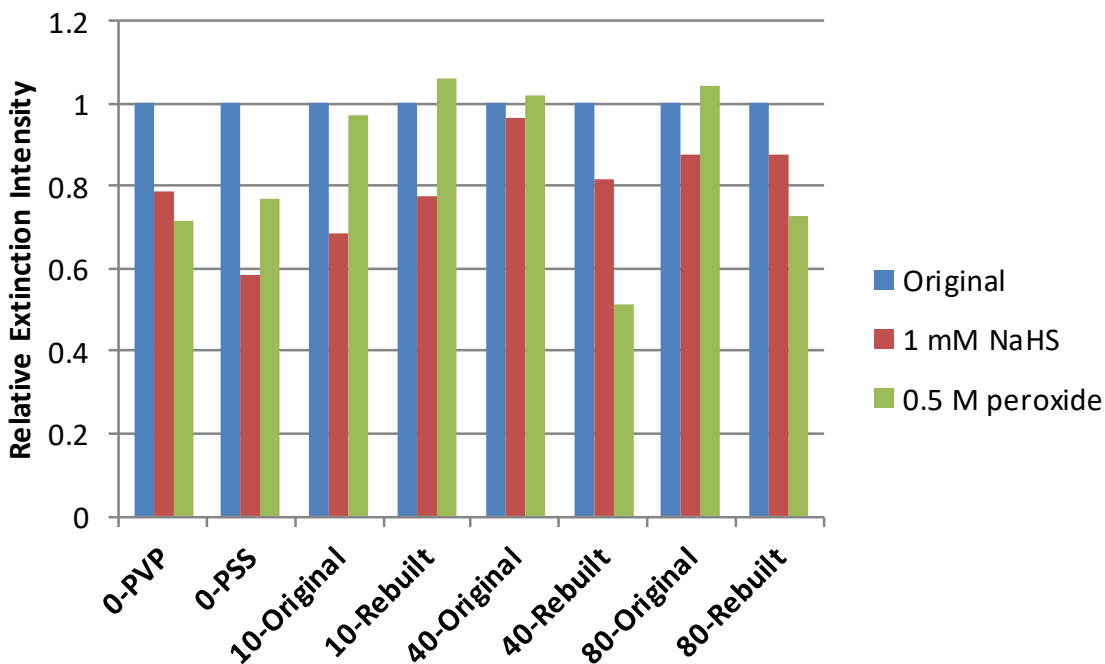


Figure 5S.17. Relative intensities of LSPR extinction for representative samples from Figures 5S.15 and 5S.16 and as prepared AgDeNPs stabilized with PSS and PVP 15 minutes after treatments with 0.1 mM NaHS and 0.5 M hydrogen peroxide. Intensities of LSPR peaks were normalized by the LSPR intensity for the samples prior to the treatment.

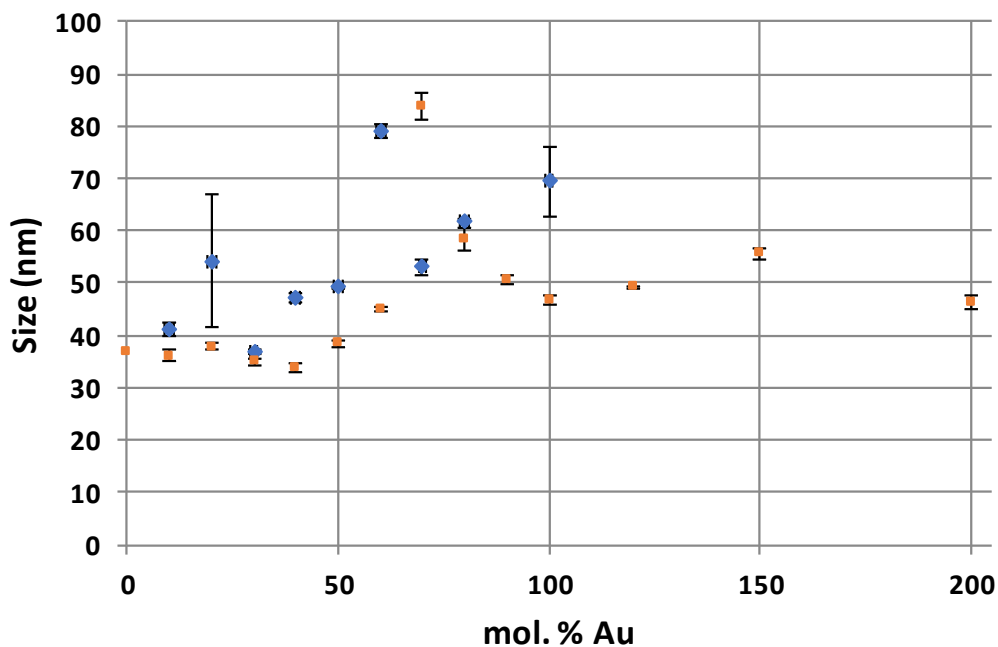


Figure 5S.18. Zeta potential measurements for Au-AgNPs samples with varying mol. % Au. Orange square symbols are for fresh samples, and blue diamond symbols are for samples that were aged for 6 months.

Sample Name: nz118 1
SOP Name: mansettings.nano
File Name: Jun 2017.dts
Record Number: 133
Date and Time: June-14-17 12:20:00 PM
Dispersant Name: Water
Dispersant RI: 1.330
Viscosity (cP): 0.8872
Dispersant Dielectric Constant: 78.5

Temperature (°C): 25.0
Count Rate (kcps): 2002.1
Cell Description: Clear disposable zeta cell
Zeta Runs: 12
Measurement Position (mm): 2.00
Attenuator: 10

	Mean (mV)	Area (%)	St Dev (mV)
Zeta Potential (mV): -40.8	Peak 1: -40.8	100.0	5.29
Zeta Deviation (mV): 5.29	Peak 2: 0.00	0.0	0.00
Conductivity (mS/cm): 0.503	Peak 3: 0.00	0.0	0.00

Result quality : Good

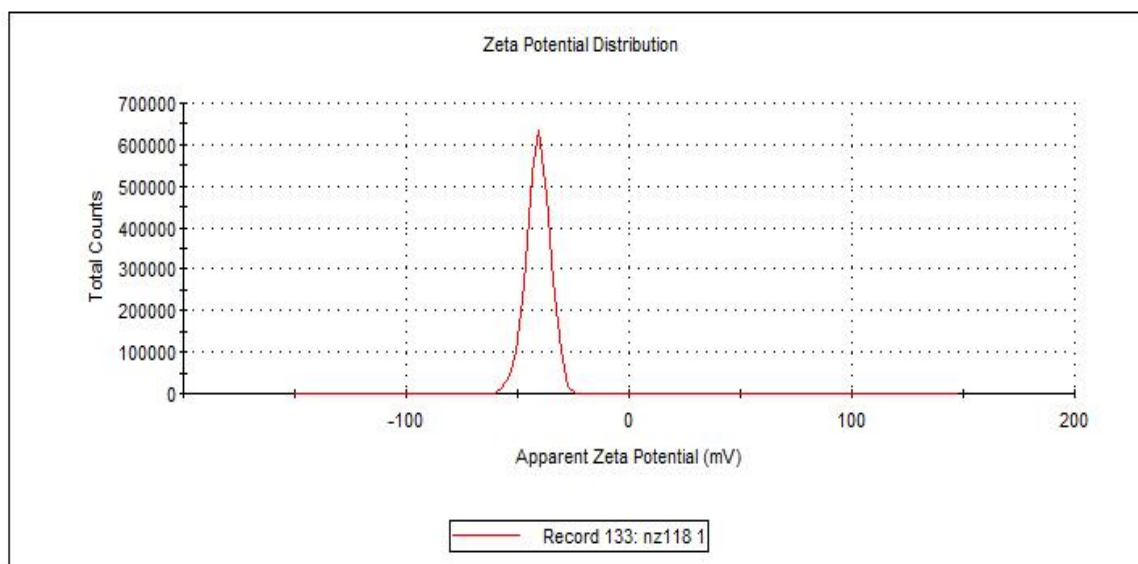


Figure 5S.19. A representative measurement data of zeta potential for 100 mol. % Au-AgNPs.

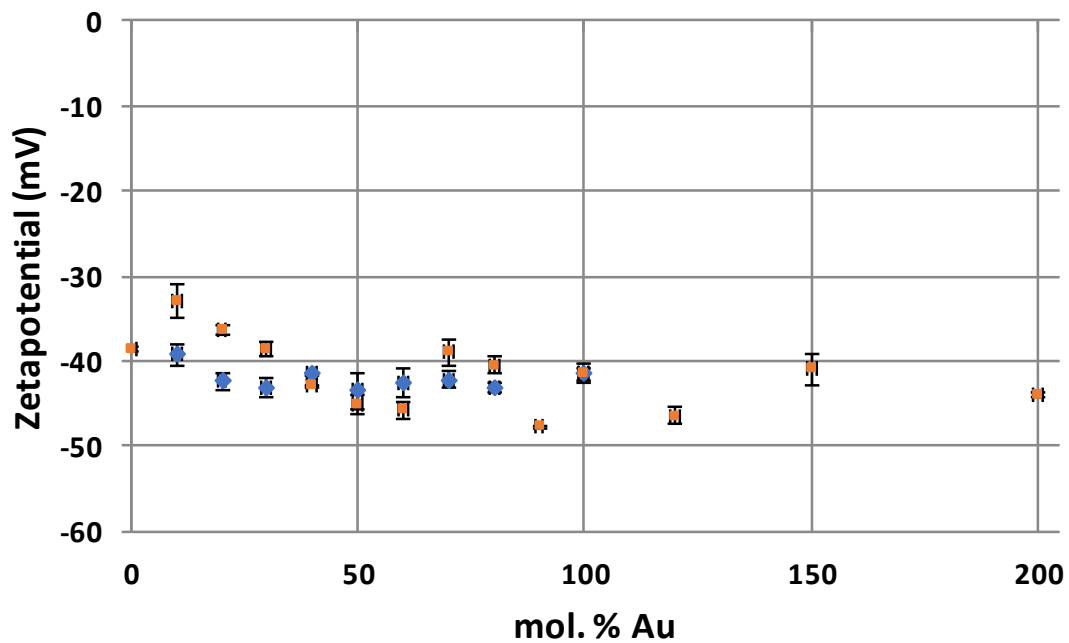


Figure 5S.20. Dynamic light scattering measurements of size (hydrodynamic radius) for Au-AgNPs samples with varying mol. % Au. Orange square symbols are for fresh samples, and blue diamond symbols are for samples that were aged for 6 months.

Sample Name: nz118- 50 x dil 3
SOP Name: mansettings.nano
File Name: Jun 2017.dts
Record Number: 96
Material RI: 1.59
Material Absorbtion: 0.010
Dispersant Name: Water
Dispersant RI: 1.330
Viscosity (cP): 0.8872
Measurement Date and Time: June-14-17 11:07:17 AM

Temperature (°C): 25.0
Count Rate (kcps): 234.3
Cell Description: Disposable sizing cuvette
Duration Used (s): 70
Measurement Position (mm): 4.65
Attenuator: 10

	Size (d.nm):	% Intensity:	St Dev (d.nm):
Z-Average (d.nm): 46.17	Peak 1: 64.68	100.0	30.71
Pdl: 0.290	Peak 2: 0.000	0.0	0.000
Intercept: 0.901	Peak 3: 0.000	0.0	0.000

Result quality : Refer to quality report

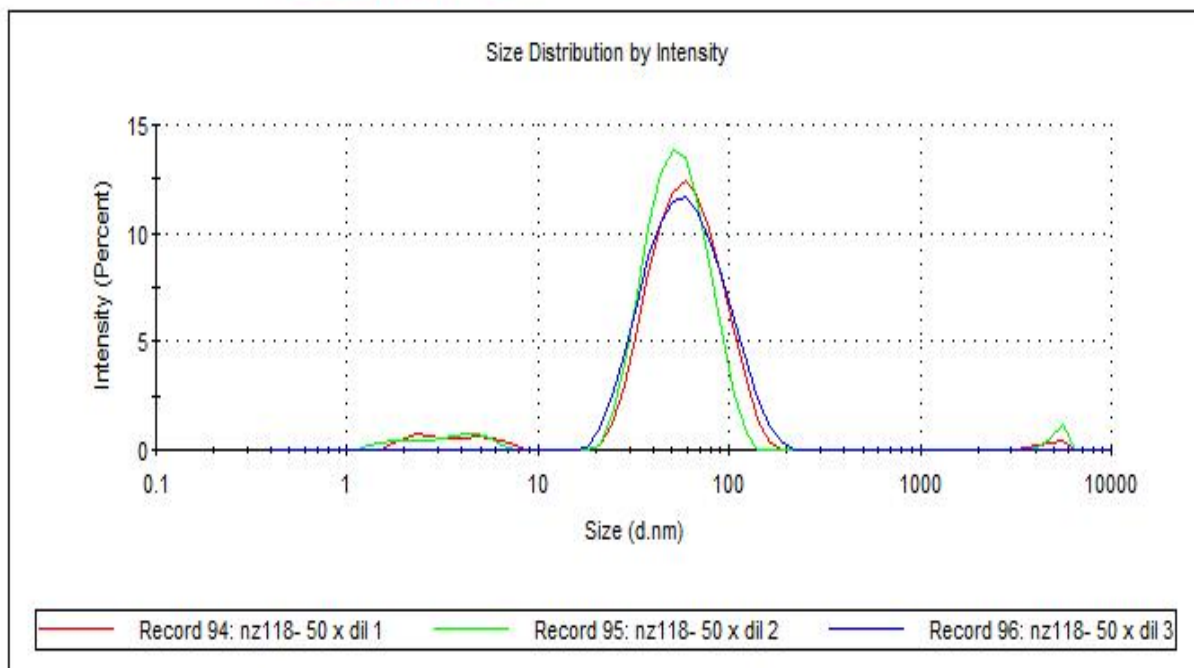


Figure 5S.21. A representative measurement data of size for 100 mol. % Au-AgNPs. Note the size deviation due to multiple scattering in the system.

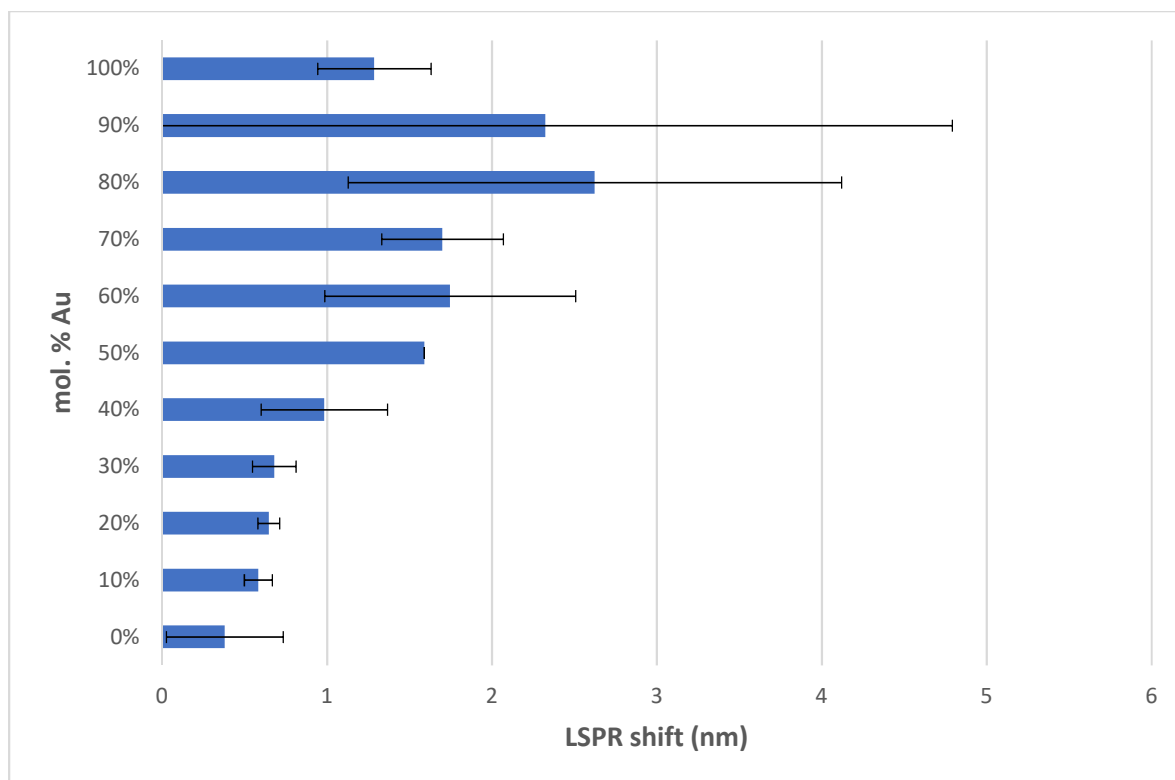


Figure 5S.22. SPR response to 10^{-8} M potassium iodide for Au-AgNPs with different mol. % Au **prior** to rebuilding.

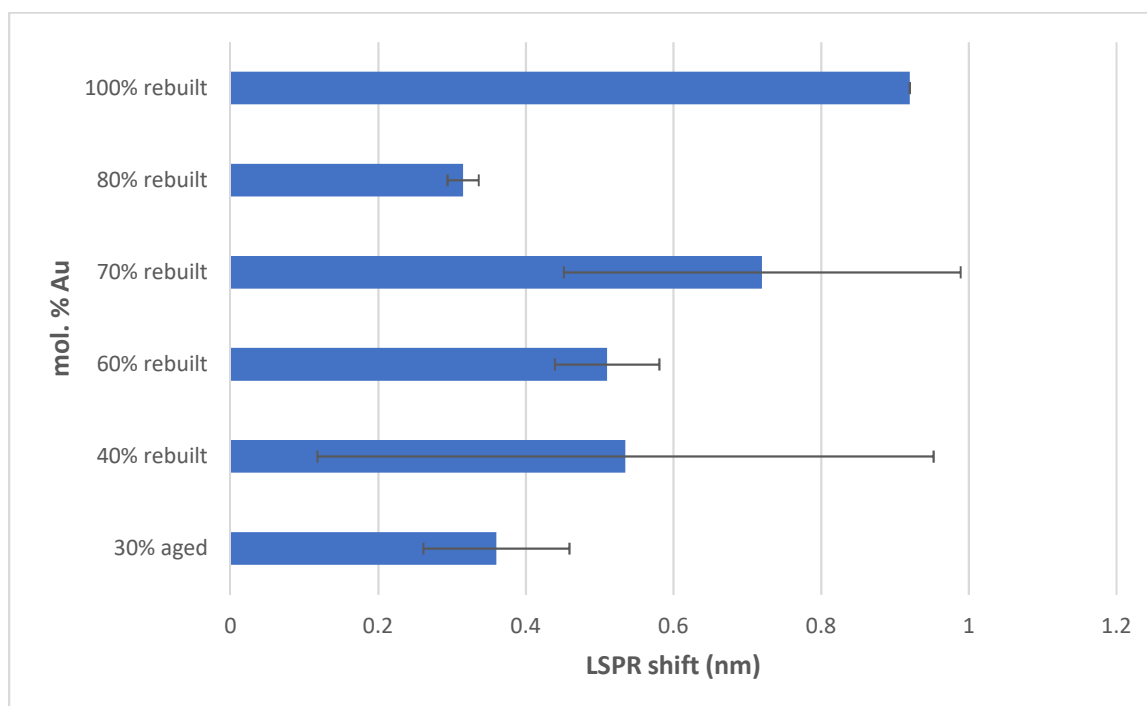


Figure 5S.23. SPR response to 10^{-8} M potassium iodide Au-AgNPs with different mol. % Au **after** rebuilding.

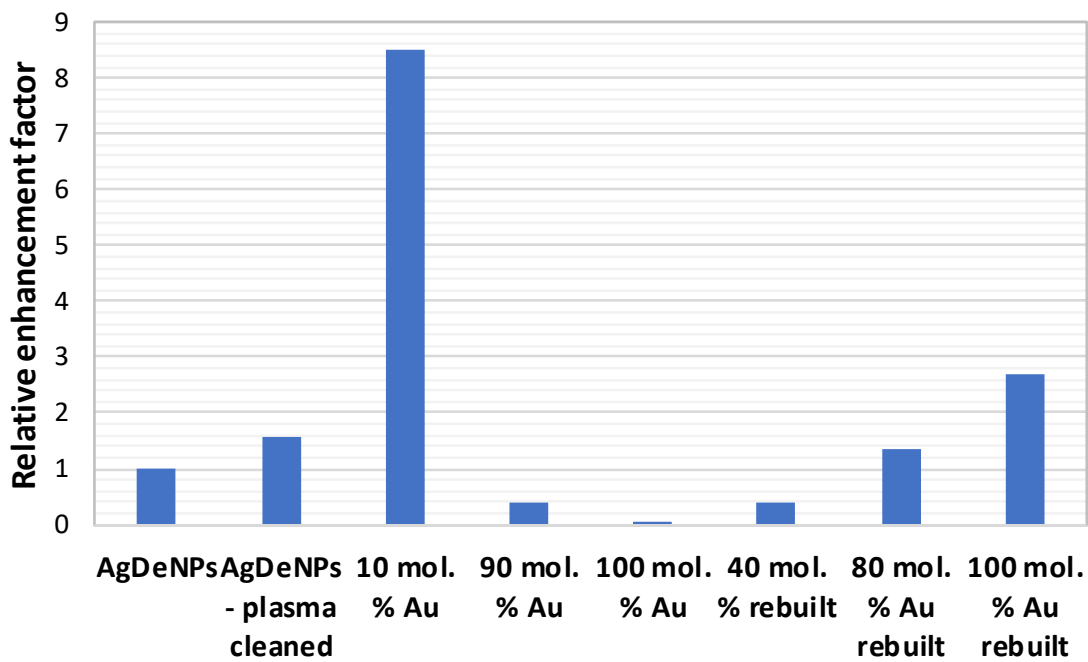


Figure 5S.24. SERS enhancement factors (relative to AgDeNPs) for Au-AgNP samples with varying mol. % Au, as prepared and rebuilt, as SERS substrates, using thiosalicylic acid as a probe molecule.

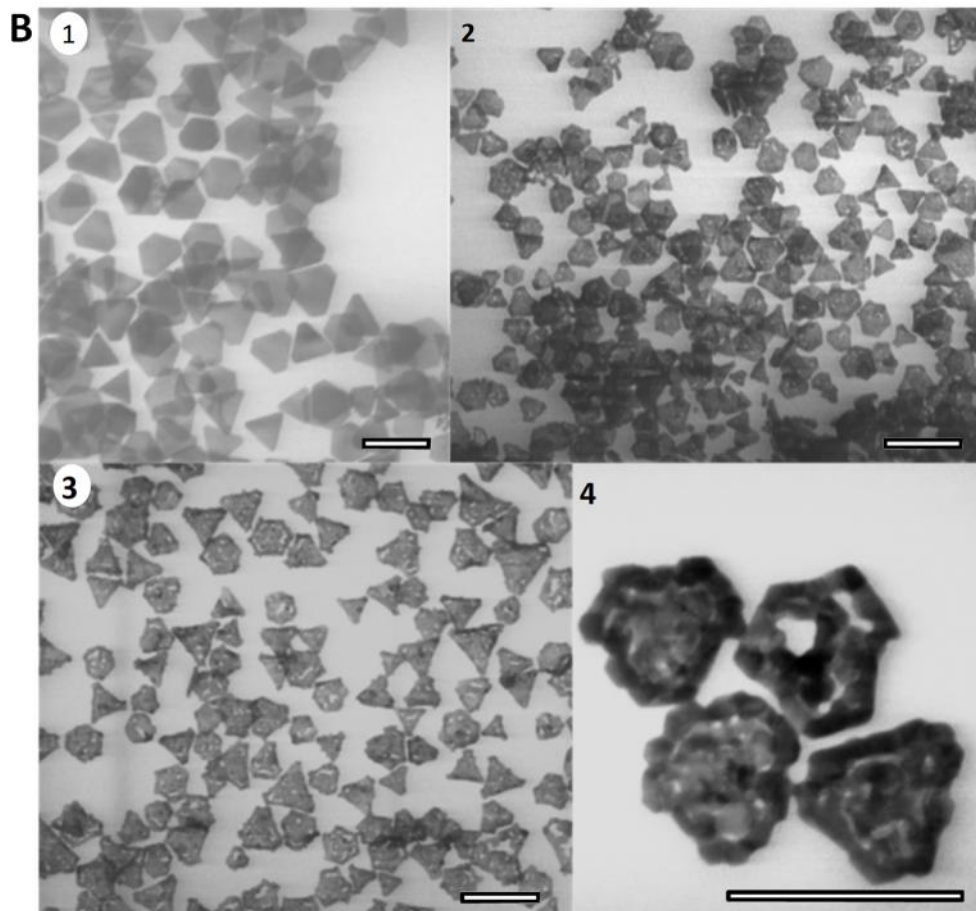
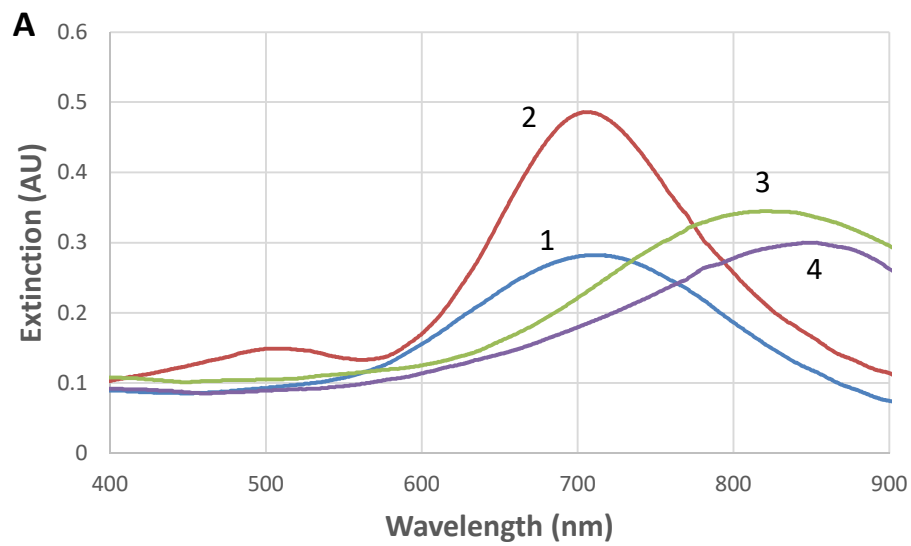


Figure 5S.25. A) UV-vis spectra and **B)** TEM images of gold-plated silver platelets and Au shells. % mol. Au is as follows **1)** 20, **2)** 100, **3)** 75, and **4)** 80. All scale bars are 100 nm.

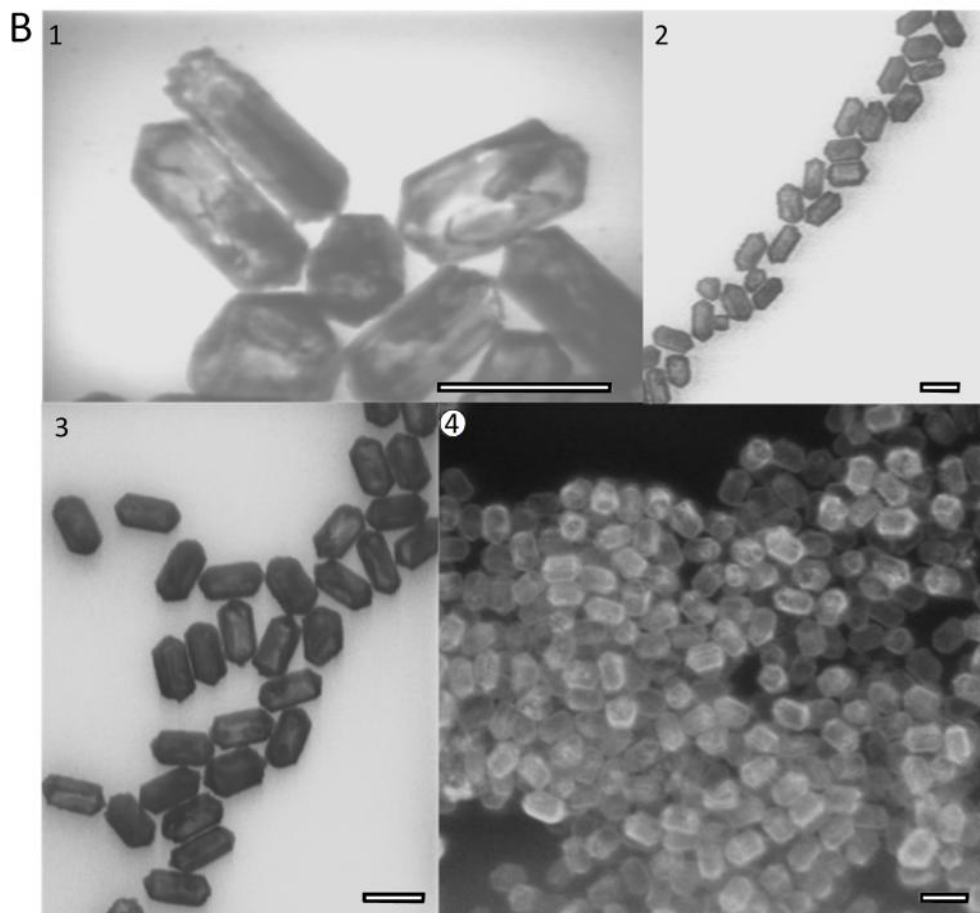
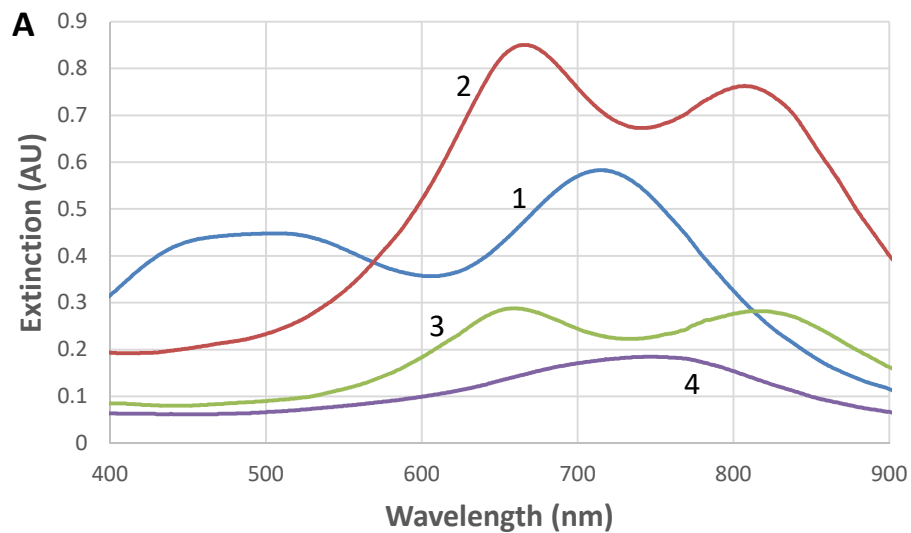


Figure 5S.26. A) UV-vis spectra and B) EM images of gold shells from silver pentagonal rods. % mol. Au is as follows: 1) 10 , 2) 30, 3) & 4) 40. 1)-3) are TEM images, and 4) is Scanning Electron Microscopy (SEM) image. All scale bars are 100 nm.

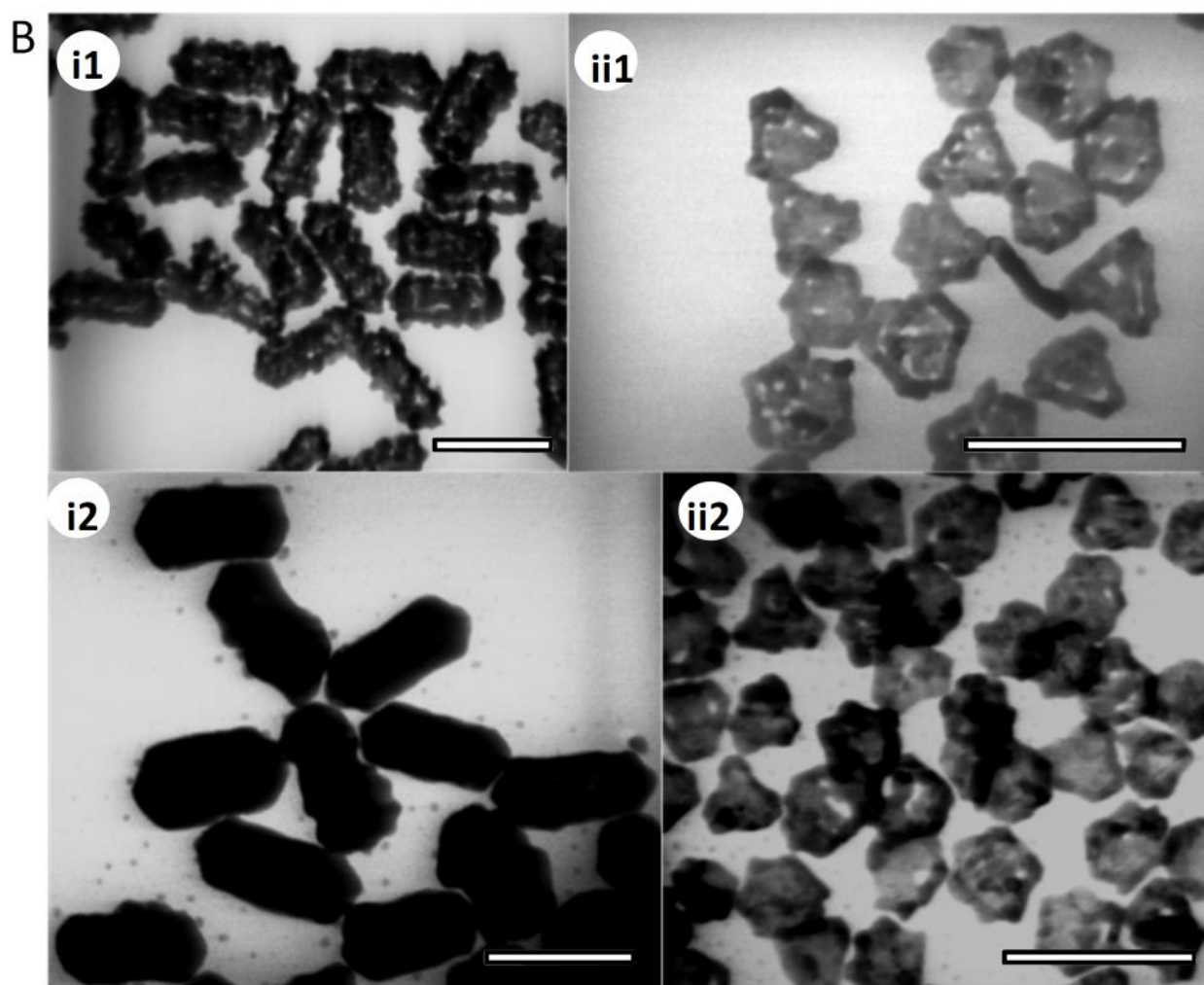
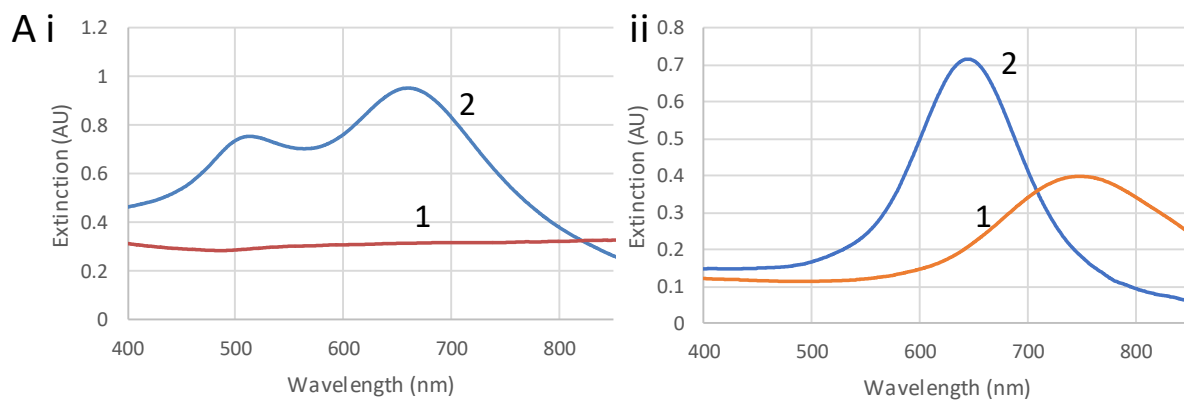


Figure 5S.27. A) UV-vis spectra and **B)** TEM images of **i)** Ag pentagonal rods with 100 mol. % Au, and **ii)** Ag platelets with 100 mol. % Au, where **1)** as prepared samples, and **2)** samples after 2-hour heat treatment at 95 °C. All scale bars are 100 nm.

The discovery of the rebuilding process was made jointly by V. Kitaev and me, the computational work was completed by J.I.L. Chen. Images were taken by V. Kitaev. My primary role was experimental, preparation of the first draft of the manuscript, figures (experimental work), and iterative refining.

5.8. References

- (1) Xia, Y.; Yang, X. Toward Cost-Effective and Sustainable Use of Precious Metals in Heterogeneous Catalysts. *Acc. Chem. Res.* **2017**, *50*, 450–454.
- (2) Li, J.; Zhao, T.; Chen, T.; Liu, Y.; Ong, C. N.; Xie, J. Engineering Noble Metal Nanomaterials for Environmental Applications. *Nanoscale* **2015**, *7*, 7502–7519.
- (3) Smith, A. F.; Skrabalak, S. E. Metal Nanomaterials for Optical Anti-Counterfeit Labels. *J. Mater. Chem. C* **2017**, *5*, 3207–3215.
- (4) Ye, H.; Yang, K.; Tao, J.; Liu, Y.; Zhang, Q.; Habibi, S.; Nie, Z.; Xia, X. An Enzyme-Free Signal Amplification Technique for Ultrasensitive Colorimetric Assay of Disease Biomarkers. *ACS Nano* **2017**, *11*, 2052–2059.
- (5) Ross, M. B.; Ashley, M. J.; Schmucker, A. L.; Singamaneni, S.; Naik, R. R.; Schatz, G. C.; Mirkin, C. A. Structure-Function Relationships for Surface-Enhanced Raman Spectroscopy-Active Plasmonic Paper. *J. Phys. Chem. C* **2016**, *120*, 20789–20797.
- (6) Reguera, J.; Langer, J.; Jiménez de Aberasturi, D.; Liz-Marzán, L. M. Anisotropic Metal Nanoparticles for Surface Enhanced Raman Scattering. *Chem. Soc. Rev.* **2017**, *46*, 3866–3885.
- (7) Liz-Marzán, L. M.; Grzelczak, M. Growing Anisotropic Crystals at the Nanoscale. *Science*. **2017**, *356*, 1120–1121.
- (8) Chen, Q.; Jia, Y.; Xie, S.; Xie, Z. Well-Faceted Noble-Metal Nanocrystals with Nonconvex Polyhedral Shapes. *Chem. Soc. Rev.* **2016**, *45*, 3207–3220.
- (9) Tan, T.; Yao, L.; Liu, H.; Li, C.; Wang, C. Precise Control of the Lateral and Vertical Growth of Two-Dimensional Ag Nanoplates. *Chem. - A Eur. J.* **2017**, *23*, 10001–10006.
- (10) Xia, Y.; Xia, X.; Peng, H. C. Shape-Controlled Synthesis of Colloidal Metal Nanocrystals: Thermodynamic versus Kinetic Products. *J. Am. Chem. Soc.* **2015**, *137*, 7947–7966.
- (11) Ruditskiy, A.; Xia, Y. The Science and Art of Carving Metal Nanocrystals. *ACS Nano* **2017**, *11*, 23–27.
- (12) Liu, P.; Qin, R.; Fu, G.; Zheng, N. Surface Coordination Chemistry of Metal Nanomaterials. *J. Am. Chem. Soc.* **2017**, *139*, 2122–2131.

- (13) Burrows, N. D.; Vartanian, A. M.; Abadeer, N. S.; Grzincic, E. M.; Jacob, L. M.; Lin, W.; Li, J.; Dennison, J. M.; Hinman, J. G.; Murphy, C. J. Anisotropic Nanoparticles and Anisotropic Surface Chemistry. *J. Phys. Chem. Lett.* **2016**, *7*, 632–641.
- (14) Santana, J. S.; Koczkur, K. M.; Skrabalak, S. E. Synthesis of Core@Shell Nanostructures in a Continuous Flow Droplet Reactor: Controlling Structure through Relative Flow Rates. *Langmuir* **2017**, *33*, 6054–6061.
- (15) Zhu, X.; Jia, H.; Zhu, X.-M.; Cheng, S.; Zhuo, X.; Qin, F.; Yang, Z.; Wang, J. Selective Pd Deposition on Au Nanobipyramids and Pd Site-Dependent Plasmonic Photocatalytic Activity. *Adv. Funct. Mater.* **2017**, *27*, 1200016.
- (16) Cortés, E. Efficiency and Bond Selectivity in Plasmon-Induced Photochemistry. *Adv. Opt. Mater.* **2017**, *5*, 1700191.
- (17) Baffou, G.; Quidant, R. Nanoplasmonics for Chemistry. *Chem. Soc. Rev.* **2014**, No. 11, 3898–3907.
- (18) Gilroy, K. D.; Ruditskiy, A.; Peng, H.-C.; Qin, D.; Xia, Y. Bimetallic Nanocrystals: Syntheses, Properties, and Applications. *Chem. Rev.* **2016**, *116*, 10414–10472.
- (19) Ye, S.; Stewart, I. E.; Chen, Z.; Li, B.; Rathmell, A. R.; Wiley, B. J. How Copper Nanowires Grow and How to Control Their Properties. *Accounts of Chemical Research*. March 15, 2016, pp 442–451.
- (20) Kim, M. J.; Flowers, P. F.; Stewart, I. E.; Ye, S.; Baek, S.; Kim, J. J.; Wiley, B. J. Ethylenediamine Promotes Cu Nanowire Growth by Inhibiting Oxidation of Cu(111). *J. Am. Chem. Soc.* **2017**, *139*, 277–284.
- (21) Wiley, B.; Sun, Y.; Xia, Y. Synthesis of Silver Nanostructures with Controlled Shapes and Properties. *Acc. Chem. Res.* **2007**, *40*, 1067–1076.
- (22) Sun, Y.; Xia, Y. Shape-Controlled Synthesis of Gold and Silver Nanoparticles. *Science* **2002**, *298*, 2176–2179.
- (23) Sun, Y.; Mayers, B.; Xia, Y. Metal Nanostructures with Hollow Interiors. *Adv. Mater.* **2003**, *15*, 641–646.
- (24) Sun, Y.; Xia, Y. Alloying and Dealloying Processes Involved in the Preparation of Metal Nanoshells through a Galvanic Replacement Reaction. *Nano Lett.* **2003**, *3*, 1569–1572.
- (25) Skrabalak, S. E.; Chen, J.; Sun, Y.; Lu, X.; Au, L.; Cobley, C. M.; Xia, Y. Gold Nanocages: Synthesis, Properties, and Applications. *Acc. Chem. Res.* **2008**, *41*, 1587–1595.
- (26) Xia, X.; Wang, Y.; Ruditskiy, A.; Xia, Y. 25th Anniversary Article: Galvanic Replacement: A Simple and Versatile Route to Hollow Nanostructures with Tunable and Well-Controlled Properties. *Adv. Mater.* **2013**, *25*, 6313–6332.
- (27) Kumar-Krishnan, S.; Estevez-González, M.; Pérez, R.; Esparza, R.; Meyyappan, M. A General Seed-

- Mediated Approach to the Synthesis of AgM (M = Au, Pt, and Pd) Core-Shell Nanoplates and Their SERS Properties. *RSC Adv.* **2017**, *7*, 27170–27176.
- (28) Zhang, L.; Liu, T.; Liu, K.; Han, L.; Yin, Y.; Gao, C. Gold Nanoframes by Nonepitaxial Growth of Au on AgI Nanocrystals for Surface-Enhanced Raman Spectroscopy. *Nano Lett.* **2015**, *15*, 4448–4454.
- (29) Sun, X.; Kim, J.; Gilroy, K. D.; Liu, J.; König, T. A. F.; Qin, D. Gold-Based Cubic Nanoboxes with Well-Defined Openings at the Corners and Ultrathin Walls Less Than Two Nanometers Thick. *ACS Nano* **2016**, *10*, 8019–8025.
- (30) Rivero, P. J.; Ibañez, E.; Goicoechea, J.; Urrutia, A.; Matias, I. R.; Arregui, F. J. A Self-Referenced Optical Colorimetric Sensor Based on Silver and Gold Nanoparticles for Quantitative Determination of Hydrogen Peroxide. *Sensors Actuators B Chem.* **2017**, *251*, 624–631.
- (31) Murshid, N.; Gourevich, I.; Coombs, N.; Kitaev, V. Gold Plating of Silver Nanoparticles for Superior Stability and Preserved Plasmonic and Sensing Properties. *Chem. Commun.* **2013**, *49*, 11355–11357.
- (32) McEachran, M.; Keogh, D.; Pietrobon, B.; Cathcart, N.; Gourevich, I.; Coombs, N.; Kitaev, V. Ultrathin Gold Nanoframes through Surfactant-Free Templating of Faceted Pentagonal Silver Nanoparticles. *J. Am. Chem. Soc.* **2011**, *133*, 8066–8069.
- (33) Hobbs, K.; Cathcart, N.; Kitaev, V. Gold-Plated Silver Nanoparticles Engineered for Sensitive Plasmonic Detection Amplified by Morphological Changes. *Chem. Commun.* **2016**, *52*, 9785–9788.
- (34) Sun, X.; Qin, D. Co-Titration of AgNO₃ and HAuCl₄: A New Route to the Synthesis of Ag@Ag–Au Core–frame Nanocubes with Enhanced Plasmonic and Catalytic Properties. *J. Mater. Chem. C* **2015**, *3*, 11833–11841.
- (35) Yang, Y.; Liu, J.; Fu, Z. W.; Qin, D. Galvanic Replacement-Free Deposition of Au on Ag for Core-Shell Nanocubes with Enhanced Chemical Stability and SERS Activity. *J. Am. Chem. Soc.* **2014**, *136*, 8153–8156.
- (36) Hunyadi, S. E.; Murphy, C. J. Bimetallic Silver–gold Nanowires: Fabrication and Use in Surface-Enhanced Raman Scattering. *J. Mater. Chem.* **2006**, *16*, 3929–3935.
- (37) Dai, H.; Zhang, L.; Wang, Z.; Wang, X.; Zhang, J.; Gong, H.; Han, J.-B.; Han, Y. Linear and Nonlinear Optical Properties of Silver-Coated Gold Nanorods. *J. Phys. Chem. C* **2017**, *121*, 12358–12364.
- (38) Polavarapu, L.; Zanaga, D.; Altantzis, T.; Rodal-Cedeira, S.; Pastoriza-Santos, I.; Pérez-Juste, J.; Bals, S.; Liz-Marzán, L. M. Galvanic Replacement Coupled to Seeded Growth as a Route for Shape-Controlled Synthesis of Plasmonic Nanorattles. *J. Am. Chem. Soc.* **2016**, *138*, 11453–11456.
- (39) Pietrobon, B.; Kitaev, V. Photochemical Synthesis of Monodisperse Size-Controlled Silver Decahedral Nanoparticles and Their Remarkable Optical Properties. *Chem. Mater.* **2008**, *20*,

5186–5190.

- (40) Murshid, N.; Keogh, D.; Kitaev, V. Optimized Synthetic Protocols for Preparation of Versatile Plasmonic Platform Based on Silver Nanoparticles with Pentagonal Symmetries. *Part. Part. Syst. Charact.* **2014**, *31*, 178–189.
- (41) Pietrobon, B.; McEachran, M.; Kitaev, V. Synthesis of Size-Controlled Faceted Pentagonal Silver Nanorods with Tunable Plasmonic Properties and Self-Assembly of These Nanorods. *ACS Nano* **2009**, *3*, 21–26.
- (42) Murshid, N.; Gourevich, I.; Coombs, N.; Kitaev, V. Gold Plating of Silver Nanoparticles for Superior Stability and Preserved Plasmonic and Sensing Properties. *Chem. Commun.* **2013**, *49*, 11355–11357.
- (43) Smith, J. G.; Jain, P. K. The Ligand Shell as an Energy Barrier in Surface Reactions on Transition Metal Nanoparticles. *J. Am. Chem. Soc.* **2016**, *138*, 6765–6773.
- (44) Zhang, Q.; Cobley, C. M.; Zeng, J.; Wen, L. P.; Chen, J.; Xia, Y. Dissolving Ag from Au-Ag Alloy Nanoboxes with H₂O₂: A Method for Both Tailoring the Optical Properties and Measuring the H₂O₂ Concentration. *J. Phys. Chem. C* **2010**, *114*, 6396–6400.
- (45) Deutsch, J. C. Ascorbic Acid Oxidation by Hydrogen Peroxide. *Anal. Biochem.* **1998**, *255*, 1–7.
- (46) Ma, Y.; Li, W.; Cho, E. C.; Li, Z.; Yu, T.; Zeng, J.; Xie, Z.; Xia, Y. Au@Ag Core-Shell Nanocubes with Finely Tuned and Well-Controlled Sizes, Shell Thicknesses, and Optical Properties. *ACS Nano* **2010**, *4*, 6725–6734.
- (47) Myroshnychenko, V.; Nelayah, J.; Adamo, G.; Geuquet, N.; Rodríguez-Fernández, J.; Pastoriza-Santos, I.; MacDonald, K. F.; Henrard, L.; Liz-Marzán, L. M.; Zheludev, N. I.; et al. Plasmon Spectroscopy and Imaging of Individual Gold Nanodecahedra: A Combined Optical Microscopy, Cathodoluminescence, and Electron Energy-Loss Spectroscopy Study. *Nano Lett.* **2012**, *12*, 4172–4180.
- (48) Palik, E. D. *Handbook of Optical Constants of Solids.*; Academic Press, San Diego, CA, **1985**.
- (49) Johnson, P. B.; Christy, R. W. Optical Constants of the Noble Metals. *Phys. Rev. B* **1972**, *6*, 4370–4379.
- (50) Pile, D. Plasmonics: True Silver. *Nat. Photonics* **2016**, *10*, 565–565.
- (51) Ghosh, S. K.; Nath, S.; Kundu, S.; Esumi, K.; Pal, T. Solvent and Ligand Effects on the Localized Surface Plasmon Resonance (LSPR) of Gold Colloids. *J. Phys. Chem. B* **2004**, *108*, 13963–13971.
- (52) Hu, M.; Chen, J.; Li, Z.-Y.; Au, L.; Hartland, G. V.; Li, X.; Marquez, M.; Xia, Y. Gold Nanostructures: Engineering Their Plasmonic Properties for Biomedical Applications. *Chem. Soc. Rev.* **2006**, *35*, 1084–1094.

- (53) Cathcart, N.; Coombs, N.; Gourevich, I.; Kitaev, V. Synthesis and Sensing Properties of D_{5h} Pentagonal Silver Star Nanoparticles. *Nanoscale* **2016**, *8*, 18282–18290.

Chapter 6: Selective Plasmonic Sensing and Highly-Ordered Metallodielectrics via Encapsulation of Plasmonic Metal Nanoparticles with Metal Oxides

The following publication details a method to create metallodielectrics by encapsulating a metal nanoparticle core with a metal oxide shell. Metal nanoparticle cores are gold-coated silver decahedra, and silica and oxides of manganese, iron, and iridium are formed through hydrolysis. Reprinted with permission from N. Cathcart, N. Murshid, P. Campbell, V. Kitaev, *ACS Appl. Nano Mater.* **2018**, *1*, 6514–6524. Copyright (2018) American Chemical Society and accessible online at: <https://pubs.acs.org/doi/abs/10.1021/acsnm.8b01964>. Referenced supplementary figures within the accompanying text are accessible online at:

https://pubs.acs.org/doi/suppl/10.1021/acsnm.8b01964/suppl_file/an8b01964_si_001.pdf.

Selective Plasmonic Sensing and Highly-Ordered Metallodielectrics via Encapsulation of Plasmonic Metal Nanoparticles with Metal Oxides

By Nicole Cathcart, Nimer Murshid, Patrick Campbell and Vladimir Kitaev

6.1. Abstract

Novel materials for sensing and metallodielectric arrays have been prepared by encapsulation of gold-protected shape-selected silver nanoparticles with a diverse range of shells including iron, manganese, and iridium oxides using a versatile deposition procedure. These shells of varying thickness, porosity, and smoothness encapsulating metal nanoparticles advantageously combine functionalities of plasmonic cores and oxide shells into resulting functional materials. In particular, the size-uniform metal oxide encapsulated metal nanoparticles (MO-MNPs) assemble into well-ordered metallodielectric arrays for plasmonic applications. The shape and the localized surface plasmon resonance (LSPR) of the metal cores are well preserved, while the chemical and colloidal stability is enhanced by the formation of oxide

shells. Metal oxide shells impart the selectivity of detection in surface enhanced Raman spectroscopy (SERS) and surface plasmon resonance (SPR) sensing. Notably, selective sub-mM SPR detection of phosphate ions has been demonstrated.

6.2. Introduction

Metal nanoparticles (MNPs) have been recognized for their unique functional nanoscale properties¹⁻³ and consequently are increasingly explored in diverse applications ranging from catalysis^{4,5} and optics^{6,7} to sensing^{8,9} and nanomedicine.¹⁰ The plasmonic properties of gold and silver MNPs by virtue of their LSPR are explored in photonic applications, in particular light-harvesting devices.¹¹ Development of sensing applications with plasmonic MNPs is especially actively studied, given a broad selection of available MNP substrates including silver and gold NPs (AgNPs and AuNPs), as well as coated and alloy NPs.^{5,12-15} Two most commonly employed sensing techniques utilizing MNPs are SERS (surface enhanced Raman spectroscopy), where metallic substrates with nanoscale features (e.g. cavities and anisotropic morphologies) greatly enhance the sensitivity of detection,¹⁶⁻¹⁹ and SPR (surface plasmon resonance) analysis, where changes at the surface of MNPs (e.g. adsorption of an analyte) are monitored through the sensitive detection of LSPR shifts.²⁰⁻²²

SPR and SERS sensing benefits from MNP modification that yields well-defined architectures,^{23,24} enabling the formation of self-assembled layers for sensing substrates, and enhancing sensitivity and selectivity of analyte detection.²⁵ Core-shell morphologies^{26,27} are a primary route established to realize such nanoscale architectures.²⁸⁻³⁰

The majority of developed NP coatings and shells are based on organic ligands and polymers, and thus exhibit limited thermal and chemical stability. To overcome these limitations, functional morphologies based on stable inorganic materials are advantageous. In particular, metal oxides (MO_x) offer a beneficial combination of stability, chemical diversity and availability of precursors with mild

synthetic preparation routes.⁴ Furthermore, metal oxides feature a wide range of properties, including dielectric constants, band gaps, specific adsorption properties and redox capabilities^{31–34} that can be used advantageously to tune and enhance functional properties of MNPs.^{35–37}

Multiple scenarios of combining MNPs and MO_x into nanoparticles and have been comprehensively classified in a recent review by Lui et al.³⁸ Three main classes of noble metal-metal oxide nanocomposites include 1) metal oxide inner core with noble metal surface deposition, 2) noble metal inner core covered with a metal oxide, and 3) fused structures (e.g. Janus noble metal-metal oxide particles).³⁸ Controlled encapsulation of MNPs in dielectrics offers direct practical benefits for multiple applications.³⁹ Formation of dielectric shells around MNPs historically started with silica, as one of the most chemically and colloiddally stable oxides,^{40–46} and remains one of the most intensely studied class of mixed metal-metal oxide (hybrid) materials.⁴⁷ Subsequent developments in the field included different oxides of MO_x -encapsulated MNPs (MO-MNPs) shells,^{48,49} as well as well-defined self-assembled films of Janus metal-metal oxide⁵⁰ or core-shell NPs.^{51,52} Another advantage of MO-MNPs is that they can form metallodielectric (MD) materials upon self-assembly or consolidation from dispersions.⁵³ MD nanocomposites offer unique optoelectronic properties,^{7,54–58} especially if regular periodic lattices are produced by self-assembly of size- and shape-uniform MNPs^{51,59} and similar systems.^{52,60} Formation of metallodielectric composites is strongly application-driven,^{61–63} the range of applications where metal-metal oxide composites demonstrated enhanced properties is diverse^{64–66} and continues to be an active research field. Given that the driving forces of this research are centered around functional properties and applications, and considering the recent progress in preparation of shape-selected MNP, the next logical step in formation of metallodielectric NPs is to employ well-defined nanoparticles that can be encapsulated in different materials with the preservation of size and shape, and the enhancement of advantageous optical properties, such as LSPR.

One challenge with preparing such nanocomposites is the lattice mismatch between the noble metal core and the metal oxide shell.⁶⁷⁻⁶⁹ In many syntheses of this type, surface-adsorbing species, such as most commonly poly(vinylpyrrolidone), are used to mediate the lattice mismatch.⁶⁹ Many reported procedures for the fabrication of MO-MNPs involve a sol-gel strategy, where MNPs are added to a metal oxide precursor in the presence of surface active species.⁶⁹⁻⁷¹ In this work, we demonstrate that shape-selected AgNPs stabilized both with poly(vinylpyrrolidone) or poly(styrene sulfonate), and properly protected by gold plating can be conveniently employed for encapsulation with a diverse range of metal oxides, including iron, manganese and iridium oxides using simple experimental protocols. The universality of the encapsulation procedure has been further demonstrated with gold NPs, as another important class of shape-selected plasmonic MNPs. Importantly, this procedure is gentle enough to coat pure AgNPs with minimal morphological changes, thus preserving LSPR sharpness. Upon encapsulation of MNPs with MO_x their advantageous LSPR properties were preserved and could be further tuned through the thickness and density of the shell. The formation of well-defined MO_x shells enhanced MNP plasmonic properties and consequently expanded the opportunities in sensing with SERS and SPR. Specifically, MNPs encapsulated with manganese and iron oxides were capable of selective SPR detection of phosphate ions through specific interactions with an oxide shell.

6.3. Results and Discussions

6.3.1. Formation and Properties of MO-MNPs.

For successful controlled deposition of oxide shells onto well-defined MNP morphologies, both shape-selected and chemically stable MNPs are required. One of the systems that satisfies both of these requirements is gold-plated AgNPs.^{14,15} With a typical ratio of gold-to-silver of 5-20 mol. %, silver remains the main component that imparts excellent optical properties, manifested in sharp LSPR peaks. The gold plating offers necessary stability for the NP morphologies to remain stable and to not degrade (e.g. by rounding) during the deposition of oxide shells. The main AgNP morphology that we have explored in this

work was decahedra (AgDeNPs),^{72,73} and encapsulation with other plasmonic MNPs have also been demonstrated for the universality of the developed procedure. Once the AgDeNPs were produced, the plating of ca. 10 mol. % Au was prepared by slow addition of tetrachloroauric acid, HAuCl₄, a readily available stable gold salt precursor.¹⁵ Using 10 mol. % of gold relative to silver greatly improves the stability while minimizing galvanic replacement of silver during gold deposition.^{14,15} In the developed plating conditions, silver remains intact, no etching or pitting are observed.^{14,15} The galvanic reaction is effectively mitigated by the slow addition of a gold precursor (5-10 hours) so that the citrate present in the system is able to serve as a reducing agent in this extended time frame, and the silver remains minimally affected.¹⁴ It is likely that the galvanic replacement between gold ions and metallic silver still takes place, since this reaction is very fast. Yet, with the very slow addition, the generated silver ions can be reduced back at the surface by the citrate present in the reaction medium. This minimization of galvanic replacement is effective until ca. 20 mol. % of gold is introduced; for the larger amounts pitting and shell formation start to dominate.¹⁴ The amount of gold used in this work (10 mol. %) is relatively small, so the sharpness of the LSPR peak is largely preserved, coming predominantly by silver, with appreciable improved stability due to gold^{13,14} – a beneficial combination for sensing.

After template MNPs are prepared, the metal oxide shells are formed through the addition of suitable precursors in conditions that allow for uniform MNP encapsulation, as well as preservation of the MNP morphology and plasmonic properties. In this work, we demonstrate great versatility of MNP templates that enable preparation of diverse oxide shells from common silica to more unique iridium oxide. A general schematic for the formation of oxide shells on Au@AgDeNP templates is presented in Figure 6.1A, with examples of oxide shells of iron, manganese and iridium oxides, as well as silica. Figure 6.1 summarizes the main features of MNP encapsulation with preserved plasmonic properties (Figure 6.1B), visualization of the shells by electron microscopy (Figure 6.1C and 6.2), and formation of periodic self-assembled arrays of metallodielectric nanocomposites (Figure 6.1D).

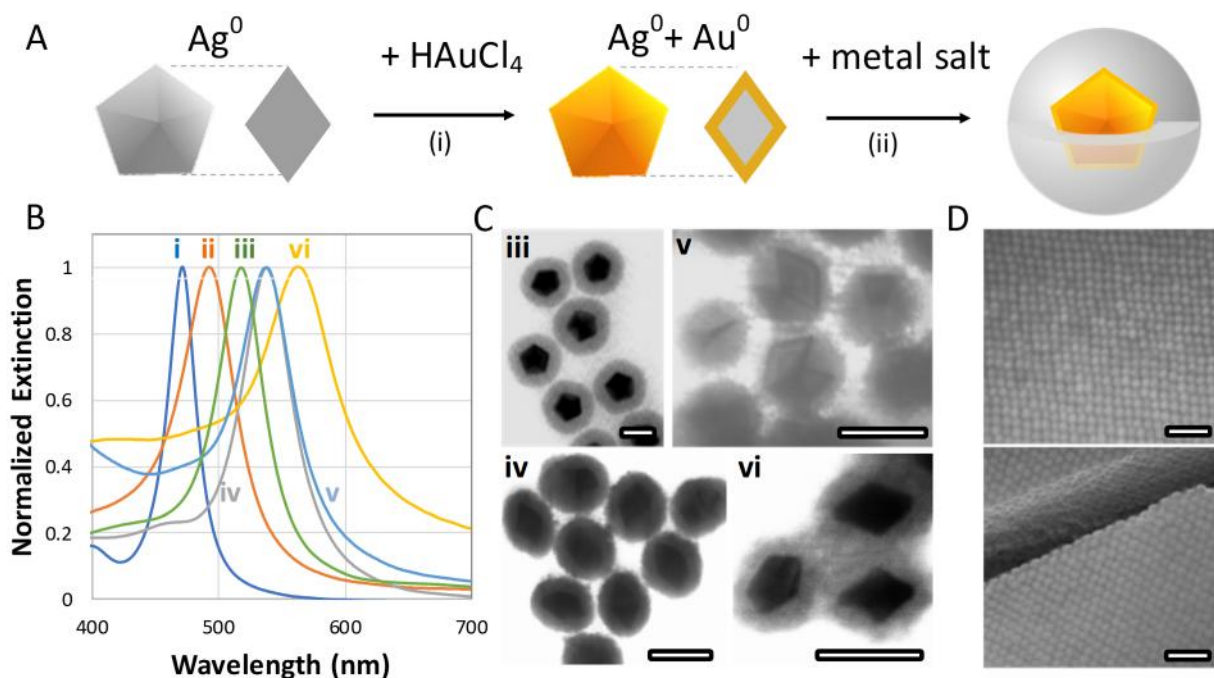


Figure 6.1. **A)** General schematic of the preparation of template plasmonic nanoparticles (Au@AgDeNPs) followed by the formation of metal oxide shells. **B)** Normalized UV-vis spectra of **i)** silver decahedral nanoparticles (AgDeNPs), **ii)** 10 mol. % Au coated AgDeNPs, **iii)** SiO₂@Au@AgDeNPs, **iv)** IrO_x@Au@AgDeNPs, **v)** FeOOH@Au@AgDeNPs, and **vi)** MnO_{2-x}@Au@AgDeNPs. **C)** Representative transmission electron microscopy (TEM) images of different MO_x@Au@AgDeNPs (numbers correspond to the spectra in B)). **D)** Scanning electron microscopy (SEM) images of IrO_x@Au@AgDeNP self-assembled arrays. Scale bars are 50 nm for C), and 250 nm for D).

Oxide shells are produced through hydrolysis of corresponding metal oxide precursors and deposition of insoluble products around the template nanoparticles. The rate of shell formation depends on several parameters, such as solution pH, ionic strength and presence of complexing ligands (e.g. citrate). To limit experimental variations and to develop most reproducible synthetic pathways not involving centrifugation (where some NPs are inevitably lost, and it is still not possible to remove ligands completely due to NP stabilization requirements), we have worked out hydrolysis conditions with as prepared dispersions of 10 mol. % Au@AgDeNPs that contain ca. 1.5 mM of citrate and 0.1 to 0.2 mM of PSS or PVP (see the Methods).

It needs to be emphasized that the encapsulation conditions were effectively optimized for the deposition of amorphous oxide shells, specifically using as-prepared MNPs with citrate present. In conditions where crystalline oxides could form, e.g. hematite formation by iron salt hydrolysis, the shells started to nucleate well-defined crystals that effectively ruins the continuity of the shell and in most cases even detaches oxide coating from the MNP surface. Thus, the oxide shell being amorphous is an important condition for the uniform and continuous encapsulation of metal cores.

inherent advantage of using plasmonic MNPs in the encapsulation is the ability to monitor the shell formation process sensitively. This monitoring can be performed by UV-vis spectroscopy or using a SPR instrument (Open SPR, Nicoya Lifesciences in our work). Given that refractive indices of oxide shells are appreciably higher than that of an aqueous medium, MO_x coating is accompanied by a significant red shift of the LSPR peaks, shown in Figure 6.1B, and discussed in more details in Figure 6.3. From the initial slope of the LSPR shifts during shell formation, shown in Figure 6S.1 in SI, we can estimate the deposition rates at room temperature as follows: $\text{Fe(II)} > \text{Fe(III)} > \text{Mn(II)} > \text{Ir(III)} > \text{Si(IV)}$ (TEOS), while noting that optimal conditions of hydrolysis for Ir(III) require higher temperatures and for Si(IV) (TEOS) – basic catalysts. An example of the control over LSPR shift in MO-MNPs is demonstrated by Figure 6S.2, where encapsulation by IrO_x can be conveniently controlled by heating time (time of deposition), in addition to the variations of the precursor amount.

The materials of the shells are comprised of different hydrolysis products. Amorphous silica, denoted as commonly accepted, SiO_2 and that can be also understood as hydrated silica with acidic groups on the surface, formally corresponding to a silicic acid.^{74,75} For iron-containing shells, produced either by hydrolysis of Fe(III) or Fe(II), the main product in the presence of chloride ions was FeOOH with an akaganeitic character (based on EM); and less defined FeOOH phases, if iron perchlorate salts were used as precursors. For iridium oxide shells – the products of hydrolysis of IrCl_3 correspond to IrO_x in the initial stages of hydrolysis where the majority of Ir is Ir(III) with some remaining chloride.^{76,77} For Mn oxides

(MnO_x) with their incredible diversity of phases due to different oxidation states of Mn, the materials of the shell is tentatively birnessite-like phases, since we observed different sheet-like structures in similar conditions of precursor hydrolysis and could also produce MnO_{2-x} shells of MNPs encapsulated in MnO_{2-x} sheet-like matrices (Figure 6S.3).

During the encapsulation, the control over the shell thickness is straightforward, and can be accomplished through both the amount of precursors and the deposition time. The summary of the attainable ranges of shell thickness and LSPR for the tested metal oxides is presented in Figure 6S.4 and Table 6S.1. While there is generally no upper boundary of the thickness of the shells (the shells can be continuously enlarged by supplying more precursors), the practical limit on the thicker shells was ca. 50 nm to still take an advantage of plasmonic properties of the core MNPs. The thick shells of IrO_x , MnO_{2-x} , silica and FeOOH are shown in Figure 6S.4 (H,D,B,F, respectively). At the same time, the ability to form well-defined thin shells was often determined by the equilibrium solubility of deposited materials. This is particularly evident for silica with its appreciable solubility of ca. 40 mg per L in water that can be even higher in presence of different salts.⁷⁴ This solubility is sufficient to dissolve or impair thin coatings upon handling and thus it limits the thinnest reliably observed silica coating to ca. 8 nm. Similarly, the thinnest coating which we observed in this work for MnO_{2-x} was 10 nm, 6-7 nm for IrO_x , and 5-6 nm for the least soluble FeOOH (the corresponding oxide-encapsulated particles are shown in Figure 6S.4 (A,G,C,E, respectively)).

Together with the thickness, porosity is another characteristic of oxide shells that is important for practical applications. Shells with different porosities, visualized by electron microscopy are presented in Figure 6.2. An observed general trend is that the most porous shells formed from the precursors with the fastest hydrolysis, as discussed above. These precursors also produce the least soluble products and can yield the thinnest shells, as is the case with FeOOH (Figure 6.2G,H). To assess porosity experimentally, samples are tested with sodium hydrosulfide, shown in Figure 6S.5. The hydrosulphide ions affect the bare

MNPs strongly – etching pure AgNPs fast and gold-plated AgNPs noticeably over longer times.^{14,15} LSPR response to 10^{-3} and 10^{-2} M hydrosulfide is recorded as SPR response traces 1 and 2 in Figure 6S.5 for AgDeNPs and Au@AgDeNPs respectively. When hydrosulfide is added to FeOOH@Au@AgDeNPs the largest changes take place (Figure 6S.5, trace 3) confirming that these are the most porous shells (as observed by EM). Next in porosity are MnO_{2-x} @Au@AgDeNPs (Figure 6S.5, trace 4), and SiO_2 @Au@AgDeNPs (Figure 6S.5, trace 6), where some penetration of hydrosulfide through the shell was observed. There was no significant response to hydrosulfide with IrO_x @Au@AgDeNPs (Figure 6S.5, trace 5) due to its dense and impenetrable shell. Shells could also partially mitigate the effect of hydrosulfide by reacting with it, although it would be most expected with iron and manganese oxides and not observed directly in the tests. It should be noted that sample disturbance (from removing, injecting, and reinserting the sample) in some cases caused up to 0.2 nm shifts in the LSPR maxima recorded by SPR.

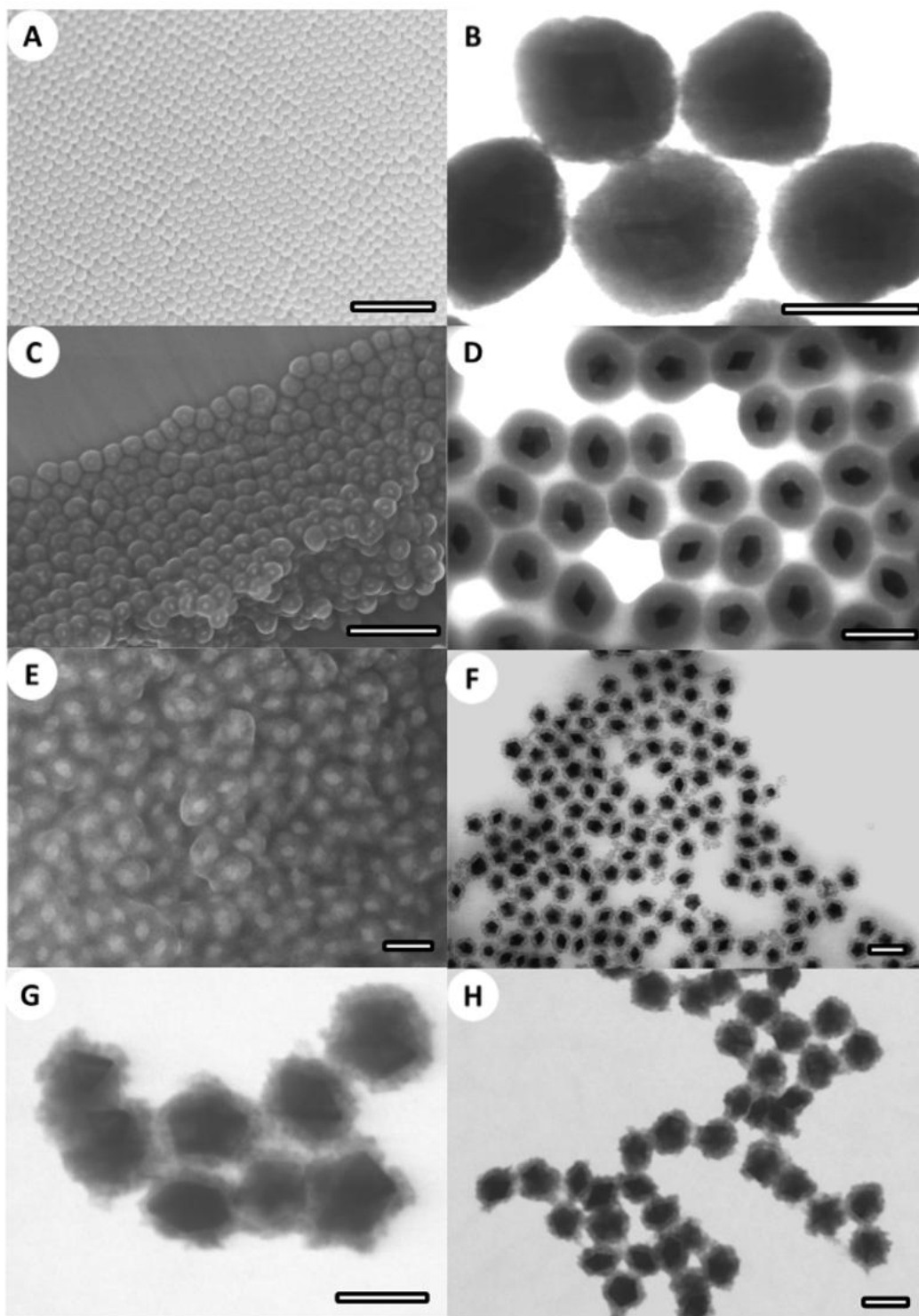


Figure 6.2. EM images of MO-MNPs with different thickness and shell porosity. Outer metal oxide shells are **A)** and **B)** IrO_x , **C)** and **D)** SiO_2 , **E)** and **F)** MnO_{2-x} , **G)** and **H)** FeOOH . A), C), and E) are scanning electron microscopy (SEM) images and the rest are transmission electron microscopy (TEM) images. Scale bars are 50 nm for B), G), and H); 100 nm for D), E), and F); and 500 nm for A) and C).

We have evaluated porosity by nitrogen adsorption-desorption isotherms and performing Brunauer–Emmett–Teller (BET) analysis for $\text{MnO}_{2-x}\text{@Au@AgDeNPs}$ (Figure 6S.6). The measured surface area is estimated as $27 \text{ m}^2/\text{g}$, which is reasonable considering that the impenetrable metal cores constitute the majority of $\text{MO}_x\text{@Au@AgDeNPs}$. The isotherm corresponds to type IV with H3 hysteresis, and the estimated pore size corresponding to MO_x layer composed of small agglomerated particles of ca. 2-5 nm, possibly of the platelet nature (birnessite-like phases), as suggested by slit-type pores from the isotherm, and which is also consistent with EM observations.

In the studies of MO-MNP stability by SPR, quite unexpected observation was the limited comparative stability of $\text{SiO}_2\text{@Au@AgDeNPs}$, where partial aggregation and sedimentation were often observed. We first attributed it to the effect of ammonia traces, but later after testing cleaned samples, this limited stability was realized to be a more general phenomenon. Systematic measurements of zeta potentials (Table 6S.2) made this clear. All other metal oxides have the values of zeta potentials in a narrow range from -35 to -42 mV that is indicative of good colloidal stability. The narrow range and similarity of the values can likely be attributed to the effect of the citrate adsorbing on the oxide surfaces and imparting an appreciable negative potential. At the same time the value of zeta potentials for silica-encapsulated MNPs is below -30 mV, and even closer to -20 mV for thinner coatings. These values are significantly lower than typical zeta potentials measured for silica colloids, ranging from -40 to -80 mV. The lower values of zeta potential in our system indicate that silica likely screens the strongly interacting metal cores the least as the least dense oxide, with the correspondingly lowest Hamaker constant. We will further address this point in our future studies. We can also note that measurements of hydrodynamic diameters of metal nanoparticles by DLS, while not reliable due to strong interactions of metal cores with the light that causes absorbance and multiple scattering, still can be used to monitor shell formation.

LSPR is the key functional property of MNPs that needs to be preserved and, ideally, enhanced and tailored during the oxide encapsulation. Figure 6.3 shows the changes in LSPR peak maxima during

the formation of MO_x shells on Au@AgDeNPs . Indeed, LSPR properties are well preserved, as evident by the vibrant colours of the stable MO-MNP dispersions and spectra (Figure 6.3, 6S.7 and 6S.8). With the increasing amounts of oxide precursor added, the LSPR maxima shift to the red, indicating thickening of MO_x shells. First, continuous increases in LSPR are observed in a range from 125 to 500 mol. %, followed by plateaus at around 1000 mol. %. Reaching plateaus in LSPR is a direct consequence of larger thicknesses of the shells (above ca. 50 nm). In thick shells, the outer layer is sufficiently removed from the metal-dielectric interface, so it is no longer interacting with the electrons at the MNP surface. As a result, any additional increases in shell thickness do not cause further shifts in LSPR peak maxima.

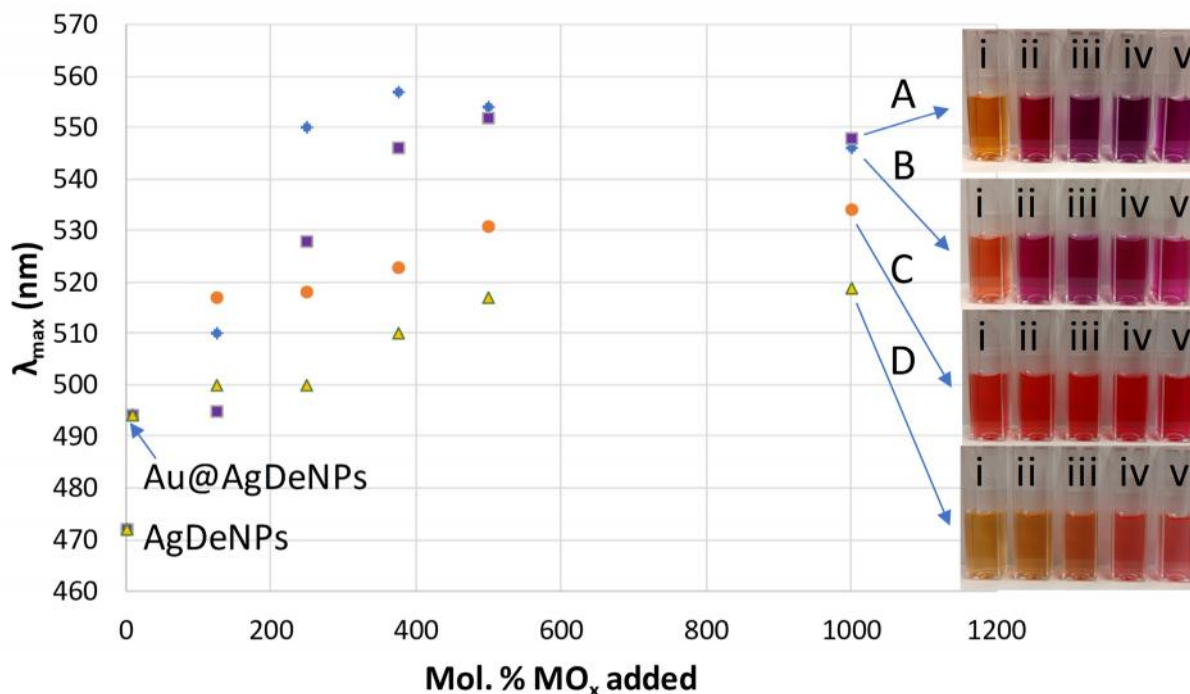


Figure 6.3. LSPR peaks (left) and optical photographs of samples (right) of MO-MNPs with varying mol. % of oxide precursors relative to silver during the shell formation. Oxide shells are **A**) IrO_x , **B**) MnO_{2-x} , **C**) FeOOH , and **D**) SiO_2 . Mol. % of oxide precursors corresponding to the samples in the optical photographs are **i**) 125%, **ii**) 250%, **iii**) 375%, **iv**) 500%, and **v**) 1000% relative to silver.

During the oxide encapsulation, the LSPR peaks of MO-MNPs can be conveniently tuned by as much as 65 nm from ca. 490 nm of Au@AgDeNPs to ca. 555 nm for $\text{MO}_x\text{@Au@AgDeNPs}$, as shown in Figures 6.1B and 6.3. Furthermore, easy variation of the concentrations of precursors enables precise tuning of the LSPR during the formation of oxide shells. The dampening of the LSPR peaks due to the partial absorbance of iron and manganese oxides in the visible range is not strong, as can be seen in Figure 6.1B and non-normalized spectra shown in Figure 6S.7.

One of the challenges in the preparation of metal nanoparticle films is the plasmonic interaction when particles come into a close contact to have an overlapping plasmon resonances, which alters the properties in the solid state when compared to dispersions. Uniform, sufficiently thick (> ca. 50 nm) coating of dielectric on MNPs decouple plasmonic interaction in concentrated dispersions and dry films. Figure 6S.8 shows the transmission spectra and photographs of AgDeNPs and $\text{IrO}_x\text{@Au@AgDeNPs}$ in both dispersions and solid films. The plasmonic properties are drastically different for AgDeNPs in dispersions and solid films produced upon drying, which are essentially metallic-like and display uniform absorbance instead of well-defined LSPR resonances of isolated AgDeNPs in dispersions. This is in great contrast to encapsulated MNPs, such as $\text{IrO}_x\text{@Au@AgDeNPs}$, where LSPR is well preserved in both concentrated dispersions and solid dry films. The optical photographs (Figure 6S.8) further attest to this stark contrast: black, metallic sheen for AgDeNPs compared to the bright, intense, purple of plasmonic $\text{IrO}_x\text{@Au@AgDeNPs}$.

The uniform coating of the size- and shape-selected MNPs yields regular well-defined MO-MNPs with the size distribution below ca. 4% that can form self-assembled arrays. We have observed formation of such arrays for $\text{IrO}_x\text{@Au@AgDeNPs}$ (Figures 6.1D and 6S.9). These self-assembled MO-MNP arrays are highly regular metallodielectric (MD) materials with tunable LSPR interactions and precisely controlled distance between metallic cores. Imaging with Atomic Force Microscopy (Figure 6S.10) confirms the regularity and mechanical robustness of arrays that are not disturbed by the scanning. For MnO_{2-x}

@Au@AgDeNPs, while the particles were uniformly coated, they interacted strongly with each other (sticking together) that disrupted formation of well-ordered colloidal arrays.⁷⁸ Similarly, for the silica-encapsulated MNPs, with their low zeta potentials, formation of highly regular arrays was not observed. FeOOH@Au@AgDeNPs were the least uniform particles and consequently did not display regular packing.

The broad applicability of the developed coating procedures to different metal nanoparticles has been demonstrated first with the formation of silica coating performed in ammonia and isopropanol. Importantly, Au@AgDeNPs survives this deposition perfectly intact chemically and colloiddally: Figure 6S.11 shows the kinetics of shell formation monitored by SPR. Secondly, we have tested metal oxide encapsulation with AuNPs of different shapes. Figure 6S.12 shows successful encapsulation of gold platelets with IrO_x. IrO_x shells were visualized by EM (Figure 6S.12), and LSPR peak shifts were clearly observed by UV-vis spectroscopy (Figure 6S.12) upon IrCl₃ addition and heating.

The encapsulation procedure is readily scalable, the formation of the shells can be performed in volumes of several hundred mL, e.g. scaling up several hundred times compared to the typical reported procedures. We have performed such scaled-up synthesis to prepare MnO_{2-x}@Au@AgDeNPs samples for BET measurements (Figure 6S.13). The photochemical preparation of precursor AgDeNPs was scaled in parallel fashion, using multiple LEDs (Figure 6S.13).

6.3.2. Sensing with MO_x@Au@AgDeNPs.

Fundamental for sensing applications, oxide-encapsulated plasmonic MNPs retain sharp LSPR peaks and sensitivity of the metallic cores with the shape preservation after the formation of oxide shells. Another necessary condition for the realization of sensing is that either the shell thickness should be smaller than the probing length at the metal-dielectric interface or the shells should be porous and penetrable to analytes. We have been able to satisfy these criteria in several prepared MO-MNP systems that offer the clear advantage of detection selectivity achieved either by interacting with analytes

selectively or by selective shell penetration. To demonstrate such proof of concept experiments, $\text{MO}_x@Au@AgDeNP$ films were prepared and tested by surface-enhanced Raman spectroscopy (SERS) and surface plasmon resonance (SPR) analysis.

Figure 6.4 shows the calculated enhancement factors for SERS comparing 5,5'-dithiobis (2-nitrobenzoic acid) (DTNB), thiosalicylic acid and rhodamine 6G as analytes and $\text{MO}_x@Au@AgDeNPs$, $Au@AgDeNPs$ and $AgDeNPs$ as substrates. Calculation details are included in Methods. Oxide shells screen metal core and the overall enhancement is lower for $\text{MO}_x@Au@AgDeNPs$ compared to bare template MNPs. At the same time, selected enhancement was observed with thiosalicylic acid, where the peak at 801 cm^{-1} (in-plane C-H bending, $\delta\text{ CH}$)⁷⁹ was enhanced more than the strongest 1031 cm^{-1} peak (C-COOH stretch, $\nu\text{ C-COOH}$)⁷⁹ of bare MNPs, shown in Figure 6S.14A. Less enhancement of the signal observed for a carboxylic group is likely due to its binding to metal oxides. The selective enhancement is potentially useful for detection of analytes that are not strongly bound to metal substrates. A positive effect of the oxides shell was also observed for the enhancement of rhodamine 6G, which is a fluorescent compound. The fluorescence often strongly interferes with Raman spectroscopy and contributes to the enhanced background noise.⁸⁰ In presence of $\text{MO}_x@Au@AgDeNPs$, the fluorescence background is noticeably suppressed to yield cleaner spectra (Figure 6S.14B). The background noise between 1379 cm^{-1} to 1429 cm^{-1} was 5 and 33 for $\text{MnO}_{2-x}@Au@AgDeNP$ substrate and in absence of the substrate, respectively.

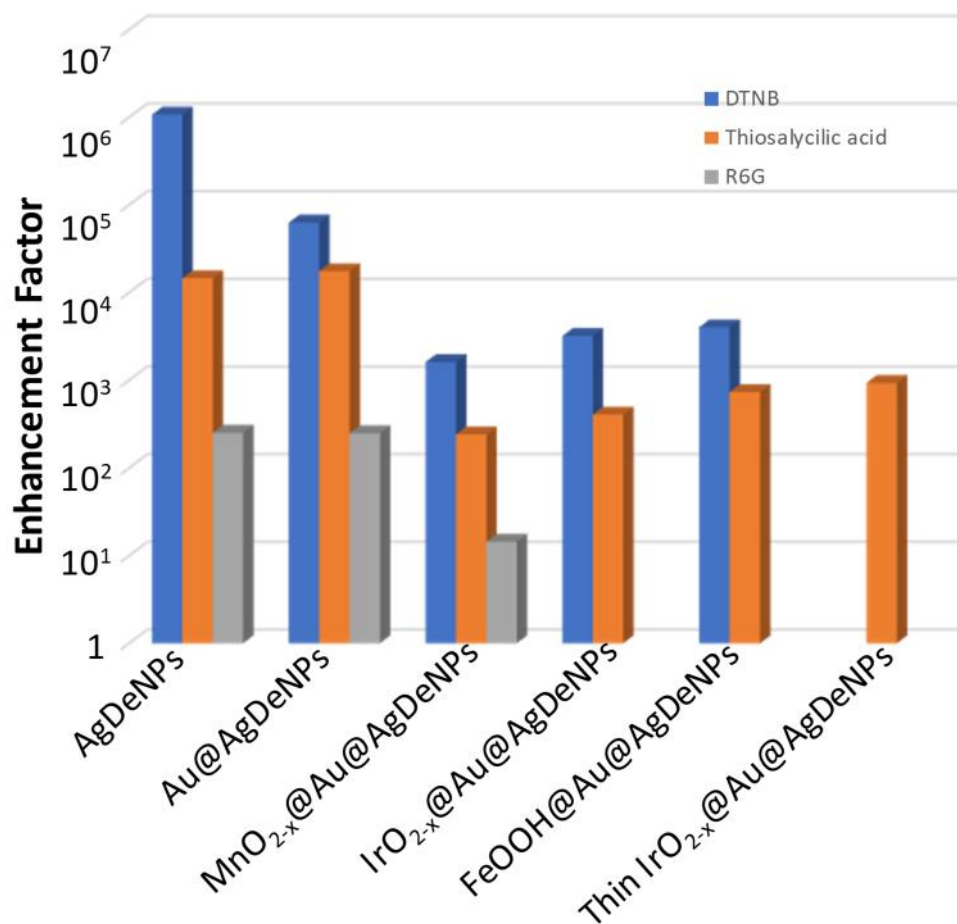


Figure 6.4. Calculated enhancement factors for NP films serving as a substrate for Raman spectroscopy of 5,5'-dithiobis (2-nitrobenzoic acid) (blue bars on the left); thiosalicylic acid (orange bars in the middle) and rhodamine 6G (grey bars on the right). See Experimental for more details.

6.3.3. SPR sensing, Selective Detection of Phosphate

SPR sensing with plasmonic MNPs rely upon sensitive changes in the energy (wavelength) of LSPR caused by changes in refractive index of the dielectric interface of MNPs. These changes can arise either in the bulk medium or due to adsorption on the species interacting with the MNP surface, such as thiolates.²⁰ Adsorption of halide species onto MNPs can be detected as well; iodide is a convenient ion to detect with MNPs very sensitively.^{21,22}

SPR results with MO-MNPs demonstrated successful detection of iodide and phosphate (Figure 6.5). Strong physisorption by iodide on gold and silver surfaces changes the metal-dielectric interface and translates into LSPR shifts, which is sensitively detected by SPR. Iodide was used to test shell penetrability and to gauge direct comparison with bare Au@AgDeNPs. No iodide detection was observed for IrO_x@Au@AgDeNPs due to their dense non-porous shells. For penetrable shells, iodide was generally detected at higher concentrations than previously reported by our group with non-coated particles.^{21,22} Readily observable LSPR shifts for FeOOH@Au@AgDeNPs and MnO_{2-x}@Au@AgDeNP films were produced at 10⁻⁵ M potassium iodide (Figure 6.5A,B). The lower limit of the iodide detection was below 10⁻⁶ M, given that the background noise was below 0.025 nm.

In the next step, we explored AgDeNPs encapsulated with iron and manganese oxides, known for their affinity to phosphate ions, for phosphate detection. Important to water and biochemical analysis, reliable phosphate detection remains challenging.⁸¹ There is no significant phosphate adsorption to MNP surface, thus it cannot be detected by bare MNPs. The shells of iron and manganese oxide are expected to bind phosphate that may translate to the SPR signal if binding takes place near the metal surface. Indeed, we were first able to detect phosphate at 1 mM with FeOOH@Au@AgDeNP films (Figure 6.5C), while the time of response was comparatively long at ca. 100 s. Noteworthy, doping FeOOH@Au@AgDeNPs with Mo(IV), known to form phosphomolybdates used in phosphate detection, enabled both the enhancement of the sensitivity (>1.5 times) and, most importantly, shortened the time of response to ca. 5 s (Figure 6.5D). In another series of experiments, we have tested phosphate detection with dispersions of MnO_{2-x}@Au@AgDeNPs. In this system, 0.1 mM phosphate can be detected, owing to the low SPR signal background (Figure 6.5E,F). Very low SPR background compared to bare MNPs is another advantageous feature of MO-MNPs. No interference of chloride at 1 mM and sulphate at 0.1 mM were observed (Figure 6.5F), thus confirming the selectivity of the phosphate detection. The influence of the shell thickness on the time and magnitude of the response of MnO_{2-x}@Au@AgDeNPs to phosphate in

shown in Figure 6S.15. The MO-MNPs with thicker shells respond appreciably faster and feature a larger magnitude of the response, since thicker oxide layers absorb more phosphate due to the accessibility of their volume. The selective phosphate detection is thus a very promising direction in applications of MO-MNPs.

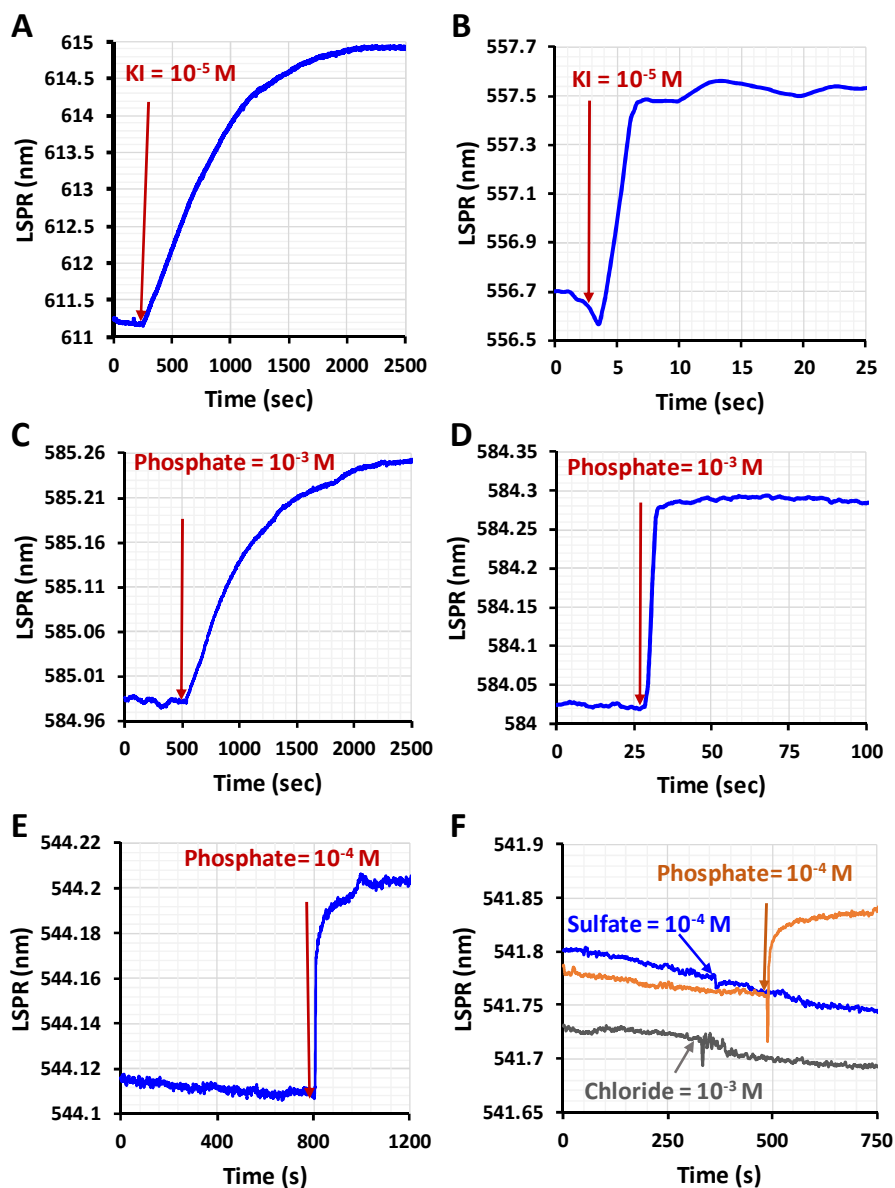


Figure 6.5. Surface plasmon resonance (SPR) response curves. **A)** and **B)** detection of 10^{-5} M iodide using films of FeOOH@Au@AgDeNPs and MnO_{2-x}@Au@AgDeNPs, respectively. **C)** and **D)** detection of 10^{-3} M of phosphate using films of FeOOH@Au@AgDeNPs and FeOOH/MoO_x@Au@AgDeNPs, respectively. **E)** and **F)** detection of 10^{-4} M of

phosphate using dispersions of $\text{MnO}_{2-x}@\text{Au}@\text{AgDeNPs}$. **F)** shows the selectivity in phosphate detection with the comparative response to 10^{-4} M sulfate and 10^{-3} M chloride.

Future work with MO-MNPs will be focused on further developments of selective detection of analytes with different oxide shells, in particular phosphate detection. Uniform MD nanocomposites of MO-MNPs will be explored in sensing and photonic applications.

6.4. Conclusions

We reported upon formation of novel functional nanoparticles and nanomaterials using a reliable protocol of formation of uniform metal oxide shells encapsulating well-defined shape-controlled metal nanoparticles with the preservation and enhancement of plasmonic properties. Deposition of several metal oxides (Fe, Mn and Ir) in mild aqueous conditions was demonstrated, while LSPR of resulting MO-MNPs could be tuned through the shell thickness and porosity. The uniformity of MO-MNPs was attested in formation of self-assembled arrays that offers a convenient pathway to metallodielectric nanocomposites. Developed MO-MNPs have been demonstrated promising for sensing, in particular selective phosphate detection by SPR utilizing the selectivity imparted by the metal oxide shells.

6.5. Methods

6.5.1. Reagents.

Silver nitrate (99%), sodium citrate tribasic dihydrate (99.5%), L-arginine (98%), sodium borohydride (>99%), hydrogen peroxide with the potassium stannate inhibitor 30–32 wt. %, in water (99.999% trace metal basis), tetrachloroauric acid (99%), potassium iodide (99%), potassium chloride (99%), sodium hydrosulfide (ACS grade), manganese (II) chloride tetrahydrate ($\geq 99.0\%$), manganese (II) perchlorate hydrate (99.0%), iron (II) perchlorate hydrate (98%), iron (II) sulfate heptahydrate ($\geq 99\%$), iron (III) chloride hexahydrate ($\geq 99\%$), iridium (III) chloride ($\geq 99.0\%$), tetraethyl orthosilicate ($\geq 99.0\%$), 5,5'-dithiobis (2-nitro-benzoic acid) (99%), thiosalicylic acid (98%), poly(diallyldimethylammonium chloride), (high molecular weight, 20 wt. % in water (PDPA, $M_w = 400,000\text{--}500,000$) all supplied by Sigma-

Aldrich, and poly(vinylpyrrolidone) (PVP, $M_w = 40,000$), 2-propanol (HPLC grade) and ammonium hydroxide (trace metal), supplied by Caledon Chemicals (Caledon, Canada), were used as received. Poly(sodium 4-styrenesulfonate) (PSS, $M_w = 70,000$, Sigma-Aldrich) was purified as follows: 2 g of PSS was dissolved in water (5 mL) and then precipitated with 5 mL of isopropanol. The precipitate was centrifuged and re-dissolved in 10 mL of mixture of water and isopropanol, 1 to 1 by volume. The last step was repeated one or two more times, and finally the precipitate was dried in an oven overnight. High-purity deionized water ($>18.2 \text{ M}\Omega \text{ cm}$) was produced using a Millipore A10 Milli-Q.

6.5.2. Synthetic Protocols.

Synthesis of precursor gold-plated decahedral silver nanoparticles (Au@AgDeNPs).

Silver decahedra (AgDeNPs) are prepared as previously reported,⁷² and then coated with 10 mol. % Au according to our recently reported procedure.¹⁵ Briefly, sodium tricitrate (1.68 mM), PVP or PSS (0.07 mM), L-arginine (8 μM), silver nitrate (0.13 mM) and sodium borohydride (1.29 mM) are combined while stirring at 400 rpm using a 12.7 mm by 3.2 mm stir bar in a 20 mL borosilicate vial (the molarities are total concentrations). After 1 hour of constant stirring, the solution darkened from pale yellow, and hydrogen peroxide (0.2 M) was added. The stir bar was removed, the sample was capped and exposed to a 450 nm LED for 14 hours. Gold precursor (HAuCl_4) was added to the prepared AgDeNP dispersion (15.7 mL) under stirring (400 rpm using a 12.7 by 3.2 mm stir bar) using a syringe pump (KDScientific) at a rate of 0.25 mL/hr. For the 10 mol. % coating, HAuCl_4 (3 mL of 0.06 mM) was loaded into a 5 mL syringe and dispensed using Teflon tubing (PTFE #18 AWG, Cole Parmer) sealed to the syringe with ethylene-vinyl acetate glue.

6.5.3. Formation of Metal Oxide Shells onto Au@AgDeNPs.

The general process of the metal oxide layer formation involved the controlled hydrolysis of metal salts in the presence of plasmonic MNP templates. For Mn, Fe, and Ir oxides, hydrolysis took place at or

above room temperature; formation of silica shells required a basic catalyst (ammonia) and alcohol media (either isopropanol or ethanol) with a controlled amount of water.

MnO_{2-x}: In a typical procedure for 500 mol. % (relative to silver in Au@AgDeNPs) MnO_{2-x} shells, MnCl₂ (200 μL of 0.01 M) was added to 10% mol. Au@AgDeNPs (3.6 mL), tightly capped and placed into an aluminum bead bath set to 80 °C for 1 hour. Hydrolysis occurred at room temperature as well, with the shell formation requiring 12-24 hours.

IrO_x: In a typical procedure for 400 mol. % IrO_x shells, 3.6 mL of 10 mol. % Au@AgDeNPs is mixed with IrCl₃ (90 μL of 0.02 M) in a 20 mL vial. The vial is tightly capped and heated at 100 °C for 20-30 minutes.

FeOOH: In a typical procedure for 1000 mol. % FeOOH shells, Fe(ClO₄)₂ or Fe(ClO₄)₃ (40 μL of 0.1 M) is added to 3.6 mL of 10 mol. % Au@AgDeNPs. The reaction occurs quickly at room temperature.

SiO₂: Typical procedure to prepare SiO₂@Au@AgDeNPs with SiO₂ shell thickness of 20 nm used the following protocol. A 4.0 mL solution of Au@AgDeNPs was first concentrated by centrifugation for 30 min at 4000 rpm. Supernatant was then removed and the concentrated Au@AgDeNPs were dispersed in 800 μL of deionized water. To this dispersion, PVP (50 μL of 0.005 M), 3.0 mL of isopropanol, and NH₄OH (200 μL of 14.8 M) were added. TEOS solution in isopropanol (diluted 200 times, 120 μL) was then added, and the vial was mixed gently and left at room temperature for 3 to 4 hours to complete the reaction.

6.5.4. Characterization.

Electron microscopy (both TEM and SEM) was performed using Hitachi S-5200 with the operating voltage of 30.0 kV. LEO 912B 120 kV energy filtered TEM with LaB₆ filament was used for HRTEM. NP dispersions were deposited on a carbon-coated formvar grid (EMS Corp.).

Measurements of zeta potential and hydrodynamic size were performed using Malvern Zetasizer Nano ZS. Brunner–Emmet–Teller (BET) data for nitrogen adsorption-desorption have been collected using

NOVA 2200e surface area and pore size analyzer (Quantachrome Instruments) at 77 K after 24-hour sample outgassing at 55 °C under vacuum.

Surface Plasmon Resonance Spectroscopy (SPR) measurements were performed using OpenSPR by Nicoya Lifesciences. 1 mL sample was measured into a 1.7-ml PMMA cell and inserted into an OpenSPR instrument, outfitted with a cell holder. After approximately 500 seconds of equilibration and establishing signal background (typical peak-to-peak noise amplitude of ca. 0.025 nm over 60-s interval), analyte of interest was injected, a cell was capped, removed and shaken roughly 10 times, and finally reinserted. The LSPR shift was measured as the difference between the maximum LSPR after injection and the equilibrated LSPR before injection. MO-MNPs films were prepared similarly to the reported procedure,⁸² where glass slides were treated with 0.01 wt. % PDDA followed by deposition of concentrated dispersions (1 mL centrifuged at 3,000 g for 30 minutes, concentrated to 10 μ L). Slides were inserted into PMMA cells and water was added, followed by an analyte of interest.

Surface Enhanced Raman Spectroscopy (SERS) data were acquired using R-3000QE fibre-optic Raman spectrometer equipped with 300 mW laser at 785 nm (RSI). Measurements were performed at 150 to 290 mW laser power with 5 s integration and 30 s frame size. 1 mL of NP solution was centrifuged at 3,000 g for 30 minutes to prepare a concentrated 10 μ L dispersion. The concentrated dispersion was dispensed onto a plasma cleaned quartz slide, spread to ca. 1 cm² and then dried in an oven at 60 °C. 10⁻⁶ M target analyte was spread to the same 1 cm² area over the film in 10 μ L increments. Peak heights at ca. 1350 cm⁻¹ for the known concentration of DTNB (-NO₂ symmetric stretch)⁸³, 801 cm⁻¹ for thiosalicylic acid (in plane aromatic C-H bending)⁷⁹, and 1320 cm⁻¹ for rhodamine 6G (in plane C-H bending)⁸⁴ were used to calculate enhancement factors. Reference spectra of the target analytes were obtained for a known concentration and area, following which the peak height per moles per area was calculated. This value was also calculated for measurements with nanoparticle films, which was then divided by the peak height/moles/area of the reference, giving a calculated enhancement factor.

UV-vis spectra were acquired with either Ocean Optics QE65000 fiber-optic UV-vis spectrometer or Cary 50Bio UV-vis spectrophotometer. Centrifugation was performed using either Thermo Scientific Legend Micro 21 or Medifuge centrifuges.

6.6. Acknowledgements

The authors gratefully acknowledge financial support from Natural Science and Engineering Research Council of Canada, Canada Foundation for Innovation, Ontario ORF-RI and ACS PRF. Ilya Gourevich and Neil Coombs are acknowledged for the assistance with the electron microscopy at the Centre for Nanostructure Imaging (University of Toronto). Nicoya Inc. is thanked for the advanced support of their instrumentation and instructive discussions. We are grateful to M. Aminur Rahman and Prof Al-Abadleh for assistance with nitrogen adsorption-desorption measurements. We also thank Stefan Stangherlin from our group for providing test samples of gold platelets.

6.7. Supplementary Information

Table 6S.1. Summary of experimental parameters for samples described in Figure 6.2 and Figure 6S.4.

Figure	Shell Type	Metal Precursor	Mol. % vs. Ag	Δ Diameter (nm)	LSPR (nm)	Δ LSPR (nm)	Experimental Treatment
6.2A	IrO _x	IrCl ₃	380	44	538	68	*
6.2B	IrO _x	IrCl ₃	400	18	556	86	*
6.2C	SiO ₂	TEOS	2400	58	514	18	*
6.2D	SiO ₂	TEOS	200	44	520	24	*
6.2E	MnO _{2-x}	MnCl ₂	200	25	588	92	heated 6 hrs 85 °C
6.2F	MnO _{2-x}	MnCl ₂	500	8	541	45	heated 3 minutes 160 °C in microwave reactor
6.2G	FeOOH	Fe(ClO ₄) ₂	10000	19	541	45	*
6.2H	FeOOH	FeCl ₃	1250	8	569	73	heated overnight at 85 °C
6S.4A	SiO ₂	TEOS	600	18	511	15	*
6S.4B	SiO ₂	TEOS	5500	58	519	23	*

6S.4C	MnO _{2-x}	Mn(ClO ₄) ₂	200	11	561	65	treated with 0.05 mM PAA (M _w =1800), 0.5 mM guanidine
6S.4D	MnO _{2-x}	Mn(ClO ₄) ₂	375	31	549	53	heated 30 mins at 95 °C
6S.4E	FeOOH	Fe(ClO ₄) ₂	250	4	541	45	*
6S.4F	FeOOH	FeSO ₄	100	14	561	72	4 hr slow addition with syringe pump
6S.4G	IrO _x	IrCl ₃	200	8	520	31	*
6S.4H	IrO _x	IrCl ₃	340	13	534	64	*

* As described in Methods section

Table 6S.2. Values of zeta potential measured for template metal nanoparticles (MNPs) and MNPs encapsulated in oxide shells (MO-MNPs). St. dev. is the standard deviation from the average of individual instrument measurements rather than from multiple runs, where the values may be lower.

Sample	Zeta potential (mV)	
	Average	St. dev.
AgDeNPs	-36.2	9.1
Au@AgDeNPs	-34.4	5.8
MnO _{2-x} @Au@AgDeNPs	-35.3	8.1
FeOOH@Au@AgDeNPs	-41.0	10.7
IrO _x @Au@AgDeNPs	-41.1	9.1
SiO ₂ @Au@AgDeNPs	-28.5	4.8

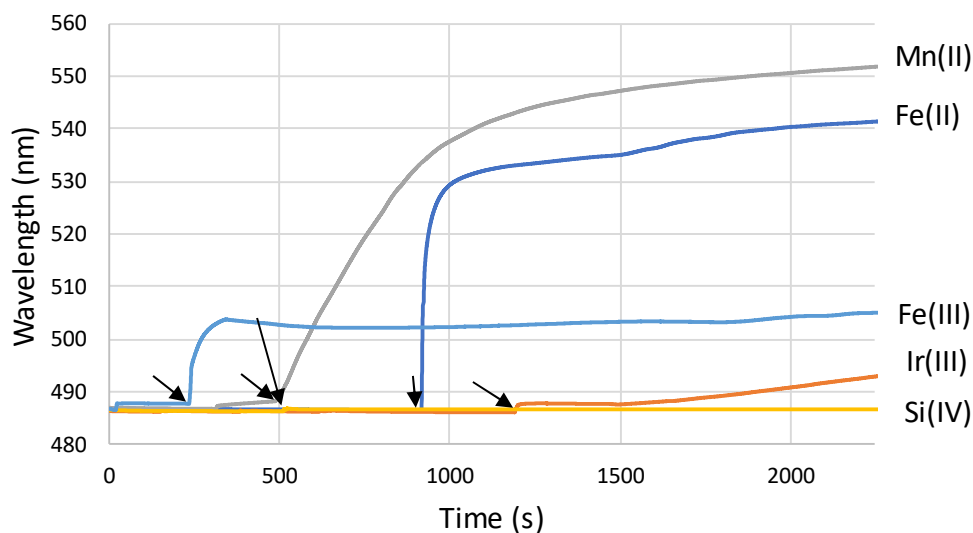


Figure 6S.1. Surface plasmon resonance (SPR) monitoring of LSPR peaks during formation of oxide shells by precursor hydrolysis at room temperature. The precursors used were the following: Mn (II) - MnCl_2 , Fe(II)- $\text{Fe}(\text{ClO}_4)_2$, Fe(III)- FeCl_3 , Ir - IrCl_3 , Si- TEOS (tetraethyl orthosilicate). The timing of precursor addition is indicated at the point of injection. Note that the room temperature conditions are not optimal for the hydrolysis of the iridium precursor that requires higher temperatures and silica precursor that requires base catalysts.

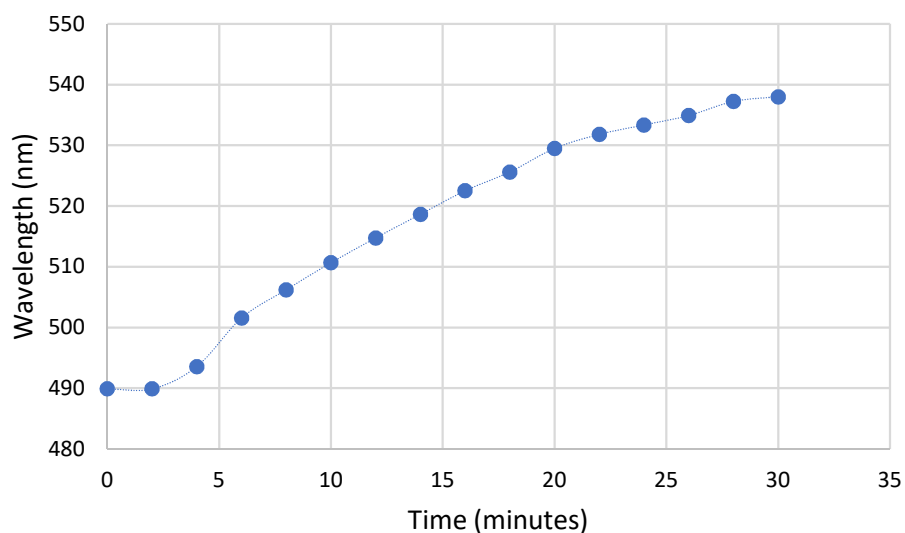


Figure 6S.2. Localized surface plasmon resonance (LSPR) peak monitoring of IrO_x shell formation by UV-vis spectroscopy. The precursor IrCl_3 (400% mol. % relative to silver in Au@AgDeNPs) was added at the initial time, while starting to heat to $100\text{ }^\circ\text{C}$. The sample was removed to measure each point. Connecting dashed line is to indicate the trend only.

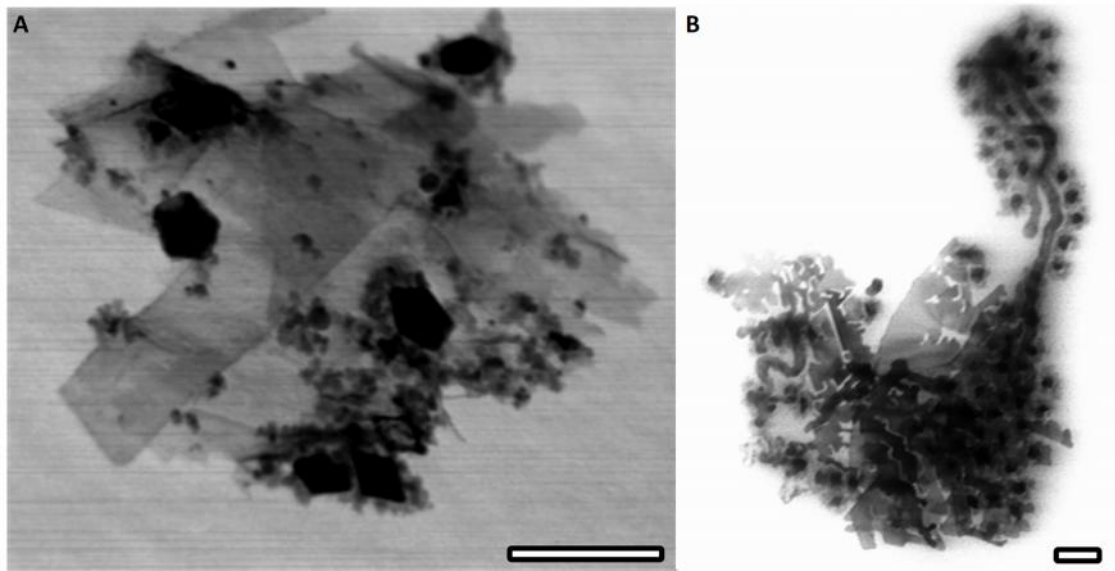


Figure 6S.3. Transmission electron microscopy (TEM) images of samples prepared with excess of Mn(II) precursors, forming layered birnessite (MnO_{2-x}) structures. All scale bars are 100 nm.

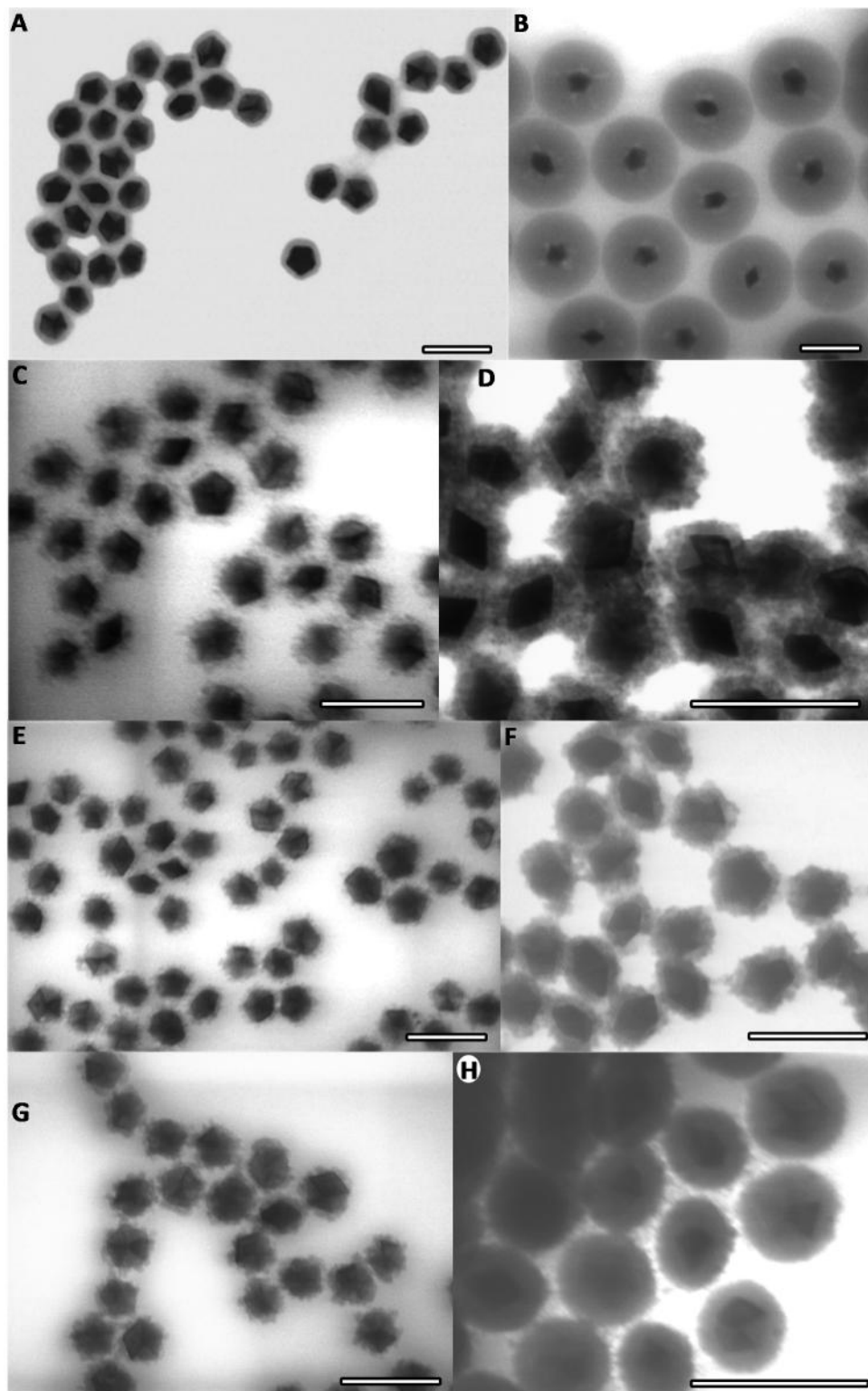


Figure 6S.4. TEM images of MO-MNPs with thin **A), C), E), and G)** and thick **B), D), F), and H)** shells. **A)** and **B)** are $\text{SiO}_2@Au@AgDeNPs$; **C)** and **D)** are $\text{MnO}_{2-x}@Au@AgDeNPs$; **E)** and **F)** are $\text{FeOOH}@Au@AgDeNPs$; and **G)** and **H)** are $\text{IrO}_x@Au@AgDeNPs$. All scale bars are 100 nm.

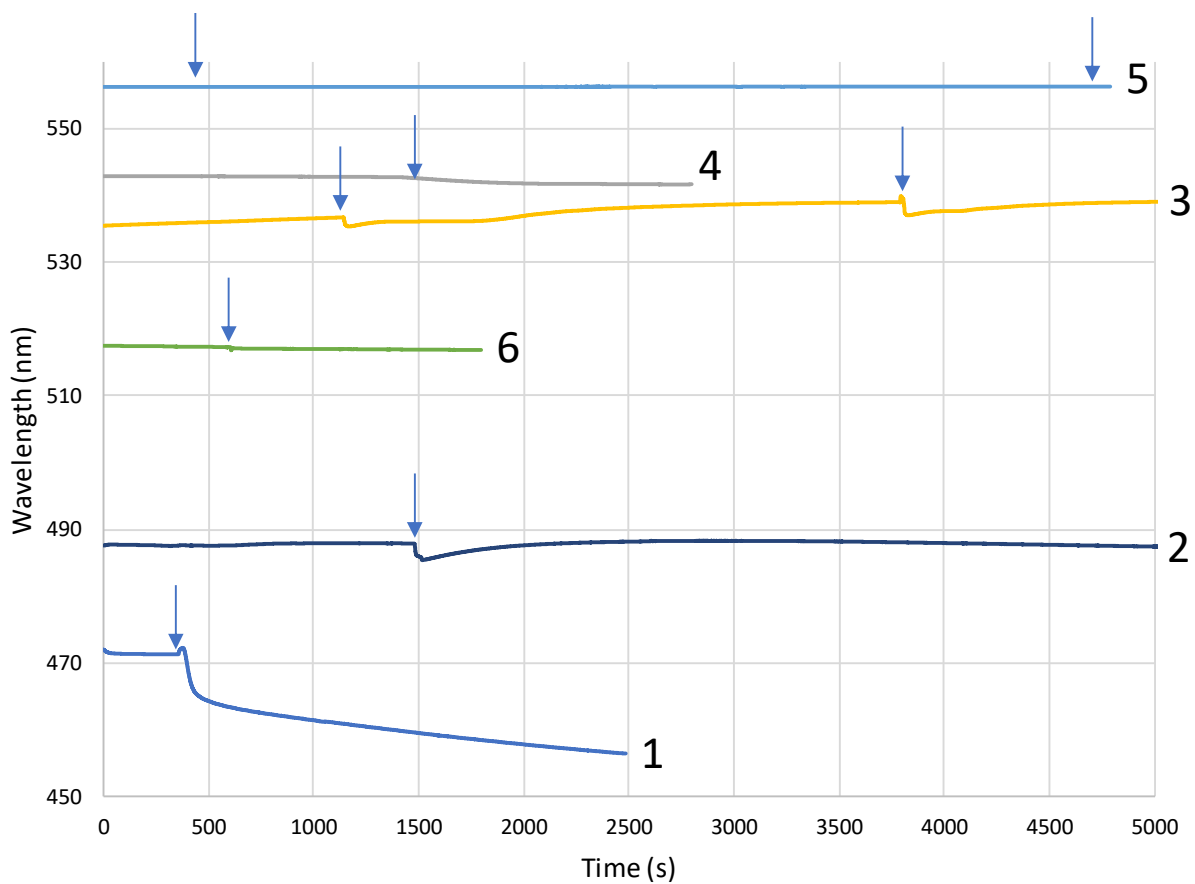


Figure 6S.5. Stability and porosity tests based on SPR response curves upon NaHS exposure for **1)** AgDeNPs, **2)** Au@AgDeNPs, **3)** FeOOH@Au@AgDeNPs, **4)** MnO_{2-x}@Au@AgDeNPs, **5)** IrO_x@Au@AgDeNPs, and **6)** SiO₂@Au@AgDeNPs. Injection times are indicated by arrows, first injection is 10⁻³ M NaHS, and second injection (if used) is 10⁻² M NaHS.

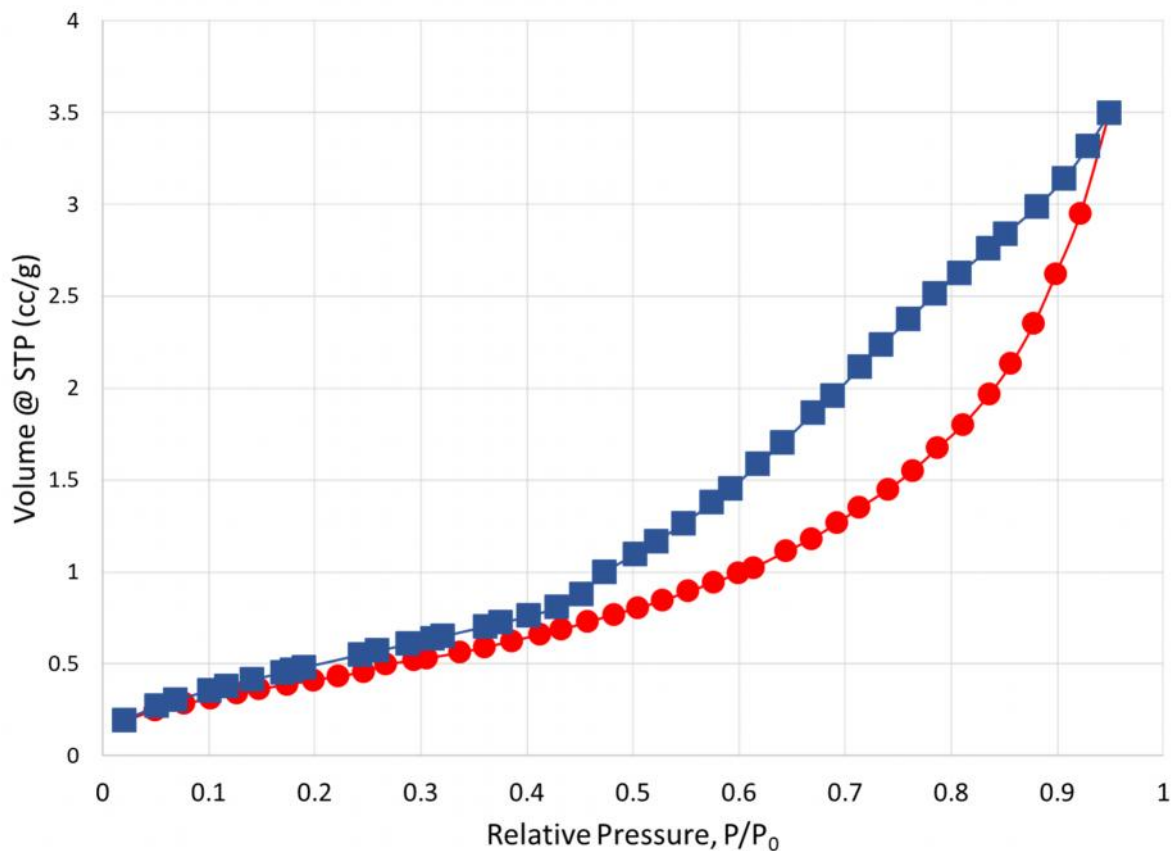


Figure 6S.6. N₂ adsorption-desorption isotherm for MnO_x@Au@AgDeNPs. Red circles are adsorption and blue squares are desorption.

Table 6S.3. N₂ adsorption-desorption results for MnO_x@Au@AgDeNPs.

	MnO _{x-2} @Au@AgDeNPs Run 1 (plotted above)	MnO _{x-2} @Au@AgDeNPs Run 2
Outgassed Mass (mg)	53.5	53.5
Specific Surface Area (m ² /g)	27.641	26.457
BET (C) Constant	18.817	23.910
Correlation Coefficient, r	0.9976	0.9998
Adsorptive	N ₂	N ₂
Adsorptive Temperature (K)	77.350	77.350
SinglePoint BET (m ² /g)	24.92	24.10
BJH method cumulative desorption pore volume (cc/g)	8.94 × 10 ⁻²	1.01 × 10 ⁻¹
DH method cumulative pore volume	8.69 × 10 ⁻²	9.85 × 10 ⁻²

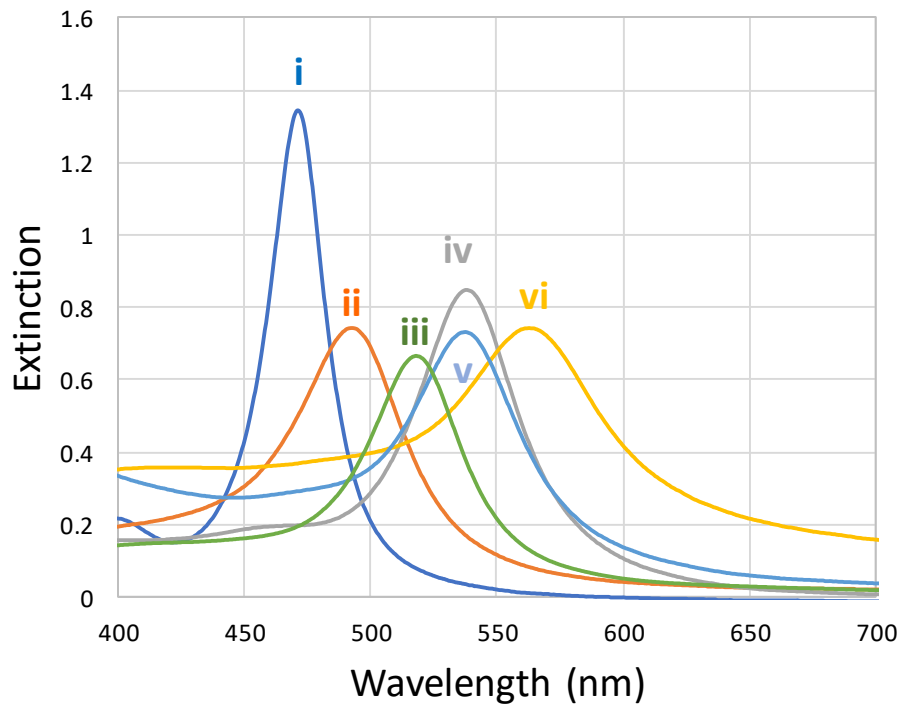


Figure 6S.7. UV-vis spectra of Figure 6.1 shown without normalization, **i)** silver decahedral nanoparticles (AgDeNPs), **ii)** 10 mol. % Au coated AgDeNPs (Au@AgDeNPs), **iii)** SiO₂@Au@AgDeNPs, **iv)** FeOOH@Au@AgDeNPs, **v)** IrO_x@Au@AgDeNPs, **vi)** MnO_{2-x}@Au@AgDeNPs. Samples were measured with 0.5-cm path length cuvettes, silver concentration is 0.13 mM for i), and 0.1 mM for ii)-vi).

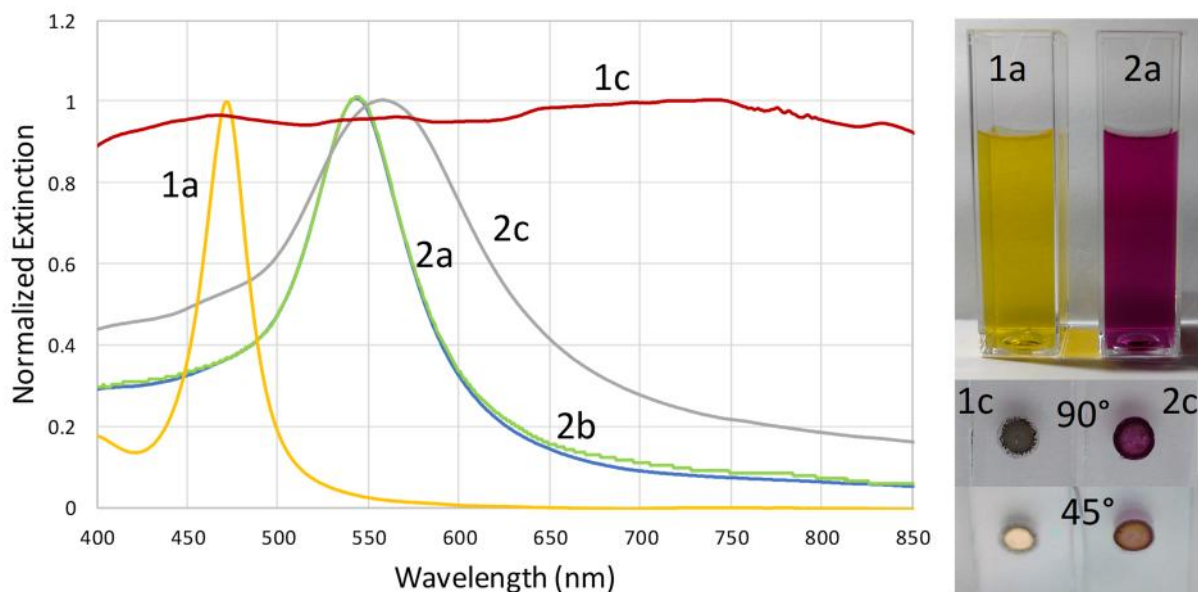


Figure 6S.8. Normalized transmission UV-vis spectra (left) and optical photographs (right) of **1**) AgDeNPs, and **2**) IrO_x@Au@AgDeNPs in **a**) as prepared dispersions, **b**) 20× concentrated dispersions (after centrifugation and supernatant removal) confined between microscope slides, and **c**) solid films (shown at 90° and 45° relative to the glass slide in optical photographs).

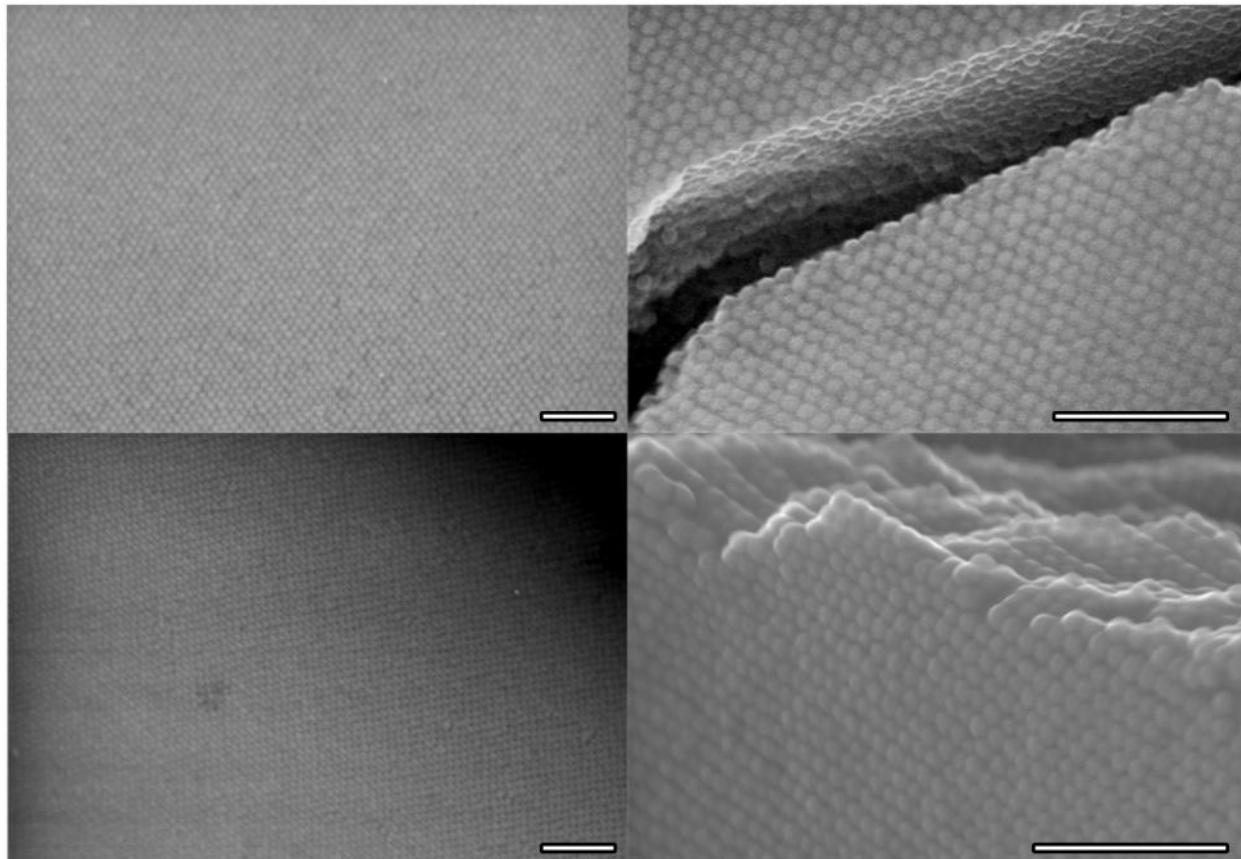


Figure 6S.9. Representative scanning electron microscopy (SEM) images of self-assembled metalodielectric arrays of $\text{IrO}_x@Au@AgDeNPs$. Samples on the left panels are prepared with 360 mol. % Ir relative to silver, and panels on the right – with 380 mol. % that correspond to ca. 12 and 13 nm thickness of IrO_x shell, respectively. All scale bars are 500 nm.

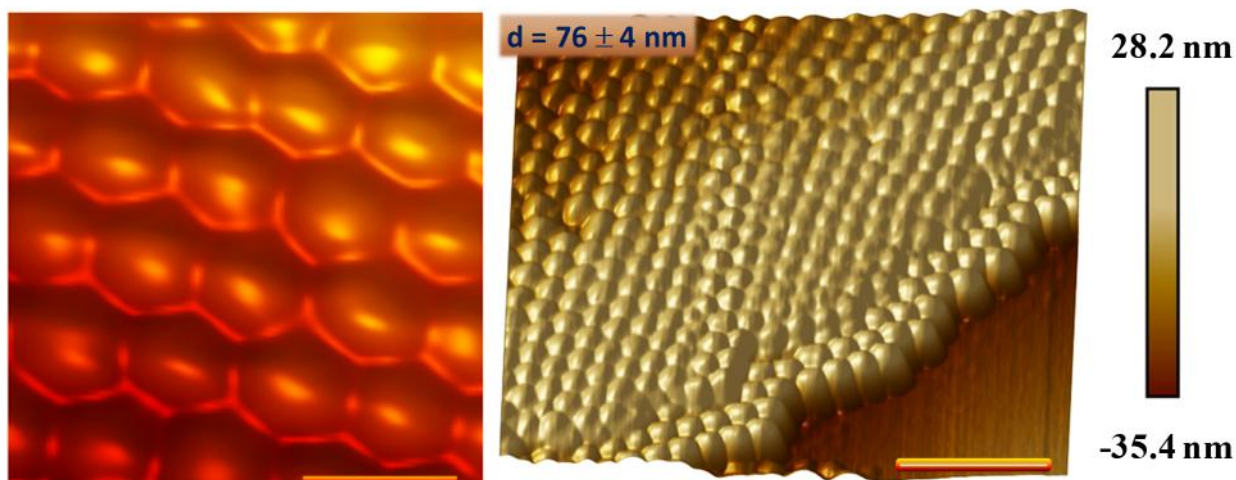


Figure 6S.10. Atomic force microscopy (AFM) images of self-assembled metallodielectric arrays of $\text{IrO}_x@Au@AgDeNPs$ prepared with 360 mol. % Ir relative to silver. Corresponding to ca. 12 nm shell thickness shell, in a good agreement with the average diameter of the coated particles measured by AFM (76 ± 4 nm). Scale bars are 100 nm on the left and 500 nm on the right.

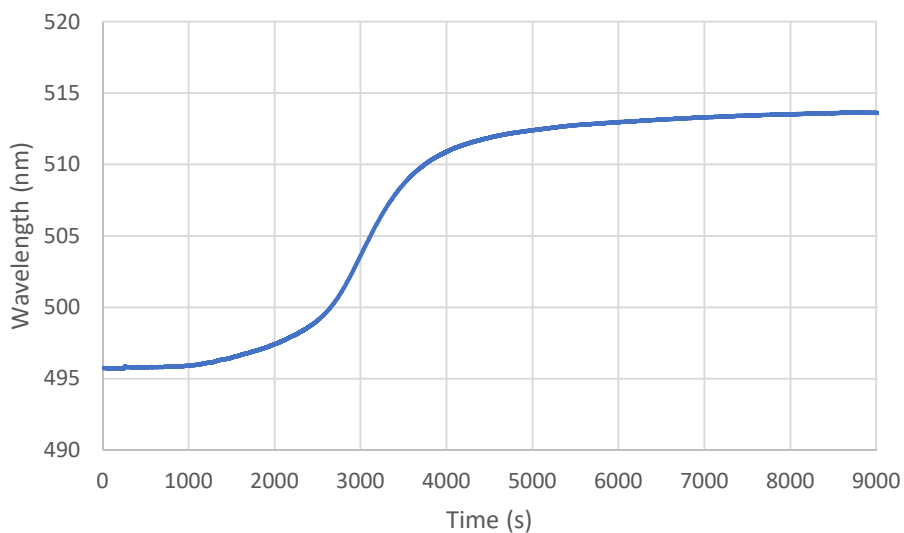


Figure 6S.11. Surface plasmon resonance (SPR) response curve of the room temperature formation of SiO_2 shells at $Au@AgDeNPs$ through hydrolysis of tetraethyl orthosilicate (TEOS) in basic media (0.75 M ammonia and 13.1 M water in isopropanol). Monitoring of SPR response started upon addition of TEOS.

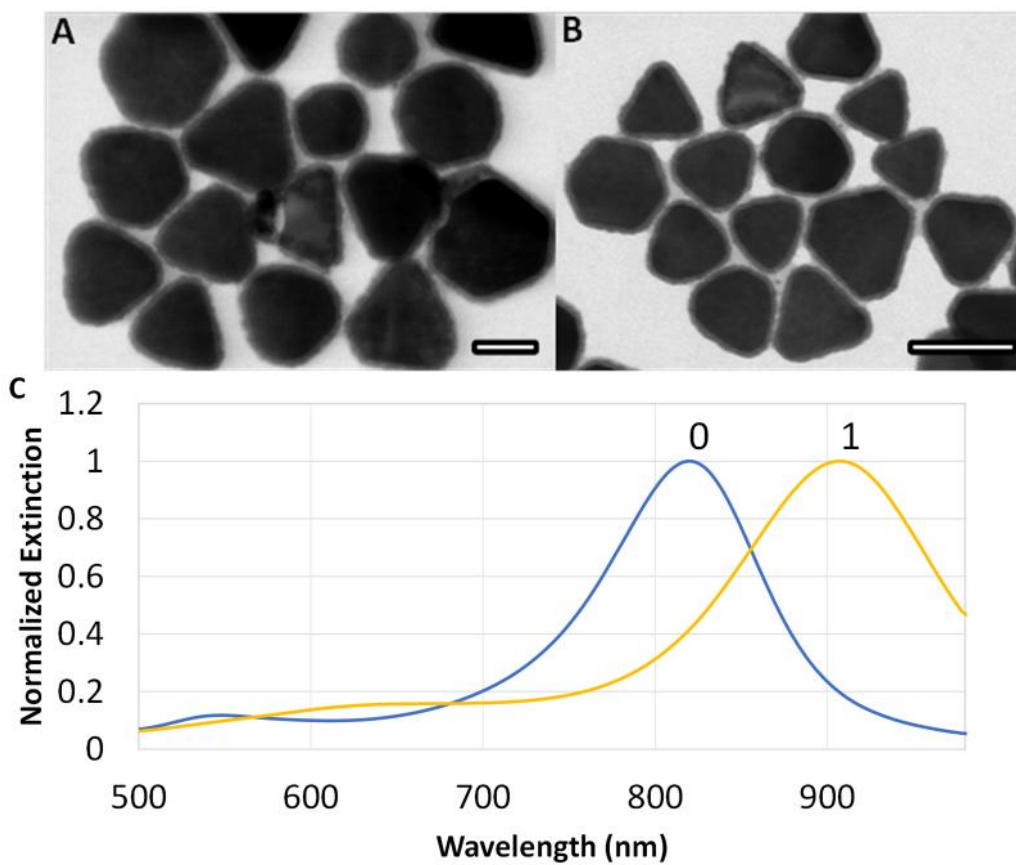


Figure 6S.12. Universality of oxide encapsulation procedure demonstrated by coating Au platelets (AuNPs) with IrO_x. **A)** and **B)** TEM images of IrO_x@AuNPs, **C)** UV-vis spectra of AuNPs prior (**0**) and after (**1**) IrO_x shell formation. Scale bars are 50 nm in A) and 100 nm in B).

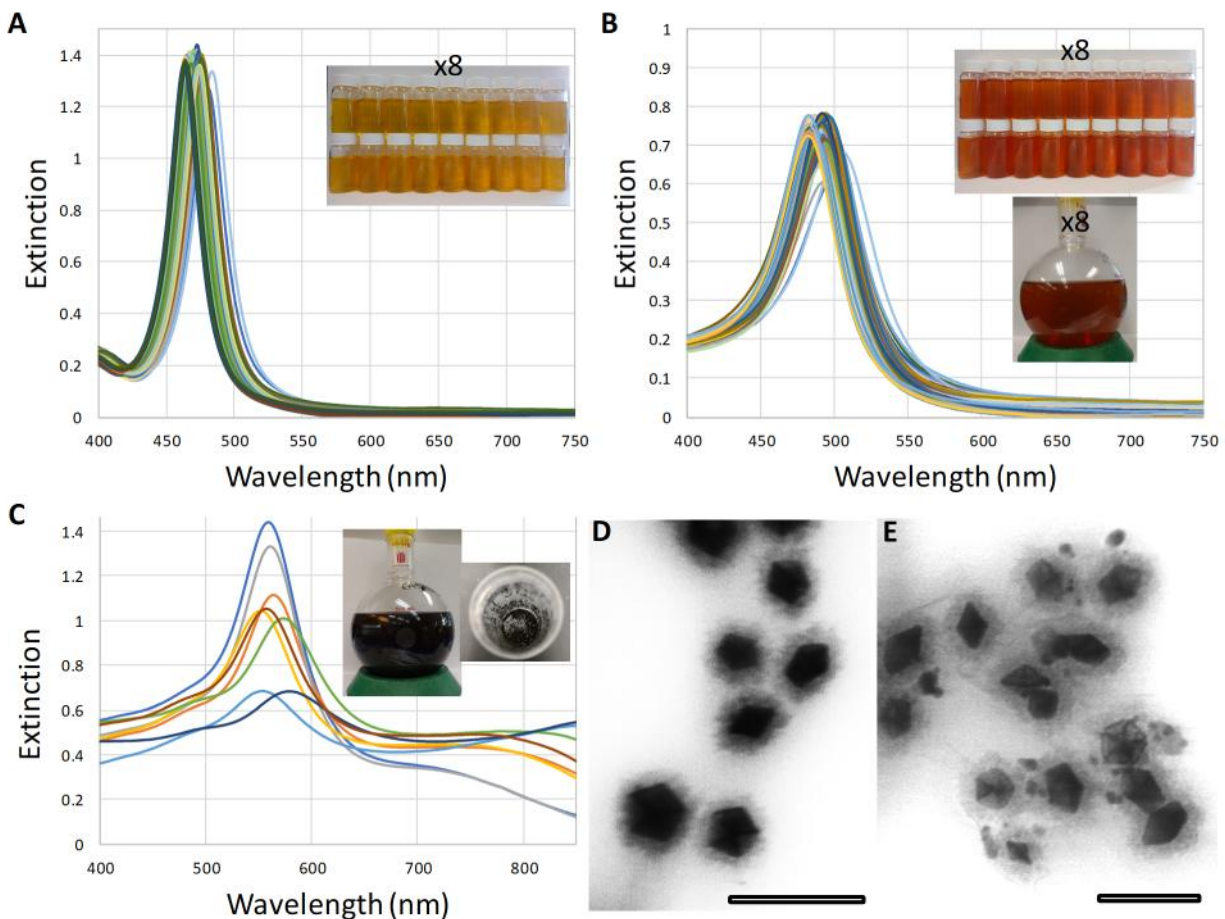


Figure 6S.13. Demonstration of scaling up the procedure with decahedral silver nanoparticles (AgDeNPs). **A-C)** UV-vis spectra of **A)** AgDeNPs synthesis of 18 by 20 ml vials repeated consecutively 8 times, **B)** 10 mol. % Au coated silver decahedra (10% Au@AgDeNPs), **C)** 800 mol. % MnO_x deposition of Au@AgDeNPs (MnO_x@Au@AgDeNPs) with inset of optical photographs of dispersions and the final dried powder. **D)** and **E)** representative transmission electron microscopy (TEM) images of MnO_x@Au@AgDeNPs for a typical deposition in **D)** and one of the deposition runs where some aggregation and/or pitting took place, observable by UV-vis peaks at ca. 800 nm in **E)**. All scale bars are 100 nm.

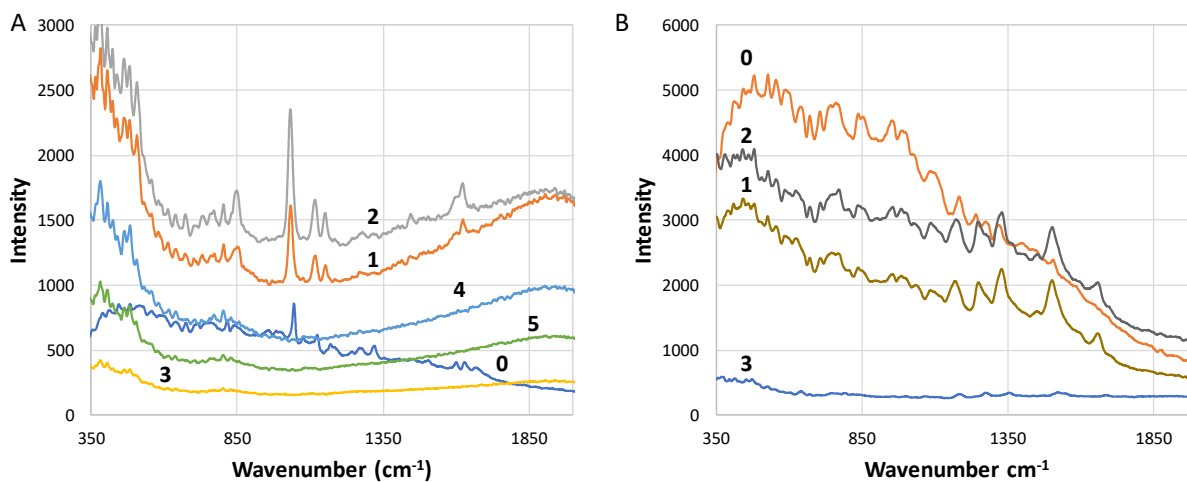


Figure 6S.14. Raman spectra of substrate-enhanced compared to non-enhanced (reference): **A)** thiosalicylic acid and **B)** rhodamine 6G. **0)** reference at higher concentrations, without NP substrate, **1)** AgDeNPs, **2)** Au@AgDeNPs, **3)** MnO_{2-x}@Au@AgDeNPs, **4)** FeOOH@Au@AgDeNPs, and **5)** IrO_x@Au@AgDeNPs as a substrate.

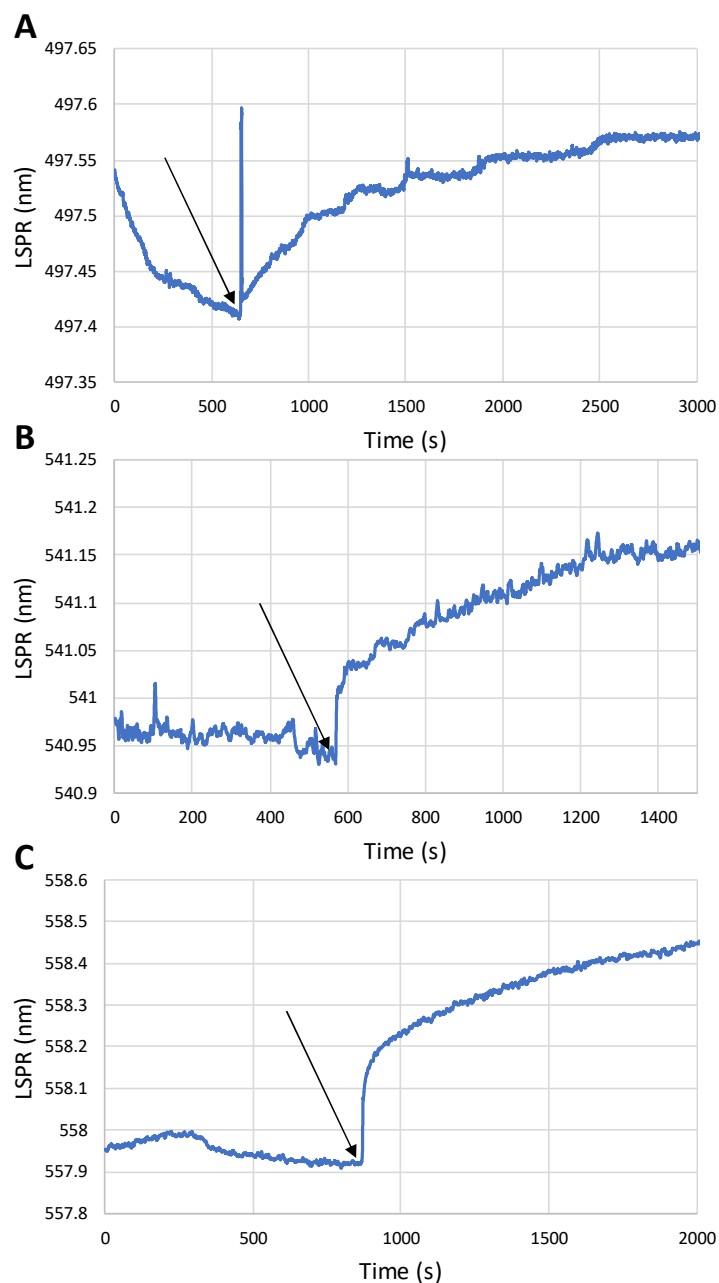


Figure 6S.15. SPR response curves of $\text{MnO}_{2-x}@\text{Au}@\text{AgDeNP}$ dispersions to 10^{-4} M phosphate for different amounts of manganese in a shell: **A)** 125 mol. % relative to silver in $\text{Au}@\text{AgDeNPs}$, **B)** 500 %, and **C)** 1000% and corresponding oxide thickness of ca. 3-5 nm, 10 nm and 15 nm, respectively. Arrows indicate the time of phosphate injection.

My contribution to this work includes coordinating experiments and collating results. I was primarily responsible for MnO_{2-x} shells, N. Murshid for SiO_2 , P. Campbell for IrO_x , and FeOOH shells were a joint

effort between myself and N. Murshid. SPR measurements were completed in collaboration with N. Murshid, SERS measurements were completed by me. The first draft of the manuscript was prepared by me, figures were primarily my responsibility, with assistance by N. Murshid. Images were taken by V. Kitaev. Iterative refining of the manuscript was a joint effort between N. Murshid, V. Kitaev, and myself.

6.8. References

- (1) Hartland, G. V.; Besteiro, L. V.; Johns, P.; Govorov, A. O. What's so Hot about Electrons in Metal Nanoparticles? *ACS Energy Lett.* **2017**, *2*, 1641–1653.
- (2) Wang, W.; Ramezani, M.; Väkeväinen, A. I.; Törmä, P.; Rivas, J. G.; Odom, T. W. The Rich Photonic World of Plasmonic Nanoparticle Arrays. *Mater. Today* **2018**, *21*, 303–314.
- (3) Li, Z. H.; Truhlar, D. G. Nanothermodynamics of Metal Nanoparticles. *Chem. Sci.* **2014**, *5*, 2605–2624.
- (4) Jiang, W.; Ji, W.; Au, C.-T. Surface/Interfacial Catalysis of (Metal)/Oxide System: Structure and Performance Control. *ChemCatChem* **2018**, *10*, 2125–2163.
- (5) Sharma, G.; Kumar, D.; Kumar, A.; Al-Muhtaseb, A. H.; Pathania, D.; Naushad, M.; Mola, G. T. Revolution from Monometallic to Trimetallic Nanoparticle Composites, Various Synthesis Methods and Their Applications: A Review. *Mater. Sci. Eng. C* **2017**, *71*, 1216–1230.
- (6) Chen, X.; Agio, M.; Sandoghdar, V. Metallodielectric Hybrid Antennas for Ultrastrong Enhancement of Spontaneous Emission. *Phys. Rev. Lett.* **2012**, *108*, 233001.
- (7) Wu, D.; Jiang, S.; Cheng, Y.; Liu, X. Three-Layered Metallodielectric Nanoshells : Plausible Meta-Atoms for Metamaterials with Isotropic Negative Refractive Index at Visible Wavelengths. *Opt. Express* **2013**, *21*, 1076–1086.
- (8) Sabela, M.; Balme, S.; Bechelany, M.; Janot, J.-M.; Bisetty, K. A Review of Gold and Silver Nanoparticle-Based Colorimetric Sensing Assays. *Adv. Eng. Mater.* **2017**, *19*, 1700270.
- (9) Ertem, E.; Diez-Castellnou, M.; Ong, Q. K.; Stellacci, F. Novel Sensing Strategies Based on Monolayer Protected Gold Nanoparticles for the Detection of Metal Ions and Small Molecules. *Chem. Rec.* **2017**, *17*, 1–11.
- (10) Pelaz, B.; Alexiou, C.; Alvarez-Puebla, R. A.; Alves, F.; Andrews, A. M.; Ashraf, S.; Balogh, L. P.; Ballerini, L.; Bestetti, A.; Brendel, C.; et al. Diverse Applications of Nanomedicine. *ACS Nano* **2017**, *11*, 2313–2381.
- (11) Yang, P.; Zheng, J.; Xu, Y.; Zhang, Q.; Jiang, L. Colloidal Synthesis and Applications of Plasmonic Metal Nanoparticles. *Adv. Mater.* **2016**, *28*, 10508–10517.

- (12) Gilroy, K. D.; Ruditskiy, A.; Peng, H. C.; Qin, D.; Xia, Y. Bimetallic Nanocrystals: Syntheses, Properties, and Applications. *Chem. Rev.* **2016**, *116*, 10414–10472.
- (13) Wu, Y.; Sun, X.; Yang, Y.; Li, J.; Zhang, Y.; Qin, D. Enriching Silver Nanocrystals with a Second Noble Metal. *Acc. Chem. Res.* **2017**, *50*, 1774–1784.
- (14) Murshid, N.; Gourevich, I.; Coombs, N.; Kitaev, V. Gold Plating of Silver Nanoparticles for Superior Stability and Preserved Plasmonic and Sensing Properties. *Chem. Commun.* **2013**, *49*, 11355–11357.
- (15) Cathcart, N.; Chen, J. I. L.; Kitaev, V. LSPR Tuning from 470 to 800 nm and Improved Stability of Au-Ag Nanoparticles Formed by Gold Deposition and Rebuilding in the Presence of Poly(Styrenesulfonate). *Langmuir* **2018**, *34*, 612–621.
- (16) Pieczonka, N. P. W.; Aroca, R. F. Single Molecule Analysis by Surface-Enhanced Raman Scattering. *Chem. Soc. Rev.* **2008**, *37*, 946–954.
- (17) Lee, S. J.; Guan, Z.; Xu, H.; Moskovits, M. Surface-Enhanced Raman Spectroscopy and Nanogeometry: The Plasmonic Origin of SERS. *J. Phys. Chem. C* **2007**, *111*, 17985–17988.
- (18) Ding, S.-Y.; You, E.-M.; Tian, Z.-Q.; Moskovits, M. Electromagnetic Theories of Surface-Enhanced Raman Spectroscopy. *Chem. Soc. Rev.* **2017**, *46*, 4042–4076.
- (19) Reguera, J.; Langer, J.; Jiménez de Aberasturi, D.; Liz-Marzán, L. M. Anisotropic Metal Nanoparticles for Surface Enhanced Raman Scattering. *Chem. Soc. Rev.* **2017**, *46*, 3866–3885.
- (20) Langer, J.; Novikov, S. M.; Liz-Marzán, L. M. Sensing Using Plasmonic Nanostructures and Nanoparticles. *Nanotechnology* **2015**, *26*, 322001.
- (21) Keunen, R.; Macoretta, D.; Cathcart, N.; Kitaev, V. Stable Ligand-Free Stellated Polyhedral Gold Nanoparticles for Sensitive Plasmonic Detection. *Nanoscale* **2016**, *8*, 2575–2583.
- (22) Cathcart, N.; Coombs, N.; Gourevich, I.; Kitaev, V. Synthesis and Sensing Properties of D_{5h} Pentagonal Silver Star Nanoparticles. *Nanoscale* **2016**, *8*, 18282–18290.
- (23) Yu, X.; Shi, L.; Han, D.; Zi, J.; Braun, P. V. High Quality Factor Metallodielectric Hybrid Plasmonic-Photonic Crystals. *Adv. Funct. Mater.* **2010**, *20*, 1910–1916.
- (24) Acimovic, S. S.; Ortega, M. A.; Sanz, V.; Berthelot, J.; Garcia-Cordero, J. L.; Renger, J.; Maerkl, S. J.; Kreuzer, M. P.; Quidant, R. LSPR Chip for Parallel, Rapid, and Sensitive Detection of Cancer Markers in Serum. *Nano Lett.* **2014**, *14*, 2636–2641.
- (25) Chen, H. M.; Pang, L.; Kher, A.; Fainman, Y. Three-Dimensional Composite Metallodielectric Nanostructure for Enhanced Surface Plasmon Resonance Sensing. *Appl. Phys. Lett.* **2009**, *94*, 073117.
- (26) Chaudhuri, R. G.; Paria, S. Core / Shell Nanoparticles : Classes , Properties , Synthesis Mechanisms

- , Characterization , and Applications. *Chem. Rev.* **2012**, *112*, 2373–2433.
- (27) Wei, S.; Wang, Q.; Zhu, J.; Sun, L.; Lin, H.; Guo, Z. Multifunctional Composite Core–shell Nanoparticles. *Nanoscale* **2011**, *3*, 4474–4502.
- (28) Zhang, C.; Chen, B.-Q.; Li, Z.-Y.; Xia, Y.; Chen, Y.-G. Surface Plasmon Resonance in Bimetallic Core–Shell Nanoparticles. *J. Phys. Chem. C* **2015**, *119*, 16836–16845.
- (29) Li, J. F.; Zhang, Y. J.; Ding, S. Y.; Panneerselvam, R.; Tian, Z. Q. Core-Shell Nanoparticle-Enhanced Raman Spectroscopy. *Chem. Rev.* **2017**, *117*, 5002–5069.
- (30) El-Toni, A. M.; Habila, M. A.; Labis, P. Design, Synthesis and Applications of Core–shell, Hollow Core, and Nanorattle Multifunctional Nanostructures. *Nanoscale* **2016**, *8*, 2510–2531.
- (31) Liu, X.; Iocozzia, J.; Wang, Y.; Cui, X.; Chen, Y.; Zhao, S.; Li, Z.; Lin, Z. Noble Metal–metal Oxide Nanohybrids with Tailored Nanostructures for Efficient Solar Energy Conversion, Photocatalysis and Environmental Remediation. *Energy Environ. Sci.* **2017**, *10*, 402–434.
- (32) Li, G.; Tang, Z. Noble Metal Nanoparticle@metal Oxide Core/Yolk-Shell Nanostructures as Catalysts: Recent Progress and Perspective. *Nanoscale* **2014**, *6*, 3995–4011.
- (33) Ray, C.; Pal, T. Recent Advances of Metal–metal Oxide Nanocomposites and Their Tailored Nanostructures in Numerous Catalytic Applications. *J. Mater. Chem. A* **2017**, *5*, 9465–9487.
- (34) Kochuveedu, S. T.; Jang, Y. H.; Kim, D. H. A Study on the Mechanism for the Interaction of Light with Nanostructures for Various Photophysical Applications. *Chem. Soc. Rev.* **2013**, *42*, 8467–8493.
- (35) Oldfield, G.; Ung, T.; Mulvaney, P. Au@SnO₂ Core-Shell Nanocapacitors. *Adv. Mater.* **2010**, *12*, 1519–1522.
- (36) Paniagua-Domínguez, R.; López-Tejeira, F.; Marqués, R.; Sánchez-Gil, J. A. Metallo-Dielectric Core–shell Nanospheres as Building Blocks for Optical Three-Dimensional Isotropic Negative-Index Metamaterials. *New J. Phys.* **2011**, *13*, 123017.
- (37) Pastoriza-Santos, I.; Pérez-Juste, J.; Carregal-Romero, S.; Hervés, P.; Liz-Marzán, L. M. Metallodielectric Hollow Shells: Optical and Catalytic Properties. *Chem. – An Asian J.* **2006**, *1*, 730–736.
- (38) Liu, X.; Iocozzia, J.; Wang, Y.; Cui, X.; Chen, Y.; Zhao, S.; Li, Z.; Lin, Z. Noble Metal–metal Oxide Nanohybrids with Tailored Nanostructures for Efficient Solar Energy Conversion, Photocatalysis and Environmental Remediation. *Energy Environ. Sci.* **2017**, *10*, 402–434.
- (39) Chen, C.; Chen, Y. Fe₃O₄ / TiO₂ Core / Shell Nanoparticles as Affinity Probes for the Analysis of Phosphopeptides Using TiO₂ Surface-Assisted Laser Desorption / Ionization Mass Spectrometry. *Anal. Chem.* **2005**, *77*, 5912–5919.

- (40) Graf, C.; Van Blaaderen, A. Metallodielectric Colloidal Core - Shell Particles for Photonic Applications. *Langmuir* **2002**, *18*, 524–534.
- (41) Tom, R. T.; Nair, A. S.; Singh, N.; Aslam, M.; Nagendra, C. L.; Philip, R.; Vijayamohanan, K.; Pradeep, T. Freely Dispersible Au@TiO₂, Au@ZrO₂, Ag@TiO₂, and Ag@ZrO₂ Core–Shell Nanoparticles: One-Step Synthesis, Characterization, Spectroscopy, and Optical Limiting Properties. *Langmuir* **2003**, *19*, 3439–3445.
- (42) Pastoriza-Santos, I.; Koktysh, D. S.; Mamedov, A. A.; Giersig, M.; Kotov, N. A.; Liz-Marzán, L. M. One-Pot Synthesis of Ag@TiO₂ Core–Shell Nanoparticles and Their Layer-by-Layer Assembly. *Langmuir* **2000**, *16*, 2731–2735.
- (43) Chen, Z.; Wang, Z. L.; Zhan, P.; Zhang, J. H.; Zhang, W. Y.; Wang, H. T.; Ming, N. B. Preparation of Metallodielectric Composite Particles with Multishell Structure. *Langmuir* **2004**, *20*, 3042–3046.
- (44) Liang, Z.; Susha, A. S.; Caruso, F. Metallodielectric Opals of Layer-by-Layer Processed Coated Colloids. *Adv. Mater.* **2002**, *14*, 1160–1164.
- (45) Guerrero-Martínez, A.; Pérez-Juste, J.; Liz-Marzán, L. M. Recent Progress on Silica Coating of Nanoparticles and Related Nanomaterials. *Adv. Mater.* **2010**, *22*, 1182–1195.
- (46) Lu, Y.; Yin, Y.; Li, Z.-Y.; Xia, Y. Synthesis and Self-Assembly of Au@SiO₂ Core–Shell Colloids. *Nano Lett.* **2002**, *2*, 785–788.
- (47) Hanske, C.; Sanz-Ortiz, M. N.; Liz-Marzán, L. M. Silica-Coated Plasmonic Metal Nanoparticles in Action. *Adv. Mater.* **2018**, *30*, 1707003.
- (48) Li, J.; Cushing, S. K.; Bright, J.; Meng, F.; Senty, T. R.; Zheng, P.; Bristow, A. D.; Wu, N. Ag@Cu₂O Core-Shell Nanoparticles as Visible-Light Plasmonic Photocatalysts. *ACS Catal.* **2013**, *3*, 47–51.
- (49) Tsuji, M.; Uto, K.; Hayashi, J.; Yoshiwara, A. Synthesis of Flower-Like AuPd@SiO₂ Nanoparticles with a Broad Light Extinction for Application to Efficient Dye-Sensitized Solar Cells. *Part. Part. Syst. Charact.* **2018**, *35*, 1700396.
- (50) Hu, H.; Ji, F.; Xu, Y.; Yu, J.; Liu, Q.; Chen, L.; Chen, Q.; Wen, P.; Lifshitz, Y.; Wang, Y.; et al. Reversible and Precise Self-Assembly of Janus Metal-Organosilica Nanoparticles through a Linker-Free Approach. *ACS Nano* **2016**, *10*, 7323–7330.
- (51) Padmanabhan, S. C.; McGrath, J.; Bardosova, M.; Pemble, M. E. A Facile Method for the Synthesis of Highly Monodisperse Silica@gold@silica Core–shell–shell Particles and Their Use in the Fabrication of Three-Dimensional Metallodielectric Photonic Crystals. *J. Mater. Chem.* **2012**, *22*, 11978–11987.
- (52) Wang, D.; Li, J.; Chan, C. T.; Salgueiriño-Maceira, V.; Liz-Marzán, L. M.; Romanov, S.; Caruso, F. Optical Properties of Nanoparticle-Based Metallodielectric Inverse Opals. *Small* **2004**, *1*, 122–130.
- (53) Jenkins, J. A.; Zhou, Y.; Thota, S.; Tian, X.; Zhao, X.; Zou, S.; Zhao, J. Blue-Shifted Narrow Localized

- Surface Plasmon Resonance from Dipole Coupling in Gold Nanoparticle Random Arrays. *J. Phys. Chem. C* **2014**, *118*, 26276–26283.
- (54) Oubre, C.; Nordlander, P. Optical Properties of Metallodielectric Nanostructures Calculated Using the Finite Difference Time Domain Method. *J. Phys. Chem. B* **2004**, *108*, 17740–17747.
- (55) Zhao, Y.; Zhang, X.-J.; Ye, J.; Chen, L.-M.; Lau, S.-P.; Zhang, W.-J.; Lee, S.-T. Metallo-Dielectric Photonic Crystals for Surface-Enhanced Raman Scattering. *ACS Nano* **2011**, *5*, 3027–3033.
- (56) Maas, R.; Verhagen, E.; Parsons, J.; Polman, A. Negative Refractive Index and Higher-Order Harmonics in Layered Metallodielectric Optical Metamaterials. *ACS Photonics* **2014**, *1*, 670–676.
- (57) de Ceglia, D.; Vincenti, M. A.; Cappeddu, M. G.; Centini, M.; Akozbek, N.; D’Orazio, A.; Haus, J. W.; Bloemer, M. J.; Scalora, M. Tailoring Metallodielectric Structures for Superresolution and Superguiding Applications in the Visible and Near-Ir Ranges. *Phys. Rev. A* **2008**, *77*, 033848.
- (58) Ahmadvand, A.; Pala, N.; Güney, D. Ö. Enhancement of Photothermal Heat Generation by Metallodielectric Nanoplasmonic Clusters. *Opt. Express* **2015**, *23*, 682–691.
- (59) Zhong, B. C.; Maye, M. M. Core-Shell Assembled Nanoparticles as Catalysts. *Adv. Mater.* **2001**, *13*, 1507–1511.
- (60) Song, D.; Li, C.; Colella, N. S.; Lu, X.; Lee, J.; Watkins, J. J. Thermally Tunable Metallodielectric Photonic Crystals from the Self-Assembly of Brush Block Copolymers and Gold Nanoparticles. *Adv. Opt. Mater.* **2015**, *3*, 1169–1175.
- (61) Lee, J.; Lee, Y.; Youn, J. K.; Na, H. Bin; Yu, T.; Kim, H.; Lee, S.; Koo, Y.; Kwak, J. H.; Park, H. G.; et al. Simple Synthesis of Functionalized Superparamagnetic Magnetite / Silica Core / Shell Nanoparticles and Their Application as Magnetically Separable High-Performance Biocatalysts. *Small* **2008**, *4*, 143–152.
- (62) Strickler, A. L.; Escudero-Escribano, M.; Jaramillo, T. F. Core-Shell Au@Metal-Oxide Nanoparticle Electrocatalysts for Enhanced Oxygen Evolution. *Nano Lett.* **2017**, *17*, 6040–6046.
- (63) Maeda, K.; Teramura, K.; Lu, D.; Saito, N.; Inoue, Y.; Domen, K. Noble-Metal/Cr₂O₃ Core/Shell Nanoparticles as a Cocatalyst for Photocatalytic Overall Water Splitting. *Angew. Chemie Int. Ed.* **2006**, *45*, 7806–7809.
- (64) Reguera, J.; Jiménez de Aberasturi, D.; Henriksen-Lacey, M.; Langer, J.; Espinosa, A.; Szczupak, B.; Wilhelm, C.; Liz-Marzán, L. M. Janus Plasmonic–magnetic Gold–iron Oxide Nanoparticles as Contrast Agents for Multimodal Imaging. *Nanoscale* **2017**, *9*, 9467–9480.
- (65) Xu, Z.; Hou, Y.; Sun, S. Magnetic Core/Shell Fe₃O₄/Au and Fe₃O₄/Au/Ag Nanoparticles with Tunable Plasmonic Properties. *J. Am. Chem. Soc.* **2007**, *129*, 8698–8699.
- (66) Teng, X.; Black, D.; Watkins, N. J.; Gao, Y.; Yang, H. Platinum-Magnetite Core–Shell Nanoparticles Using a Sequential Synthesis. *Nano Lett.* **2003**, *3*, 261–264.

- (67) Zhang, J.; Tang, Y.; Lee, K.; Ouyang, M. Nonepitaxial Growth of Hybrid Core-Shell Nanostructures with Large Lattice Mismatches. *Science* **2010**, *327*, 1634–1638.
- (68) Rai, P.; Majhi, S. M.; Yu, Y.-T.; Lee, J.-H. Noble Metal@metal Oxide Semiconductor Core@shell Nano-Architectures as a New Platform for Gas Sensor Applications. *RSC Adv.* **2015**, *5*, 76229–76248.
- (69) Sun, H.; He, J.; Wang, J.; Zhang, S.-Y.; Liu, C.; Sritharan, T.; Mhaisalkar, S.; Han, M.-Y.; Wang, D.; Chen, H. Investigating the Multiple Roles of Polyvinylpyrrolidone for a General Methodology of Oxide Encapsulation. *J. Am. Chem. Soc.* **2013**, *135*, 9099–9110.
- (70) Goebel, J.; Joo, J. B.; Dahl, M.; Yin, Y. Synthesis of Tailored Au@TiO₂ Core-shell Nanoparticles for Photocatalytic Reforming of Ethanol. *Catal. Today* **2014**, *25*, 90–95.
- (71) Sakai, H.; Kanda, T.; Shibata, H.; Ohkubo, T.; Abe, M. Preparation of Highly Dispersed Core/Shell-Type Titania Nanocapsules Containing a Single Ag Nanoparticle. *J. Am. Chem. Soc.* **2006**, *128*, 4944–4945.
- (72) Murshid, N.; Keogh, D.; Kitaev, V. Optimized Synthetic Protocols for Preparation of Versatile Plasmonic Platform Based on Silver Nanoparticles with Pentagonal Symmetries. *Part. Part. Syst. Charact.* **2014**, *31*, 178–189.
- (73) Pietrobon, B.; Kitaev, V. Photochemical Synthesis of Monodisperse Size-Controlled Silver Decahedral Nanoparticles and Their Remarkable Optical Properties. *Chem. Mater.* **2008**, *20*, 5186–5190.
- (74) Dove, P. M.; Han, N.; Wallace, A. F.; De Yoreo, J. J. Kinetics of Amorphous Silica Dissolution and the Paradox of the Silica Polymorphs. *Proc. Natl. Acad. Sci.* **2008**, *105*, 9903–9908.
- (75) Belton, D. J.; Deschaume, O.; Perry, C. C. An Overview of the Fundamentals of the Chemistry of Silica with Relevance to Biosilicification and Technological Advances. *FEBS J.* **2012**, *279*, 1710–1720.
- (76) Bestaoui, N.; Prouzet, E. A Chimie Douce Route to Pure Iridium Oxide. *Chem. Mater.* **1997**, *9*, 1036–1041.
- (77) Xu, D.; Diao, P.; Jin, T.; Wu, Q.; Liu, X.; Guo, X.; Gong, H.; Li, F.; Xiang, M.; Ronghai, Y. Iridium Oxide Nanoparticles and Iridium/Iridium Oxide Nanocomposites: Photochemical Fabrication and Application in Catalytic Reduction of 4-Nitrophenol. *ACS Appl. Mater. Interfaces* **2015**, *7*, 16738–16749.
- (78) von Freymann, G.; Kitaev, V.; Lotsch, B. V.; Ozin, G. A. Bottom-up Assembly of Photonic Crystals. *Chem. Soc. Rev.* **2013**, *42*, 2528–2554.
- (79) Fateixa, S.; Girão, A. V.; Nogueira, H. I. S.; Trindade, T. Polymer Based Silver Nanocomposites as Versatile Solid Film and Aqueous Emulsion SERS Substrates. *J. Mater. Chem.* **2011**, *21*, 15629–

15636.

- (80) Cadusch, P. J.; Hlaing, M. M.; Wade, S. A.; McArthur, S. L.; Stoddart, P. R. Improved Methods for Fluorescence Background Subtraction from Raman Spectra. *J. Raman Spectrosc.* **2013**, *44*, 1587–1595.
- (81) Law Al, A. T.; Adeloju, S. B. Progress and Recent Advances in Phosphate Sensors: A Review. *Talanta* **2013**, *114*, 191–203.
- (82) Ung, T.; Liz-Marzán, L. M.; Mulvaney, P. Gold Nanoparticle Thin Films. *Colloids Surfaces A* **2002**, *202*, 119–126.
- (83) Wang, Z.; Zong, S.; Chen, H.; Wu, H.; Cui, Y. Silica Coated Gold Nanoaggregates Prepared by Reverse Microemulsion Method: Dual Mode Probes for Multiplex Immunoassay Using SERS and Fluorescence. *Talanta* **2011**, *86*, 170–177.
- (84) Jensen, L.; Schatz, G. C. Resonance Raman Scattering of Rhodamine 6G as Calculated Using Time-Dependent Density Functional Theory. *J. Phys. Chem. A* **2006**, *110*, 5973–5977.

Chapter 7: Philosophical Takeaways

7.1. Perspectives in Biological and Chemical Sciences

At the beginning of my PhD program, I took one of the required courses, BH800: Perspectives in Biological and Chemical Sciences. This course brought together PhD students of Biological and Chemical Sciences from varying disciplines and research areas to discuss, present, and appreciate the diversity of research in the program. To be exposed to this diversity at the start of my research was an eye-opening experience and helped establish an understanding of the connections between various fields of study and implementing an integrative approach in my own research. Each project in the program falls under three core framework research strengths: **1.** structure and reactivity, **2.** environment and health, and **3.** biotic interactions. Through the preparation of our presentations for each research strength and how it related to our research interests while conversely participating in discussions led by classmates, we each honed our scientific inquiry skills. To conclude this work, my projects will be discussed introspectively in the context of the framework of these three research strengths and the established research goals.

7.1.1. Structure and Reactivity of Nanoscale Building Blocks

My research is heavily centered in structure and reactivity, especially the aspects of the relationship between size, shape, and composition of metal NPs and their properties, e.g. localized surface plasmon resonance (LSPR) and corresponding applications. Much of my work is focused on designing nanostructures (size, shape, and composition) to tailor desirable properties for the chosen applications. For me, the most fascinating aspect in nanoparticle synthesis is the creativity: starting with a morphology idea and designing nanostructures, using inspiration from art techniques (etching, coating, selective protection), seeing the dramatic shape and size changes accessible with fine chemical variations and constructing diverse functional nanoscale entities. Perhaps the most enjoyable part of preparing silver and gold nanoparticles is the colourful colloids, and the ability to make rainbows everyday. These

nanoscale building blocks were not just picturesque colloiddally or structurally, they can be used as powerful components in sensing applications, essentially investigating the relationship between structure and reactivity.

The two main applications explored were surface enhanced Raman spectroscopy (SERS) and surface plasmon resonance (SPR) that both rely heavily on the LSPR of metal nanoparticles. In Chapter 3, I demonstrated that silver could be controllably reduced at the vertex of a seed NP by blocking the surface with a polymer, controlling reactivity and enabling the subsequent bimorphic structure to form.¹ This new structure integrated gaps/grooves which provide localized electromagnetic (EM) hot spots for signal enhancement in Raman. One of the challenges with SERS is reproducible EM hot spots; in a NP film/substrate there can be localized enhancement with a lot of hot spots, and areas with none.² With specialized SERS microscopy, EM hot spots on substrates can be mapped, however, these will vary with analyte binding and may not be practical for experimental diagnostics.³ An alternative to engineering nanostructures with tips/grooves/gaps is magnetic concentration, a project I contributed to with SERS testing. Combining maghemite ($\gamma\text{-Fe}_2\text{O}_3$) NPs with silver decahedral NPs, and magnetically concentrating the particles on the side of a cuvette reproducibly gave hotspots and enhancement factors.⁴ In Chapter 4, silver decahedral stars were prepared, demonstrated to be excellent substrates in SERS, and could be used for SPR sensing. The tips of the stars were created using surface blocking for specific reduction of silver at the vertices of the decahedral seeds.⁵ This synthesis was one of the most colourful to observe: when the tips of the stars were growing, the colour of the colloid changed from yellow to orange to pink/red and then to purple/blue for the largest stars (Figure 4.2). The stars made excellent substrates for SERS, owing to the tips,⁵ giving our highest calculated enhancement factors, rivalling our previous work with silver flowers (faceted prisms).⁶

A consistent challenge in SPR testing was the stability of silver when exposed to analytes. Instead of measuring a LSPR shift due to adsorption of analytes onto NPs, morphological changes of the NP also

contributed to the observed variation. One could look at this as an issue and move on or could consider capitalizing upon the great enhancement provided by these analyte-induced morphological changes. In Chapter 4, stars were used in SPR sensing experiments detecting 10^{-10} M KBr reproducibly, which is much lower than the World Health Organization limits of bromide in drinking water (ca. 6×10^{-6} M).⁷ Since silver from the tips of the stars was observed to rearrange (reducing the 'spikiness' of the points), adequate aging was required to allow for this process to occur, and was not related to analytes (but could be enhanced/prevented with additives).⁵ Capitalizing on the enhancement from morphological changes, I collaborated on an additional study where analytes induced cavitation or pitting in silver decahedra that were thinly coated in gold. The creation of pits shifted the LSPR on average 1 nm more within 1-5 minutes, and even greater with longer exposure/measurement times.⁸ The key to pit creation was a thin gold coating of <5 mol. % relative to silver, which did not completely cover the surface of the silver NP. When using higher mol. % of gold, coating regimes change from plating (5-30 mol. %) to galvanic replacement of silver and generation of gold shells at 30+ mol. %.⁹

As discussed previously in Chapter 2, gold has superior chemical nobility when compared to silver. Coating silver NPs with gold provides a 'best of both worlds' opportunity to improve stability while maintaining sharp LSPRs of silver, imparting superior optical properties to AgNPs. This strategy has been used for many years in our lab,¹⁰ however, it wasn't until a collaborative project with Nicoya Lifesciences, Inc., where decahedral gold shells were essentially mass-produced, that silver rebuilding was observed. When silver is galvanically replaced by gold, silver ions remain in solution (unless removed by centrifugation), and in the presence of citrate can reincorporate into silver-gold alloyed nanostructures.⁹ This process is accompanied by a drastic colour change from the pale blue of gold shells to bright pink, purple, or red (Figure 5.3), after about one week. Not only was this discovery significant for nanoparticle synthesis and the improved stability for applications, it drives home the importance of observation and

monitoring LSPR/colloidal stability over time. It also makes me wonder how many other things were missed due to lack of proper observation/time. Hindsight is always 20/20.

In the same respect, looking back and wondering “why didn’t we try this and that sooner” is how the untold story of Chapter 6 begins. After coating nanoparticles with gold and/or silica for several years, using different metals had not been successful. That was until iridium (III) chloride was tried in the same way we had been using tetrachloroauric acid. While it didn’t work as expected, iridium was hydrolyzed and formed iridium oxide (IrO_{2-x}); that experiment by a Master’s student in our lab, Patrick Campbell, started an “all hands-on deck” collaborative project with all lab members involved. Testing all of the metal salts in our chemical inventory, we focused on four metal oxide shells, each co-author with their ‘expertise’, and Chapter 6 was completed. Presenting a straightforward method to coat metal nanoparticles with metal oxide shells combines properties from both NP types. As an added bonus, the metal oxide shells have been found to impart selectivity for plasmonic sensing applications. In the role of the first author, I was responsible for a major experimental part, tying results together, preparing figures, and writing a cohesive story, and I learned several important lessons (or re-learned) during this process; the importance of communication, setting clear expectations, and the absolute necessity for organization while collaborating.

Reflectively, key takeaways extend further than the scientific discoveries and reports; embracing serendipity and creativity, while maintaining organization has enabled me to accomplish this research on structure and reactivity. Knowing the reactivity of nanoscale blocks and their applications provides the first piece to bridging the gap between potential and reality; understanding safe usage and bioavailability are also important to establishing their new, yet to be realized, applications.

7.1.2. Environmental and Health Aspects of Nanoscale Building Blocks

We know that properties of matter on the nanoscale vary from atomic or bulk forms; this very fact has been used to generate this entire thesis. The risks and the rewards of using nanoparticles should be carefully weighed prior to implementation in the environment or health. Considerations of safety are paramount to applied use of nanoparticles; in many cases, the same properties for advantageous treatment, remediation, or diagnostics can also be disadvantageous for the environment, biota, or human health.¹¹ Several modeling studies have been completed comparing the predicted environmental concentrations (PEC) with the predicted no effect concentrations (PNEC) for different NPs. Mueller and Nowack compared risk quotients (PEC/PNEC) for nano-Ag, nano-TiO₂, and carbon nanotubes, and report the highest value for nano-TiO₂.¹² Risk quotients for nano-SiO₂, -iron oxides, -Al₂O₃, -CeO₂, and quantum dots were also modeled, and were reported to be 3-7 orders of magnitude below 1 indicating no expected risk.¹³ Even with low/limited predicted risk, proper disposal and environmental considerations when using nanoparticles should be encouraged. In completing this PhD work, ca. 10 000 vials of nanoparticles were prepared, with NP volumes varying from 2 mL to 18 mL (averaging 7 mL), 99 % of which was water. Instead of disposing >70 L of aqueous solution as a hazardous waste containing a very low amount of nanoparticles and/or metal salt, the water was evaporated, and only ca. 20 grams of sludge had to be disposed (Figure 7.1)



Figure 7.1. Waste disposal procedure from left to right: from vials to beaker for evaporation (or re-purposed solvent bottles), to NP sludge.

How chemicals are handled and disposed needs to be properly considered when managing synthesis (and following green chemistry principles). We are proud to have made the conscious decision to use water as a main solvent, as Roger A. Sheldon wrote, “The best solvent is no solvent” but if a solvent is needed then water is recommended.¹⁴ Additionally, we have avoided the use of hexadecyltrimethylammonium bromide (CTAB) as a capping agent due to its toxicity and environmental danger.¹⁵ We are quite proud of the knowledge we have been able to gain and contribute while reducing waste and limiting environmental impact.

7.1.3. Biotic Interactions of Nanoscale Building Blocks

Several years ago, in an interdepartmental collaboration with Dr. Lucy Lee, the cytotoxicity of our silica and silver decahedral NPs were tested with fish cell lines.¹⁶ The unpublished silver decahedra results actually slightly improved cell survival just above statistically significant, compared to the published low toxicity (>100 $\mu\text{g}/\text{mL}$ required for 24 h EC_{50}) determined for silica. A correlation between size and toxicity was established, with smaller NPs having greater effects.¹⁶ Recently, we have made a serendipitous

discovery of a mold colony that started to grow in our metal nanoparticle waste. Observing that it was thriving in mixed media of metal NPs (silver, gold, metal oxides) with citrate, polymers, and a number of unknown chemicals, we transferred a portion to a vial with citrate solution (which would reduce likelihood of metal NP instability), shown in Figure 7.2A. Citrate also provides some protection from metal toxicity through chelation,¹⁷ and its inclusion as nutrient allows for growth to occur.¹⁸ Noting the stability of the mold, and the release of nanoparticles into solution, samples were transferred into separate vials containing increasing concentrations of silver nitrate (Ag^+ source). Monitoring mold samples in these solutions over three months, we observed that silver was reducing on the mold's surface at higher exposure concentrations. According to Dr. Robin Slawson (Biology Department), silver can accumulate on the surface of microorganisms (being reduced), or will be taken up by the cells and inhibit regulatory functions.¹⁹ Silver reduction is the likely detoxification pathway taken by this mold based on observation of black silver accumulations and growth inhibition. The fact that this microorganism grew in the NP waste is good evidence of their non-toxic behaviour, and the limited persistence of metal ions in the waste solution.

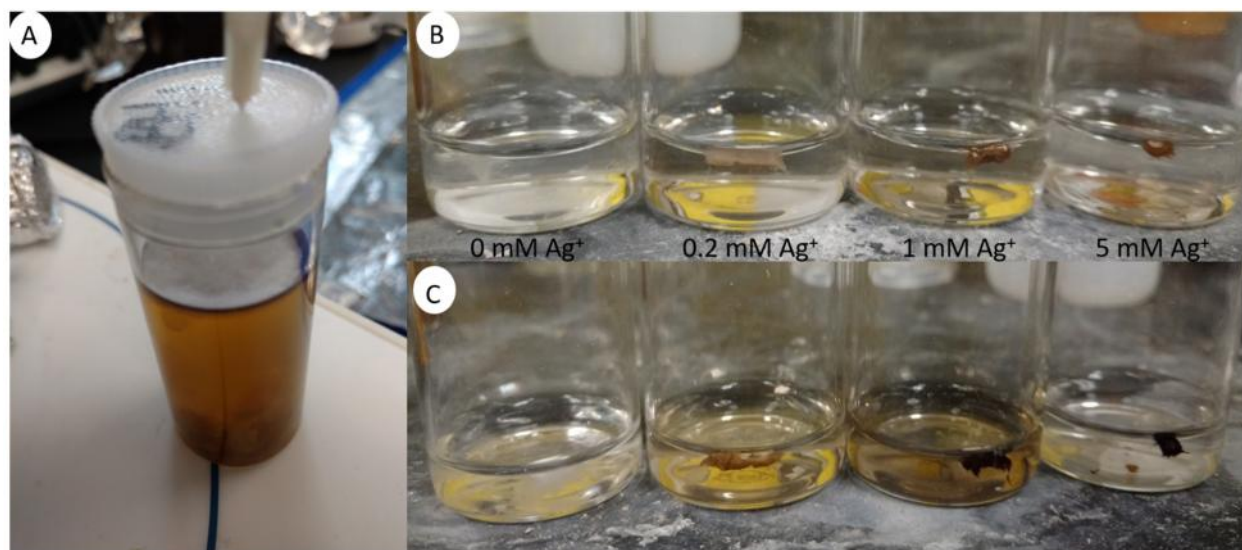


Figure 7.2. Optical photographs of mold exposure to Ag^+ over time. **A)** original mold from waste in citrate solution, mold exposed to varying concentrations of Ag^+ (labelled on figure), **B)** after one month and **C)** after three months.

Samples of ca. 2 mm of the original mold were also put into silver decahedral solutions, that have a silver concentration of 0.13 mM (Figure 7.3). Observing limited depositions and change over 3 months, we can tentatively confirm the initial assessment about Ag^+ being the contributing factor to toxicity. Some inhibition is observed with respect to growth, however, the visually unchanged sample can suggest that our NPs are relatively benign and citrate protection is maintaining stability and limiting Ag^+ release.

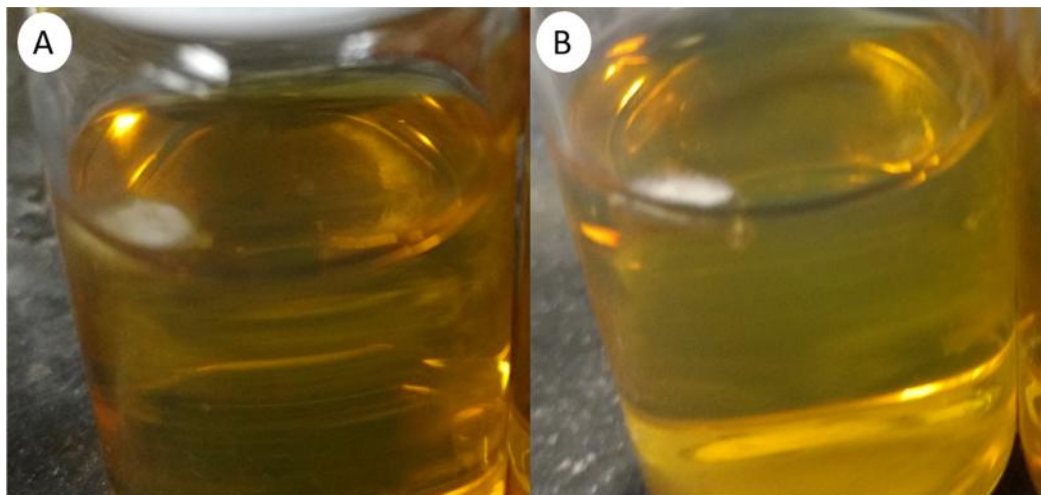


Figure 7.3. Photographs of mold in silver decahedral NP solutions **A)** original, **B)** after 3 months.

Optical (Figure 7.4) and electron microscopy (Figure 7.5) images were also prepared comparing the original specimen to those exposed to Ag^+ and decahedra. Dark and light field images were used to provide an assessment of the amount of silver taken up by the mold. Visually the mold exposed to 0.2 mM Ag^+ appears to be completely encased in metallic silver (Figure 7.4B), while the sample exposed to silver decahedral NP solution (Figure 7.4C) is closer in resemblance to the original mold sample (Figure 7.4A) as can be compared from the brightness of the images.

To determine the structure of the mold and if the uptake of particles had taken place, the sample exposed to a silver decahedral colloidal solution was imaged using electron microscopy (Figure 7.5).

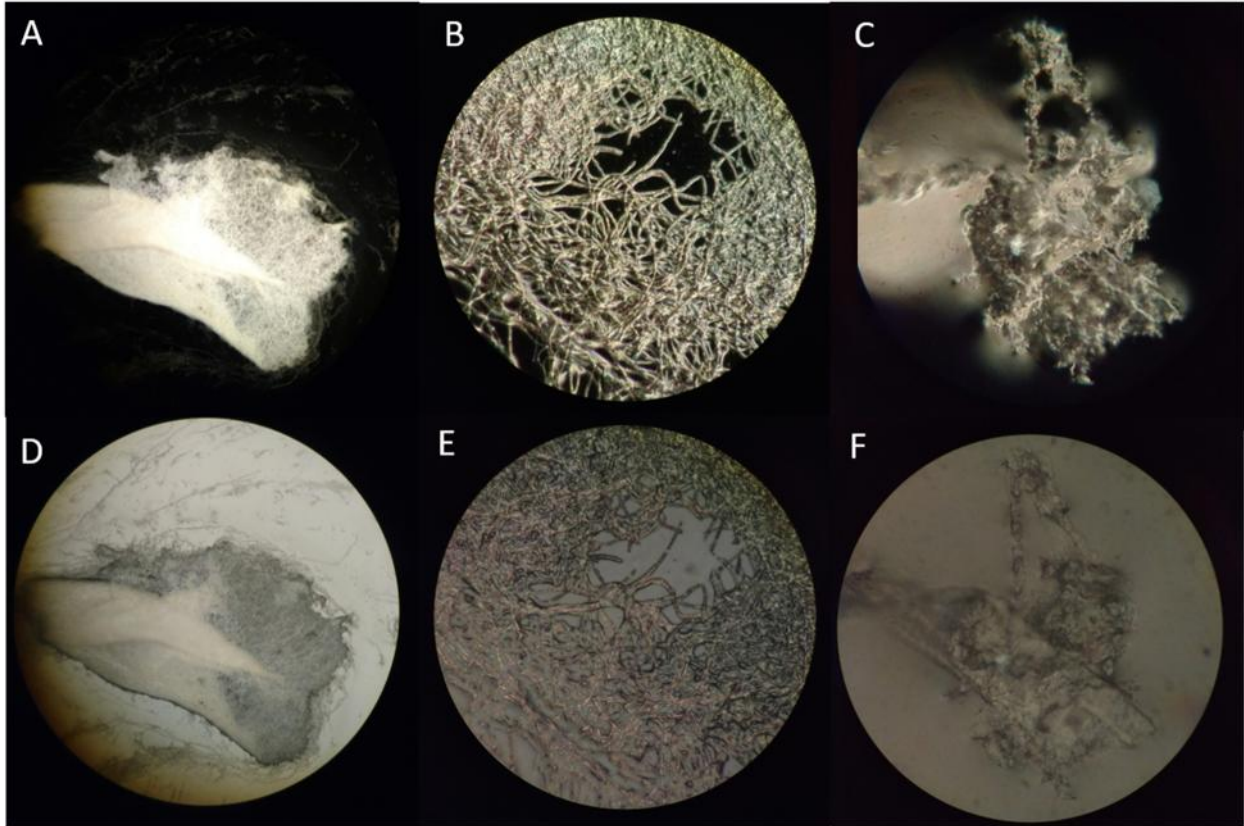


Figure 7.4. Optical microscopy images of **A&D**) original mold from waste beaker (1 mm circle diameter), **B&E**) mold exposed to 0.2 mM Ag⁺ for 3 months (450 μm circle diameter), and **C&F**) mold exposed to silver decahedra colloidal dispersions for 3 months (400 μm circle diameter). **A-C**) are dark field images, and **D-F**) are bright field images.

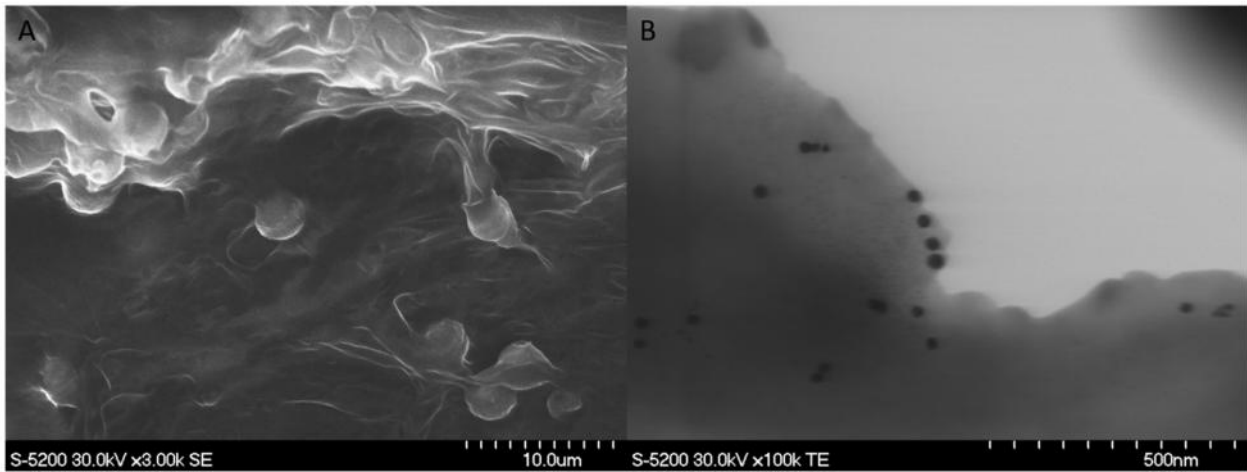


Figure 7.5. **A)** Scanning electron microscope and **B)** transmission electron microscope image of mold exposed to silver decahedra colloidal solution for 3 months.

Notably, the growth of the mold on waste nanoparticle solutions is a testament to the relative safety of these metal NP colloidal solutions.

7.2. General Conclusion

The work presented in this PhD thesis includes the preparation of nanoscale building blocks (NBBs) with well-defined and tunable functional properties and their development for specific applications. Three types of nanoparticles were prepared with a focus on metal nanoparticles for plasmonic sensing. Metallodielectric nanoparticles were also prepared for sensing applications, and lastly metal oxide nanoparticles synthesis, preliminary photoelectrochemistry results and potential for environmental remediation were discussed (Appendix 1). An improved understanding of size and shape control in the synthesis of these NPs has been attained to contribute to the field; the gap between potential and realized applications has been minimized.

7.3. Future Perspectives

From my standpoint, for the potential of NP-based sensing to be realized, solid substrates would be the most reliable and transportable system. We have started work on preparing NP films, learning many incompatible methods along the way. Most importantly, functionalization will be key for any practical tests where a simple yes/no confirmation is achieved. Both of these are topics of my proposed postdoctoral work that will expand upon what has been achieved in this work. With respect to cost and potential, metal oxides are a great option for many applications, the performance that can be enhanced with noble metal doping; this route would have been interesting to be able to explore in more depth.

7.4. References

- (1) Cathcart, N.; Kitaev, V. Symmetry Breaking by Surface Blocking: Synthesis of Bimorphic Silver Nanoparticles, Nanoscale Fishes and Apples. *Sci. Rep.* **2016**, *6*, 32561.
- (2) Sergiienko, S.; Moor, K.; Gudun, K.; Yelemessova, Z.; Bukasov, R. Nanoparticle–nanoparticle vs. Nanoparticle–substrate Hot Spot Contributions to the SERS Signal: Studying Raman Labelled

- Monomers, Dimers and Trimers. *Phys. Chem. Chem. Phys.* **2017**, *19*, 4478–4487.
- (3) Willets, K. A. Super-Resolution Imaging of SERS Hot Spots. *Chem. Soc. Rev.* **2014**, *43*, 3854–3864.
 - (4) Frank, A. J.; McEneny-King, A.; Cathcart, N.; Kitaev, V. Homogeneously Magnetically Concentrated Silver Nanoparticles for Uniform “Hot Spots” in Surface Enhanced Raman Spectroscopy. *RSC Adv.* **2015**, *5*, 73919–73925.
 - (5) Cathcart, N.; Coombs, N.; Gourevich, I.; Kitaev, V. Synthesis and Sensing Properties of D_{5h} pentagonal Silver Star Nanoparticles. *Nanoscale* **2016**, *8*, 18282–18290.
 - (6) Cathcart, N.; Kitaev, V. Multifaceted Prismatic Silver Nanoparticles: Synthesis by Chloride-Directed Selective Growth from Thiolate-Protected Clusters and SERS Properties. *Nanoscale* **2012**, *4*, 6981–6989.
 - (7) World Health Organization (WHO). *Bromide in Drinking-Water Background Document for Development of WHO Guidelines for Drinking-Water Quality*, World Health Organization, Geneva, **2009**.
 - (8) Hobbs, K.; Cathcart, N.; Kitaev, V. Gold-Plated Silver Nanoparticles Engineered for Sensitive Plasmonic Detection Amplified by Morphological Changes. *Chem. Commun.* **2016**, *52*, 9785–9788.
 - (9) Cathcart, N.; Chen, J. I. L.; Kitaev, V. LSPR Tuning from 470 to 800 nm and Improved Stability of Au–Ag Nanoparticles Formed by Gold Deposition and Rebuilding in the Presence of Poly(Styrenesulfonate). *Langmuir* **2018**, *34*, 612–621.
 - (10) McEachran, M.; Keogh, D.; Pietrobon, B.; Cathcart, N.; Gourevich, I.; Coombs, N.; Kitaev, V. Ultrathin Gold Nanoframes through Surfactant-Free Templating of Faceted Pentagonal Silver Nanoparticles. *J. Am. Chem. Soc.* **2011**, *133*, 8066–8069.
 - (11) Nowack, B. *Nanotechnology: Environmental Aspects*; Krug, H. F., Ed.; Wiley-VCH Verlag GmbH & Co. KGaA, Weinheim, Germany, **2008**.
 - (12) Mueller, N. C.; Nowack, B. Exposure Modeling of Engineered Nanoparticles in the Environment. *Environ. Sci. Technol.* **2008**, *42*, 4447–4453.
 - (13) Wang, Y.; Nowack, B. Environmental Risk Assessment of Engineered Nano-SiO₂, Nano Iron Oxides, Nano-CeO₂, Nano-Al₂O₃, and Quantum Dots. *Environ. Toxicol. Chem.* **2018**, *37*, 1387–1395.
 - (14) Sheldon, R. A. Green Solvents for Sustainable Organic Synthesis: State of the Art. *Green Chem.* **2005**, *7*, 267–278.
 - (15) Duan, H.; Wang, D.; Li, Y. Green Chemistry for Nanoparticle Synthesis. *Chem. Soc. Rev.* **2015**, *44*, 5778–5792.
 - (16) Vo, N. T. K.; Bufalino, M. R.; Hartlen, K. D.; Kitaev, V.; Lee, L. E. J. Cytotoxicity Evaluation of Silica Nanoparticles Using Fish Cell Lines. *Vitr. Cell. Dev. Biol. - Anim.* **2014**, *50*, 427–438.
 - (17) Gadd, G. M.; Griffiths, A. J. *Microorganisms and Heavy Metal Toxicity*. *Microb. Ecol.* **1977**, *4*, 304–317.
 - (18) de la Fuente, J. M.; Ramírez-Rodríguez, V.; Cabrera-Ponce, J. L.; Herrera-Estrella, L. Aluminum

Tolerance in Transgenic Plants by Alteration of Citrate Synthesis. *Science* **1997**, 276, 1566–1568.

- (19) Slawson, R. M.; Lee, H.; Trevors, J. T. Bacterial Interactions with Silver. *Biol. Met.* **1990**, 3, 151–154.

Appendix 1: Metal oxide nanoparticles as photoelectrochemical anodes and their potential for environmental remediation

A1.1. General Introduction

Metal oxide nanoparticles (MONPs) are used in sensing,¹ catalysis,² and environmental remediation³ applications owing to their diverse properties.⁴ A further discussion on MONP properties and applications is provided in Chapter 2. There is a current pursuit to use earth-abundant materials as (photo)electrochemical catalysts to split water into hydrogen (for fuel) and oxygen.⁵ MONPs have also been used as catalysts or sorbent materials for environmental remediation of water and soil.⁶⁻⁸ Required for electrochemical water splitting are an anode where the oxygen evolution reaction (OER) occurs, a cathode where the hydrogen evolution reaction (HER) takes place and an electrolyte.⁹ Metal oxide nanoparticles have shown potential to catalyze the OER as anode materials.¹⁰ Iron oxides have an ideal combination of tailorable electronic and magnetic properties through varied accessible oxidation states and polymorphs while also being abundant with low biotoxicity.¹¹ Manganese oxides have gained increasing interest owing to the manganese cluster in photosystem II as a natural water oxidation catalyst.¹²

A1.2. Synthesis Methods

The MONPs studied in this PhD work are iron oxides and manganese oxides. Iron oxides are common in nature and their nanoparticles are straightforward to synthesize in the lab. There are a wide range of procedures to prepare MnO_{2-x} nanoparticles including spray deposition,¹³ by reduction of potassium permanganate (KMnO_4) with a polyelectrolyte,¹⁴ or through sonication.¹⁵ Representative images of the akageneite, hematite and manganese oxide nanoparticles for this PhD work are shown in Figure A1.1.

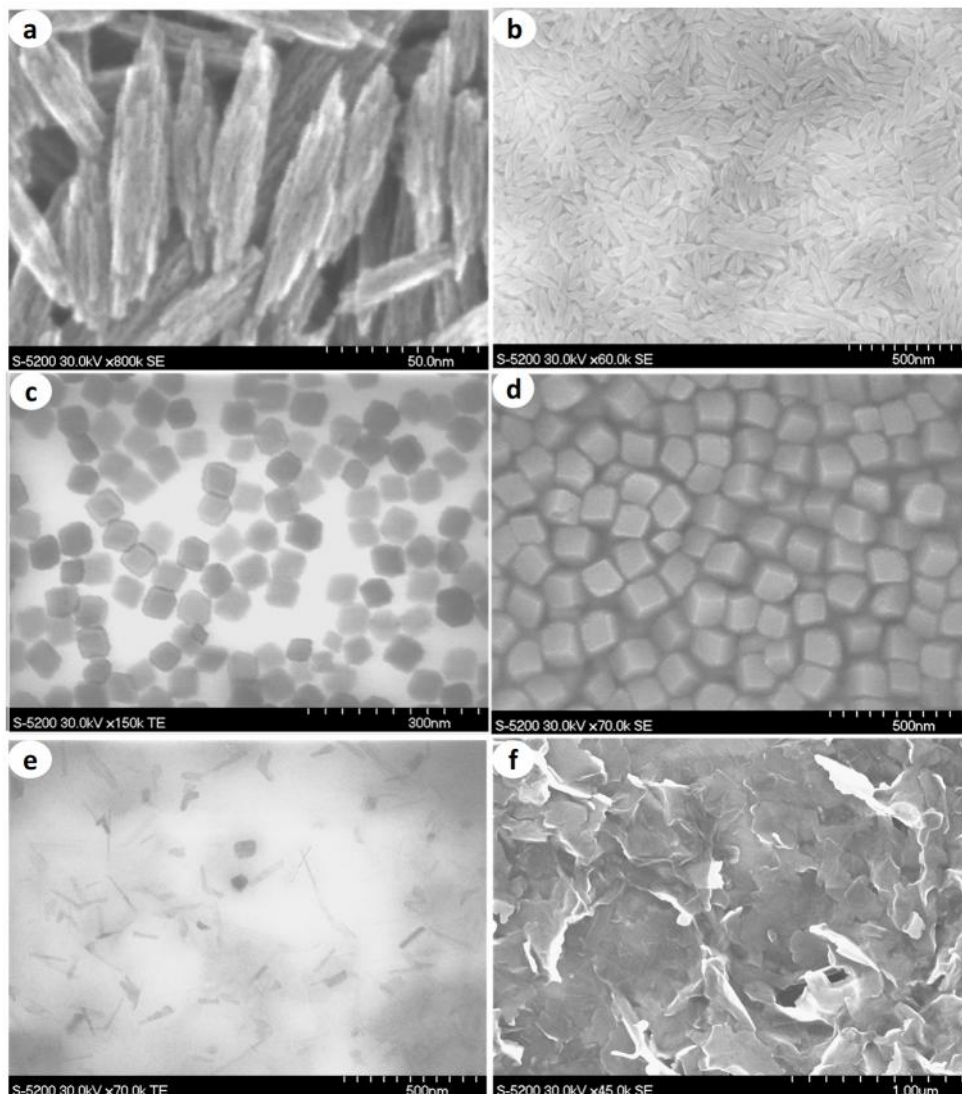


Figure A1.1. Representative electron microscopy images of a) and b) akageneite, c) and d) hematite and e) and f) MnO_{2-x} nanoparticles.

A1.3. Experimental Details

A1.3.1. Iron Oxide Nanoparticle Synthesis

Iron oxide nanoparticles/iron oxyhydroxide nanoparticles are prepared by dissolving an iron salt (typically FeCl_3) in water, and then either heated or exposed to light (white LED) for >24 hours to produce hematite or akageneite respectively. 5 mM solutions were prepared by combining 27 mg of ferric chloride hexahydrate ($\text{FeCl}_3 \cdot 6\text{H}_2\text{O}$) and 20 mL of Millipore treated ultrapure water. Concentration is important to

mediate pH and to allow for effective hydrolysis. Concentrations greater than 15 mM limited conversion to hematite due to higher pH.

A1.3.2. Synthesis of Manganese Oxide NPs

Manganese oxide NPs were prepared by combining 1.8 mL Millipore treated water with 100 μL of 0.01M MnCl_2 , 50 μL of 0.02 M polyacrylic acid ($M_w = 1800$), 50 μL of 0.15 M NaOH, and 50 μL of 0.2 M H_2O_2 . Upon addition of hydrogen peroxide, the solution turns pale yellow, and develops over 5-10 minutes to orange.

A1.3.3. Photoelectrochemical Set-Up

The photoelectrochemical set up consisted of a platinum cathode, a voltage generator, a programmable DC load (to confirm voltage), an ammeter (to measure current), glassy carbon or fluorine-doped tin oxide (FTO)-coated glass slides as substrates for anode deposition, an electrolyte solution (typically 0.15 M NaOH) and LEDs as light sources. The photoelectrochemical cell setup is shown in Figure A1.2.



Figure A1.2 A photograph of a photoelectrochemical cell set up used in my PhD work.

Templating metal oxide nanoparticles as films onto the glassy carbon or FTO (shown above) and then measuring the changes in the current with exposure to light enables us to determine the photocurrent density of the films. Water will split electrolytically when the applied voltage is 1.23 V¹⁶ as such, it is important to achieve and reliably measure the reaction at lower voltages. High photocurrent densities are one of the parameters to optimize, however, the charge transfer efficiency also needs to be considered, which is the driving force for chemical reactions of the electrolyte.¹⁷

As a preliminary step, metal oxide NP dispersions were dried on FTO, inserted into the photoelectrochemical cell set up, allowed to equilibrate until a constant current was established, and then illuminated with a white LED (to simulate solar light). The photocurrent densities are calculated by the average increase in current (μA) over the size of the NP film (cm^2). Table 2.1 summarizes the photocurrent density of a variety of metal oxide photoelectrodes reported in the literature and several examples from this PhD work.

Table A1.1. Summary of photocurrent density measured with various metal oxide photoelectrodes

Anode Composition	Substrate	Voltage (V)	Reference Electrode	Photocurrent density ($\mu\text{A}/\text{cm}^2$)	Electrolyte	Light intensity (mW/cm^2)	Ref.
Hematite	FTO	0.7	RHE	0	1 M NaOH	100	18
Hematite	FTO	0.7	RHE	0	1 M NaOH	Solar Light 16S - 300 solar simulator	19
Hematite (iron oxide)	FTO	0.7 (+0.2)	SCE	0	NR	NR	20
Hematite + Si	FTO	0.7 (+0.2)	SCE	0	1 M NaOH	100	21
Hematite + Ge	FTO	0.3 (+0.2)	SCE	100	1 M NaOH	150	22
Hematite + Ir	FTO	0.7	RHE	0	1 M NaOH	100	23
BiVO_4 + Co-Pi	FTO	0.7	RHE	250	0.5 M K_2SO_4	100	24
Hematite + Co-Pi	FTO	0.7	RHE	0	1 M NaOH	100	25
Ta_3N_5	FTO	0.7 (+0.2)	Ag/AgCl	70	0.1 M Na_2SO_4	300	26
MnO_2	Glassy Carbon	0.7		102	1 M NaOH	100	VK lab
RuO_2	Glassy Carbon	0.7		24	0.15 M NaOH	100	VK lab
Hematite	FTO	0.7		230	0.15 M NaOH	100	VK lab

A1.4. Future Work – Photoelectrochemistry

One of the possibilities to improve photocurrent densities are to use mixed metal oxides, or doped metal oxides. Additionally, determining templating/film stabilities and processing (heat treatment) will be an important part for implementation. The development of a full cell for both half reactions of water splitting will be necessary for potential implementation; considerations of electrolyte and cathode will be required. In addition to water splitting, use of the current generated can also be used to degrade contaminants, for example, chlorinated organics to chloride and CO_2 .²⁷

A1.5. Future Work- Environmental Remediation

Magnetic separation of heavy metals is a promising route to environmental remediation; for example, maghemite has been demonstrated to adsorb arsenic (V) and then both can be removed magnetically.²⁸ Maghemite NPs coated with PVP have also been used to adsorb and remove the emerging contaminants, Tonalide, Bisphenol-A, Triclosan, Metalachlor, Ketoprofen, and Estriol, from aqueous solutions.²⁹ Optimizing the surface of magnetic NPs by polymers (type, molecular weight, charge, etc.) is a desirable and potentially fruitful direction for removal of environmental contaminants. A further step would be to use MONPs as catalysts to degrade contaminants, ideally photochemically (solar), in a combined adsorption-degradation pathway.

Previously, there has been success in our lab removing phosphorous from wastewater with Iron Oxide NPs and hydrogen peroxide. Continuing this work and expanding to other contaminants is a viable research direction.

A1.6. References

- (1) Sun, Y.-F.; Liu, S.-B.; Meng, F.-L.; Liu, J.-Y.; Jin, Z.; Kong, L.-T.; Liu, J.-H. Metal Oxide Nanostructures and Their Gas Sensing Properties: A Review. *Sensors* **2012**, *12*, 2610–2631.
- (2) Kung, H. H. *Transition Metal Oxides : Surface Chemistry and Catalysis*; Elsevier, Amsterdam, **1989**.
- (3) Hua, M.; Zhang, S.; Pan, B.; Zhang, W.; Lv, L.; Zhang, Q. Heavy Metal Removal from Water/Wastewater by Nanosized Metal Oxides: A Review. *J. Hazard. Mater.* **2012**, *211*, 317–331.
- (4) Lu, J. G.; Chang, P.; Fan, Z. Quasi-One-Dimensional Metal Oxide Materials—Synthesis, Properties and Applications. *Mater. Sci. Eng. R Reports* **2006**, *52*, 49–91.
- (5) Roger, I.; Shipman, M. A.; Symes, M. D. Earth-Abundant Catalysts for Electrochemical and Photoelectrochemical Water Splitting. *Nat. Rev. Chem.* **2017**, *1*, 0003.
- (6) Adeleye, A. S.; Conway, J. R.; Garner, K.; Huang, Y.; Su, Y.; Keller, A. A. Engineered Nanomaterials for Water Treatment and Remediation: Costs, Benefits, and Applicability. *Chem. Eng. J.* **2016**, *286*, 640–662.
- (7) Wan, S.; Wu, J.; Zhou, S.; Wang, R.; Gao, B.; He, F. Enhanced Lead and Cadmium Removal Using Biochar-Supported Hydrated Manganese Oxide (HMO) Nanoparticles: Behavior and Mechanism. *Sci. Total Environ.* **2018**, *616–617*, 1298–1306.

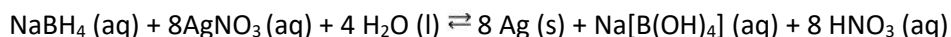
- (8) Peng, J.; Song, Y.; Yuan, P.; Cui, X.; Qiu, G. The Remediation of Heavy Metals Contaminated Sediment. *J. Hazard. Mater.* **2009**, *161*, 633–640.
- (9) Li, X.; Hao, X.; Abudula, A.; Guan, G. Nanostructured Catalysts for Electrochemical Water Splitting: Current State and Prospects. *J. Mater. Chem. A* **2016**, *4*, 11973–12000.
- (10) Harriman, A.; Pickering, I. J.; Thomas, J. M.; Christensen, P. A. Metal Oxides as Heterogeneous Catalysts for Oxygen Evolution under Photochemical Conditions. *J. Chem. Soc. Faraday Trans. 1 Phys. Chem. Condens. Phases* **1988**, *84*, 2795.
- (11) Tartaj, P.; Morales, M. P.; Gonzalez-Carreño, T.; Veintemillas-Verdaguer, S.; Serna, C. J. The Iron Oxides Strike Back: From Biomedical Applications to Energy Storage Devices and Photoelectrochemical Water Splitting. *Adv. Mater.* **2011**, *23*, 5243–5249.
- (12) Loll, B.; Kern, J.; Saenger, W.; Zouni, A.; Biesiadka, J. Towards Complete Cofactor Arrangement in the 3.0 Å Resolution Structure of Photosystem II. *Nature* **2005**, *438*, 1040–1044.
- (13) Takashima, T.; Hashimoto, K.; Nakamura, R. Mechanisms of PH-Dependent Activity for Water Oxidation to Molecular Oxygen by MnO₂ Electrocatalysts. *J. Am. Chem. Soc.* **2012**, *134*, 1519–1527.
- (14) Luo, Y. Preparation of MnO₂ Nanoparticles by Directly Mixing Potassium Permanganate and Polyelectrolyte Aqueous Solutions. *Mater. Lett.* **2007**, *61*, 1893–1895.
- (15) Zhu, S.; Zhou, H.; Hibino, M.; Honma, I.; Ichihara, M. Synthesis of MnO₂ Nanoparticles Confined in Ordered Mesoporous Carbon Using a Sonochemical Method. *Adv. Funct. Mater.* **2005**, *15*, 381–386.
- (16) Rossmeisl, J.; Logadottir, A.; Nørskov, J. K. Electrolysis of Water on (Oxidized) Metal Surfaces. *Chem. Phys.* **2005**, *319*, 178–184.
- (17) Chu, S.; Li, W.; Yan, Y.; Hamann, T.; Shih, I.; Wang, D.; Mi, Z. Roadmap on Solar Water Splitting: Current Status and Future Prospects. *Nano Futur.* **2017**, *1*, 022001.
- (18) Sivula, K.; Zboril, R.; Le Formal, F.; Robert, R.; Weidenkaff, A.; Tucek, J.; Frydrych, J.; Grätzel, M. Photoelectrochemical Water Splitting with Mesoporous Hematite Prepared by a Solution-Based Colloidal Approach. *J. Am. Chem. Soc.* **2010**, *132*, 7436–7444.
- (19) Tahir, A. A.; Wijayantha, K. G. U.; Saremi-Yarahmadi, S.; Mazhar, M.; McKee, V. Nanostructured α-Fe₂O₃ Thin Films for Photoelectrochemical Hydrogen Generation. *Chem. Mater.* **2009**, *21*, 3763–3772.
- (20) Bora, D. K.; Braun, A.; Constable, E. C. “In Rust We Trust”. Hematite – the Prospective Inorganic Backbone for Artificial Photosynthesis. *Energy Environ. Sci.* **2013**, *6*, 407–425.
- (21) Cesar, I.; Kay, A.; Gonzalez Martinez, J. A.; Grätzel, M. Translucent Thin Film Fe₂O₃ Photoanodes for Efficient Water Splitting by Sunlight: Nanostructure-Directing Effect of Si-Doping. *J. Am. Chem. Soc.* **2006**, *128*, 4582–4583.
- (22) Sanchez, H. L.; Steinfink, H.; White, H. S. Solid Solubility of Ge, Si, and Mg in Fe₂O₃ and Photoelectric Behavior. *J. Solid State Chem.* **1982**, *41*, 90–96.
- (23) Tilley, S. D.; Cornuz, M.; Sivula, K.; Grätzel, M. Light-Induced Water Splitting with Hematite: Improved Nanostructure and Iridium Oxide Catalysis. *Angew. Chemie* **2010**, *122*, 6549–6552.

- (24) Abdi, F. F.; van de Krol, R. Nature and Light Dependence of Bulk Recombination in Co-Pi-Catalyzed BiVO₄ Photoanodes. *J. Phys. Chem. C* **2012**, *116*, 9398–9404.
- (25) Zhong, D. K.; Cornuz, M.; Sivula, K.; Grätzel, M.; Gamelin, D. R. Photo-Assisted Electrodeposition of Cobalt–phosphate (Co–Pi) Catalyst on Hematite Photoanodes for Solar Water Oxidation. *Energy Environ. Sci.* **2011**, *4*, 1759–1764.
- (26) Chen, Y.; Liang, S.; Wen, L.; Wu, L. A TaON Nano-Photocatalyst with Low Surface Reduction Defects for Effective Mineralization of Chlorophenols under Visible Light Irradiation. *Phys. Chem. Chem. Phys.* **2013**, *15*, 12742–12747.
- (27) Martínez-Huitle, C. A.; Ferro, S. Electrochemical Oxidation of Organic Pollutants for the Wastewater Treatment: Direct and Indirect Processes. *Chem. Soc. Rev.* **2006**, *35*, 1324–1340.
- (28) Tuutijärvi, T.; Lu, J.; Sillanpää, M.; Chen, G. As(V) Adsorption on Maghemite Nanoparticles. *J. Hazard. Mater.* **2009**, *166*, 1415–1420.
- (29) Alizadeh Fard, M.; Vosoogh, A.; Barkdoll, B.; Aminzadeh, B. Using Polymer Coated Nanoparticles for Adsorption of Micropollutants from Water. *Colloids Surfaces A Physicochem. Eng. Asp.* **2017**, *531*, 189–197.

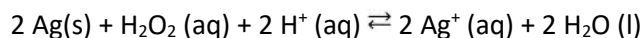
Appendix 2: Methods and Glossary

A2.1. Decahedra NP synthesis

Colloidal solutions of decahedra are prepared in a 20 mL borosilicate vial with a stir bar (3 mm by 12.7 mm), on a stir plate set to 350 rpm. 14.0 mL Millipore water, 520 μL of 0.05 M tricitrate, 23 μL of 0.05 M poly styrene sulfonate (or 25 μL of 0.05 M poly(vinyl pyrrolidone)), 25 μL of 0.005 M arginine, 400 μL of 0.005 M silver nitrate and 200 μL of 0.1 M sodium borohydride are combined in order with constant stirring. The solution will turn pale yellow with the addition of sodium borohydride. The reduction of silver by sodium borohydride is described by the following reaction:



After 50 minutes to 1 hour the solutions darken in colour to a more vibrant yellow, and 300 μL of 10.4 M hydrogen peroxide is added. The oxidative etching of hydrogen peroxide establishes a redox equilibrium between the silver's reduction from sodium borohydride and oxidation from hydrogen peroxide:



With the hydrogen peroxide addition, the solution starts to bubble; 10 minutes elapse before removing the stir bar (magnetically) and putting the cap on the vial. The vial is then put on a 450 nm LED for 14 hours. Photos of the LED set up are presented in Figure 5S.2A.

A2.2. Measuring NP size

From EM images, a ruler is used to determine lateral size according to the schematic below:

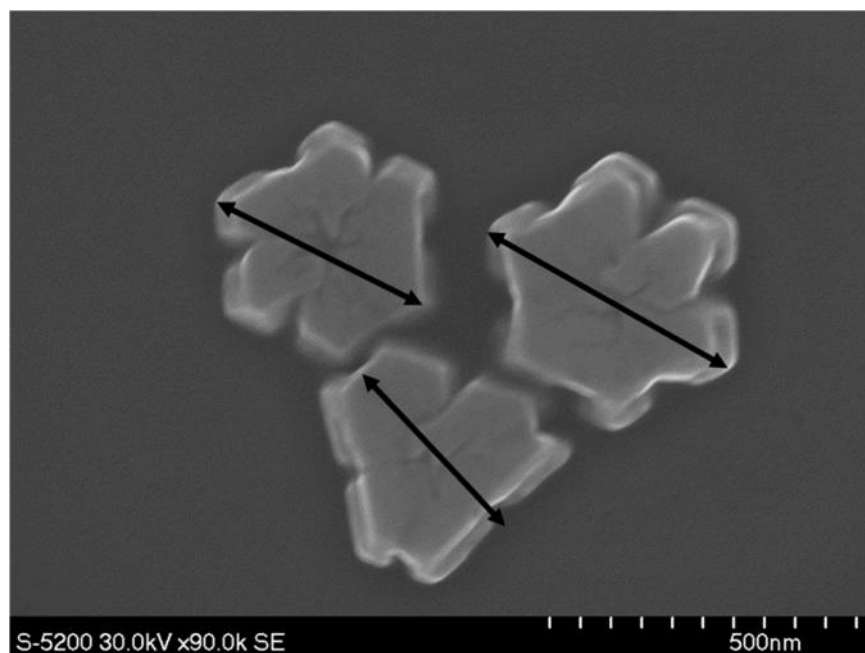


Figure A2.1. Scanning electron microscopy image of faceted silver platelets with drawn lines across lateral dimensions to measure size.

Inputting the values (in cm) into excel, the average is calculated, and is then converted to nm using the scale bar of the image (e.g. scale 500 nm = 3.8 cm, particle = 500 nm/3.8 cm × 2.8 cm = 368 nm)

A2.3. Surface plasmon resonance sensing measurements

First, the instrument (OpenSPR) is turned on and the software is initiated, dark and light references are taken (using software); then 1 mL of NP solution is pipetted into a half cell (PMMA cuvette, path length 0.5 cm), which is subsequently placed into the OpenSPR instrument fit with a cell holder (Figure A2.2).

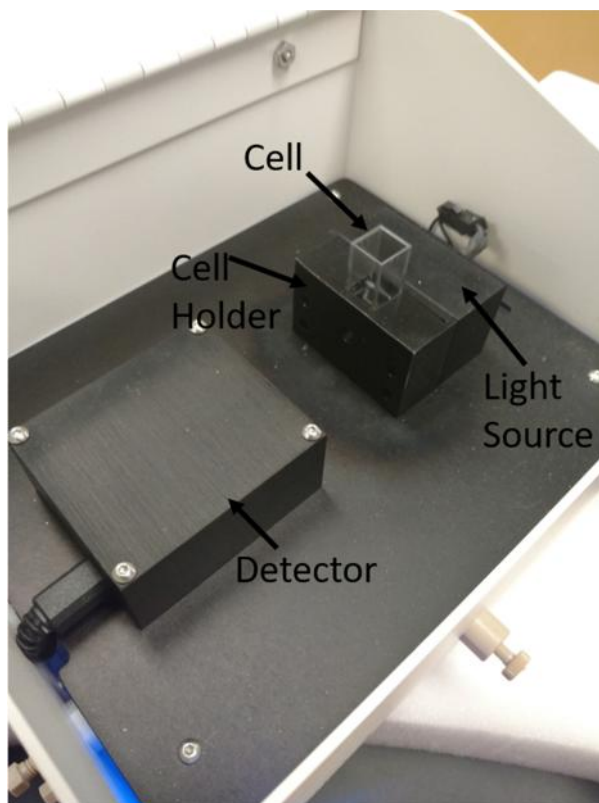


Figure A2.2. Photograph of OpenSPR instrumental set-up for SPR measurements.

Following the software's prompts, data fitting starts, selecting the LSPR peak and recording it with time. After 5-10 minutes, the peak stabilizes, at which point the analyte of interest is added by a pipette (injected). A cell cap is added to the cuvette containing the NP solution and analyte, it is removed to mix (by shaking), and replaced in the cell holder to continue measurements. This process takes less than 5 seconds. At the end of the measurement, the data populates an Excel file with two columns, one for the time in seconds, one for the LSPR peak in nm. This data is then used to make SPR graphs. To determine LSPR shifts with the analyte, the LSPR peak at the time of injection is subtracted from the LSPR peak at 100 seconds after injection.

A2.4. Surface enhanced Raman spectroscopy measurements

1 mL of colloidal NP solution was centrifuged at 3000 g for 30 minutes, separating the solution into a concentrated NP pellet, and supernatant. The supernatant was removed by a pipette, leaving 10 μL of a concentrated dispersion. The concentrated dispersion was dispensed onto a plasma cleaned quartz slide, spread to ca. 1 cm^2 and then dried in an oven at 60 $^{\circ}\text{C}$. A spectrum was taken of this film by inserting the quartz slide into the sample holder and starting the laser with the software.

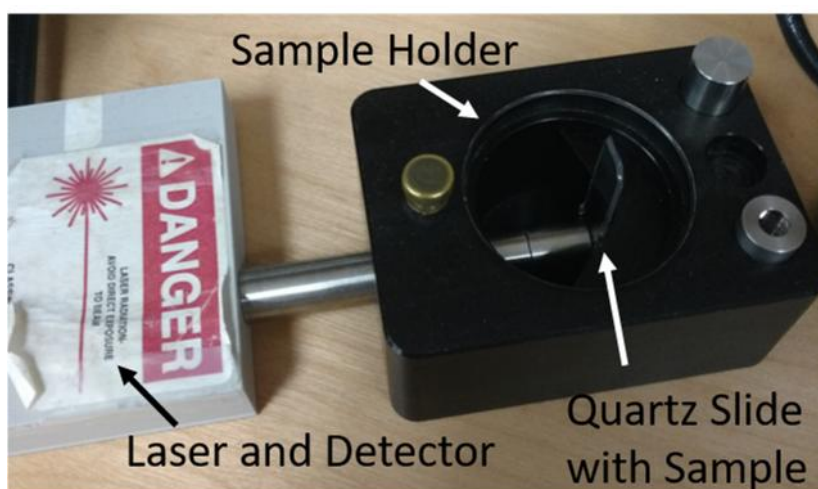


Figure A2.3. Photograph of laser and sample holder set up for surface enhanced Raman spectroscopy measurements.

For surface enhancement measurements, a known concentration of target analyte is spread to the same 1 cm^2 area over the film in 10 μL increments, the film was dried, and a spectrum was taken. Once a spectrum with discernable peaks is obtained, a chosen peak's intensity can be compared to that of the non-enhanced analyte. For example, with 5,5'-dithiobis(2-nitrobenzoic acid), a strong peak at ca. 1330 cm^{-1} is detected. In the non-enhanced measurement, 9.08 $\times 10^{-6}$ moles/ cm^2 this peak has an intensity of 698, and for the enhanced measurement (with silver decahedra), 1.25 $\times 10^{-11}$ moles/ cm^2 this peak is 1031. Calculating the peak intensity per moles per area (intensity/(moles/ cm^2)) for each of these

measurements gives 7.6×10^7 and 8.2×10^{13} for the reference and enhanced measurements, respectively. To calculate the enhancement factor, the enhanced (intensity/(moles/cm²)) is divided by the reference, giving an enhancement factor of 1.07×10^6 in this example.

Measurements were performed at 290 mW laser power with 30 s integration and frame sizes, set by tuning laser power on the instrument, and in the software.

A2.5. Glossary

Adatom – an adsorbed atom on a nanoparticle surface.

Analyte – a chemical species of interest to identify.

Decahedron – a polyhedron with 10 faces, in this work referring to a pentagonal bipyramid, Johnson solid J₁₃). Johnson solids are a set of polyhedra made of regular polygons at each face (not required to be the same polygon as with Platonic solids).

Doping – the addition of a trace impurity element to change properties. Many gemstone colours are due to doping; for example, the red colour of ruby is due to chromium ions in aluminum oxide.

Physisorption – a physical adsorption process that minimally disturbs the electronic structure of the atom or molecule.

Platonic solids – a set of five most symmetric polyhedra constructed by polygonal faces with equal sizes and angles meeting the same number of vertices: tetrahedron (4 faces), cube (6 faces), octahedron (8 faces), dodecahedron (12 faces), and icosahedron (20 faces).

Surface enhanced Raman spectroscopy – Raman scattering enhanced by roughened metal films or nanoparticles. Photons are scattered inelastically (having a different energy after interaction than before).

Surface plasmon resonance – oscillation of electrons at the interface of two materials induced by light.

In metal films, this resonance propagates along the surface, in metal nanoparticles the resonance is localized, and is then called localized surface plasmon resonance.

Surface plasmon resonance spectroscopy- a measure of a change in the interaction of light with either a metal film or nanoparticles through adsorption onto their surface. The adsorption changes the resonance at the surface of the metal.

UV-vis spectroscopy - a branch of spectroscopy dealing with the interaction of light (in the ultraviolet to visible range) with matter. In this work, UV-vis spectroscopy is used to measure the absorbance and scattering of light from nanoparticle colloidal solutions. The wavelength of light that is absorbed is complementary to that which is observed.

